Numerical simulation of forced ignition using LES coupled with a tabulated detailed chemistry approach

Subramanian Vallinayagam Pillai Vallinayagam Pillai

École Doctorale – S.P.M.I.I.

THÈSE

Présentée par

V. Subramanian

Pour l'obtention du grade de

Docteur de l'Institut National des Sciences Appliquées de Rouen

Discipline :	Energétique.
Spécialité :	Mécanique des Fluides.
Formation Doctorale :	Sciences Physiques, Mathématiques et de l'Information pour l'Ingénieur.
Laboratoire d'Accueil :	UMR-CNRS-6614-CORIA.

Numerical Simulation of Forced Ignition Using LES Coupled with a Tabulated Detailed Chemistry Approach

Le 12 janvier 2010

Membres du Jury

Rapporteurs :

Epaminondas Mastorakos	Professeur, Cambridge University, Royaume-Uni
Olivier Colin	Ingénieur Chercheur, Institut Français du Pétrole (IFP)

Examinateurs :

Denis Veynante	Directeur de Recherche, École Centrale Paris (EM2C)
Ananias Tomboulides	Professeur, University of Western Macedonia

Directeurs de thèse :

Pascale Domingo	Chargée de Recherche CNRS, INSA de Rouen
Luc Vervisch	Professeur, INSA de Rouen

Acknowledgments

Words fall short as I express my heartfelt acknowledgement to all those people who make me feel fortunate for where I stand today. With this ecstatic feeling of completing my doctoral thesis, when I rewind and play back the wonderful memories of my stay from day one, I see plenty of faces who had supported me through this journey in one way or the other. It is my greatest pleasure to use few front pages of my thesis to express my heartfelt gratitude to them.

My earnest and foremost acknowledgement goes to my thesis advisors Dr. Pascale Domingo and Prof. Luc Vervisch, who offered me a great opportunity to pursue my Ph.D in France, under their esteemed guidance. I enjoyed an overwhelming technical support from Dr. Domingo throughout the entire course of this thesis work. Every-time, when I faced challenges with my research work, Dr. Domingo spared her valuable time and offered inspirational advices and solutions through series of interactive dialogues. She had the patience to explain me the functioning of CFD routines, an important process for a person like me who never had any exposure to CFD coding at the start of this work. Beside being a guide, Dr. Domingo offered an excellent moral support and showed great caring, which, I otherwise would have missed being so far from my family.

Prof. Vervisch inspired me with his ever energetic and enthusiastic approach in dealing with research problems. During the three years of my Ph.D, I have seen in him an excellent advisor who can bring the best out from his students, an outstanding researcher who can constructively criticize research and a nice human being who is honest, fair and helpful to others. I cannot forget his invaluable inputs and hints during the developmental stage of mono-dimension flamelet solver, which finally helped us to have a beautiful publication in *Combustion and Flame* journal. Prof. Vervisch also provided me plenty of opportunities to attend project meetings and seminars, which not only helped me to improve my presentation skills but also gave me a chance to travel around Europe.

I am deeply indebted to Prof. Mastorakos of Cambridge University (UK), for his support and suggestions during this work. He also was kind enough to provide the experimental data for validation and also offered advices and clarifications at critical junctures. Dr. Ahmed of Cambridge University deserves my sincerest gratitude for providing me with the experimental data. I wish to thank all the members of my thesis jury, for their presence on the final day of presentation and their constructive criticism as well as kind encouragement.

A special thanks to Dr. Ganesan, who had introduced me to CORIA lab and helped me set-up my stay in Rouen. I am grateful to Mrs. Isabelle Lebon, who had kindly tolerated my

broken French and helped me through many administrative formalities and booked the travel tickets for many of my trips. Thanks to my dear colleagues Guillaume Godel (who offered me a good company in lab for three years and also helped me in preparing French abstract), Nicolas Enjalbert, Cindy Merlin and Grégory Bonomeau. I really enjoyed our mini basketball sessions we used to have in our bureau during the break. I would like to appreciate the help offered by my seniors Guido Lodata and Alexandre Naudin during the group meeting and several other occasions. Hearty thanks to each and everyone in the research team of *Laboratoire de Mécanique des Fluides Numérique*.

CORIA lab is an unforgettable place to do research work and I would like to thank all the members of the CORIA family. I would like to specially thank my dearest friends Arnab, Ouissem, Dahn, Fon and Mechline. The lunch and coffee break chit-chats were really refreshing and helped me overcome the work stress.

Most important of all, I would like to thank my beloved mother, my sister, my brother in-law and all my relatives for being a source of constant moral courage and inspiration.

Lastly, I would like acknowledge the financial support given by the European project TIMECOP-AE (Towards innovative methods for combustion prediction in aero- engines) and CNRS (Centre national de la recherche scientifique), who paid my salary during the complete duration of the thesis.

Abstract

Numerical Simulation of Forced Ignition Using LES coupled with a Tabulated Detailed Chemistry Approach

The optimization of the ignition process is a crucial issue in the design of many combustion systems. Large eddy simulation (LES) of a conical shaped bluff body turbulent non-premixed burner has been performed to study the impact of spark location on ignition success. The chemistry part of the simulation is done using tabulated detailed chemistry approach. This burner was experimentally investigated by Ahmed et al at Cambridge (UK).

The present work focuses on the case without swirl for which detailed measurements are available. First, cold flow measurements of velocities and mixture fraction are compared with their LES counterparts, to assess the prediction capabilities of simulations in terms of flow and turbulent mixing.

Time history of velocities and mixture fraction are recorded at selected spots, to probe the resolved probability density function (pdf) of flow variables, in an attempt to reproduce, from the knowledge of LES resolved instantaneous flow conditions, the experimentally observed reasons of success or failure of spark ignition. A flammability map is also constructed from the resolved mixture fraction pdf and compared with its experimental counterpart. LES of forced ignition is then performed using flamelet fully detailed tabulated chemistry combined with presumed pdfs (PCM-FPI).

Various scenarios of flame kernel development are analyzed and correlated with typical flow conditions observed in this burner. The correlations between velocities and mixture fraction values at the sparking time and the success or failure of ignition are then further discussed and analysed. The rate of flame development during successful or unsuccessful ignition events are analysed and compared against experimental observations.

Finally, from asymptotic flame analysis, a novel approach has been proposed to include flame straining effects in the PCM-FPI method developped at CORIA-CNRS. The new model overcomes the problem associated with classical PCM-FPI closure to model kernel quenching due to intense local turbulence. Computations are done including the flame straining effects and the effect brought by the new model on kernel development is analysed in detail.

Keywords: Large eddy simulation, Spark ignition, Laminar flamelets, Turbulent flames

Résumé

Modélisation de la combustion turbulente. Application des méthodes de tabulation de la chimie détaillée Í'allumage forcé

L'optimisation des systèmes d'allumage est un paramètre critique pour la définition des foyers de combustion industriels. Des simulations aux grandes échelles (ou LES pour Large-Eddy Simulation) d'un brûleur de type bluff-body non prémélangé ont été menées afin de comprendre l'influence de la position de la bougie sur la probabilité d'allumage. La prise en compte de la combustion est basée sur une méthode de tabulation de la chimie détaillée (PCM-FPI pour Presumed Conditional Moments - Flame Prolongation of ILDM). Les résultats de ces simulations ont été confrontés des résultats expérimentaux disponibles dans la littérature. Dans un premier temps, les mesures de vitesse et du champ de richesse froid sont comparées aux résultats de la simulation pour évaluer les capacités de prédiction en terme de structure de l'écoulement et de mélange turbulent. Un suivi temporel des vitesses et de la fraction de mélange est réalisé différents points pour déterminer les fonctions de densité de probabilité(ou PDF)des variables caractéristiques de l'écoulement, partir des champs résolus en LES. Les PDFs ainsi obtenues servent l'analyse des phénomènes d'allumages réussis ou déficients rencontrés expérimentalement. Des simulations d'allumage forcé ont été effectués pour analyser les différents scénarios de développement de la flamme. Les corrélations entre les valeurs locales (fraction de mélange, vitesse) autour de la position d'allumage et les chances de succès de développement du noyau de gaz brlés sont alors discutées. Enfin, une extension de la méthode PCM-FPI avec prise en compte des effets d'étirement est développée l'aide d'une analyse asymptotique, puis confrontée aux résultats de mesures expérimentales.

Mots-clés : Simulation aux grandes échelles, Allumage forcé, Flammelettes laminaires, Flammes turbulentes

Table of Contents

List of Figures

List of Tables

Notation

Roman symbols

Symbol	Definition
c	Normalised progress variable
c_p	Specific heat capacity at constant pressure
c_v	Specific heat capacity at constant volume
C_s	Smagorinsky model constant
$\mathcal{D}_\phi$	Mass diffusivity of ϕ
Da	Damköhler number
D_c	Burner diameter
D_f	Bluff-body diameter
D_o	Outer diameter of the annular gap
e	Total energy per unit mass (internal + kinetic)
$e_{internal}$	Internal energy per unit mass
E_s	Spark energy
F	Flammability factor
F_2	Second-order structure function
$F_2^{(n)}$	Filtered second-order structure function (n times)
$\overline{F}_Q$	Surface flux vector of Q
g_{ij}	Velocity gradient tensor
G	Filter operator convolution kernel
h	Grid spacing
k	Turbulent kinetic energy
K	Stretch
Ka	Karlovitz number
ℓ	Integral length-scale
$\mathcal{L}$	Markstein length
Le	Lewis number
m_i	Mass fraction of species i
Ma	Markstein number
$\hat{n}, n$	Unit normal vector
P	Thermodynamic pressure
P_b	Burning factor
P_Q	Rate of production/destruction of Q
Pr	Prandtl number
$P(x)$	Probability density function of x

$P(x\|y)$	Conditional probability of x for given y
Q	A scalar quantity
r	Radial position from burner symmetric axis
R	Gas constant, $\mathcal{R}/W$
$\mathcal{R}$	Universal gas constant
Re	Reynolds number
s	Stoichiometric mass ratio of fuel to air
s_{ij}	Symmetric part of the square of the velocity gradient tensor
S	Sutherland temperature
S_{ij}	Resolved velocity gradient tensor
Sc	Schmidt number
$\dot{S}_{K_\phi}$	Stretch leakage term
S_L	Laminar flame speed
S_L^0	Unstretched laminar flame speed
S_χ	SGS scalar dissipation
t	Time
t_s	Sparking time
T	Temperature
T_{ref}	Reference temperature (Sutherland's Law)
$\boldsymbol{u}$, u_i	Velocity (vector and tensor notation)
u'	Fluctuating velocity scale, $k^{1/2}$
u_η	Kolmogorov velocity-scale
U	Free stream velocity
U_b	Bulk velocity
V	Volume
V_s	Spark volume
W	Molecular weight
$\boldsymbol{x}$, x_i	Position vector (vector and tensor notation)
$\mathrm{X_i}$	Mole fraction of species
Y_i	Mass fraction of species i
Y_c	Progress of reaction
Y_{cv}	Variance of Y_c
Y_F	Fuel mass fraction
z	Axial position along burner axis
Z	Passive scalar, Mixture fraction
Z_v	Scalar variance of mixture fraction

Greek symbols

Symbol	**Definition**
α	Heat diffusivity
γ	Specific heat ration, c_p/c_v
Γ	Gamma function
δ_{ij}	Kronecker delta
δ_L, δ_F	Flame thickness

Δ	Filter cutoff length
$\overline{\varepsilon}$	Average rate of energy dissipation
η	Kolmogorov length-scale
μ	Dynamic viscosity
μ_{ref}	Dynamic viscosity at reference temperature T_{ref}
ν	Kinematic viscosity, μ/ρ
ν_{t}	Eddy-viscosity
ξ	Flame normal coordinate
ρ	Mass density
Σ	Flame surface density
τ	Flamelet time
τ_ℓ	Integral time scale
τ_c	Chemical time scale
τ_{ij}	Viscous stress tensor; SGS stress tensor
ϕ, Φ	Scalar
χ	Scalar dissipation rate
Ψ_{ij}	Resolved shear stress tensor
Ψ_K	Resolved stretch
$\dot{\omega}$, $\dot{\omega}_e$, $\dot{\omega}_q$, $\dot{\omega}_c$	Chemical source terms
Ω	Mean local burning rate

Subscripts

Symbol	**Definition**
b	Burnt gas
F	Fuel
m	Mean value
max	Maximum
min	Minimum
tot	Total
O	Oxidizer
p	Products
r	Reactants
sgs	Sub-Grid Scale
st	Stoichiometry

Superscripts

Symbol	**Definition**
0	Reactant feeding stream
d	Deviatoric part
Eq	Equilibrium value
P	Products

s	Averaged over sparking duration

Special operators

Symbol	Definition
$\overline{\varphi}$	Filtering
$\widetilde{\varphi}$	Favre-filtering, $\overline{\rho\varphi}/\overline{\rho}$
$\langle\varphi\rangle$	Statistical averaging
$\hat{\varphi}$	Volume averaging

Acronyms

Symbol	Definition
BC	Boundary Conditions
BML	Bi-Modal Limit
CDR	Confinement Diameter Ratio
CFD	Computational Fluid Dynamics
CFL	Courant-Friedrich-Lewy condition
CRZ	Central Recirculation Zone
DLES	Detached Large-Eddy Simulation
DNS	Direct Numerical Simulation
EBU	Eddy Break-Up model
EDM	Eddy Dissipation model
FF	Flammability Factor
FGM	Flamelet Generated Manifold
FPI	Flamelet Prolongation of ILDM
FSF	Filtered Structure Function
FV	Finite Volume
ILDM	Intrinsic Low-Dimensional Manifold
LDA	Laser-Doppler Anemometry
LES	Large-Eddy Simulation
LODI	Local One-Dimensional Inviscid relation
NS	Navier-Stokes equations
NSCBC	Navier-Stokes Characteristic Boundary Conditions
PCM	Presumed Conditional Moment
PLIF	Planar Laser Induced Fluorescence
RANS	Reynolds Averaged Navier-Stokes
RHS	Right Hand Side
RK	Runge-Kutta scheme
RMS	Root Mean Square
SiTCom	Simulation of Turbulent Combustion
SGS	Sub-Grid Scale
URANS	Unsteady Reynolds Averaged Navier-Stokes
WALE	Wall-Adapting Local Eddy-viscosity model

Part I

Large Eddy Simulation

CHAPTER 1

Introduction

1.1 General introduction

Being basic life quality indicator of mankind, energy consumption is ever increasing with daily needs and day to day developments. Substantial portion of this energy is derived from fossil fuel combustion. Based on the present rate of energy consumption, International Energy Agency (IEA) [50] predicted that energy demand may get doubled in the next two decades. With limited reserve of fossil fuel source, it is a big challenge in-front of researchers to tackle this situation either by finding new sources of energy or by optimising the existing methods of energy consumption. Considerable efforts have been put in this direction by the research community to explore alternate sources of energy, preferably renewable and long lasting. However, the energy derived from fossil fuel sources continued to be disproportionately large fraction (nearly 90%) of the total world energy consumption mainly due to it's simplicity in usage [169]. Besides the limited availability, the non-optimized utilisation of fossil energy also poses problem to the environment in the form of pollutant, which are emitted during the process of combustion. A thorough understanding of combustion science is thus important to efficiently utilise the energy obtained from fossil fuels without producing an adverse environmental damage.

In a generic manner, combustion is defined as a rapid exothermic reaction that liberates substantial energy as heat and flames, as combustion reactions have the ability to propagate through a suitable medium [49]. The fuel and oxidiser interact at the molecular level during the process of oxidation, during which, hundreds of elementary reaction takes places along with formation and depletion of thousands of intermediate species. Even for simpler hydrocarbon combustion, the process passes through a complicated set of elementary sub-reaction steps, which are coupled to each-other, generally in a non-linear fashion. The process of combustion optimisation and control needs a proper insight of what happens in all these stages. Experiments can answer some of the questions concerning combustion, however with some known limitations. First of all, the cost associated with experiments are quite high so that it would be cumbersome to experimentally analyse in detail every systems involving combustion. Sophisticated instrumentation is necessary for experimental data collection for a such kind of analysis, where the operating environment is harsh and the time scales of processes are in

the order of nanosecond. Numerical simulation of combustion is an alternate choice to closely study the behaviour of system involving flow and reactions, which is being done in the field broadly known as Computational Fluid Dynamics (CFD). The central task of CFD is to possibly represent the exact description of the technical processes using mathematical models for understanding the dynamic behaviour of the system considering the regularities and thereby making possibly reliable predictions of the future evolution of the system. In general, the CFD prediction will be compared against the experimental results done in controlled fashion with known parameters, in order to calibrate the models used to describe the problem. The well-tuned mathematical CFD models will be further used to predict complicated processes, which are difficult for experimental access. Moreover, level of details of results obtained from CFD simulation made it attractive compared to experimental approaches. However, CFD is not considered to eliminate the need of experiments, but it refines the ideas and helps us to understand the system thoroughly and to give more insight to the experimental data to arrive to some logical conclusions. Thus, CFD and experiments are used altogether in the study of behaviour of the physical process involving flow and reactions.

1.2 CFD tools for turbulent flows

Fluid flows governed by Navier-Stokes equations have been solved numerically since the early days of computers. The flow can be classified as laminar, turbulent or transitional based on the inertia forces and viscous forces acting on the flowing fluid parcel. When the motion of a fluid is considerably slow or the viscosity of the moving fluid is high, then the movement of the fluid tend to be very regular and smooth. This type of fluid flow is considered to be laminar. When the velocity of the fluid is increased by some means, or the viscosity of the moving fluid is less, then the fluid motion becomes irregular and chaotic, then called as turbulent flow. The flow regime between laminar and turbulent flow is termed as transitional, where the flow irregularities will start appearing. This theory was first pointed out by Reynolds in 1883, because of whom the popular dimensionless quantity "Reynolds number" (Re) is then being used to quantify the regime of fluid flow. Accordingly, Re is defined as

$$Re = \frac{\rho U \ell}{\mu} \tag{1.1}$$

where U is the mean flow velocity, ℓ is the characteristic length of the system (for instance, diameter in the case of pipe) and μ is the viscosity coefficient or dynamic viscosity. As per the definition, the laminar regime corresponds to low Reynolds number and turbulent regime corresponds to high Reynolds number.

The governing Navier-Stokes equation is a set of partial differential equations stem from the basic law of conservation of mass/energy, Newton second law of motion and Newton's law of viscosity. Computation of flow involves solving this set of equations numerically with proper initial and boundary conditions after discretizing the equations. Finding numerical solution of these equations is a challenging job due to the inherent non-linearity associated with these equations and also the strong coupling between the dependent variables. Particularly, while dealing with turbulent flow, the large range of time and length scales generated by the Navier-Stokes equations require a very fine mesh resolution. In general, the CFD tools for solving Navier-Stokes equations fall under three main categories depending on the treatment

of equations namely Reynolds-Averaged Navier-Stokes (RANS) equations, Direct Numerical Simulation (DNS) and Large-Eddy Simulation (LES).

The most widely used CFD tool in industry for real time applications is RANS. As the name suggests, RANS solves the equation of averaged flow quantities after performing *Reynolds decomposition* as follows

$$f(x,t) = \bar{f}(x) + f'(x,t) \tag{1.2}$$

Here $f(x,t)$ can be any dependent variable in the flow field such as density, velocity, pressure etc. The variable is decomposed into mean $\bar{f}(x)$ and fluctuating components $f'(x,t)$. This is done by ensemble averaging (or time averaging in case of steady turbulent flow) the Navier-Stokes equation. This decomposition, however introduces unclosed terms, famously known as *Reynolds stress* in the equation of mean velocities, which requires modelling[1]. In most of the practical engineering applications, in the turbulent flow environment, the interest lies on predicting the mean flow variables, where the RANS modelling perfectly suits the purpose. The computational requirements for RANS calculations are several order lesser than any other CFD tools for similar configuration, which makes it attractive for industrial applications and simulation of massive, real time geometries. However, there are some shortcoming with RANS modelling. Firstly, the complete information of turbulence is lost, and only the evolution of mean quantities are described. The entire spectrum of turbulent eddies needs to be modelled, for which, some general assumption like eddy dissipation and universality needs to be invoked on all turbulent eddies, which is not exactly true for all scales of eddies. Nevertheless, RANS simulations are simple and, in most of cases sufficient to simulate and predict the quantities of interest with considerably less cost using readily available models.

DNS of turbulence is the most conceptually straightforward approach for the solution of turbulent flows. In DNS computations, the Navier-Stokes equations are solved with specified initial conditions for entire spectrum of scales in the turbulent flow field. It is like performing an experiment, but on a computer rather than in the experimental test bed, due to which DNS is also sometimes referred as "numerical experiments". The one main advantage of going for DNS is that, there is no need to develop any turbulence model as the entire turbulent scales are resolved by the DNS domain. However, there is a catch in this approach, especially when the Re is high i.e. well developed turbulent flow. The resolution of mesh need to be enough fine to capture the smallest possible eddy in the flow, termed as "Kolmogorov eddy", which always scales inversely with Re. In a small scale industrial configurations, with normal operating conditions and prevailing turbulence, the size of the Kolmogorov eddy would be in the orders of millimetre or even micrometer sometimes. It is estimated that the number of grid points needed for a three dimensional, cold-flow simulation is proportional to $9/4$ power of the Re. The situation could be more complicated in the case of reactive flow simulation. This limited the DNS to handle only low Re, simple geometry computations. Even the most powerful High Performance Computing (HPC) machines available today would take years together to perform a fullscale DNS calculation of a realtime large-scale system, even in frozen flow simulation with no chemical reaction. Though, the real world engineering application of DNS appeared to be remote, DNS is a useful tool to validate some basic hypothesis which we make during constructing turbulent closure models for other CFD tools. Notice however

[1]These terms represent the convection by unresolved velocity fluctuations.

that DNS of laboratory experiments will be soon feasible because of the measurable size of the device.

LES is a technique intermediate between the DNS of turbulent flows and RANS equations, thereby combining the advantages of both RANS and DNS. The central idea behind LES is to directly compute the large energy containing scales in flow and model the small scale eddies. The advantages with this approach are readily evident. The large eddies are generally geometry dependent and not self-similar, for which, direct computation is the best choice. On other hand, small eddies are universal and dissipative in nature and so the turbulent model based on such assumptions are very relevant. Thus, the LES demands less computational requirements than DNS for similar computation, but gives more information than a RANS simulation due to the fact that the computation is inherently unsteady. Though, the mesh requirement for LES simulations are heavier than RANS computations, the advent of High Performance Computing machines enabled us to approach small scale industrial problem with moderate Re using LES. In many ways, LES represents a logical compromise by providing accurate, high fidelity solutions at affordable cost. In general, the cost of an LES of a high Reynolds number flow is comparable to DNS of a similar low Reynolds flow. However, when LES and DNS are compared at the same Reynolds number, the cost difference is enormous. In this case, LES can provide nearly the same information and accuracy as DNS for quantities of engineering interest but at a fraction of the cost. When compared with RANS, LES is seen to provide much more accurate data and, perhaps equally important, more complete data, such as frequency spectra and pressure fluctuations, but at a cost that can be several orders of magnitude higher than RANS. However, relative to the remaining alternative of physical testing, the cost of LES appears quite reasonable, and as the cost of computing will decline in the coming years, LES is expected to compete not only with RANS but also with laboratory experiments in providing accurate design data with fast turnaround time and low cost. This is especially true in applications of LES to gas turbine combustors and internal combustion engines, where the Re are low and flows are unsteady and separated. These conditions are suitable for economical LES, and they have posed difficulty for RANS computations.

1.3 Background and Motivations

Gas turbines are classified as heat engines which are used for power generation notably in aviation sector and industrial applications. Flame stabilisation is an important issue during the design of gas turbine combustors. Unlike Internal Combustion engines, gas turbines have the concepts of flashback, liftoff and blowoff, which need to be taken care of during it's operation. Flame stabilisation is a process of anchoring flame at one desired location and provide resistance to flashback, liftoff and blowoff over the device's operating range [160]. In order to achieve this, the oncoming fresh mixture must have precisely the same speed to balance the flame speed so as to render the flame stationary. This is rather a difficult task to accomplish and, even if it can be done, it is also too restrictive in the operational range of the combustor. The principle of flame stabilization is to provide some mechanism through which the flame burning intensity can be automatically modified so that the flame is afforded sufficient flexibility to adjust its location, orientation, and configuration in a nonuniform, temporally varying flow field. Thus not only static equilibrium can be attained between the flow velocity and the

flame speed in a localized region, there is also sufficient flexibility for the flame to accommodate changes in the operation conditions so as to attain dynamic equilibrium [91].

Flame stabilisation could be achieved by different means either aerodynamically by introducing swirl in the combustor or geometrically by introducing an obstacle in the flow and so on. The obstacles are often termed as flame holders or bluff-body flame stabilizers. Bluff-bodies are a class of aerodynamic blunt geometries that are intentionally introduced in the passage of flow in order to induce separation of flow on the leeward side of the body. Most of the practical gas turbine burners adopt bluff-body configuration in the view of achieving improved flame stabilisation [51], termed as bluff-body stabilisation, for instance in ramjets, turbo-jet afterburners, nozzle mixing burners etc. Bluff-body stabilisers are often employed in burners with high free stream velocity and high power density. Bluff-body stabilisation comes under geometrical flame holding mechanism, where a re-circulation zone created at the wake behind the bluff-body anchors the flame [48, 72]. The presence of bluff-body in a high velocity stream creates a low pressure wake zone where flow reversal takes place. This increases the residence time of the fluid inside the burner. Bluff-body stabilisers are generally classified according to their shape viz. disc shaped, cylindrical and V-gutter flame stabilisers. The length and width of the central re-circulating wake zone is a function of bluff-body dimensions and flow parameters, which also controls the mass and energy transfer between the recirculation zone and the outer-flow. The dimensions of the wake zone play a vital role in flame stabilisation, providing the impetus to sustain the flame. The introduction of blockage in the flowing combustion mixture stream increases the turbulence level due to vortex shedding and flow separation, which enhances the mixing. Furthermore, the combustion products trapped inside the recirculation zone may serve as a source of ignition by continuously igniting the incoming air fuel mixture. In an axi-symmetric bluff-body burner, the flow emerges out of an annular gap formed due to intrusion of bluff-body on the main stream flow. The jet injected via this annular gap, deviates slightly radially outward and envelopes the central re-circulating bubble, which continuously traps energy from the main streams and maintains the turbulence level. Farther downstream, the flow behaves similarly to a fully established round jet flow [153]. The unique aerodynamics and flow field properties of such bluff-body configuration have motivated several research studies, both experimental and numerical [26, 51, 52, 64, 66, 69, 117, 153]. Most of the reported numerical works were concentrated on aerodynamics and cold flow mixing of bluff-body burners, whereas reacting flow simulation are rarely done. Reactive flow simulation poses a great challenge to engineers and researchers due to its complex flow and chemistry interactions, even for simple configurations [118]. The wide range of time and length scales involved in such studies made it more theoretically complicated and computationally expensive. Large Eddy Simulation (LES) was proved to be relatively simple and reasonably accurate in handling such kinds of problems [167].

Forced ignition study is not new to combustion community as numerous studies have focussed on forced ignition in internal combustion engines [133, 155]. However, few have considered spark ignition of nonpremixed burners [25, 135], mainly because these burners, as those found in gas-turbines, operate in combustion regimes that are, overall, steady. Nevertheless, the growing interest in optimization of aeronautical engine relight in high altitude motivates studies of nonpremixed burner forced ignition [4]. Even though the gas turbines engines are exhaustively tested for wide range of operating conditions before put forth into operation, oc-

casionally, when the aircraft faces an unprepared air field, the combustor loses the flame. This is particularly true for defence aircrafts, which normally would be operated without prior planning and also in adverse environmental conditions. Sometimes, taking off from a wet runway produces a risk of ingestion of excessive amounts of water and ice which can lead to flame extinction in gas turbine engines. In addition, it is becoming increasingly familiar to operate gas turbines in fuel lean operating conditions due to stringent emission regulations and efficiency concerns, thus combustion being more susceptible to instabilities and blow off. This demands more careful design of ignition devices and of it's placement in the combustion chamber to ensure reliable and faster re-lightening in case of flame's blow out. In case of flameout of engines, the spark location is a crucial parameter to efficiently re-light the engine and put back the engine in operation as early as possible before the aircraft looses considerable altitude. The forced ignition phenomenon observed in such burners are highly transient in nature. Various factors influences the development of spark kernel from the moment of spark deposit, until the complete flame establishment period. The favourable ignition spots for sparking in these burners are not just a function of mixture fraction, but also of the velocity fluctuations which will transport the flame kernel from the ignition spot. The success of spark in initiating the flame and the rate of flame development thus become a complex function of flow field variables.

The phenomenon of spark ignition in bluff-body stabilised turbulent burner has been experimentally analysed and reported by Ahmed [3], from Cambridge University. This study was performed on a laboratory scale bluff-body burner with CH_4+air mixture and detailed the distribution of mean velocity, fluctuation of velocity, mean mixing field and their corresponding fluctuations depending on several combinations of air and fuel flow rate and also with and without the presence of aerodynamic swirl. Further attempts were made to lighten the burner by introducing electric spark at various locations inside the burner, locally featuring different flow and mixing conditions. The development of the ignition kernels were observed leading to success and failure of the flame and a complete ignition probability map was given for different burner locations. The experimental study revealed the optimum spark location of the burner for certain fixed flow parameters. Interestingly, the optimum zone for successful lightening of this burner could not be only anticipated based on either the mixing patterns or the velocity patterns. Based on the findings, there is a close interplay of both of these fields in the dynamics of kernel evolution. Also, this experimental work raised several open questions concerning the survival of ignition kernel in a highly turbulent flow environment, which stimulated discussions about kernel vortex interactions. Very detailed measurements were done by this experimentalist and the findings are well documented [3, 4]. Although, detailed cold-flow analysis were performed and the kernel evolution was tracked with high resolution digital camera, there were certain instances where this information is insufficient to explain the ignition kernel behaviour. The kernel would be moving in three dimensional space and thus would be facing different instantaneous flow and mixing fields, which influences the kernel growth along with the history of flow and mixing fields which the kernel had already encountered. Simultaneous measurement of all this information in a hot-flow environment is difficult for experimental access. An unsteady three dimensional numerical simulation could fairly describe the associated physics with the spark ignition and give an insight to the experimentally observed phenomenon. This is the motivation for the present numerical study. The present work focuses on the case without swirl for which detailed measurements are available. The principal objectives of this work are given below. The organisation of this thesis is given

at the end of this chapter.

1.4 Objectives of this study

The principal objective of this study is to use the LES tool to explore the possibility of performing a reactive flow simulation of transient forced ignition phenomena in a turbulent ambience. The ignition experiments performed in Cambridge burner is chosen as a reference for validating the simulation results and to systematically verify the applicability of LES for such highly unsteady, reacting flow simulation. The ultimate aim is to compare the results with the experimental counterpart thereby analysing and answering few open questions raised by the experimentalist. This main-task is broken into the following list of sub-tasks to facilitate constructing the roadmap for this study.

- To perform a large-eddy simulation of frozen flow and mixing behind the conical shaped bluff-body burner and validate the results of mean velocity, mean mixture fraction distributions and their turbulent fluctuations with the available measurements.
- To use tabulated detailed chemistry approach to numerically simulate forced ignition and flame spreading in the bluff-body wake and compare the kernel dynamics with experimental observations in the context of success of ignition.
- Using the light of information obtained from LES calculations to bring-out the possible linkage between the flow, mixing fields on the success/failure of the ignition kernel thereby completing the experimental analysis.

1.5 Outline of the thesis

The present thesis is organized in 7 chapters:

Chapter 2 contains a brief summary about the literature on numerical and experimental investigations of annular jets and LES of reactive bluff-body flows. This is followed by an overview of fundamentals of combustion simulation, basic tools of combustion modelling, different modes of combustion and their relative treatment in numerical modelling. The theory behind chemistry tabulations are discussed at the end of this chapter.

Chapter 3 starts with description of the governing equations for LES. The filtering of Navier-Stokes equation in LES is discussed and then followed by different Sub-Grid Scale (SGS) models tried in this numerical work. The second half of this chapter covers the description of the flow solver. The general details about the numerical schemes, pre and post-processing techniques are discussed. The general assumptions and simplifications made during the computations are discussed. The treatment of detailed chemistry using tabulation using PCM-FPI is presented.

Chapter 4 starts with the overview of the experimental configurations studied in this numerical work. The following section describes the cold flow simulation case and the associated parameter settings. The distribution of components of velocity and turbulent fluctuations are presented. The quality of this LES calculation are discussed based on the criterion

proposed by Pope [129]. The mixture fraction field and it's corresponding fluctuation are presented and compared against measurements. The Probability Density Function (PDF) of mixture fraction are constructed from the history of information about mixing fields and the "Flammability factor" distribution are discussed in detail. All the cold flow predictions are compared with the available experimental data and discussed in detail.

Chapter 5 introduces the ignition spots chosen for analysing spark ignition. Then the model used for forced ignition and relevant assumptions are discussed. The time history of flow variables at these ignition spots are presented in this chapter. The analysis of forced ignition at different time instances are detailed and the results are compared against shot-by-shot evolution of experimental observation. The similarities and differences observed between experiments and simulation are explored in this chapter.

Chapter 6 starts with a literature survey about kernel turbulence interaction followed by discussion about the need for accounting for strain effects in burning rate closure. Following section deals with the introduction of new closure model developed to incorporate the effect of stretch on turbulent burning rate of developing ignition kernel in a global manner. The quenching of ignition kernel due to flame stretching is demonstrated numerically and discussed in this chapter. Finally, a LES computation with increased mesh resolution is reported and the possible mesh dependency of the solution is discussed.

Chapter 7 summarises the discussions of different chapters and brings-out conclusions drawn from this numerical study. The later part of this chapter suggests some possible extension of this numerical study for future research.

CHAPTER 2

Literature Review and Fundamentals

Contents

2.1 Flow around immersed bodies

In general, a body immersed in a flow will experience both externally applied forces and moments as a result of the flow about its external surfaces. The forces include drag force, lift force and the moments include rolling and pitching moment. These forces and moments are generally a function of body geometry, orientation of the body and flow conditions. By suitably manipulating the above said parameters, it is possible to achieve desirable forces and moments according to the requirements. For instance, in airfoil (used in air-plane wings), it is desirable to have high lift force and less drag force. The flow around the streamlined airfoil remains attached, producing no boundary layer separation and comparatively small pressure drag, which result in higher lift to drag ratio. The flow around an airfoil follows the contour of the body as seen in Fig. 2.1. Thus the flow remain attached and no boundary layer separation takes place to cause any significant pressure drag.

However, the bluff-bodies, as they used in burners for flame stabilisation are intended to produce a low pressure recirculation zone behind it. So, here the functional difference dictates the bluff-body to produce significant pressure drag. Fig. 2.2 depicts a schematic picture of a flow field, while being obstructed by a bluff-body. Flow separation takes place here and vortices are formed due to rolling-up of shear layer.

Bluff-body flame holders are widely used in industrial burners and in gas turbine engines for stabilising the flame. For instance, as mentioned in chapter 1, bluff-bodies are used in all

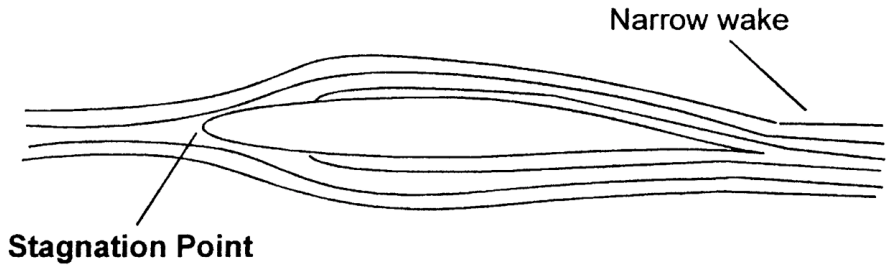

Figure 2.1: Flow over a streamlined body

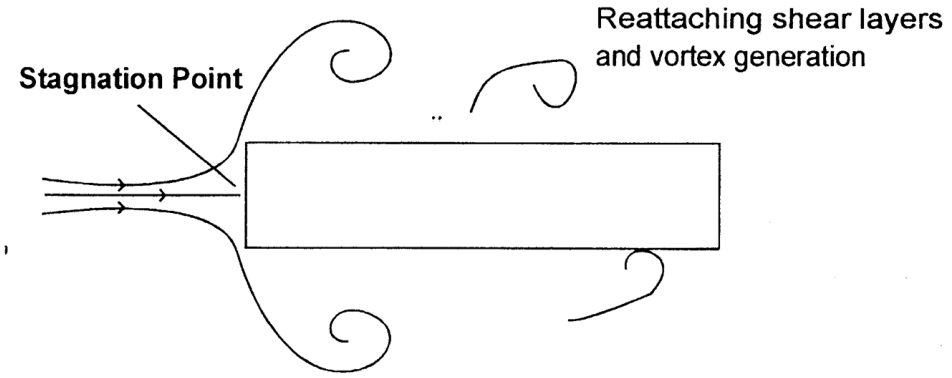

Figure 2.2: Flow around a bluff-body

variant of ramjets for flame stabilisation. Fig. 2.3 shows a schematic ramjet engine employing a "V-gutter" shaped bluff body to hold the flame. By design, ramjets are free of any rotary device and so the air is compressed only by the forward motion of the aircraft. This necessitates the engine to operate on high speed condition, where the air approaching the engine inlet will normally be at supersonic speed. The supersonic diffuser placed at the inlet performs the job of compressor thereby increases the pressure and reduce the air velocity by "ramming effect". This is followed by a injection of fuel into the compressed air and then the charge is fed to the combustor. It is to be noted that the air-fuel mixture speed is more or less sonic and so it needs some device to stabilise the flame. This is the place where bluff-body plays the role as seen in Fig. 2.3. It thus, introduces a sudden expansion in the flow forming an energetic mechanism for turbulence production, which enhances mixing and produces a low speed recirculation zone for promoting ignition of incoming mixture. Also, over most of the operating regime of the ramjet engine, the temperature of the incoming air if much lower than the ignition temperature of the mixture and so a heat source is needed to raise the mixture temperature before burning it. The recirculation zone, which normally is filled with hot combustion products serves this purpose by supplying the required heat to raise the mixture temperature, which eventually will burn.

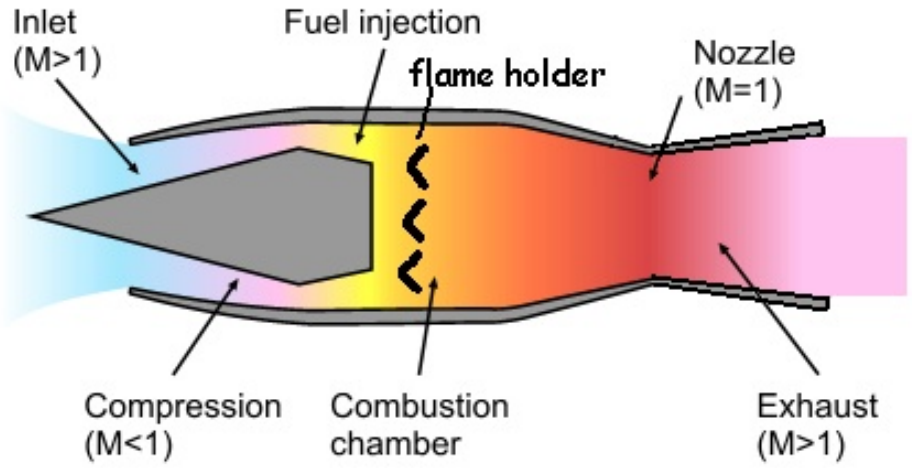

Figure 2.3: Schematic view of a supersonic ramjet engine employing bluff-body flame-holder

2.2 Bluff-body burners and annular jets

To achieve high power densities, the flow velocity of the reactant entering the combustion chamber needs to be increased without causing flame blowout, a condition at which the flames are carried away by the flow out of the combustion chamber. The laminar flame speed of most of the hydrocarbon fuels in air are less than or around 40 cm/s. But, in many practical devices like turbo jets and ramjets, in which high power density is of primary importance, the reactant flow velocity would be in the order of few hundred m/s. This necessitates some means to stabilise the flame. In practice, this stabilisation is accomplished by causing some of the combustion products to continuously recirculate inside the combustion chamber. Introducing swirl, flame holders, pilot jets are some of the possible techniques, sometimes used in combination for flame stabilisation. Flame holders are devices intruded in flow stream to create obstruction thereby creating a wake behind them. The flow emerges out of an annular gap formed by the obstruction and, the resulting wake usually creates a low pressure region where flow reversal takes place. The intrusion of bluff-body also enhances turbulence level and thus improves the mixing inside the combustion chamber. The wake zone ahead of the bluff-body traps high temperature burned products and thus serves as a source of ignition for the fresh incoming mixture. The bluff-body aerodynamics has been a subject of discussion in many research studies, both experimental and numerical.

2.2.1 Aerodynamics of annular jets

The bluff-body aerodynamics has been experimentally analysed and reported by plenty of researchers [4, 26, 51, 52, 67, 117, 153]. Esquiva-Dano *et al* [52] analysed the effect of bluff-body geometry on flame stabilisation process in a non-premixed burner featuring central fuel injection. They used a disk shaped and a tulip shaped (conical) flame holders and analysed the

mechanism of flame stabilisation with increasing air to fuel jet velocities. The blockage ratio[1] of these two configurations are the same but the tulip shaped body is more streamlined than the disc shaped one and so leads to an expansion of boundary layer. Their results shown that the dimensions of the resulting recirculation zone behind the bluff-body wake differ both in height and width, due to the difference in the flow divergence produced. In the stabilisation diagram, five different characteristic modes of flames are observed and reported. The tulip shaped bluff-body produces a wider range of regime for flame stabilisation than the disc shaped one, due to difference in the aerodynamics, which also influences the mixing. Balachandran [10] made an experimental attempt to visualise the flow field downstream of a conical shaped bluff-body burner. He reported the presence of two distinct recirculation zone; a central recirulation zone (CRZ) at the wake of the bluff-body and a side recirculation zone (SRZ) formed between the burner confinement and the core jet region. There existed two shear layers; an outer shear layer between the CRZ and core annular jet, inner shear layer between the annular jet and SRZ respectively. He measured the height and width of the central recirculation zone to be 1.5 and 1 times the diameter of bluff-body respectively. Experimental investigation of annular jet with a central air injection and swirl was reported by Al-Abdeli *et al* [7]. Emphasis was placed on discerning typical flow structures and on discovering the influence of controlling parameters on the downstream regions of the jet and the recirculation within. It was shown that the formation of a downstream recirculation zone, hence the onset of vortex breakdown, depends not only on the swirl number but on other flow parameters such as the axial velocity of the primary swirling air, or its Reynolds number. Together, these two parameters appear to control the radial spread of the flow. Spatially, the progression towards downstream recirculation with changes in flow parameters was seen to occur around a fixed location in the streamwise direction.

Literature on numerical simulation of bluff-body aerodynamics are limited and the topic is relatively young to the modelling community. This is due to the problem associated with modelling principal phenomenon of bluff-body flows, i.e. the unsteady shedding of vortical structures from the obstacle, hinges on the interaction between mean-transient motion and residual turbulence, which require an unsteady simulation technique to capture all these flow physics. An appropriate treatment of turbulence is crucial for the simulation quality. When attention is drawn to industrial applications, a direct resolution of the turbulent motion is, however, unfeasible as the associated grid resolution would cause prohibitive computational expenses. Delaunay *et al* [40] used a $k-\epsilon$ model to investigate the flow field around variety of bluff bodies. A cube, a house model, a bridge model and a hoarding model were tested during this work. The results did not agree well with the experimental results, and the reasons suggested were inability of $k-\epsilon$ model to simulate recirculating flows, and use of wall functions in a non-developed boundary layer. They also mentioned that the inlet boundary condition could not be reproduced exactly, which might have caused the disagreement in the results. The fundamental difficulty with RANS is that the model coefficients are calibrated by DNS or experiments of some typical fully developed and steady turbulent flow, which makes the turbulence models insensitive to transition onset location and further weakens the accuracy of RANS in predicting time dependent flows. Unsteady RANS(URANS) technique had also been tried to simulate flow past a circular cylinder, to analyze the prediction capability of URANS in unsteady separated turbulent flows [175]. Although URANS showed improved prediction

[1]The blockage ratio of the annular jet is defined as the ratio between the area blocked due to the presence of bluff-body to the total inlet area [3, 49]

in mean velocity profiles, the predicted Reynolds stress distribution, and thus the velocity fluctuations, are far from experimental measurement. Similar problem has been reported by Zhu *et al* [176] while using hybrid RANS/PDF method. Generally, unsteady statistical modeling approaches (URANS) rely on the formal existence of a spectral gap between the time scales of the mean transient flow and the residual turbulence. This gap does not almost exist in bluff-body flows. Particularly in the wake regime, the duration of the flow distortion due to unsteady effects is much smaller than the intrinsic time scale of the turbulence and the assumption of a spectral gap is excessively violated. Rodi [136] compared the potential of LES and RANS in the simulation of flow past a bluff-body in both two dimensions and three dimensions. He proved the conceptual advantage of LES over RANS in the simulation of such a flow scenario, which involves phenomenon like separation and reattachment, unsteady vortex shedding and bimodal behaviour, high turbulence, large-scale turbulent structures as well as curved shear layers. The severe under-prediction of turbulent fluctuations are attributed to the use of 2-dimensional simulation techniques, in which the low frequency variations of shedding motions due to 3D effects are neglected. Three-dimensional LES results were significantly better than RANS and even quantitatively matched well with experimental data, suggesting clearly that LES is more suited and has great potential for calculating these complex flows. Taglia *et al* [153] too have emphasised the need of performing three dimensional simulation for annular jets, pointing the vortex shedding and flow separation phenomenon observed in bluff-body flows. Their work also revealed the origination of flow asymmetry due to non-linearity of Navier-Stokes equations, in bluff-bodies with high blockage ratio. The turbulent fluctuation observed in the recirculation zone is mainly due to the large scale structures, which reinforces the need of computing it directly using unsteady simulation tools. LES of bluff-body aerodynamics in a swirling unconfined flow has been reported by Fujimoto and co-workers [65]. With a low swirl number, a compact and strong recirculation zone was created behind the bluff-body. In addition, a secondary recirculating region was created at mid-stream section. At the mid-stream region of the flow field, a high-speed rotating and non-recirculating collar-like structures were generated with a constricted flow field. When the swirl number was increased, the recirculation zone behind the bluff-body appeared to be elongated. The secondary recirculating region observed in the mid-stream section was also disappeared. This study pointed out the differences observed in development and distribution of large scale helical shaped vortex structures and their distributions with swirl number and primary jet velocity. Their prediction in the mean velocity profiles were in good agreement with experimental ones despite the use of simple inlet boundary description. However, the RMS profiles show significant variation from measurements, which stressed the importance of proper inlet boundary definition for such kind of flows, which are inherently three dimensional and highly transient.

2.2.2 Bluff-body flames

The mechanism of flame stabilization behind bluff-bodies in premixed systems was experimentally studied by Scurlock [142], Williams *et al* [172] and Fabri *et al* [53]. Variations in the equivalence ratio, inflow velocity and pressure, flame-holder shape and size, fuel type and turbulence intensity were considered. The results of the studies have shown that turbulence increases the effective flame velocity, but the stability of the flame is decreased by increasing the turbulent intensity. The shape of the bluff-body was found to have a small effect on the flame stability and the blow-off velocity exhibits a direct dependence on the inflow pressure

(blow-of velocity will increase when pressure increases). In later years, a vast amount of more complex experimental studies on bluff body stabilized flames have been carried out and some, considered more relevant to the current study, are highlighted. Cheng and co-workers [28–30] conducted a series of measurements of premixed bluff body stabilized flames, focusing mostly on the aspects of flame-turbulence interactions (e.g., velocity and transported scalar spectra, turbulence transport properties, and Reynolds stress). Balachandran [10] investigated acoustically excited bluff-body stablized premixed/partially premixed flames and it's response to large excitation amplitudes (Cambridge burner). Ahmed [3] studied forced ignition and flame spreading in the same burner, in a partially premixed scenario and come up with an ignition probability map for different air/fuel velocity combinations and swirl.

Numerical simulation attempts have been made to predict the flow field behind a bluff-body wake using different numerical tools such as RANS, URANS etc. However, the quality of prediction was insufficient in the case of bluff-body flames, for instance see [35]. Merci and co-workers [109] performed RANS simulation of piloted methane air non-premixed flame. However they did not use the standard $k - \epsilon$ model, which relates Reynolds stresses with the local mean velocity gradient through a linear expression. Instead, a relationship between the Reynolds stresses and the strain rate and vorticity tensors is used, with terms up to third order (and thus called as "cubic turbulence model"). This way, the influence of the mentioned complex flow phenomena on turbulence is accounted for to some extent. The work pointed out that the improvement however is very moderate with the new cubic model, especially in the region downstream of the recirculation zone. The important conclusions of this work are that the turbulence model influences the result, independently of whether the flow is reacting or not. In the reactive flow cases, a correct prediction of the flow field guarantees, in the absence of strong extinction effects, a good prediction of mixture fraction and major species, even when a simple chemistry model is used. Recent advancement in the field of large eddy simulation (LES) to treat Sub-grid scale (SGS) chemistry [167], has motivated numerical simulations of reacting cases using LES, due to which, in recent days, encouraging results started appearing in literature. Asrag et al [48] performed simulation of non-premixed, swirling jets with two geometric swirl numbers and central fuel injection velocities. While visualising the flow field for the low central fuel injection case with intense swirl, apart from the base recirulation zone, they also observed a vortex breakdown bubble at the downstream side due to the swirl. When the central fuel injection velocity is increased, then the vortex breakdown bubble disappeared with only the base recirculation zone remaining in the downstream. This was attributed to the reason that the adverse pressure gradient generated by the swirl is not strong enough to overcome the axial momentum generated by the central fuel jet. Their predictions were in good agreement with measurements in mean velocity, but the RMS fluctuations were under-predicted. Especially, the peak RMS fluctuations at the inner and outer shear layer at the region close to the bluff-body lip were clearly missed in the predictions. Nevertheless, they succeeded in reproducing most of the major species and temperature profiles of experiments in a bluff body stabilised swirled non premixed flame, though the chemistry was described using a global one step equation. Fureby et al [67] performed experimental investigation and LES of swirled flow and reported the difference in the flow field between cold and hot case. They also pinpointed the necessity of rigourous enforcement of boundary conditions, which is often overlooked in LES computations. Stone and Menon [149, 150] and Duwig *et al* [46] conducted LES of partially premixed combustion in swirling flows using spatially and temporally variable in flow equivalence ratio. An analysis of the dynamic response

of the combustor to these variations in equivalence ratio has shown that the heat release oscillations caused by the variation in the equivalence ratio can either enhance, or damp the pressure oscillations in the combustor. Raman *et al* [131] performed LES simulation of Sydney burner, which is a non-premixed bluff-body flame featuring central fuel injection surrounded by coflowing air. The predicted results were in good agreement in both velocity and mixing profiles and reasonably well in reactive species profiles compared to first order based RANS simulation [85] and other PDF based simulations of similar configuration [113]. This study emphasises the purpose of going to unsteady numerical simulation like LES for simulating such bluff-body configurations. Kempf *et al* [84] also performed LES simulation of Sydney bluff body burner, by treating the chemistry with a steady diffusion flamelet model. The steady flamelet model captures the right species and temperature distribution at most of the burner region, particularly where the flow field values, especially the mixture fraction, was better matching with the experimental results. The authors reported the importance of resolution requirements for capturing the flow field properties, which also further influences the reactive case predictions. To summarise, most of the numerical studies focussed on bluff-body stabilised flame have been done using unsteady simulation tool, primarily LES. The reported literature contain exhaustive information on LES capturing unsteady flow and flame dynamics behind a bluff-body wake, where the flame is established. The unsteadiness predominantly arises due to the complex flow field and the interacting vortex bubbles in the wake zone. However no attempts were made to use LES to simulate ignition and flame spreading in a bluff-body configuration, at-least until the start of the present numerical work, although, very recently, forced ignition of bluff-body burner has been reported with LES [158]. The ignition problem is inherently unsteady, even when the flow is steady. In the bluff-body case with strong turbulence, where the flow features strong unsteadiness, modelling ignition adds up the degree of complexity.

2.3 Spark ignition and modelling

Spark ignition is a process of initiating combustion in air fuel mixture by carrying-out high density energy deposition in a suitable position of the mixture thereby forming an ignition kernel, which subsequently propagates and consumes the reactants. The purpose of the spark is twofold; it heats the mixture at the electrode gap abruptly to high temperature in order to initiate a thermal explosion and moreover, it has to supply a high concentration radical pool to the reaction zone and thus promote a chain explosion. The most popular way of generating spark is through electrical discharge and ionising the gas between spark plug electrodes, though laser induced spark ignition is also becoming used nowadays. The electrical spark is generated by an electrical igniter, popularly known as spark plug. It involves two conducting electrodes separated by a small gap, known as spark gap. These electrodes are connected to an electrical circuit, which builds massive voltage difference across the spark gap. Once the voltage exceeds the dielectric strength of the gases in the spark gap, the gases become ionized. The ionized gas becomes a conductor and allow electrons to flow across the gap. Spark plugs usually require voltage in excess of 12,000-25,000 volts to 'fire' properly, although it can go up to 45,000 volts to produce hotter spark. Along with this, the supply of current will be adjusted to obtain longer duration spark. Studies on spark ignition applied to internal combustion engine are widely popular due to the fact that piston engines have intermittent power cycles and so every

cycle needs a spark and thus efficient sparking system is mandatory for better combustion, performance and emission characteristics. On other hand, in gas turbines which function on open Brayton cycle, there is a sustained combustion with a stable flame due to the continuous flow of reactants. However, gas turbines are also employed with spark igniters, which will be used while starting the engine and re-lighting the engine in case of flame loss. The discharge in the small gap between the electrodes depends on many parameters, such as spark energy, gas composition, heat losses, the flowfield, and many more. Four different phases are identified during the sparking process. They are the pre-breakdown, the breakdown, the arc discharge and the glow discharge phase [9, 100, 101].

The timing and duration of each phase is dictated by the characteristics of the ignition circuit (including the spark plug). Pre-breakdown is the time period when the voltage of the coil is building until it is either large enough that a spark can jump the gap or, if the required breakdown voltage exceeds the capacity of the coil, a misfire will occur. Typically, this phase lasts for one nanosecond [107]. There is no energy deposition as there is no current flowing through the spark gap. As soon as enough ionizing electrons are produced to make the discharge self-sustaining, breakdown occurs. At breakdown, a highly conductive streamer (passage for electrons) is initiated, which leads to a sharp rise in current and sudden fall in voltage across the gap [101]. This phase lasts for approximately 10 nanoseconds. There is very little energy deposition because of the short duration of this phase. Typically, between 0.3 and 1 mJ of energy, is deposited during breakdown and the temperature reaches approximately 6000K thereby building pressures of up to 300 bar [156, 157]. Breakdown may be perceived as a barrier that needs to be crossed to obtain a spark. In the first phase of the ignition process, the properties of the combustible mixture are dominated by the shock wave, which is emitted during the expansion of the hot plasma channel. Once breakdown occurs, the next phase, arc, begins. Arc is caused by the *thermionic*[2] emission of electrons from the cathode surface. The voltage drops rapidly to a low value (of around 50 V). The current starts to fall and the voltage stays at a constant value until a threshold value of the current is reached. The cathode surface temperature rises to 3000 K, which is above the melting temperature of the cathode material at typical pressures. For this reason, the majority of the cathode erosion takes place during the arc phase. The electrons emitted from these pools are required to sustain the arc. The arc phase typically lasts for 10 microseconds and energy deposition is of the order of 1 mJ. Glow is the final phase of the spark. During glow, the mechanism of the emission of electrons from the cathode surface changes. The glow phase begins when the dominance of the thermionic emission of electrons ends. The bombardment of positive ions on the electrode surface now becomes the dominant mechanism. Since this mechanism has a very low efficiency, the current decays to a low value (less than 1 A). The voltage, on the other hand, rises to a higher value (around 500 V). The glow phase is thus characterized by low currents and high voltages. The glow phase lasts for about 3 ms. During this period, 30-100 mJ of energy is deposited, which is far more than for the other three phases. This is mainly due to the fact that the duration of glow is longer. The glow ends when the current in the gap decays to near zero. A precise modelling of spark includes all these physical processes.

The successful attempt to study these spark phases dates back to 1979, when Maly and co-

[2]Thermionic emission is the heat-induced flow of charge carriers from a surface or over a potential-energy barrier. This occurs because the thermal energy given to the carrier overcomes the forces restraining it. The charge carriers can be electrons or ions, and in older literature are sometimes referred to as "thermions". The thermionic emission of electrons is known as thermal electron emission.

workers [101] tried to experimentally investigate the initiation and propagation of flame fronts in lean methane air mixtures at 4 bar[3] using time resolved interferometry. Their experiment revealed that the influence of initial overpressure in the spark kernel expansion dominates only during the first $200\mu s$ and then the heat conduction and diffusion start dominating, the same conclusion was made by Ziegler *et al* [177]. This work also illustrated that the breakdown phase is far more efficient ($\approx 95\%$) than other phases in energy transfer and thus best suited for inflaming mixtures. Later on, Maly [100] developed an ignition model accounting for non-stationary nature of the ignition process. He found that for low turbulence levels, flame front is promoted by the turbulence as compared to expansion in a stagnant mixture. Increasing turbulence levels, however, creates an adverse impact on the developing kernel and finally quenches it. The work suggested that it is advantageous to have an early kernel expansion stage at low turbulence until a sufficiently large radius has been attained to withstand higher turbulence levels. Bradley and co-workers [6] published their work on theoretical computations of thermal spreading rates from the initial spark channel for both laminar and turbulent conditions. They found that even under turbulent conditions the early stages of thermal spread occur principally through the agency of molecular conduction. They also performed experiments for cross validation and found that the initiating kernel moves away from the spark gap with a velocity close to the r.m.s, turbulent velocity. For general ignition, under laminar conditions, they reported that flame kernel radius should be at-least the same order that of the laminar flame thickness. Spark modelling with detailed reaction mechanisms, combined with electrodynamical modelling including ionisation was performed by Thiele *et al* [156]. The modeling also includes an equation for the electrical field. The computations show that the influence of the shock wave on all processes dominates during the first few microseconds. This is an encouraging results for developing simplified spark model by neglecting the highly complicated transients processes occurring during early breakdown phase of spark.

In 3-dimensional CFD simulations, it is not practical to resolve the process in detail, because practical numerical grid sizes and time steps are larger. A simple and robust modelling technique to represent a overall ignition process is thus required. The Discrete Particle Kernel Ignition (DPIK) developed by Fan *et al* [54] is one such type of model, which was later extended by Tan *et al* [155] and used in RANS simulation. Accordingly, the kernel flame surface positions are marked by Lagrangian marker particles and the evolution of spherical kernel radius was governed by the heat and mass transfer equations. The ignition gradually switches to the combustion model once the ignition kernel exceeds a critical radius that is related to the integral turbulent length scale. Fig. 2.4 schematically represents DPIK model and the thermodynamics processes associated with it. Duclos et al *et al* [43] developed Arc and Kernel Tracking Ignition Model (AKTIM) for RANS simulation using lagrangian tracers, which later was extended to LES computations [134] based on flame surface density formulation. Here flame surface density is related to mean flame surface evolution during the sparking process and then after the transition period switched to regular filtered flame surface density transport equation.

Apart from these more sophisticated spark modelling techniques, there are also plenty of numerical work carried out using simplified modelling of spark ignition [25, 25, 77, 81, 90, 116, 158]. Accordingly, the spark is modelled as a source term in the energy equation lasting

[3]The study focussed on spark ignition applied to internal combustion engines where the air fuel mixture will be normally compressed and then ignited by spark.

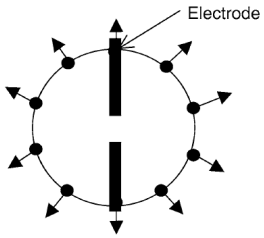

Fig. 1. Discrete particle ignition kernel.

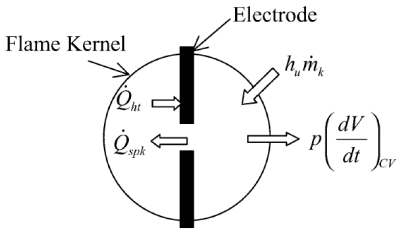

Figure 2.4: Thermodynamic system representing DPIK model [155]

over the spark duration. This technique, even-though neglects the associated complex physics during the initial stages of ignition, has rendered satisfactory results in the prediction of flame spreading following forced ignition. This simplified approach has been adopted in the present work too and further details about the spark modelling procedure will be discussed in chapter 5.

2.4 Reactive flow modelling

Simulation of process involving chemical reaction is a problem with added degree of complexities and needs to be dealt more carefully. A thorough knowledge of combustion technology, fluid dynamics, thermodynamics, mass transfer and heat transfer are prerequisite as the process includes all these phenomenon and interacting together. Fig. 2.5 shows the interaction of various physical phenomenon involved in a chemical reactions.

To describe the mixing between the reactants due to convection, molecular diffusion and turbulent transport, the fluid mechanical properties must be known. To describe the chemistry between the reactants, a precise knowledge of detailed chemical reaction scheme is absolutely required. Detailed chemistry schemes are built from knowledge of fundamental reaction kinetics. There could be situation where either of fuel or oxidizer, even sometimes the both, are in liquid phase. In many practical situations, liquid fuels will be injected into gaseous oxidizer environment thus a two phase system is encountered. The injected liquid interacts with gases, involves droplet breakdown and evaporation accompanied with turbulent mixing and then reacts chemically. Description of this system needs significant understanding of mass transfer, heat transfer and fluid mechanics. The heat generated due to combustion could be transferred via three modes of heat transfer viz. conduction, convection and radiation, which must be addressed along with the information of physical properties of species participating in the system evolution. Thus, combustion itself is a complicated phenomenon to model numerically even for a simplified configuration. The presence of turbulence further adds up the challenge. Besides

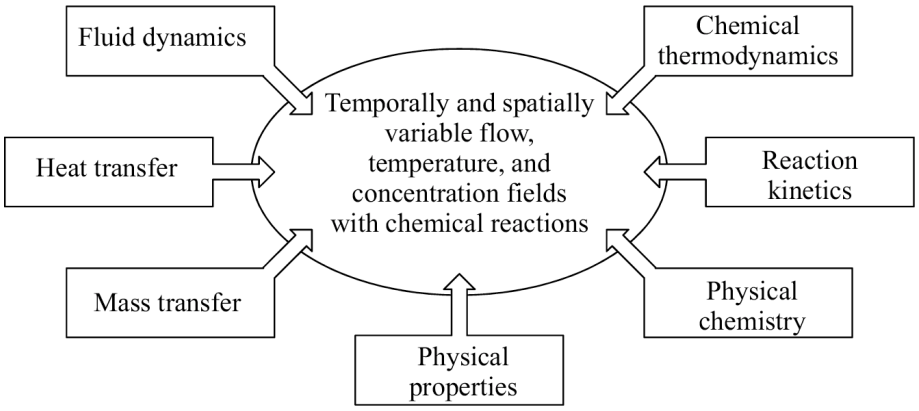

Figure 2.5: Area of knowledge important for process simulation

the diversity of scales brought into play by the turbulence, combustion occurs at molecular levels and involves a multitude of elementary chemical reactions, each with its own characteristic length scale. If one is to consider simultaneously the entire range of scales involved, the problem becomes a lot more complex. The effects of the turbulence are generally advantageous for the efficiency of the combustion, since turbulence enhances the mixing of component chemical species and heat, but adverse effects upon combustion can also occur, if the turbulence level is sufficiently high to create flame extinction. In turn, combustion may enhance the turbulence through dilatation and buoyancy effects caused by the heat release. Thus, a thorough understanding of the combustion process occurring in a combustor, for instance, would require first understanding the interplay and interdependency between combustion and turbulence. As far as the simulation of turbulent field with chemical reactions are concerned, it should be noted that the turbulent processes and reactions, progress at very different length scales and time scales. The models developed for dealing with such system should thus take this into consideration when there is a close coupling between these two. In certain occasions, these differences in time and length scales are exploited to make simplifying assumption to build models, for instance the flamelet theory [120], high activation energy limit asymptotic analysis [94] etc. However appealing through its simplicity, and popular for the variety of combustion models based on it, these hypothesis do not always hold true and accurate modelling of combustion processes occurring in a real application combustor requires more insight into the matter.

The classical problem in dealing with turbulent combustion modelling is the model to express the rate of reaction. The rate of reaction not only controls the creation and destruction of species during evolution, but also affects the heat release rate, which in-turns affects the turbulence via *Flame-generated turbulence* [125]. Even though the effect of turbulence on combustion is generally well understood, the reciprocal effect, the impact of combustion on turbulence is still a matter of some debate in the scientific community. First, the heat released by chemical reaction during the combustion process causes volumetric expansion and buoyancy in the surrounding flow. On the other hand, the increase in temperature causes an increase in the gas viscosity, and therefore, in the turbulent dissipation. In a turbulent environment, generally, the mean reaction source term is the quantity of interest. However, it is not possible

to express mean reaction rate analytically from the knowledge of mean reaction concentration and mean thermodynamics properties of the system. This is mainly due to the non-linearity associated with the chemical sources. Taylor's expansion of mean reaction rate for a simplified single fuel and oxidiser case could be seen in [167], which shows the fundamental problem in turbulent combustion modelling.

The definitions for concentrations are primarily required to describe the chemical transformation between species. Some of these relations will be given here. The mole fraction is one of these definitions, which is described as:

$$\mathrm{X}_i = \frac{\mathrm{n_i}}{\mathrm{n_{tot}}}, \mathrm{i} = 1, 2, ...\mathrm{n_{tot}} \tag{2.1}$$

where $\mathrm{n_i}$ is the number of moles of species i and $\mathrm{n_{tot}}$ is the total number of moles. The mass $\mathrm{m_i}$ of all molecules of all species is related to its number of moles as:

$$\mathrm{m}_i = \mathrm{W_i n_i} \tag{2.2}$$

where W_i is the molecular weight of species i. The mass fraction of the species is defined as:

$$\mathrm{Y}_i = \frac{\mathrm{W_i}}{\mathrm{W}} \mathrm{X_i} \tag{2.3}$$

where W is the mean molecular weight.

In reacting flows transport of mass, momentum and energy are crucial phenomena and it is often useful to relate the various transport coefficients together in dimensionless numbers. Following are the few dimensionless quantities frequently referred in reactive flow simulations. The Prandtl number (Pr) is defined as:

$$Pr = \frac{\nu}{\alpha} = \frac{\text{Momentum diffusivity}}{\text{Heat diffusivity}} \tag{2.4}$$

The Schmidt number (Sc) is defined as:

$$Sc = \frac{\nu}{D} = \frac{\text{Momentum diffusivity}}{\text{Mass diffusivity}} \tag{2.5}$$

The Lewis number (Le) is defined as:

$$Le = \frac{\alpha}{D} = \frac{\text{Heat diffusivity}}{\text{Mass diffusivity}} \tag{2.6}$$

Damköhler number is defined as

$$Da = \frac{\tau_\ell}{\tau_c} = \frac{\text{Characteristic turbulent time scale}}{\text{Characteristic chemical time scale}} \tag{2.7}$$

Here the characteristic turbulent timescale will be normally the eddy turn-over time of the integral scale ($\tau_\ell = \ell / u'$) and the chemical time is given by $\tau_c = \delta_L / S_L$. Here ℓ is the integral length scale, u' is the velocity fluctuation, δ_L is the laminar flame thickness and S_L is the laminar burning speed. Karlovitz number (Ka) is defined as the inverse of Damköhler number defined with reference to time scale of Kolmogorov eddy.

$$Ka = \frac{1}{Da(\eta)} = \frac{\delta_L}{\eta} \frac{u_\eta}{S_L} \tag{2.8}$$

These dimensionless numbers defined above along with Reynolds number (as defined in Chapter 1) are widely used in reactive flow simulation.

Turbulent flame normally involves hundreds of species and thousands of reactions, which must be accounted for complete description of the system.The description of these interactions can be simplified by the use of non-dimensional scalars, namely the mixture fraction and the reaction progress variable. These scalars are discussed below.

2.4.1 Mixture fraction

Mixing play a important role in diffusion and partially premixed flame. Moreover, during combustion, there are plenty of intermediate species created and consumed by the reaction. The local reactant concentration depends drastically on the mixing process. So it is quite important to describe the mixing in terms of some measurable quantity, and in practice this is done by defining a non-dimensional one, called mixture fraction. The simple definition for mixture fraction is the fraction of mass coming from the fuel stream in the reactant mixture. Mixture fraction is conserved and it is a passive scalar, which means that it changes only due to convection and diffusion but not due to the combustion process. Mathematically, it can be expressed as

$$Z = \frac{sY_F - Y_O - Y_0^0}{sY_F^0 + Y_O^0} \tag{2.9}$$

Where Y_F and Y_O represent mass fraction of fuel and mass fraction of oxidiser respectively. The subscript '0' refers to their corresponding concentrations in fuel and oxidiser feeding stream. By definition, the mixture fraction takes a value 1 in fuel stream and 0 in air stream. Mixture fraction is widely used in non-premixed combustion and partially premixed combustion modelling. It is convenient to write an equation for this normalised scalar and it reads

$$\frac{\partial \rho Z}{\partial t} + \nabla \cdot (\rho \mathrm{u} Z) = \nabla \cdot (\rho \mathcal{D} \nabla Z) \tag{2.10}$$

The above equation can be solved along with traditional Navier-Stokes equation to analyse the evolution of mixing between fuel and oxidizer.

Mixture fraction also be defined based on element conservation [16]. Chemical species are consumed and produced during chemical reaction, wheareas the elements like C, H, N or O are unaffected. The element mass fraction of the chemical element j is given by

$$Z_j = \sum_{i=1}^{n} \frac{a_{ij} W_j}{W_i} Y_i \tag{2.11}$$

where a_{ij} is a matrix counting the number of element j atoms in species molecule named i and n is the number of species in the mixture. A conservation equation could be written for the Eq. (2.11) without a source term. Now it could be possible, following Eq. (2.9), to define a mixture fraction based on element mass fraction. From the element mass fraction of the mixture several conserved scalars can be derived for the definition of the mixture fraction. In principle, any element may be used for this scope but because the different species involved in a combustion process diffuse at different rates the value of the mixture fraction distributions may be different depending on the element selected. Care should be taken while using this definition

by mentioning the element considered for mixture fraction definition with the presence of preferential diffusion. Consider a three component system C, H, O as given below

$$\nu_c C + \nu_H H + \nu_O O \longrightarrow Products \tag{2.12}$$

where ν_j is the number of atoms of element j in the mixture. The mixture fraction can be expressed in terms of element mass fractions as follows [16]

$$Z = \frac{Z_C/(\nu_C W_C) + Z_H/(\nu_H W_H) + 2(Z_{O,2} - Z_O)/(\nu_O W_O)}{Z_{C,1}/(\nu_C W_C) + Z_{H,1}/(\nu_H W_H) + 2Z_{O,2}/(\nu_O W_O)} \tag{2.13}$$

Here the fuel stream is denoted with index 1 and oxidizer stream is denoted with index 2. The mixture fraction is one of most important quantities for describing non-premixed combustion. According to Bilger [12], the fast-chemistry assumption implies that the instantaneous concentrations species and the temperature are functions only of the conserved scalar and this can drastically simplify the solution of reacting flow problems in the limit of fast chemistry.

2.4.2 Reaction progress variable

In premixed turbulent combustion modelling, the progress of reaction from reaction through products are traced using another normalised scalar called reaction progress variable, which is denoted by c. Unlike mixture fraction scalar, the progress of reaction scalar is an active one, meaning that, the value of c can be changed by not only convection and diffusion transport but also with the presence of reaction. The value of progress variable is 0 in unreacted fresh mixtures and 1 in completely burnt products, which are in equilibrium.

In a closed system, the reaction progress variable c can be defined as some suitable function, which monotonically increases during reaction. The usual choice in adiabatic premixed combustion model is the normalised temperature, which takes the form as shown below.

$$c = \frac{T - T_{reactant}}{T_{adiabatic} - T_{reactant}} \tag{2.14}$$

where T is the local temperature at any certain time instance during the reaction progress, $T_{reactant}$ is the fresh reactant temperature and $T_{adiabatic}$ is the adiabatic flame temperature for that mixture. In certain occasion, where the temperature rise is non-monotonic, for instance, in non-adiabatic combustion system, the linear combination of normalised species concentration is taken as the marker for tracing the progress of reaction. It could be either fuel or oxidizer, depending on whether the pre-mixture is lean or rich. Then the equation (2.14) takes the form

$$c = \frac{Y_{F,O} - Y^0_{F,O}}{Y^P_{F,O} - Y^0_{F,O}} \tag{2.15}$$

Here $Y_{F,O}$ stands for either mass fraction of fuel or oxidizer, superscript '0' refers to their concentration in fresh reactant mixture, superscript 'P' refers to the concentration in burnt products. It may be also possible to use the stable end products of the combustion phenomenon for defining the reaction progress variable. This method is used in the present numerical study and the relevant definition will be given in the upcoming chapter.

The definitions discussed above fit well for premixed combustion. However, with non-premixed combustion where the combustibles mixtures are highly inhomogeneous, there exists

another reactive scalar in usage called reactedness (R). The expression of calculating reactedness from mass fraction of fuel (Y_F) oxidizer (Y_O) and product (Y_P) species is as follows

$$R = 1 - \frac{\min\left(\frac{Y_O}{s}, Y_F\right)}{\sum_{i=1}^{n} Y_{P_i} + \min\left(\frac{Y_O}{s}, Y_F\right)} \tag{2.16}$$

where s is the stoichiometric mass ratio of fuel and air. The principal differences between expression (2.16) and the different definitions of the progress variable c listed before is that the reactedness R always assumes unity when one of the reactants is completely consumed. But this is not the case if the progress variable c is computed with equation (2.15) in local fuel rich flame situations, because even if the oxygen is completely consumed c indicates erroneously that there is still a potential for chemical reactions.

2.5 Modes of combustion and modelling

Generally, combustion can be classified according to several creteria. One of the most relevant classifications is made depending on the way the reactant species are mixed prior to entering the combustion chamber. Thus, there are two classical modes of combustion namely nonpremixed and premixed combustion. However, the phenomenon of partially premixed combustion, which occurs in many practical circumstances is actually addressed by current development of models. A general overview of these combustion modes and the modelling approaches that have been proposed in the literature are now discussed.

2.5.1 Non-Premixed Combustion

The fuel and oxidizer are present on either side of the reaction zone in non-premixed combustion. The schematic representation of a non-premixed system could be seen in Fig. 2.6. The fuel and air (oxidizer) are separated by a thin region called diffusion zone, where molecular diffusion, mixing takes place and where the flame is established. The local mixture fraction changes from 1 to 0 across this diffusion zone while moving from fuel to air. The flame is located where the local mixture fraction is stoichiometric (Z_{st}). Since, the continuous combustion requires the diffusion of air and fuel in the reaction zone, the combustion is mixing controlled. Thus, this type of combustion is also called diffusion combustion. Moreover, in diffusion combustion, the flame does not benefit from a self-induced propagation mechanism. Hence non-premixed combustion doesnt have any reference flame speed like premixed flames. This fact makes non-premixed combustion more sensible to turbulent perturbations. Non-premixed flames generally involve very high peak temperature thereby leading to high nitrogen oxides emission. The amount of heat transported away from the reaction zone is exactly balanced by the amount of heat released in a steady diffusion flame. Fig. 2.7 depicts the generic structure of diffusion flame. It could be noted that the gradients of fuel and oxidiser mass fraction are of opposite sign, which is typical for a diffusion flame.

The widely used models for non-premixed combustion simulation can be classified into two major categories depending on the hypothetical assumptions made in the speed of chemical reactions. They are infinitely fast chemistry models and finite rate chemistry models. The former case is where the chemical reactions are considered to be faster compared to turbulent

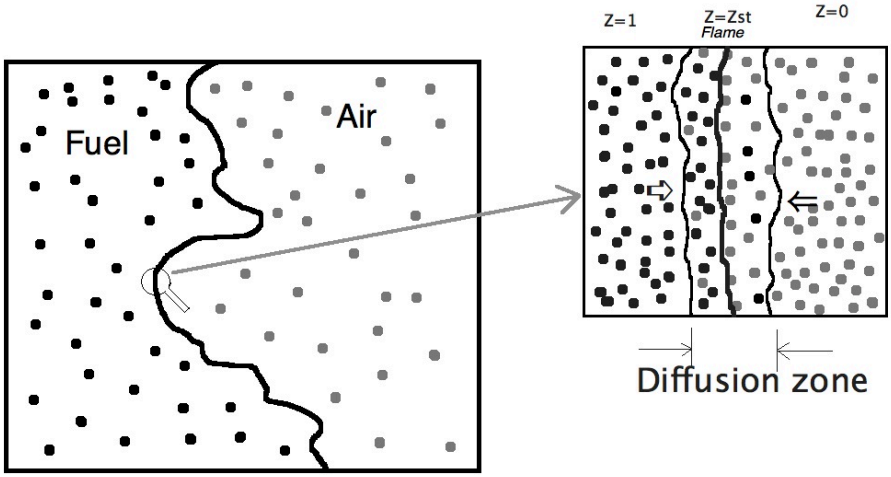

Figure 2.6: Sketch for non-premixed combustion system

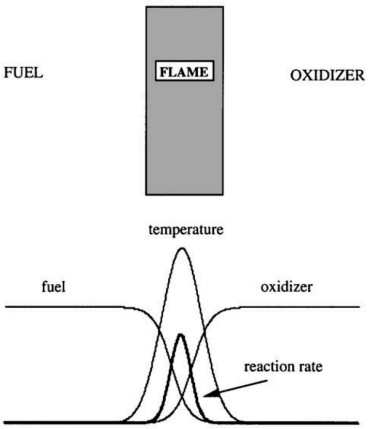

Figure 2.7: Mono-dimensional flame structure of a diffusion flame [167]

time scales. In the second type, the time scales of reactions are of same order than those of the turbulence. The finite-rate chemistry models are further classified in to three main groups. Flamelet models, PDF transport and Conditional Moment Closure (CMC) models. The essential modelling background for each of these approaches are discussed now.

The Eddy dissipation model

The Eddy dissipation model (EDM) falls under fast chemistry models, which is the simplest but widely used model for practical applications. At present, the industrial combustion community often use more generic combustion models like Eddy Dissipation model (EDM) [99], which is less costly. This model is also called "mixed is burnt" model because the reaction rate is

proportional to the turbulent mixing. This model is based on single step chemistry and the mean reaction rate is expressed as follows

$$\overline{\omega} = \overline{\rho} A \frac{\epsilon}{k} \min\left(\overline{Y}_F, \frac{\overline{Y}_O}{s}, \frac{B\overline{Y}_P}{1+s}\right) \tag{2.17}$$

Here A, B are model constants and s is the stoichiometric mass ratio. This description explicitly states that the turbulent cascading process from integral down to the molecular scales controls the chemical reactions as long as mixing is rate determining rather than chemistry. The reaction rate is assumed equal to the slower of the chemical reactions and the rate governed by turbulent mixing. When reactants mix at the molecular level, they instantaneously form products. This model cannot predict the minor stable species very accurately, however, calculates the heat release rate with good accuracy in many industrial combustion applications and so widely used for it. However, the model constants used here need to be tuned within a wide range to obtain reasonable results for a particular problem, limiting the overall prediction capabilities of this approach.

The assumption of infinitely fast chemistry is rather not completely true in moderate and highly turbulent flows, where the time scale of turbulence is comparable with reaction time scale. In such conditions, introducing finite-rate chemistry is important so as to be in a position to predict pollutant formation and other non-equilibrium phenomenon such as extinction, re-ignition etc. The important finite-rate chemistry models are discussed now.

Laminar flamelet model

The model based on laminar flamelet theory [120] is quite familiar in combustion modelling field. This comes under finite-rate chemistry model which is valid for moderate turbulent regimes. This model views the flame as tiny laminar burning flamelets embedded in turbulent flow field, thus the scale separation hypothesis is invoked here. The central assumption of this model is that the time scales of turbulence is considerably bigger than time scale of reaction. That inherently means that the smallest turbulent eddy is too big compared to the local reaction zone thickness and thus cannot penetrate the reaction zone. All the eddy could do is just wrinkling the flame and so the the inner flame structure remains laminar, as seen in Fig. 2.8. This is a strong assumption, however it is not completely unphysical considering the actual situation with moderate turbulence. With this assumption, the chemistry and the turbulence can be handled separately. It is to be noted that the species diffusion within the flame is rate determined and so this theory is way different from EDM model discussed before. The turbulence can affect the reaction rate by varying the flame thickness and thus the species dissipation rate across the reaction zone of the burning flamelet. The laminar flames can be computed *a priori* using detailed chemistry and the data can be stored in the form of flamelet libraries. These calculations can be done in mono-dimensional mixture fraction space with a coupling parameter called "scalar dissipation rate" (χ_Z). The reactive flow solver has to compute the mixture fraction and scalar dissipation rate distribution, thus all the species and thermodynamic variables can be read from the flamelet library by relating to the conserved scalar, the mixture raction, in case the assumption of equal diffusivity for all the species is applied. The unsteady laminar flamelet equation reads [120]

$$\rho \frac{\partial \mathbf{Y}}{\partial \tau} = \frac{\rho}{Le} \frac{\chi_Z}{2} \frac{\partial^2 \mathbf{Y}}{\partial Z^2} + \dot{\omega} \tag{2.18}$$

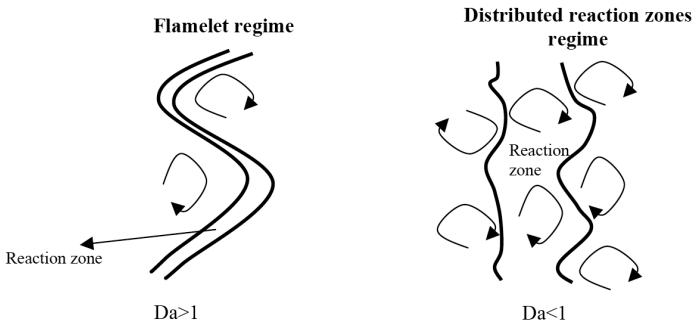

Figure 2.8: Effect of turbulence on the structure of the reaction zone

where $\mathbf{Y} = [Y_1, Y_2....Y_n, T]$ is the vector of species and temperature and $\dot{\omega}$ denotes their respective chemical source term.

The effect of turbulence on the burning flamelets can be described using a parameter called scalar dissipation rate (χ_Z) , which accounts for the effect of turbulent eddies on the flame structure. This term is calculated from the mixture fraction gradients in physical space and can be transposed to composition space. Higher level of χ_Z characterises strong diffusion inside the flamelet and thus increases heat and mass transfer within the flamelet. There is a critical maximum limit for this χ, termed as quenching scalar dissipation limit ($\chi_{Z\ q}$), beyond which the flame ceases to exist due to excessive heat and molecular diffusion from the reaction zone. In turbulent flames, this modelled term is a function of the inverse of the turbulent time scale (k/ε) and the variance of the mixture fraction ($Z"^2$), which accounts for the residence time of turbulent eddies and the fluctuations of mixture fraction about it's mean respectively.

Locally, the flamelets have a planar mono-dimensional structure with sufficiently small flame thickness. So, the reaction zone can be regarded as a configuration with opposed jet whose velocity fields are given by potential flow solution. The stagnation velocity gradient for such configuration is termed as strain rate a, which is inversely proportional to it's characteristic aerodynamic time. In principle, strain rate in physical space is equivalent to χ_Z in composition space. However, while discussing the impact of turbulence in diffusion flames, it is considered appropriate to use χ_Z, rather than a, due to the fact that χ_Z accounts for the gradient of mixture fraction [57]. However, one can also use strain rate to describe the turbulence-flame interaction. Generally, strain rate is used in the context of premixed turbulent flames rather than non-premixed systems.

The regime of validity of the flamelet assumptions hold only when certain conditions are satisfied. These condition are, in general, expressed in non-dimensional numbers like Reynolds number (Re), Damköhler number (Da) and Karlovitz number (Ka) [167], which are defined before. The laminar flamelet model can be applied for the regime where the $Da \gg 1$ and $Ka < 1$.

When the intensity of turbulence is increased, then the validity of the flamelet theory starts breaking. Then the turbulent eddies are strong enough to get into the flame structure and the local flame is no more planar and mono-dimensional. Refer the Fig. 2.8 for the case $Da < 1$, which describes this situation. The turbulent eddies can not only wrinkle the flame front, but also can penetrate the flame and thicken the flame. Under this conditions, the flame can no

longer be regarded as a laminar thin burning pocket. With an intense turbulence, the eddy can even tear the inner reaction zone thereby leading to flame quenching. Laminar flamelet theory cannot describe this flame regime.

Probability density function approach

Models based on transported Probability Density Function (PDF) show promising results, even in dealing with situations where $Da < 1$ [127]. It was a pioneering work by Pope, who developed a method for solving the composition joint PDF equations to predict the properties of the turbulent reactive flow fields. In the numerical point of view, transported PDF formulation possesses high dimensionality for which, the usual technique like finite difference or finite volume are not very attractive due to the memory constraints. Pope [127], therefore used a Monte-Carlo simulation technique. This method treats the turbulent reacting flow as an ensemble of particles so that each particle has its own position and composition and travels in the flow with instantaneous velocity. The particle state is described by its position, velocity and reactive scalars and the particle properties are described by stochastic Lagrangian models.The main advantage of PDF based method is that the chemical source term appears in closed form and thus no modelling is needed. The mean turbulent reaction rate are computed with the help of joint probability density functions as shown below.

$$\overline{\dot{\omega}_R} = \int_{Y_1}\int_{Y_2}...\int_{Y_N}\int_{T} \omega_k\,(Y_1, Y2...Y_N, T)\;\; P(Y_1, Y_2...Y_N, T) dY_1\; dY_2...dT \tag{2.19}$$

Hence, the trouble of the closure of the thermo-chemical interaction in reacting flows is then shifted to the calculation of the joint probability density function. In practice it is shown that it is very difficult to presume the shape of a joint PDF depending on more than two variables, so balance equations must be derived to close the problem. The transport equation is solved for the evolution of the single-point, single-time joint scalar, or joint velocity-scalar, PDF. Mass and Pope [106] have proposed a method that reduces the number of independent variables to a minimum while still maintaining a high accuracy. This is the method of Intrinsic Low Dimensional Manifolds (ILDM), which will be briefly discussed in the final section of this chapter.

The positive point about transported PDF method is the appearance of chemical source in closed form. Moreover the assumption regarding the flame structure is no longer needed in PDF methods. However, there exist few challenges; certain term like turbulent transport terms, molecular mixing term in the PDF transport equation need modelling. Since in single point PDFs information about the neighbouring points are not available all these gradient terms need modelling. This represents the weak point of PDF methods, also because in combustion reactions occur at the molecular level controlled by molecular mixing. The performance of PDF models depends strongly on the closure chosen to simulate mixing processes. In the end these methods have a very uncertain fortune in LES context.

Conditional moment closure

Bilger [13] and Klimenko [16] independently developed Conditional Moment Closure (CMC) model for turbulent non-premixed unsteady flames. There are two different mathematical procedures to derive the CMC model; the joint PDF method by Klimenko [16] and the decomposition method by Bilger [13]. However, they yield the same form of the CMC equation,

which gives substantial credence to the model.The main concept behind CMC is to find how the reactive scalars (e.g. temperature, species mass fractions) depend on conserved scalar; for instance mixture fraction in non-premixed systems. Accordingly, the spatial and temporal fluctuations of the unconditionally averaged quantities like species concentrations can be obtained by integrating conditionally averaged values over tha range of conserved scalar values after weighting with local PDF of the conserved scalar [15]. In non-premixed combustion, mixture fraction can be used as a conditioning variable for the conserved scalar. All the unconditioned variables can be related to this conditioned conserved scalar. DNS calculation showed that CMC model provide improved prediction over steady non-premixed flamelet model [151].

The first-order CMC model assumes that the conditional fluctuations are negligible and that the conditional chemical source term is only a function of the first-order moments, like, the conditional species concentrations and temperature. This closure assumption may be inaccurate for flame stabilization problems. If the fluctuations of the reactive scalars at a given mixture fraction value are small, the first order CMC can result in accurate predictions in non-premixed turbulent combustion. Using first order CMC the Favre species mass fractions are computed by the following integral:

$$\widetilde{Y}_k = \int_0^1 \left(\overline{Y_k|z^*}\right)\ p\left(z^*\right) dz^* \tag{2.20}$$

Here $\left(\overline{Y_k|z^*}\right)$ is the conditional average of Y_k conditioned on z^*, which is given by.

$$\left(\overline{Y_k|z^*}\right) = \int_0^1 Y_k p\left(Y_k|z^*\right) dY_k \tag{2.21}$$

$p\left(Y_k|z^*\right)$ here denotes the conditional PDF of Y_k, which is calculated from joint pdf of Y_k, z^*

$$p\left(Y_k|z^*\right) = \frac{p\left(Y_k, z^*\right)}{p\left(z^*\right)} \tag{2.22}$$

If the fluctuations of the reactive scalars at a given mixture fraction value are large, then the first order CMC is no longer applicable. One possible improvement is to close the conditional chemical source term using a second-order approximation [89]. Similar to the flamelet approach the assumption of a thin reaction zone is not particularly good for CMC since CMC is not expected to be valid for very thin reaction zones [87]. The links between finite chemistry models and the assumptions used in these models were discussed in detail in literature [88].

Although the transported PDF models and CMC show improved prediction capabilities for minor combustion species like CO, NO_x in turbulent non-premixed flames, their usage is limited in industrial applications mainly due to the computational cost associated with them.

2.5.2 Premixed combustion

In premixed systems, fuel and oxidiser are well mixed thus making a homogenous mixture. A picture of premixed flame from Bunsen burner could be seen in Fig. 2.9. Unlike diffusion flame which is diffusion controlled, the premixed flames are reaction controlled, because the mixture is well mixed and ready to burn. Due to this, normally, more safety measures need to be taken while dealing with premixed flame, which can be potentially hazardous due to

Figure 2.9: Picture showing premixed flame from a Bunsen burner. The small white circle denotes a portion of reaction layer on the flame surface.

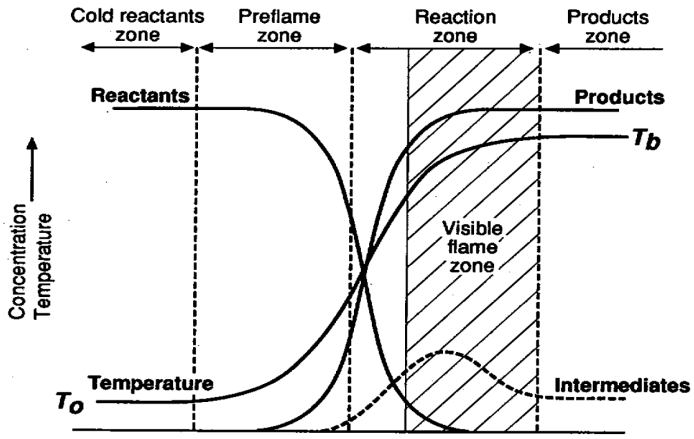

Figure 2.10: Mono-dimensional flame structure of a premixed flame [160, 167]

it's self-propagating capability. The propagation of the flame front due to the local imbalance between diffusion of heat and chemical composition of the mixture. In contrast to non-premixed combustion the position of the reaction zone is not defined by the diffusion of reactants, but by balancing the local convective velocity of the reactants with the rate of consumption of the reactants, which corresponds to the flame speed. The structure of premixed flame could be seen in Fig. 2.10. In contrast to diffusion flame, both fuel and oxidiser mass fraction gradients are of same sign across the premixed flame.

The premixed combustion regimes can be represented in the Borghi diagram shown in Fig. 2.11. There are two extreme regimes in this diagram: the well-stirred reactor regime and the eddy breakup regime. In the well-stirred reactor regime, the chemistry is so slow that all the

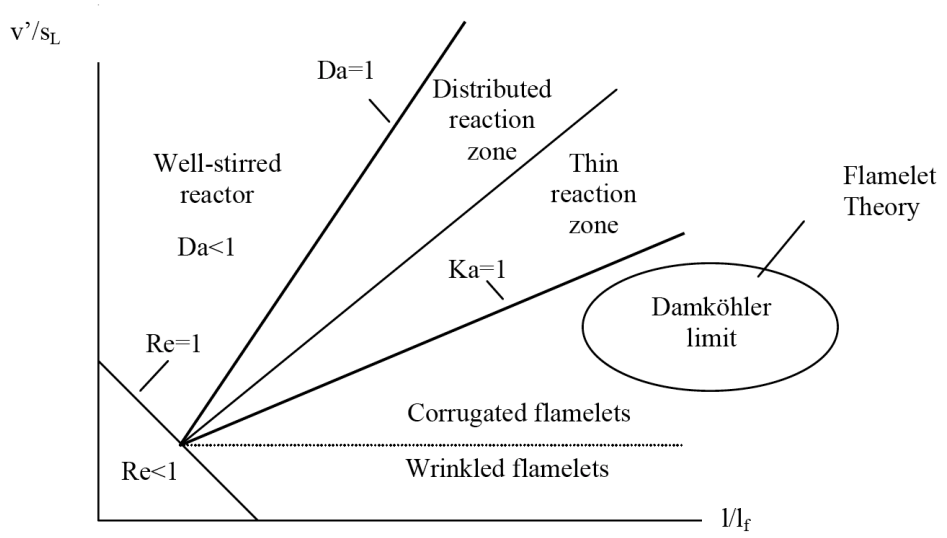

Figure 2.11: The Borghi diagram for turbulent premixed combustion regimes [125]

species are always locally well mixed and chemical reactions proceed at a kinetics-dominated rate. The eddy breakup regime is the opposite limit of infinitely fast chemistry and infinitely slow molecular transport. As soon as a turbulent eddy mixes reactive gases that have suitable thermodynamic states, these are burnt instantaneously.

Eddy Break-Up Model

The Eddy Break-Up Model (EBU) proposed by Spadling [148] is an alternate practical option for premixed combustion modelling of complex configurations. As indicated before for non-premixed flames(EDM), the EBU too is based on the assumption that the chemistry is fast compared to turbulent transport. The mean reaction rate is then controlled by the rate at which the turbulence can bring the fresh reactants into contact with hot products. The mean reaction rate, according to this model reads

$$\overline{\dot{\omega}}_F = C_{EBU}\overline{\rho}\frac{\epsilon}{k}\sqrt{\widetilde{Y_F''^2}} \tag{2.23}$$

C_{EBU} is the model constant and the Favre variance $\widetilde{Y}_F''^2$ quantifies the species mass fraction fluctuation magnitude. The reaction rate for progress variable (c) can be written as [167].

$$\overline{\dot{\omega}}_c = -C_{EBU}\overline{\rho}\frac{\epsilon}{k}\sqrt{\widetilde{c''^2}} = C_{EBU}\overline{\rho}\frac{\epsilon}{k}\widetilde{c}(1-\widetilde{c}) \tag{2.24}$$

For example, Del Taglia *et al* [154] used this model for understanding the heat release phenomenon in a commercial household burner. Eddy break-Up model tends to overestimate the reaction rate, especially in highly strained region where the turbulent mixing time is large (flame holder wakes, walls etc...). Again, the real advantage of this model lies in the low computational costs, but obviously this simple approach is not able to predict minor combustion products and non-equilibrium effects.

Bray-Moss-Libby model

The Bray-Moss-Libby model (BML) is a classical model initiated by Moss and Bray [111]. This model views the flame as a infinitely thin entity and is basically derived for the case where $Re \gg Da \gg 1$. The model assumes the pdf of the progress variable c to be a two delta function distribution i.e. quasi-bimodal distribution. Thus the probability of c may be written as

$$\overline{P}(c*) = \alpha\delta(c^*) + \beta\delta(1 - c^*) \tag{2.25}$$

where α, β are respectively the probability to find fresh and burnt gases in a particular location. A systematic development of this equation to find mean reaction rate may lead to recover the EBU model equation (can be refereed in [167]). The only difference between EBU and BML model is that the BML model involves proper theoretical derivation by clearly mentioning the assumptions, whereas EBU is developed based on phenomenological approach.

Flame surface density approach

Another approach in premixed flame modelling is the flame surface density (FSD) description [102, 125, 133, 159, 167] where the flame is described as a geometrical entity. It is identified as a thin interface between fresh gases and burnt products. The flame is thus assumed to be very thin and the flame surface density Σ is introduced. By definition, flame surface density is the amount of available flame area (δA) per unit volume (δV). The flame surface can be convected, diffused, strained and curved by the turbulent velocity field. The flame surface density measures the available flame area δA per unit volume δV. The mean reaction rate of a species i is then modeled as:

$$\overline{\dot{\omega}}_i = \dot{\Omega}_i \Sigma \tag{2.26}$$

where Ω_i is the mean local burning rate per unit flame area integrated along the normal direction to the flame surface. There are two ways to estimate the flame surface density Σ; by using an algebraic relation or by solving a transport equation for Σ. An algebraic relation for flame surface density can be given as follows [120]

$$\Sigma \sim \frac{\overline{c}(1 - \overline{c})}{\hat{L}_y} \tag{2.27}$$

where $\overline{c}$ is the mean progress variable and $\hat{L}_y$ is the crossing length scale. Geometrical consideration [159] and statistical description [128] have lead to more rigourous derivation of balance equations for flame surface density equation, but with few unclosed terms. A simple version of Σ balance equation, in the context of RANS simulation may look like [70, 120]:

$$\frac{\partial \Sigma}{\partial t} + \frac{\partial \widetilde{u}\Sigma}{\partial x_i} = \frac{\partial}{\partial x_i}\left[\frac{\nu_t}{\sigma_\Sigma}\left(\frac{\partial \Sigma}{\partial x_i}\right)\right] + \alpha_0 \frac{\epsilon}{k}\Sigma - \beta_0 S_L \frac{\Sigma^2}{\widetilde{c}(1 - \widetilde{c})} \tag{2.28}$$

Here σ_Σ denotes turbulent Schmidt number. The three right-hand side terms in Eq (2.28) correspond respectively to the turbulent transport of the flame surface density, the increase of flame surface area due to the strain rate induced by turbulent flow motions and the destruction of flame surface by consumption of the intervening reactants. The concept of flame surface density has been successfully applied for variety of LES [41, 76] and RANS [70] simulations.

G-field method

G-field equation method, which is also known as level-set method, falls under geometric flame description technique like FSD approach [119, 167]. The level set approach describes the flame front, which is represented by an arbitrary isosurface Go of a scalar field G, whose evolution is described by a kinematic equation, termed as G-equation. G-equation is derived to introduce the propagation of the fronts [171]. The G- equation may be written as:

$$\frac{\partial \mathrm{G}}{\partial t} + \mathrm{u_c}\nabla \mathrm{G} = \mathrm{w}|\nabla \mathrm{G}| \tag{2.29}$$

where w is the relative velocity of the iso-surface. This equation is only defined at the premixed flame surface, which is a iso-scalar surface

$$\mathrm{G}(x,t) = \mathrm{G_0} \tag{2.30}$$

where $\mathrm{G_0}$ is arbitrary but fixed. Based on the role of G-equation in the description of premixed flames, it can be viewed as an analogous field equation like mixture fraction balance equation for non-premixed case. The internal flame structure needs not to be resolved on the computational mesh, which is the main advantage of this G-field equation method. Generally, the G(x), which is several orders times thicker than the flame needs to be resolved. The coupling required between species or energy balance equation is a difficult problem. The rate of heat release and the consumption of reactants are controlled by the consumption speed Sc as follows:

$$\rho_u S_c = \int_{-\infty}^{\infty} \dot{\omega} d\xi \tag{2.31}$$

where ρ_u is the fresh gas density and ξ is the spatial coordinate along the normal direction to the flame front. Note that S_c can be different from propagation speed (w) especially for the flame front which is curved. This coupling is the key modelling point in G-equation model and different formalisms are proposed to deal with this [167]. For instance, the coupling is done between the turbulent flame speed S_T and w. Starting from the filtered progress variable equation, the following equation for G-field can be derived.

$$\frac{\partial \widetilde{\mathrm{G}}}{\partial t} + \widetilde{\mathrm{u}}_\mathrm{c}\nabla \widetilde{\mathrm{G}} = \frac{\rho_u}{\overline{\rho}}\mathrm{S_T}|\nabla \widetilde{\mathrm{G}}| \tag{2.32}$$

This formalism is a good candidate for the simulation of large systems, where they don't need resolving the flame brush. However, this method needs a model for turbulent flame speed and care should be taken to model the effect of turbulence on propagation and turbulent transport [112].

Thickened flame model

Thickened flame model was developed by Colin *et al* [34] in the context of LES for premixed flame. The principal motive of this study was to capture the flame front in a LES mesh, which is, in general, several times thicker than the flame. This is achieved by artificially thickening the flame by multiplying the flame thickness with a thickening factor 'F', which is high enough (normally takes a value between 5 to 30). Then, the flame is thick enough to be captured

by LES mesh. The laminar flame speed of the thickened flame is maintained the same, while performing this artificial thickening. This is achieved by multiplying the thermal and molecular diffusivities α and D by F, and the reaction rate $\dot{\omega}$ by 1/F. The transport equation for species balance in a premixed flame, while incorporating this atrificial thickening may look like

$$\frac{\partial \rho Y_F}{\partial Ft} + \frac{\partial \rho u Y_F}{\partial Fx} = \frac{\partial}{\partial Fx}\left(\rho(DF)\frac{\partial Y_F}{\partial Fx}\right) + \frac{\dot{\omega}_F}{F} \tag{2.33}$$

As the flame is artificially thickened from δ_L to $F\delta_F$, the interaction between turbulence and chemistry is modified because the Damköhler number (Da), which compares turbulent and chemical time scales, is decreased by a factor F. To account this, an efficiency factor E is introduced introduced in the above equation. This thickened flame model has been successfully tested for variety of premixed configurations [34, 63, 116].

Laminar flamelet model

The flamelet model discussed for diffusion flame has also been extended for premixed flame [120]. The assumption with flamelet model is that the premixed flame is thin and continuous, possess the properties of laminar flamelets. The flame structure for such flamelet can be obtained by performing strained laminar flamelet calculation in mono-dimension. Suitable reaction progress variable can then be defined to map the reaction space in to a progress variable sub-space. The value of any scalars such as species concentration, reaction rate of species and temperature can then be calculated by knowing the value of reaction progress variable [21].

$$\widetilde{\Phi} = \int_{-\infty}^{\infty} \Phi(c)\overline{P}(c)dc \tag{2.34}$$

Where $\overline{P}(c)$ represents the filtered probability density function. The shape of this PDF are determined from the first and second statistical moments i.e. mean and variance of the progress of reaction. Bradley *et al* [21] applied this model to a jet stirred conical reactor and compared the predicted results of stable species with measurement and found good agreement. This model better describes the region where turbulence intensity is moderate and the reactions zone stays intact. In the Borghi diagram in Fig. 2.11, the region where the flamelet assumption holds true is below the line $Ka = 1$. Laminar flamelet model was adopted in this numerical work while preparing chemistry table and more details concerning this will be presented in chapter 3

PDF approach and CMC method

The PDF transport equation model and CMC model exist for premixed flame simulation too. Both of these models are originally developed for non-premixed combustion, later extended for premixed case. In PDF model for premixed system, instead of mixture fraction, here the transport equation is solved for the PDF of progress of reaction [130]. There are unclosed terms involving turbulent micro-mixing and reactions, which are to be modelled here in the PDF transport model for premixed flames. In CMC for premixed combustion, the conditional quantity is the progress variable, which is analogous to mixture fraction for non-premixed case. Although these methods are rich in modelling ingredients, at present, they are not so often used in the combustion industry due to the high computational cost involved with it.

2.5.3 Partially premixed combustion

Partial premixed combustion is encountered in a situation where some initial premixing occurs in reactants in non-premixed combustion system. In this type of combustion a fuel stream is mixed with air or air mixed with fuel; the fresh reactants in this system mix before reaching the reaction zone. This pre-mixing, outside the flammability limits, leads to the phenomenon of partially premixed combustion. Both streams improve the starting conditions for the mixing process in the pre-flame zone. This helps in achieving a reduction in the maximum temperature while keeping the flame stable. Therefore, the emission problem for non-premixed flames and the flame propagation and stability problems for premixed flames could be handled by this hybrid flame. Flame stabilisation using burnt gas recirculation is a typical example for partially premixed system where the reaction zone is fed by the mixture of reactants and burnt products. There are different technical applications where partial premixing is definitely important:

- In laminar or turbulent non-premixed jet flames, oxidizer and fuel may mix each other before ignition. This is the typical situation of jet flames lift-off, when flames are not attached to the mouth of the jet burner. This configuration may be chosen in large industrial burners because the lifting of the flame can avoid the erosion of the burner material. This is the canonical problem for studying partially premixed combustion.

- After quenching the reaction zone, the reactants can mix leading to the possibility of re-ignition and combustion in a partially premixed regime.

- In auto-ignition systems, like in Diesel engines, some part of the nonhomogeneous mixture can mix before the auto-ignition occurs.

- In most devices where a spray of liquid fuel is injected, partially premixed flame propagation is observed, as in gasoline direct injection engines or in aircraft jet engines.

An interesting phenomenon of partially premixed combustion is observed when in laminar flows the flow velocity is of the same order of the flame speed. In this case a triple flame may stabilize the combustion. First observed by Phillips [123], triple flame is a classical representation of a partially premixed flame that contains a fuel-rich premixed reaction zone, a fuel-lean premixed reaction zone, and a nonpremixed reaction zone. Fig. 2.12 shows a schematic representation of a freely propagating triple flame. Three distinct burning branches are visible in a triple flame, viz. a lean premixed tail, a rich premixed tail, and a trailing diffusion flame sandwiched between the two branches [123]. All the three branches are connected at a cusp, called triple point, which will be propagating along the stoichiometry.

The mode of partially premixed combustion is relatively new in industrial application and thus, unlike completely premixed and non-premixed cases, limited efforts have been made so far to compute partially premixed system and compare the predictions with measurement. Generally, the models developed for non-premixed system [14] and premixed system [60] are extended to partially premixed one considering the degree of partial premixing. However, this approaches are not strictly correct at all circumstances. For instance, in the work of Fiorina *et al* [61] they investigated the applicability of the flamelet tabulation technique (originally devised for simulating premixed flames) to approximate the chemical structure of partially premixed flames. Their results showed that when fresh fuel/oxidizer mixture equivalence ratio

takes values within the flammability limits, the results obtained with premixed flamelet technique showed good agreements. However they indicated that when fresh fuel/oxidizer mixture equivalence ratio takes values outside the flammability limits, the diffusive fluxes in the mixture fraction space started dominating and the results become worse. The fluxes in mixture fraction space (represented as scalar dissipation rate in composition space) are neglected in the premixed tabulation. In general, in composition space representation, the partially premixed flame includes three scalar dissipation rates namely the scalar dissipation rates of mixture fraction and reaction progress variable and a cross scalar dissipation rate, which cannot be only accounted by the models developed for either pure premixed combustion or non-premixed combustion [114].

It is still not clear whether the formulations based on premixed or non-premixed is well suited to model partially premixed system. As mentioned before, the lifted jet diffusion flame exhibits a partially premixed flame at the flame base propagating against the flow. There is still a debate whether this stabilisation process is governed by premixed flame propagation [47] or diffusion flame quenching at the flame base [121]. Predicting the lift-off height is probably the most severe test for any model for partially premixed combustion. This is because the turbulence there is quite intense due to the high shear in the jet.

Rogg *et al* [137] have first proposed the formulation for extending the laminar flamelet model for non-premixed combustion, by accounting for the partially premixed phenomenon. They defined a new term called "Premixedness parameter" to characterise the degree to which the reactant streams of a flamelet are premixed. Analog to the flamelet model for the diffusion flame, they proposed extended flamelet model for diffusion flame showing partially premixed structures suggests that any scalars, such as species concentration or temperature are functions of three variables, i.e. modified mixture fraction (in order to include partial premixing), scalar dissipation rate and the premixedness parameter. This extended model showed appreciable results with high Re turbulent partially premixed flame. Favier *et al* [55] proposed a model based on two scalar level set approach for the modelling of the turbulent partially premixed combustion. This model combines the flamelet models of premixed and non-premixed combustion. Veynante *et al* [166] proposed a combined flamelet model based on the concept of flame surface density. A balance equation is solved for flame area for unit volume for each zone in the partially premixed regime namely premixed, non-premixed and non reactive mixing zone. This model showed better prediction in heat release and burning speed of partially premixed flames.

Recently, a five dimensional manifold method was proposed for preparing chemistry tabulation for a system involving premixed, diffusion and partially premixed flames [114]. The so called Multidimensional Flamelet-generated Manifold (MFM) equations are derived from basic conservation equations, systematically projected in composition space, which includes dissipation rates in mixture fraction and progress of reaction space as well as a cross-scalar dissipation rate. The details regarding the MFM method and validation can be found in the publication attached in the end of this thesis. The main advantage of MFM is that it naturally describes hybrid combustion regime such as partially premixed.

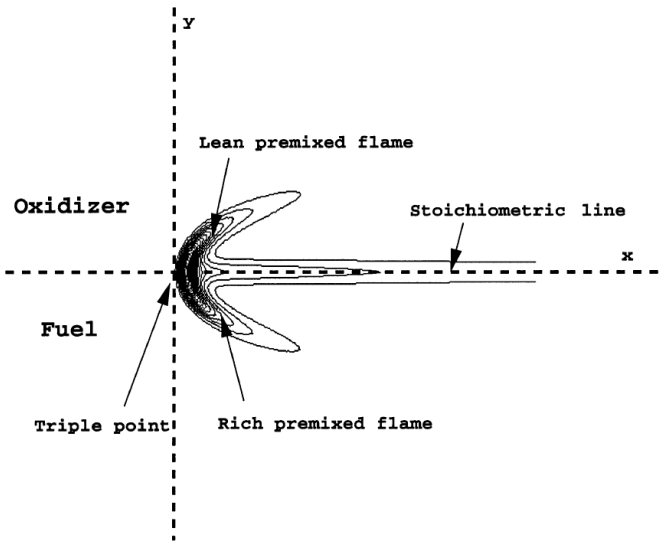

Figure 2.12: Sketch of a freely propagating triple flame [167]

2.6 Chemistry reduction and tabulation

One of the major issues of numerical combustion simulation is the right definition of a reaction mechanism. As seen before, although the models could be developed based on the assumption of infinitely fast chemistry, these models cannot predict some real behaviours of combustion system, for instance auto-ignition. When the prediction of intermediate species and pollution is of interest, clearly the above said assumption cannot be made. The next possible options is the use of skeletal chemistry schemes derived from the detailed schemes. However, this is a tedious process to optimally choose the definite number of sub-sets of reactions and species to satisfactorily describe the over-all reaction. This choice is not always trivial and unique, which is more or less problem dependent. The remaining final option is the complete detailed chemistry to accurately describe the process. But, this requires a huge amount of memory and calculation time. Moreover, the time step would be too small to be numerically treated. Due to the too high level of complexity in turbulent reactive flow modelling, tabulating chemistry is a way to include the complexity of detailed chemistry while keeping computing requirements sufficiently low. In some situations, where the detailed schemes become cumbersome, a reduced chemical scheme is proposed to better represent the chemical response of the system by only accounting the rate determining chemical paths (for example ILDM [106] and ISAT [144]). The basic idea behind the chemical reduction stems from the fact that the time scales involved in chemical reactions can be classified as into fast and slow reactions. In a conventional reduction technique, usually the partial equilibrium and steady state assumptions are invoked for particular reactions which are classified as fast reactions [122]. The species involved in these reactions are then considered to be created and consumed at a very high rate and thus remain in equilibrium. For a system with N number of species, and the assumption of M among the N are in equilibrium, the the total number of equation to be solved reduced from N to $N - M$. This reduction also significantly reduces the computational burden by removing the *stiff* fast chemical scales from the system.

Generally, the choice of fast time scales are done by hands which requires a prior knowledge about the chemical kinetics of the system involved. This is a complicated task, especially when handling complex hydrocarbon combustion is concerned. Also the validity of the steady state assumption is quite narrow in the band of thermodynamic states, which means that the species, which are considered in steady state at some low temperature range need not be in steady state when the temperature raises. To tackle this problem, the time scale analysis are done automatically in recently developed methods. Computational Singular Perturbation (CSP) [161] and Intrinsic Low Dimensional Manifold (ILDM) [106]. In CSP analysis to project out the fast time scales from the detailed chemical source term, whereas in ILDM technique the fast and slow chemical processes are separated by using an eigenvalue analysis of the Jacobian of the chemical source term. It is to be noted that both CSP and ILDM are merely a mathematical formalism to differentiate and select the fast time scales, for which, the equilibrium hypothesis is invoked further.

The steady state assumption for fast time scales are sometimes less efficient and not always relevant. For example, at low temperatures, the number of species remaining in quasi-equilibrium is less, in which neither ILDM scheme nor CSP reduction are applicable. In these reduction strategies, only the time scale of reaction rates are considered for time scale separation by neglecting convection and diffusion. At low temperature, the reaction rate terms are not very dominating and the convection and diffusion are then non-negligible.

This drawback of applicability of ILDM at low temperature region has been overcome by Gicquel *et al* [71], who developed Flamelet Prolongation of ILDM (FPI) and Van Oijen [162] who developed Flamelet Generated Manifolds (FGM). Both the techniques are based on projection of laminar partially premixed flame solution in a reduced sub-space. For this, freely propagating laminar flamelet simulation are done including convection and diffusion. These techniques combine the advantage of flamelet technique with dimension reduction techniques. The flamelet equation for species and temperature evolution then reads [42]

$$\rho_0 S_L \frac{\partial Y_i}{\partial x} = \frac{\partial}{\partial x}\left(\rho \mathcal{D}_i \frac{\partial Y_i}{\partial x}\right) + \dot{\omega} \tag{2.35}$$

where ρ_0 is the fresh premixture density, S_L is laminar burning velocity. Fully detailed chemical schemes can be conveniently used for such laminar calculations, which are one-dimensional. Numerical codes are readily available for solving one dimensional unstrained premixed flamelets, for instance PREMIX code from CHEMKIN package. Eq. (2.35) constitutes a boundary value problem, where the boundaries are fresh gas and fully burnt conditions. The solution consists of species and reaction profiles across discrete point in the flame coordinate. At every point the flamelet solution can now be retrieved by the flame coordinate. These flame coordinates can be conveniently replaced by reaction progress variable (Yc) defined in section 2.4.2, which are having one-to-one correspondence. Such flamelet simulation can be performed for a wide range of initial mixture condition, defined by mixture fraction and the results can be collected in a table $Y_i(Z, Y_c)$, for which, the parameters are Z and Y_c. This table will be normally prepared prior to the three-dimensional reactive flow calculations. Transport equation are solved for these parameters. The coupling between the flow and chemistry is done via these variables, through which the chemistry informations are read and reconstructed via multilinear interpolation.

This FPI technique has been successfully used in different numerical studies to simulate premixed, non-premixed and partially premixed cases [42, 60, 132]. In general, the length

scales associated with combustion are far lesser than the flow length scales, which necessitates a precise SGS modelling to mimic the mixing occurring at LES sub-filter level. Presumed conditional moment (PCM) closures have been proposed for treating the SGS part of mixing [164], which is a PDF based closure approach. The shape of the PDF of the SGS quantities are presumed to follow a beta distribution, which could be constructed from the first and second moments of the scalars, for which transport equations are solved. THE PCM-FPI technique has been successfully tested in variety of configurations [41, 42, 132] involving stable flame. But, so far, PCM-FPI has never been tried to simulate ignition and transient flame spreading problems. In this work, such an attempt has been made to describe the kernal development followed by forced ignition using LES combined with PCM-FPI. More details about the model will be given in chapter 4.

2.6.1 Basic steps of tabulated chemistry scheme

The basic idea of the tabulation technique is that the the variables of a chemical mechanism are not independent. The structure of the flame could be studied as a function of some few controlling variables (for example temperature, mixture fraction, progress of reaction etc). The basic steps involved in tabulation technique are listed below

- Study and analyse the flame structures closely to reduce the number of independent variables to find the the degrees of freedom of the chemical system.
- Choose one or a linear combination of independent variables, which would be the parameters of the table. The number of parameters determines the dimension of the table, and so, minimum possible parameters should be considered to keep the table size and thus the computation cost low.
- Create a table that contains some relevant chemical terms, parameterized by the chosen variables
- use the resulted look-up table to calculate all other thermodynamic and chemical properties.

CHAPTER 3

Governing equations and solver description

Contents

3.1 Governing Equations of LES

3.1.1 Filtering in LES

Large Eddy Simulation stands in the middle of the range of turbulent prediction tools, between Direct Numerical Simulation (DNS), in which all scales of turbulence are solved and Reynolds Averaged Navier-Stokes (RANS) calculations, in which all the scales are modeled. In LES, the large, energy containing scales of the motion are simulated numerically, while the small and unresolved sub-grid scales and their interactions with the large scales are modeled. The objective of LES is to compute the largest structures of the flow, typically, the structures larger than the computational grid size. The large scale motions are generally much more energetic than the small scale motions and feature long life time. They are also strongly dependant on

burner geometry. Their size and the strength make them the most effective transporters of the conserved properties. LES is a three dimensional, time dependent and computationally expensive method. On the other hand, compared to DNS, the computational costs are much more reasonable. Many of the combustion models have recently been extended for use in large eddy simulations. In this approach, the averaging operator is not the ensemble average, but a filter which is a local weighted average over a volume of fluid. Consequently, the LES-formulation employs filtered flow variables, denoted by $\overline{\rho}, \overline{p}, \widetilde{u}_i$. The basic filtering is denoted by an overbar, from which a related filtering, needed for compressible flows and denoted by a tilde, is derived. The filtering depends on the filter width, which is a characteristic spatial length-scale. The scales larger than the filter width are called resolved scales whose contributions are computed numerically and the scales smaller than filter size are called sub-grid scales (SGS), whose effects are modelled. Any flow variable f is decomposed into two parts; a large-scale contribution $\widetilde{f}$ and a small-scale contribution f''. The filtering operation is mathematically expressed as

$$\overline{f}(\mathbf{x}) = \int_{\Omega} f(\xi) G(\mathbf{x}, \xi) d\xi \tag{3.1}$$

where $\mathbf{x}$ and ξ are vectors in the flow domain denoted as Ω. The filter function G depends on the parameter Δ, called the filter width. The filter kernel satisfies the following condition

$$\int_{\Omega} G(\mathbf{x}, \xi) d\xi = 1 \tag{3.2}$$

for all the $\mathbf{x}$ in the flow domain Ω. For variable density compressible fluid flow, Alexandre Favre [56] introduced a related filter operation, which is known as Favre filtering or density weighted filtering. Accordingly,

$$\widetilde{f} = \frac{\overline{\rho f}}{\overline{\rho}} \tag{3.3}$$

Following this, any flow variable can be decomposed into $f = \widetilde{f} + f''$. Typical filters commonly used in LES, the top-hat, Gaussian and spectral cut-off filter, are listed in table 3.1.1. The symbol Δ_i denotes the filter width in the $i-$direction, whereas Δ is defined as

$$\Delta = (\Delta_1 \Delta_2 \Delta_3)^{1/3} \tag{3.4}$$

For constant Δ_i, the filter functions in table. 3.1.1 can be written as $G(\mathbf{x} - \xi)$. In this case the filter operation is a convolution integral. It is linear[1] and commutes with partial derivatives [139]. The corresponding Favre filter is also linear, but does not commute with partial derivatives.

The filtering operation in LES could be classified in to two types, viz. explicit filtering and implicit filtering. In the explicit filtering technique, specified filter kernel is used to filter the functions, and thus the unresolved fluxes are then termed as sub-filter fluxes. But, in many case, the filtering is implicit, meaning that the grid itself will be used as a filter. So the size of the filter becomes the grid size and the sub-filter fluxes are then called sub-grid fluxes. In most LES, the reduction to a discrete grid and the numerical differentiation scheme are interpreted as implicit filtering or grid filtering LES, and no filtering operation is explicitly

[1] A linear filter is the filter whose output is a linear function of the input. Any output value of a linear filter is the weighted mean of input values.

Filter	Filter function in real space	Filter function in Gaussian space
top-hat	$\begin{cases} \frac{1}{\Delta^3} & \text{if } \lvert\mathbf{x}-\xi_i\rvert < \Delta_i/2 \\ 0 & \text{otherwise.} \end{cases}$	$\prod_{i=1}^{3} \frac{sin(\Delta_i k_i/2)}{\Delta_i k_i/2}$
Gaussian	$\left(\frac{6}{\pi\Delta^2}\right)^{3/2} e^{-6\left(\frac{(x_1-\xi_1)}{\Delta_1^2}+\frac{(x_2-\xi_2)}{\Delta_2^2}+\frac{(x_3-\xi_3)}{\Delta_3^2}\right)}$	$e^{-(\Delta_1^2k_1^2+\Delta_2^2k_2^2+\Delta_3^2k_3^2)/24}$
spectral cut-off	$\prod_{i=1}^{3} \frac{sin(k_c(x_i-\xi_i))}{\pi(xi-\xi_i)}$ with $kc = \frac{\pi}{\Delta_i}$	$\begin{cases} 1 & \text{if } \lvert k_i\rvert < k_c \\ 0 & \text{otherwise.} \end{cases}$

Table 3.1: Filter kernel functions in real space and spectral space for different types of LES filters.

present in the simulation. But, when there is a strong change in the computational grid sizes in the domain, particularly with non-uniform or unstructured grids, the filtering operation also become non-uniform with implicit filtering technique. Explicit filtering ensures uniform filtering of high frequency components, irrespective of the grid size variation and thus controls the numerical error arising with finite-difference methods [98]. Nevertheless, implicit filtering is straightforward and easy to code and so widely used in LES computations.

3.1.2 Filtered Navier-Stokes equation

The LES filters are applied on conventional Navier-Stokes of mass, momentum and energy equations to obtain filtered LES equations. Accordingly, the filtered mass balance equation, following usual notation reads

$$\frac{\partial \overline{\rho}}{\partial t} + \frac{\partial \overline{\rho}\widetilde{u}_j}{\partial x_j} = 0 \tag{3.5}$$

Mass conservation equation (3.5) formally looks identical to traditional Navier-Stokes equation, but with Favre filtered primitive quantities. This is a positive point with Favre filtering as far as compressible flow is concerned, whereas the equation may become cumbersome with Reynolds averaging, in which, terms with density fluctuations will appear.

The filtered momentum equation, following summation convention reads

$$\frac{\partial \overline{\rho}\widetilde{u}_i}{\partial t} + \frac{\partial \overline{\rho}\widetilde{u}_i\widetilde{u}_j}{\partial x_j} = -\frac{\partial \overline{p}}{\partial x_i} + \frac{\partial \overline{\Psi}_{ij}}{\partial x_j} - \frac{\partial}{\partial x_j}\left[\overline{\rho}(\widetilde{u_iu_j} - \widetilde{u}_i\widetilde{u}_j)\right] + \overline{F_i} \tag{3.6}$$

In the above equation (3.6), the third term in RHS corresponds to the unresolved SGS term, which arises due to filtering the non-linear convection term in the original Navier-Stokes equation, which needs to be modelled in LES. The second term in Eq. (3.6) is the resolved viscous

stress term. For Newtonian fluids, these stresses are proportional to the rates of deformation, i.e. resolved strain tensor. Following tensor notations, it is represented as

$$\overline{\Psi}_{ij} = 2\mu_l \overline{S}_{ij} - \lambda \delta_{ij} \overline{S}_{kk} \longrightarrow \text{Resolved shear stress} \tag{3.7}$$

$$\overline{\rho}(\widetilde{u_i u_j} - \widetilde{u}_i \widetilde{u}_j) = \tau_{ij} \longrightarrow \text{Unresolved SGS stress} \tag{3.8}$$

In Eq. (3.7) the first term with dynamic viscosity μ is to relate stresses to linear deformation. The second term, with λ relates stresses to volumetric deformation. For gases, the value of λ is usually assumed equal to $(2/3)\mu_l$ [141], where μ_l is the laminar dynamic viscosity. $\overline{S}_{ij}$ is the resolved strain tensor, constructed from resolved velocity fields as shown below.

$$\overline{S}_{ij} = \frac{1}{2}(u_{i,j} + u_{j,i}) = \frac{1}{2}\left(\frac{\partial \widetilde{u}_i}{\partial x_j} + \frac{\partial \widetilde{u}_j}{\partial x_i}\right) \tag{3.9}$$

δ_{ij} is the Kronecker delta. The last term in Eq. (3.6) $\overline{F}_i$ denotes the component of body force acting on i^{th} direction.

Applying filter on energy equation results in

$$\frac{\partial \overline{\rho}\widetilde{e}}{\partial t} + \frac{\partial \overline{\rho}\widetilde{u}_i\widetilde{e}}{\partial x_i} = -\frac{\partial \overline{u}_i\overline{p}}{\partial x_i} + \frac{\partial}{\partial x_j}\widetilde{u}_i\overline{\Psi}_{ij} - \frac{\partial}{\partial x_j}\widetilde{u}_i\tau_{ij} + \overline{\frac{\partial q_i}{\partial x_i}} \tag{3.10}$$

Here the energy refers to the total energy, which is the sum of internal energy and kinetic energy.

In Eq. (3.10), the third term in RHS corresponds to unresolved SGS energy fluxes, which needs to be closed with a LES model. Gradient transport hypothesis will be normally used to express this term. The last trem in Eq. (3.10) q_i denotes the heat flux vector.

The unclosed SGS stress term in equations (3.6) and (3.10) need modelling effort, which should be constructed from the computed filtered quantities. This is often done by extrapolating the information of the resolved LES field to find the unresolved contributions. Following eddy viscosity assumption, the SGS stress term would be normally expressed in terms of turbulent viscosity (ν_t). Thus, modelling SGS terms implies modelling eddy viscosity ν_t, from which equation (3.6) can be closed.

$$\tau_{ij} = -2\overline{\rho}\nu_t\widetilde{S}_{ij} - \frac{2}{3}\overline{\rho}\nu_t\delta_{ij}\widetilde{S}_{kk} \tag{3.11}$$

3.2 Subgrid-scale stress modelling in LES

The Subgrid-scale (SGS) model has a central importance in LES computations, as the quality of the results heavily depends on the SGS modelling. The importance of SGS model becomes more and more relevant while the mesh size of LES computation becomes coarser. The SGS model should properly quantify the energy drained in the SGS level, from the available information of resolved scales. A proper SGS model should also represent interaction between small scales. In few occasions, there could be flow of energy from small scales to large scales, termed as backscattering, which should be included in a good SGS model. The SGS model also should ensure adequate dissipation by unresolved scales due to viscous effects, because, using

numerical methods that are energy conservative, the only way for turbulent kinetic energy to leave the resolved modes is by dissipation provided by SGS modelling. The rate of dissipation must be determined by the large scale structures of the flow rather than being imposed arbitrarily by the model. Variety of SGS models have been and are still being developed and tested by different groups and every model has it's own advantages and disadvantages. The three models which have been used in the present work are briefly discussed below.

3.2.1 Smagorinsky model

Smagorinsky model is the well-known and widely used SGS model developed by a meteorologist Joseph Smagorinsky during 1963 [146], which is based on equilibrium hypothesis. The main advantage of this model is it's simplicity. The model assumes that the eddy viscosity is proportional to the subgrid characteristic length scale and to the characteristic turbulent velocity taken as the local strain rate. The subgrid characteristic length scale is equal to the largest unresolved scale, which is equal to the size of the filter i.e. the LES filter size Δ. The expression for eddy viscosity reads as

$$\nu_t = (C_s\Delta)^2 \widetilde{|S|} \tag{3.12}$$

$$\overline{|S|} = \sqrt{2\widetilde{S}_{ij}\widetilde{S}_{ij}} \tag{3.13}$$

Incase of implicit filtering and for non-uniform mesh case

$$\Delta = (\Delta_1\Delta_2\Delta_3)^{1/3} \tag{3.14}$$

The constant used in Eq. (3.12) can be deduced based on Lilly's theory. The typical value of C_s takes anything between 0.1 to 0.2, depending on the flow configuration. For isotropic turbulence case, it would be normally 0.2, whereas for shear flows in channel, it is around 0.065. The suitable value of C_s should be guessed *a priori*, which is quite tricky with Smagorinsky formulation. Also, Smagorinsky formula is fully dissipative and thus not capable of accounting for energy backscattering. The model also has been criticised for not having proper near wall scaling and being over dissipative at boundary layers [115]. Despite these drawbacks, Smagorinsky model is widely accepted model and produced satisfactory results with variety of configurations.

3.2.2 Filtered structure function model

Métais *et al* [110] developed Structure Function (SF) model, which was later extended by Ducros *et al* [44] as Filtered Structure Function model (FSF). The filtered structure function model overcomes certain drawback of Smagorinsky model, with a little more added physics in the model derivation. This model showed improved prediction of spatially growing simulation of the transition to turbulence of flat-plate boundary layers, for which, the classical Smagorinsky formulation is over dissipative and re-laminarises the flow. The eddy viscosity here reads

$$\nu_t(\mathbf{x},\Delta,t) = 0.0014C_K^{-3/2}\Delta\left(\widetilde{F}_2^{n=3}(\mathbf{x},\Delta,t)\right)^{1/2} \tag{3.15}$$

where $C_K = 1.4$ is the Kolmogorov's constant and $\widetilde{F}_2^{n=3}$ is the second order filtered structure function which represents the local kinetic energy spectrum and is calculated from the resolved

velocity field as follows.

$$\widetilde{F}_2(\mathbf{x}, \Delta, t) = \langle ||\widetilde{u}(x+r,t) - \widetilde{u}(x,t)|| \rangle_{||r||=\Delta} \tag{3.16}$$

In Eq. (3.15), the exponent $n = 3$ over $\widetilde{F}_2$ indicates that the structure function has been applied to the resolved velocity field thrice using a Laplace filter.

3.2.3 WALE model

The Wall-Adapting Local Eddy (WALE) viscosity model was developed by Nicoud *et al* [115], is based on the square of the resolved velocity gradient tensor. This model includes the effect of strain rotation and thus gives better prediction in the region where vorticity dominates irrotational strain. Unlike the Smagorinsky and FSF model, WALE model reproduces proper near wall scaling i.e. $\nu_t = \mathcal{O}(y^3)$. The WALE model is also invariant to coordinate translation due to the fact that only local information is used for constructing eddy viscosity rather than neighbouring points, which is an added advantage of it. The eddy viscosity here casts into:

$$\nu_t = C_{\mathrm{w}}^2 \Delta^2 \frac{(\widetilde{s}_{ij}^d \widetilde{s}_{ij}^d)^{3/2}}{(\widetilde{S}_{ij}\widetilde{S}_{ij})^{5/2} + (\widetilde{s}_{ij}^d \widetilde{s}_{ij}^d)^{5/4}} \tag{3.17}$$

C_{w} is a true model constant which takes a value between 0.55 to 0.66. S_{ij} is calculated as from resolved velocity gradients.

$$\widetilde{S}_{ij} = \frac{1}{2}\left(\frac{\partial \widetilde{u}_i}{\partial x_j} + \frac{\partial \widetilde{u}_j}{\partial x_i}\right) \tag{3.18}$$

$\widetilde{s}_{ij}$ is the traceless symmetric part of the resolved velocity gradient tensor, which can be calculated as shown below:

$$\widetilde{s}_{ij}^d = \frac{1}{2}\left(\widetilde{g}_{ij}^2 + \widetilde{g}_{ji}^2\right) - \frac{1}{3}\delta_{ij}\widetilde{g}_{kk}^2 \tag{3.19}$$

$$\widetilde{g}_{ij}^2 = \widetilde{g}_{ik}\widetilde{g}_{kj} \tag{3.20}$$

Here g_{ij} is the notation used for velocity gradient, calculated using $\partial u_i / \partial x_j$.

3.3 Description of flow solver

The flow solver used in this numerical work is an in-house developed one, called as SiTCom solver, which stands for "Simulating Turbulent Combustion". The early development of SiTCom started a decade ago, and the code was eventually updated with more sophisticated models and advanced numerical schemes. Vast amount of work had been carried-out in CORIA using SiTCom solver and results are extensively validated. These work ranges from LES of lift-off height prediction for partially premixed jet flames [42], LES prediction of NO_x in a farthest downstream region of a non-premixed jet flame [73], LES of high Re impinging jet [96], DNS and LES of round and planar premixed jet flames [97] and so on. The complete solver is written in FORTRAN 77 language and enabled with Message Passing Interface (MPI) protocol to perform massively parallel computations, typically can able to run over several thousand processors.

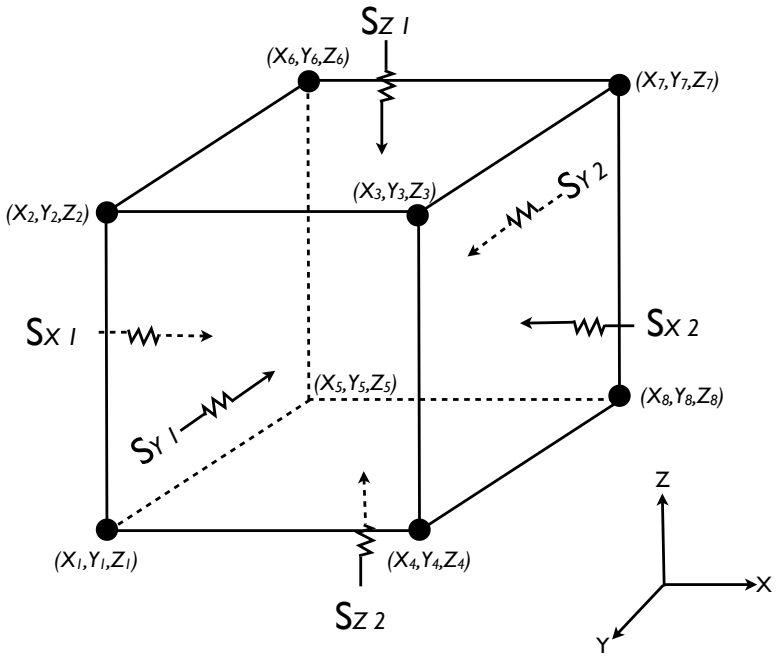

Figure 3.1: Schematic showing a finite volume cell. The fluxes (S) crossing the boundary are represented as by arrow (cumulative of these fluxes constitutes the second term in Eq. (3.21))

3.3.1 Computational grid

SiTCom is a structured code that adopts explicit cell-centred finite volume formulation in a cartesian coordinate system. This topology of cell arrangement allows for efficient array storage and book-keeping of cell information. Finite volume formulation is well known for its advantages, while being used for advection diffusion equation (for instance Navier-Stokes equations). Also, finite volume method is known for its numerical robustness. The solver discretises the physical space of the computational domain into determined number of hexahedral finite volume cells. The Navier-Stokes equations are discretised and represented in these finite volume cells and expressed in integral form (then eventually will be written as algebraic equations); the integral over the control volume is equated to the sum of the surface fluxes crossing the boundaries of the cell. The general form of conservation equation in integral form reads

$$\frac{d}{dt}\int_{V(\vec{\mathbf{x}},t)} Q dV + \oint_{S(\vec{\mathbf{x}},t)} \overline{F}_Q.\hat{n}dS = \int_{V(\vec{\mathbf{x}},t)} P_Q dV \tag{3.21}$$

Here Q represents any conserved quantity (for example mass, momentum or enthalpy) averaged over the control volume, F_Q represent the net fluxes across the faces of the control volume and P_Q denotes the rate of production of Q within the volume V. The first term in Eq. (3.21) represents the time variation of Q within the control volume V and the second term quantifies net surface fluxes (in Navier-Stokes equation, this includes both convective and diffusive fluxes).

Fig. 3.1 shows the schematic of a finite volume cell, with six quadrilateral faces and 12 linear edges (4 per face, edges shared). The collocated meshing scheme is adopted in this

solver, meaning that all the primitive variables are stored in the same cell centre along with the components of velocity vectors. The main advantage with collocated grid is that it guarantees momentum conservation over the entire control volume. However, the calculation of surface fluxes need the velocity vector at interface between the cells, which is normally interpolated from the cell centred values.

3.3.2 Basic assumptions

Following are few basic assumption used in the solver

- Continuum assumption; Properties of fluid are assumed to vary continuously in space and thus continuously differentiable.
- Ideal gas relations are invariably used for every all mixtures of fluids (air+methane) considered in this study. Let the pressure be donated by P, specific volume by v, temperature by T and characteristic gas constant by R, the followings relation holds:

$$Pv = RT \tag{3.22}$$

- The fluid is considered to be Newtonian, thus enabling us to express the shear stress in-terms of velocity gradients.
- The Lewis number is assumed to be unity; i.e. the heat diffusivity is assumed equal to mass diffusivity.

3.3.3 Numerics

The numerical schemes used in this solver version is discussed now. In the Eq. (3.21), the first term denotes rate of change of any volume averaged conserved quantity and can be recast as

$$\frac{d}{dt}\int_{V(\vec{\mathbf{x}},t)} Q dV = \frac{d}{dt}[\hat{Q}] \tag{3.23}$$

where $[\hat{Q}]$ here is the volume averaged quantity. The second term, which is the surface flux term, is the summation of convective and diffusive fluxes, and can be expressed, in the context of finite volume formulation as follows,

$$\oint_{S(\vec{\mathbf{x}},t)} \overline{F}_Q \cdot \hat{n} dS = \sum_{i=1}^{6} [F_Q] S_i \tag{3.24}$$

The convective surface flux term of the Navier-Stokes equation is treated with fourth order skew-symmetric like schemes, proposed by Ducros *et al* [45]. The convective flux of a i^{th} cell at a face located at $i + 1/2$ is calculated as follows

$$\begin{aligned} F_{Q,i+1/2,}^{Convective} &= \frac{1}{3}\left(\hat{Q}_i + \hat{Q}_{i+1}\right)(\hat{u}_i + \hat{u}_{i+1}) \\ &- \frac{1}{24}\left[\left(\hat{Q}_i + \hat{Q}_{i+2}\right)(\hat{u}_i + \hat{u}_{i+2}) + \left(\hat{Q}_{i-1} + \hat{Q}_{i+1}\right)(\hat{u}_{i-1} + \hat{u}_{i+1})\right] \\ &+ \frac{1}{3}\left[\frac{1}{2}\left(\hat{Q}_i\hat{u}_i + \hat{Q}_{i+1}\hat{u}_{i+1}\right) - \frac{1}{4}\left(\hat{Q}_i + \hat{Q}_{i+1}\right)(\hat{u}_i + \hat{u}_{i+1})\right] \end{aligned} \tag{3.25}$$

Convective flux $\Longrightarrow$ Skew symmetric like scheme

Here $\hat{u}_i$ is the filtered velocity component normal to the cell surface for which the flux is calculated. The diffusive fluxes of Navier-Stokes equation are calculated using fourth order centred schemes [58]. Accordingly the diffusive fluxes at the interface $i + \frac{1}{2}$, for uniform structured grid is calculated using the following formulation

$$F_{Q,i+1/2}^{Diffusive} = \frac{7}{12}\left(\left[\mathcal{D}_Q \frac{\partial \hat{Q}}{\partial x}\right]_i + \left[\mathcal{D}_Q \frac{\partial \hat{Q}}{\partial x}\right]_{i+1}\right) - \frac{1}{12}\left(\left[\mathcal{D}_Q \frac{\partial \hat{Q}}{\partial x}\right]_{i+2} + \left[\mathcal{D}_Q \frac{\partial \hat{Q}}{\partial x}\right]_{i-1}\right) \quad (3.26)$$

Diffusive flux $\Longrightarrow$ Fourth order centered scheme

Here $\mathcal{D}_Q$ is the diffusivity of the conserved quantity. The gradient of $\hat{Q}$ in Eq. (3.26) is calculated as follows;

$$\left[\frac{\partial \hat{Q}}{\partial x}\right]_i = \frac{[Q]_{i+\frac{1}{2}} S_{i+\frac{1}{2}} - [Q]_{i-\frac{1}{2}} S_{i-\frac{1}{2}}}{V_i} \quad (3.27)$$

where $[Q]_{i+\frac{1}{2}}$ is the value of $\hat{Q}$ at the cell interface, which is calculated from cell centred values using Taylor's expansion around the interface location, up to fourth order accuracy:

$$[Q]_{i+\frac{1}{2}} = \frac{7}{12}(\hat{Q}_i + \hat{Q}_{i+1}) - \frac{1}{12}(\hat{Q}_{i+2} + \hat{Q}_{i-1}) + \mathcal{O}(\Delta x^4) \quad (3.28)$$

Artificial dissipation

Explicit artificial dissipation has been added to convective numerical fluxes calculated by Eq. (3.25) to suppress any spurious oscillations. This is achieved by adding a solution dependent viscosity called as *numerical viscosity*. A widely used scheme of this type has been developed by Jameson, Schmidt and Turkel [78] and is generally known as Jameson-Schmidt-Turkel scheme or JST for short. The dissipation term proposed is a blend of second order and fourth order terms, and the choice of order of dissipation is dictated by a switch on pressure values [152].

3.3.4 Time integration

The time integration is done using explicit low storage Runge-Kutta scheme proposed by A. A. Wray [173]. Two memory locations are sufficient for one primitive variable for time integration, while maintaining third order accuracy in time. This considerably reduces the memory space requirement for storing the dependent variable during time advancement. The time evolution of the conserved variable can be written in following simplest form:

$$\frac{d\hat{Q}}{dt} = \mathcal{R}.\mathcal{H}.\mathcal{S}(\hat{Q}^{(n)}) \quad (3.29)$$

The right hand side of the equation ($\mathcal{R}.\mathcal{H}.\mathcal{S}$) is the residual calculated by the summation of convective fluxes, diffusive fluxes, numerical dissipation terms and the sources. Expanding Eq. (3.29) using a first order forward approximation yields

$$\hat{Q}^{(n+1)} = \hat{Q}^{(n)} + \Delta t \;\; \mathcal{R}.\mathcal{H}.\mathcal{S}(\hat{Q}^{(n)}) \quad (3.30)$$

Here the superscript $\hat{Q}^n$ denotes the variable at an arbitrary time and $\hat{Q}^{n+1}$ is the value of $\hat{Q}$ at very next time step; i.e. after Δt. The residual $\mathcal{R}.\mathcal{H}.\mathcal{S}(\hat{Q}^n)$ is calculated with the value of $\hat{Q}$ at n^{th} time instance. The time step for this calculation is limited by CFL[2] criterion. The CFL number used in this computation is 1. The integration of Eq. (3.29) is done in three substeps as follows

- First sub-step of Runge-Kutta 3:

$$\hat{Q}^{(1)} = \hat{Q}^{(n)} + \frac{1}{4}\Delta t \;\; \mathcal{R}.\mathcal{H}.\mathcal{S}(\hat{Q}^{(n)}) \tag{3.31}$$

$$\hat{Q}^{(2)} = \hat{Q}^{(n)} + \frac{8}{15}\Delta t \;\; \mathcal{R}.\mathcal{H}.\mathcal{S}(\hat{Q}^{(n)}) \tag{3.32}$$

- Second sub-step of Runge-Kutta 3:

$$\hat{Q}^{(2)} = \hat{Q}^{(1)} + \frac{5}{12}\Delta t \;\; \mathcal{R}.\mathcal{H}.\mathcal{S}(\hat{Q}^{(2)}) \tag{3.33}$$

- Third sub-step of Runge-Kutta 3:

$$\hat{Q}^{(2)} = \hat{Q}^{(1)} + \frac{3}{4}\Delta t \;\; \mathcal{R}.\mathcal{H}.\mathcal{S}(\hat{Q}^{(2)}) \Longrightarrow \hat{Q}^{(n+1)} \tag{3.34}$$

There is no extra memory requirement with the above time advancement formulation (only memory used by Q^n and Q^{n+1} are sufficient), which is the significant advantage of using this method.

3.3.5 Boundary conditions

Boundary conditions (BC) are the set of conditions prescribed at the boundaries of the computational domain. The solution of a transient problem is highly dependent on initial and boundary conditions and proper enforcement of boundary conditions is thus an important task to keep the solution bounded and keep the problem *well-posed*[3]. The SiTCom solver is equipped to handle the following varieties of boundary conditions.

- Inflow boundary
- Outflow boundary
- Periodic boundary
- Symmetric boundary
- Wall boundary

[2]CFL stands for Courant-Friedrichs-Lewy condition, which is a necessary condition for convergence for solving partial differential equations, while explicit time-marching schemes are used for the numerical solution. Mathematically, for one-dimensional advection equation, it is expressed as $\frac{u\Delta t}{\Delta x} < C$, where u is the advection velocity, Δx is the mesh size, Δt is the time step and C is the CFL number.

[3]According to mathematic definition, a problem is said to be well-posed subjected to the following conditions; there exist a solution, the solution is unique and the solution depends continuously on the boundary and/or initial conditions.

Appropriate boundary condition can be chosen by choosing the boundary flag at the input file, which will be supplied while generating the mesh and initialising the variables. The inlet and outlet boundary conditions are adopted with Navier-Stokes Characteristic Boundary Condition (NSCBC)[4] treatment proposed by Poinsot and Lele [126]. Compressible solvers are prone to possess and magnify the numerical noises generated at the boundary due to the fact that higher order numerical schemes are generally non-dissipative. NSCBC makes the boundaries to be transparent to spurious oscillations and allow them to leave the computational domain, which unless otherwise will perturb the solution. NSCBC incorporates the physical conditions into the formulation of the characteristic BC, using the concept of the local one-dimensional inviscid relations (LODI). The LODI relations provide compatible relations between the physical boundary conditions and the amplitudes of the characteristic waves crossing the boundary. Using LODI relation, the incoming waves can be calculated from the amplitudes of the outgoing waves assuming the flow is locally one dimensional. This provides a much better approximation of the characteristic waves across the boundary. A three-dimensional version of NSCBC has been recently proposed by Lodato *et al* [95] to treat the non-orthogonal numerical waves travelling across the boundary. The solver version used in this computation, however adapted the one-dimensional version of NSCBC.

Pseudo turbulence injection

In the case of transient numerical simulation, the inflow velocity imposed on the inlet boundary should be synthesised with suitable fluctuating components of velocity to reproduce the instabilities present in the experiments[5]. The fluctuating component introduced at the inflow should be of enough magnitude to recover the statistical properties of flow. The simplest approach to force turbulence is to super-impose white noise on the mean velocity profile in the inflow boundary. A further elaboration would be a white noise that would produce the proper single-point statistics. However, attempts in this direction have failed owing to the rapid dissipation of Nyquist-frequency signals by the sub-grid scale models [65, 86]. A good synthetic model of the turbulence fluctuations at the inflow is expected to give good predictions not only close to the inlet plane of injection but also at the farthest downstream region.

Klein *et al* [86] came up with a novel technique to impose correlated time-dependent inlet perturbations, using a spectral filter to generate fluctuations of prescribed length scales. This method is used in SiTCom solver to create inlet velocity fluctuations. The constructed velocity time series reproduce specified second moment single point statistics as well as a locally prescribed autocorrelation function. The non-dimensional assumed shape of the autocorrelation function is made dimensional at each point using input turbulent length scale. This method is not only very simple and efficient, but also quite flexible and easy to code.

[4]The NSCBC is based on an analysis of the characteristic waves of the Euler equations, transposed to Navier-Stokes equation with a assumption stating that the waves from the Navier-Stokes equations are associated only with the hyperbolic part.

[5]Another solution is to use a secondary simulation to model the region before the inlet section and tune the inlet to obtain a required correlated fluctuations at the inlet plane. Even a simple boundary treatment could suffice, as the disturbances are allowed to develop naturally as part of the solution of time-dependent Navier-Stokes equation. However, this could be an significant addition in the computational overhead, especially if the configuration is complex.

3.3.6 Pre and post processing

The SiTCom solver also includes it's own pre and post-processing routines. The full simulation can thus be performed in three steps viz. initialisation, main computation and post-processing. An input file is supplied to the initializing routine to determine the size of the computation, dimensions of the domain and the boundary conditions. The first step during initialisation is the mesh generation and slicing the domain into appropriate number of sub-domains for enabling parallel processing. The set of primitive variables and the initial time ($t = 0$) are then initialised in every sub-domain and the initial fields are written in separate *bloc-files*[6] Likewise, at the end of the main computation, the solver writes as many number of instantaneous and average field results files. The post-processing step performs the assembly of these result files to reconstruct the complete domain once again and generates date files, which can be read by *Tecplot* or *Paraview* data visualising softwares. The post-processing routine can able to generate 2D and/or 3D averaged field files as well as transient data files to analyse the statistical results and create animations respectively.

3.4 SGS combustion modeling - PCM-FPI

Various methods have been proposed to tabulate the high complexity of combustion chemistry, to keep LES computing requirements sufficiently low. One approach consists of considering archetype laminar combustion model problems, so-called flamelets, which are filtered with presumed pdfs to account for unresolved sub-grid scale fluctuations. It is termed here as "Presumed Conditional Moment- Flamelet Prolongation of Intrinsic low-dimensional manifold (PCM-FPI) [62, 164]; details concerning the background of this modeling approach applied to LES may be found in [41, 42, 68, 168]. Presumed conditional moment is a probability density function based approach, originally developed in the context of RANS [138] and then later extended for LES computations [164]. The details concerning the FPI-PCM, which includes table generation and coupling with the solver are now discussed in detail.

3.4.1 Flamelet Prolongation of ILDM

Flamelet prolongation of ILDM (FPI) is a flamelet based reduction technique developed by Gicquel *et al* [71], fundamentally derived from the principle of ILDM, which has been introduced in Chapter 2. FGM (Flamelet Generated Manifold) is another variant of FPI, which is in phenomenologically similar to FPI and developed by Van Oijen *et al* [162]. FPI includes an analysis of characteristic chemical time scale of a given system to construct a low-dimensional manifold for given thermodynamic conditions (pressure, equivalence ratio etc.). The FPI tabulation technique overcomes certain drawbacks of ILDM technique (for instance , the adaptability of ILDM in calculations involving auto-ignition, flame propagation and extinction etc.).

[6]The bloc-file is the input file for every single processor, supplied to the solver during main computation. The boundaries of these bloc-files are appropriately flagged to communicate to the neighbouring bloc-files with the help of MPI (Message Passing Interface) calls.

Principle of FPI

The basic principle of FPI technique is to map the complex detailed reaction path in a reduced set of sub-space, thus any point in the reaction space can be retrieved by just defining these sub-space variables. The general choice of sub-space variables are equivalence ratio/mixture fraction and the progress of reaction. Among these control variables, the former quantifies the degree of mixing whereas the later measures the degree of progress of reaction. In simple hydrocarbon combustion, only one reaction progress variable would be sufficient to suitably map the complete reaction sub-space, however one can also define more than one reaction progress variable. In-fact the accuracy of FPI technique is enhanced by increasing the number of control variables. On the other hand, this also substantially increases the dimension of the table and thus the memory requirements to handle it. Nevertheless, certain situations like non-adiabatic combustion need more control parameters due to increased degree of freedom of the chemical system.

Laminar flamelet calculation

The solver used in this numerical study was adopted with a chemistry tabulation for methane air combustion. In case of methane-air mixtures, the mixture fraction can be used to characterise the initial premixture. Mono-dimensional laminar flames can be simulated for every mixture fraction within the flammability limit. For methane air,

- Stoichiometric mixture fraction $Z_{stoichiometric} = 0.055$
- Lean mixture fraction $Z_{lean} = 0.028$
- Rich mixture fraction $Z_{rich} = 0.089$

The detailed reaction mechanism GRI 3.0 is used for computing the laminar premixed flames using PREMIX [83] solver. GRI 3.0 scheme [147] is meant for methane air system, which includes 53 species and 375 elementary reaction steps. For a freely propagating premixed flame the following equation holds:

$$\rho_0 S_L \frac{\partial \phi_i}{\partial x} = \frac{\partial}{\partial x}\left(\rho \mathcal{D}_{\phi_i} \frac{\partial \phi_i}{\partial x}\right) + \dot{\omega}_{\phi_i} \tag{3.35}$$

Here ϕ_i can be any scalar like mass fraction of species, temperature and enthalpy. The mono dimensional flame structure can be conveniently regarded in the flame coordinate x and thus the scalars can be labelled as

$$\phi_{FPI} = \phi(Z, x) \tag{3.36}$$

The physical space x can be transposed into composition space, here referred as reaction progress variable (as introduced in section 2.4.2). For methane air combustion, one possible definition for progress of reaction is the linear combination of mass fraction of major product species like CO and CO_2, as adopted in many earlier studies [42, 73]. Accordingly,

$$Y_c = Y_{CO} + Y_{CO_2} \tag{3.37}$$

Y_c here increases monotonically from 0 to Y_c equilibrium while moving from fresh gas to fully burnt state. The requirement of the definition of Y_c dictates that there exists a one-to-one

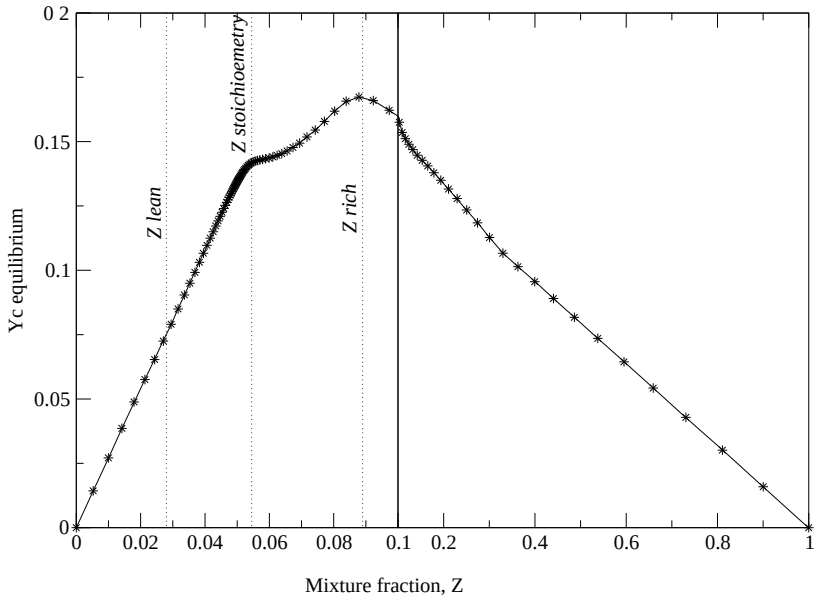

Figure 3.2: Equilibrium value of Y_c for the range of mixture fraction (Z). The abscissa is zoomed in the region around stoichiometry.

correspondence between Y_c and all the scalars occurring in Eq. (3.35). Now it is possible to eliminate the flame co-ordinate x from Eq. (3.35) using Eq. (3.37). Eq. (3.36) can be now be written as

$$\phi_{FPI} = \phi(Z, Y_c) \tag{3.38}$$

Thus, it is possible to express any state within the flamelet by just defining the mixture fraction (Z) and progress of reaction (Y_c). Such flamelet can be computed for all equivalence ratio within the flammability limits. In the zone exterior to the flammability limits, in principle, no flame can exist and the zone is primarily dominated by diffusion process. In this zone i.e. $Z \in [0, Z_{lean}]$ and $Z \in [Z_{rich}, 1]$, a linear interpolation is adopted for all scalars and thermodynamic variables.

Fig. 3.2 depicts the equilibrium value of Y_c computed for the range of mixture fraction for methane air flame. The flammability region is dominated by strong reaction and thus more number of flamelet simulations are done within this zone. The mixture fraction space between 0 and 1 is divided into 100 values, and the Z mesh is clustered near the stoichiometric mixture fraction. Eq. (3.35) is solved for every mixture fraction (i.e. fresh mixture fraction corresponds to $Y_c = 0$), after discretising Eq. (3.35) in x space (later projected in Y_c space). The Y_c space too has 100 mesh points with regular spacing and so the dimension of the table, up to now is 100×100.

3.4.2 Presumed conditional moment

In the SiTCom solver, the subgrid-scale effects are treated using Presumed Conditional Moment (PCM) method. The closure here is based on a filtered Beta probability distribution, initially developed for non-premixed system [164] and later extended to premixed flames [41]. Two versions of SGS modeling are adopted in this numerical work, the first one does not account for the impact of flame stretching on the burning rate of the reference flamelets, the second includes a stretch correction. The former case, which is the classical PCM sub-grid model, is discussed in detail in this section. The modification made to this model to incorporate the stretch effects will be discussed in the upcoming chapter. In this numerical study, the flame evolution followed by forced ignition is analysed in a partially premixed system (the details about the burner configuration and mixture conditions will be elaborated in the following chapter). However, in the SGS combustion models discussed here, only premixed laminar flamelets are considered, mainly for three reasons: (i) the turbulent mixing rate is high in this burner and sparking occurs in already mixed reactants; (ii) once the burning kernel formed after energy deposit, partially premixed flame propagation is expected to play an important role in flame spreading, (iii) it was shown in previous studies, that most of non-premixed combustion properties in terms of energy release are reproduced by premixed flamelet tabulation, at least for equivalence ratio below 1.8[7] [42, 61].

In LES, we normally deal with space filtered quantities. Space filtered quantities are denoted as $\overline{\varphi}(\underline{x},t)$, the mass weighted filtered scalars and chemical source terms read,

$$\overline{\rho}\widetilde{\varphi} = \overline{\rho\varphi} = \overline{\rho}\int_0^1 \left(\overline{\varphi \mid Z^*;\underline{x},t}\right)\widetilde{P}(Z^*;\underline{x},t)\,dZ^* \tag{3.39}$$

where ρ is the density and $\left(\overline{\varphi \mid Z^*;\underline{x},t}\right)$ is the filtered conditional mean of φ, estimated for the mixture fraction value $Z = Z^*$; $\widetilde{P}(Z^*;\underline{x},t)$ is the mass weighted filtered probability density function of mixture fraction Z. This filtered probability density function is here presumed to take a Beta shape. For any variable x, the Beta PDF distribution is given by

$$P(x) = x^{\alpha-1}(1-x)^{\beta-1}\frac{\Gamma(\alpha+\beta)}{\Gamma(\alpha)\Gamma(\beta)} \tag{3.40}$$

where $\Gamma(.)$ denotes the Gamma distribution and α and β are controlling parameters, which determine the shape of the PDF. They are given by

$$\alpha = \mu\gamma \tag{3.41}$$

$$\beta = (1-\mu)\gamma \tag{3.42}$$

$$\gamma = \frac{(\mu-1)\mu}{\sigma} - 1 \tag{3.43}$$

where μ denotes the mean of the variable x and σ denotes the variance. The mixture fraction PDF is assumed to take the shape of the PDF defined in Eq. (3.40).

[7] This condition will be verified while discussing the mixing field of computation, in chapter 4, for this burner configuration

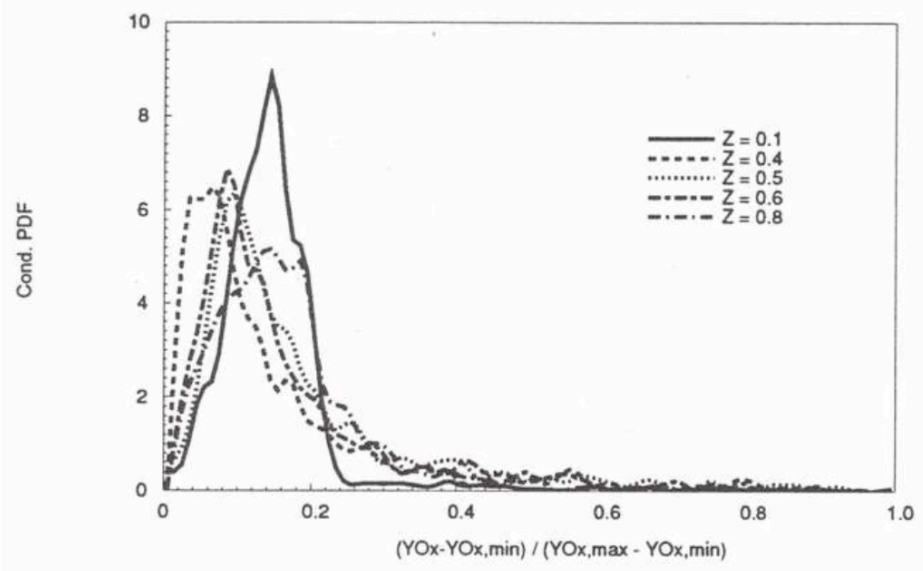

Figure 3.3: Conditional PDF $P(c|Z^*)$ for few mixture fraction from DNS calculation [163]

A normalized progress variable is also defined, as Y_c normalized by its equilibrium value $c = Y_c/Y_c^{Eq}$. This normalized varibale takes a value of 0 in fresh gases and 1 in fully burnt state, for all mixture fraction defined. The value of Y_c^{Eq} for methane air mixtures can be seen in Fig. 3.2. The filtered conditional mean is then given as:

$$\left(\overline{\varphi \mid Z^*; \underline{x}, t}\right) = \int_0^1 \varphi^{FPI}(Z^*, c^*)\overline{P}(c^*; \underline{x}, t)dc^* \tag{3.44}$$

where, φ^{FPI} is a scalar or a source term araising from the flamelets calculations by solving Eq. (3.35) and $\overline{P}(c^*; \underline{x}, t)$ is the filtered sub-grid scale probability density function of normalised progress of reaction, which is also presumed to follow a Beta distribution. As mentioned before, the above equation does not include any terms which account for stretch induced burning rate reduction. But, the effect of flame front wrinkling due to the eddies are taken into account through sub-grid scale PDF distribution.

A simple hypothesis of statistical independence is assumed between Z and c, which enables us to express the joint probability distribution as the product of two marginal probability distribution of Z and c. This assumption is indeed verified by DNS calculations [163], where the conditional PDF of c is indifferent for a range of mixture fraction as seen in Fig. 3.3 and Fig. 3.4.

This assumption of statistical independence between Z and c (not Y_c) was previously discussed in [42, 164] and thus leads to $\left(\overline{c|Z^*}\right) \approx \overline{c}$. It should be emphasised that the assumptions only holds for normalised reaction progress varible c, and not for Y_c or any other quantities φ_i extracted from table. Also, it would not be valid for transient ignition. In this work an

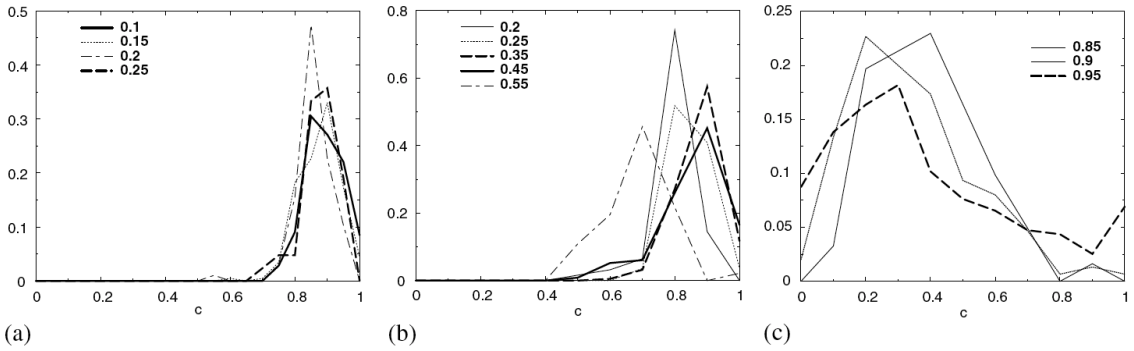

Figure 3.4: Conditional PDF $P(c|Z^*)$ from Sandia D flame at three radial positions where the local mixture fraction is lean, near stoichiometric and rich respectively [11]. The Z^* values are indicated in the graph.

already established flame kernel is always assumed. Then, Eq. (3.39) can be written as

$$\tilde{\varphi} = \int_0^1 \int_0^1 \varphi^{FPI}(Z^*, c^*) \overline{P}(Z^*; \underline{x}, t) P(c^*; \underline{x}, t) dZ^* dc^* \tag{3.45}$$

Eq. (3.45) can be used to find any filtered scalar quantity, provided the two marginal probability density functions are known. The $\varphi^{FPI}(Z^*, c^*)$ can be taken from the table generated by PREMIX solver, as explained in FPI technique. The two marginal pdfs $\widetilde{P}(Z^*; \underline{x}, t)$ and $\overline{P}(c^*; \underline{x}, t)$ are presumed to take a Beta distribution. The shape of this PDF can be retrieved from the first two statistical moments, the mean and the variance of mixture fraction and reaction progress variable. Finally, we need four variables to find the mass filtered scalar quantities, two filtered mean and two variances of Z and Y_c. The variance of Z can be calculated according to

$$Z_v = \widetilde{ZZ} - \tilde{Z}\tilde{Z} \tag{3.46}$$

This needs transport equations for $\widetilde{Z^2}$ and $\tilde{Z}$, and subtracting the square of the later one from the former. Instead, a direct equation for Z_v can be solved by filtering and subtracting the equations for Z and Z^2. The second method is adopted in SiTCom solver for the variance of Z. On the other hand, for Y_c variance, the first method is adopted by solving an equation of $\widetilde{Y_c}$ and $\widetilde{Y_c Y_c}$ [42]. Ideally, all set of equations should be equivalent. However, numerical errors could easily arise when the variance Y_{c_v} is transported and so it is preferable to solve an equation for $\widetilde{Y_c^2}$ [41, 165]. Thus, four sets of scalars are needed to read the filtered quantities from the table viz. $\widetilde{Z}, Z_v, \widetilde{Y_c}, \widetilde{Y_c Y_c}$. Apart from the basic Navier-Stokes equation, SiTCom solves four additional balance equations, one for each above mentioned scalar [42]. The balance equation for filtered mixture fraction reads

$$\frac{\partial \overline{\rho} \tilde{Z}}{\partial t} + \nabla \cdot (\overline{\rho} \tilde{\mathbf{u}} \tilde{Z}) = -\nabla . \overline{\tau}_Z + \nabla \cdot (\overline{\rho} \mathcal{D} \nabla \tilde{Z}) \tag{3.47}$$

The above equation is derived by direct application of LES filtering on mixture fraction transport equation i.e. Eq. (2.10) discussed in chapter 2. The first term on the right hand side of

Eq. (3.47) denotes the SGS turbulent fluxes; $\overline{\tau}_Z = \overline{\rho \mathbf{u} Z} - \overline{\rho}\tilde{\mathbf{u}}\tilde{Z}$. This can be calculated using gradient transport hypothesis, by knowing the sub-grid scale diffusivity, in-turns calculated from sub-grid scale eddy viscosity and Schmidt number.

The transport equation for mixture fraction variance, following Eq. (3.46), can be written as

$$\frac{\partial \overline{\rho} Z_v}{\partial t} + \nabla \cdot (\overline{\rho}\tilde{\mathbf{u}} Z_v) = -\nabla \cdot \overline{\tau}_{Z_v} + \nabla \cdot (\overline{\rho}\mathcal{D}\nabla Z_v) - 2\overline{\tau}_Z \cdot \nabla \tilde{Z} - 2\overline{s}_{\chi Z} \tag{3.48}$$

Once again, the SGS flux term $\overline{\tau}_{Z_v}$ is closed using gradient transport hypothesis. The last term in Eq. (3.48) is the SGS scalar dissipation term, which measures the SGS turbulent mixing rate. Scalar dissipation rate can be decomposed into resolved and SGS parts:

$$\overline{\rho}\widetilde{\chi}_Z = \overline{\rho D |\nabla Z|^2} = \overline{\rho} D |\nabla \widetilde{Z}|^2 + \overline{s}_{\chi Z} \tag{3.49}$$

where D is the molecular diffusivity of Z.

The SGS mixture fraction dissipation rate appearing in the Z_v balance equation is expressed using a linear relaxation closure, which equates scalar mixing time scale with turbulent time scale (Δ^2/ν_T).

$$\overline{s}_{\chi Z} = \frac{\overline{\rho} Z_v}{\Delta^2/\nu_T} \tag{3.50}$$

with Δ the local filter size and ν_T the SGS eddy viscosity. It is convenient to normalise the variance of mixture fraction, which then can be written as

$$S_Z = \frac{Z_v}{\tilde{Z}(1-\tilde{Z})} \tag{3.51}$$

Here S_Z is called segregation factor or unmixedness of mixture fraction. The asymptotic limits of S_Z are 0 and 1. A value of $S_Z = 0$ indicates that the PDF is a dirac delta function peaked at it's mean value. In other words, the mixture inside the sub-grid is well mixed and nearly homogenous. A value of $S_Z = 1$ indicates that the mixture fraction distribution within the sub-grid scale follows a bi-modal PDF.

The transport equation of $\widetilde{Y}_c$ and $\widetilde{Y_c Y_c}$ can be derived;

$$\frac{\partial \overline{\rho}\tilde{Y}_c}{\partial t} + \nabla \cdot (\overline{\rho}\tilde{\mathbf{u}}\tilde{Y}_c) = -\nabla \cdot \overline{\tau}_{Y_c} + \nabla \cdot (\overline{\rho}\mathcal{D}\nabla \tilde{Y}_c) + \overline{\dot{\omega}}_{Y_c} \tag{3.52}$$

$$\frac{\partial \overline{\rho}\widetilde{Y_c^2}}{\partial t} + \nabla \cdot (\overline{\rho}\tilde{\mathbf{u}}\widetilde{Y_c^2}) = -\nabla \cdot \overline{\tau}_{Y_c^2} + \nabla \cdot (\overline{\rho}\mathcal{D}\nabla \widetilde{Y_c^2}) - 2\overline{\rho\chi_{Y_c}} + 2\overline{Y_c \dot{\omega}}_{Y_c} \tag{3.53}$$

In Eq. (3.52) the last term in right hand side is the sum of burning rates of CO and CO_2 and filtered using Eq. (3.45). It is to be noted that Y_c here is a reactive scalar since a source term in the transport equation is present, whereas Z is a passive scalar with no source terms in it's balance equation.

For Y_c, the progress of reaction, its dissipation rate expression can be closed using simply the formulation followed for mixture fraction dissipation rate i.e. by using linear relation of variance. However, it should be remembered that the progress of reaction is an active scalar and thus it is sensitive to chemistry. The scalar gradients of mixture fraction can be only modified by sub-grid scale velocity fluctuations, whereas the scalar gradient of reaction progress variable can be affected by both SGS velocity fluctuations as well as the SGS reactions. Even the later

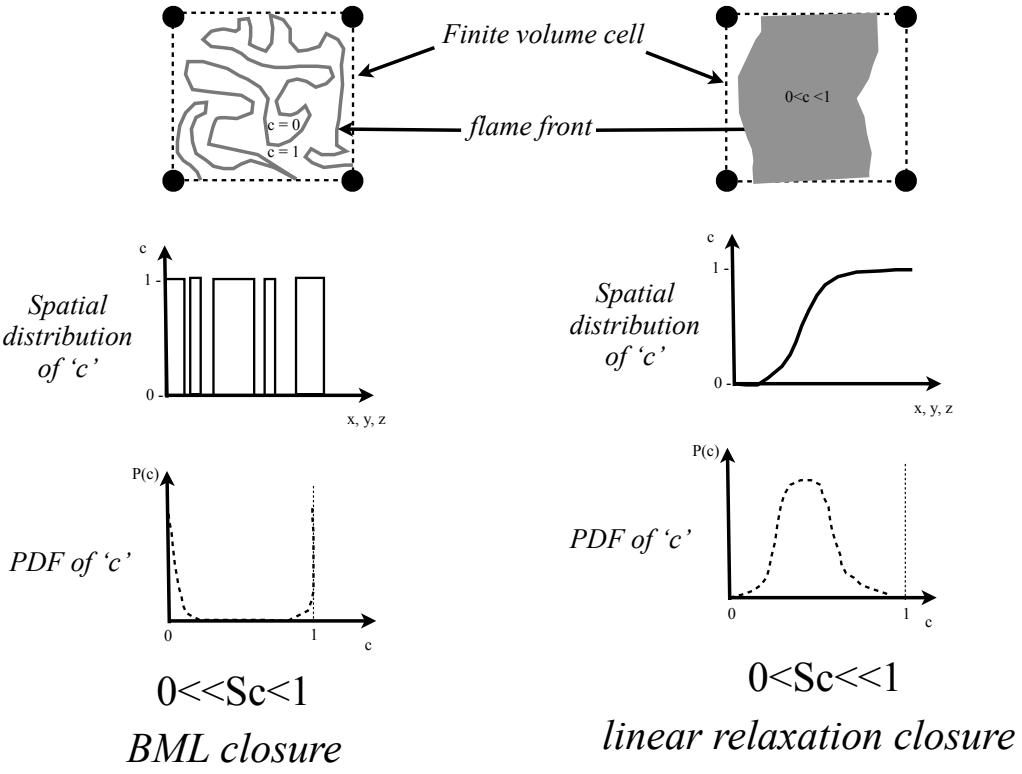

Figure 3.5: Asymptotic limits of sub-grid scale variance of progress of reaction

can have a strong effect if the reaction rate is intense and thus the scalar dissipation rate term should properly mimic this effect. Linear relation closure is appropriate when the SGS probability distribution exhibits a quasi-Gaussian distribution; i.e. weak level of segregation of Y_c. When strong reaction zone are present within the sub-grid scale, the PDF becomes bi-model and spatial distribution of progress variable takes a form of telegraphic signal, by switching between fresh mixture and fully burnt conditions. Fig. 3.5 depicts a picture of two extreme limits of the segregation factor of reaction progress variable. The closure for SGS scalar dissipation rate of progress of reaction, following [42], is as follows:

$$\overline{s}_{\chi_{Y_c}} = (1 - S_c)\frac{\overline{\rho}(\widetilde{Y_c^2} - \widetilde{Y}_c^{\,2})}{\Delta^2/\nu_T} + S_c\left(-\overline{\rho}\mathcal{D}|\nabla\widetilde{Y}_c|^2 + \overline{Y_c\dot{\omega}}_{Y_c} + \overline{Y_c^{Eq}\dot{\omega}}_{Y_c}/2\right) \tag{3.54}$$

with $S_c = (\overline{c^2} - \overline{c}^2)/(\overline{c}(1-\overline{c}))$, the unmixedness of the progress variable ($S_c \in [0,1]$), $\dot{\omega}_{Y_c}$ denotes the chemical source of Y_c. The first term in Eq. ((3.54)) accounts for low unmixedness levels, corresponding to quasi-gaussian SGS pdfs, the second results from the BML theory [23], where the flame is seen as a thin interface separating fresh and burnt gases, with bi-modal pdfs.

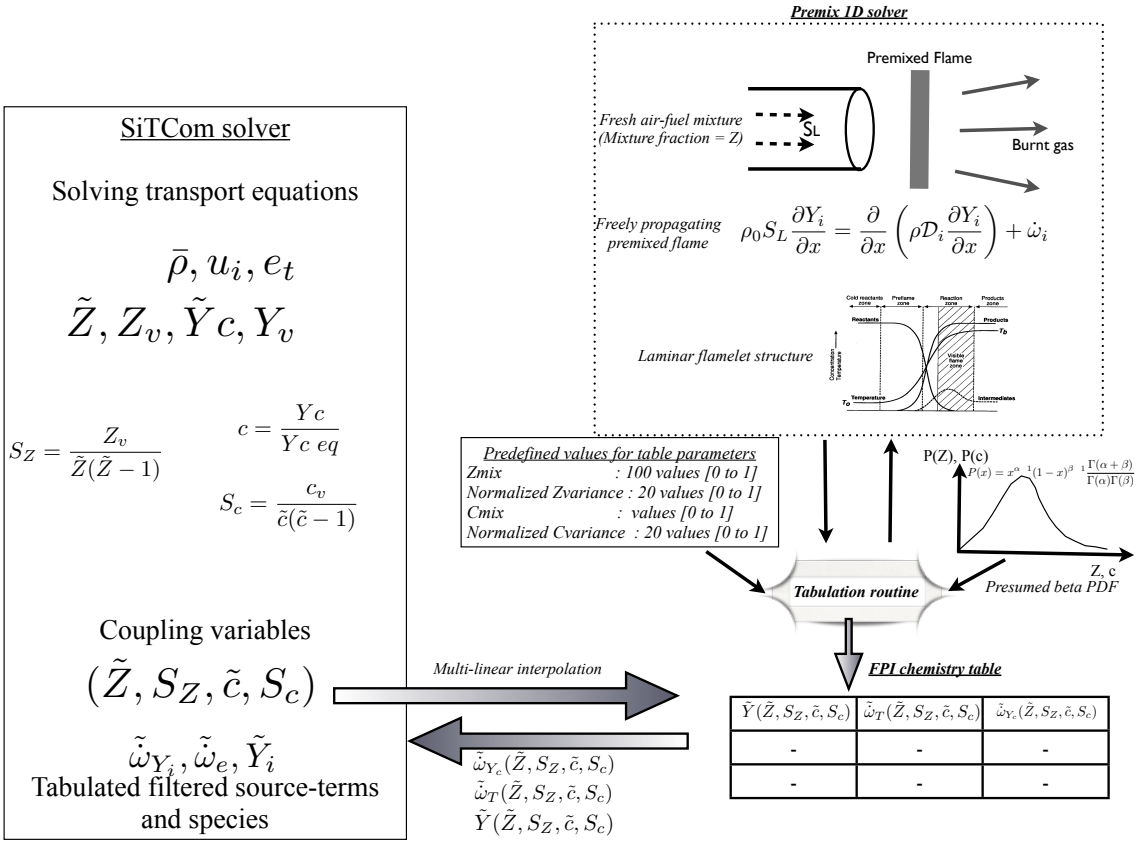

Figure 3.6: Flow chart showing the PCM-FPI tabulation technique and the coupling between SiTCom and the chemistry table.

3.4.3 Tabulation and coupling

As mentioned before, SiTCom solves addition equation for four scalars and supplies the value of $\tilde{Z}, S_Z, \tilde{c}, S_c$. This four set of variables constitute the parameters for the chemistry tabulation. The chemistry table is computed and stored prior to the main simulation. The table generating routine first computes the laminar flamelets and creates a library of variables with two parameters; i.e. $\varphi^{FPI}(Z, c,)$. Further, it considers 20 equally spaced segregation values between $0, 1$ for both mixture fraction and progress of reaction and constructs the Beta PDF and generates the integrated values of φ^{FPI}. This results in $100 \times 20 \times 100 \times 20$ values of φ^{FPI} for every variable stored in the table. SitCom reads the tabulated values from the computed set of table parameters. The flow chart of this complete table generation and coupling with SiTCom can be seen in Fig. 3.6. The table is loaded in every processor during the main simulation. At the end of every time step, SiTCom supplies the table parameters and the values from the table are retrieved via multilinear interpolation. Thus all relevant thermochemical quantities, filtered species mass fractions and filtered sources are obtained by just solving only four additional equations in the main solver.

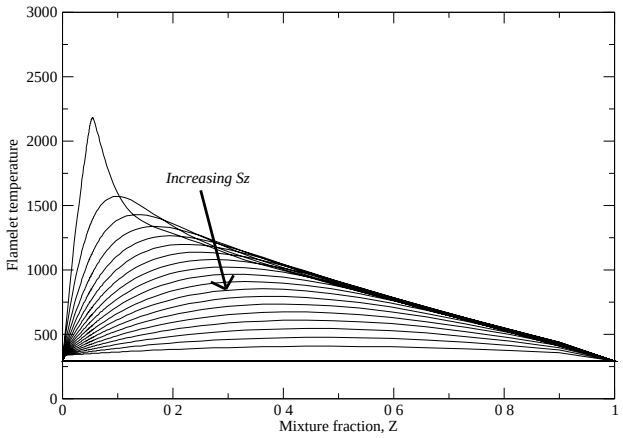

Figure 3.7: Flamelet temperature with varying segregation factor ($S_z = 0 \rightarrow 1$)

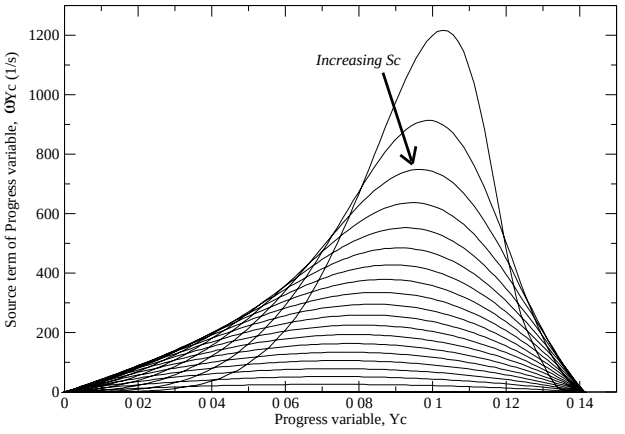

Figure 3.8: Source term of progress variable with varying segregation factor ($S_c = 0 \rightarrow 1$) for a stoichiometric methane-air mixture

The sensitivity of filtered quantities for the various segregation level can be obtained by plotting the tabulated value for different segregation factor by fixing the rest of the table parameters. For instance, the effect of increasing sub-grid scale unmixedness of mixture fraction on filtered temperature can be seen in Fig. 3.7. The state here corresponds to fully burnt products and thus $c = 1$ with no unmixedness i.e. $S_c = 0$. When S_Z is increased from zero, the filtered temperature shows reduction, especially in the stoichiometric region. However,

in the rich mixture fraction side, when the unmixedness is increased from zero, the filtered temperature initially shows a slight increase. Because, with a non-zero segregation in Z and with a rich mean mixture fraction, the contribution of near-stoichiometric mixture is accounted statistically, which increases the filtered temperature.

Similar observation can also be made to analyse the effect of segregation of reaction progress variable, by fixing the mixture fraction (Z) and unmixedness of Z (S_Z). Fig. 3.8 depicts the filtered source term of Y_c for stoichiometric methane-air mixture in progress variable space for various unmixedness level in Y_c. The source term $\dot{\omega}_{Y_c}$ takes a maximum value for $S_c = 0$ at around $Y_c \approx 0.1$, this mximum drops with increasing S_c. While in the region where Yc is close to 0 or Yc is close to Yc^{Eq}, the increase in S_c increases the filtered burning rate. The reason is once again due to the statistical averaging around mean value with a non-zero variance. Notice that for a high level of segregation, the source takes the form of a bi-modal limit (BML) burning rate.

The coupling between the chemistry table and the solver is now discussed. As mentioned before, SiTCom solves the transport equation of density, velocity components and total energy. The heat release source term read from the chemistry table is treated as the source term[8] for the total energy equation. The addition of heat release source increases the internal energy, which is calculated by subtracting the kinetic energy from the total energy. Temperature can be extracted from internal energy using the following thermodynamic relation

$$e_i = \int_{T_0}^{T} C_v(T) dT + e_0 \tag{3.55}$$

where C_v is the specific heat capacity at constant volume for the gas mixture considered, T_0 is the reference temperature and e_0 is the internal energy at reference temperature. The gas mixture C_v can be calculated from the mass fraction and specific heats of the species as shown below.

$$C_v = \sum_{i=1}^{n} Y_i C_{v_i} \tag{3.56}$$

Temperature can be calculated using Eq. (3.55), and using this temperature, the density and pressure can be recalculated and used for subsequent iteration.

[8]The additional source terms can be added along with this source term to account for external energy supply, for instance the energy deposited by spark. This part will be discussed in chapter 5.

CHAPTER 4

Test cases and Cold flow results

Contents

The details concerning the experimental set-up and results of frozen flow and mixing are discussed in this chapter. Details about the target experiment are given in the first section. The initial settings of the computations are addressed in detail. Further, the test cases considered for the cold flow computations are briefed. The results of instantaneous and statistical flow and mixing fields are compared against the available experimental results. The turbulent fluctuations of resolved and unresolved fields are discussed and their relative contributions are analysed to explore the quality of this LES computation. The computed probability density function map of the burner was explored to anticipate the ignition characteristics of various zones. The crucial burner regimes are identified based on the velocity and mixture fraction distributions and few spots are selected for further analysing ignition.

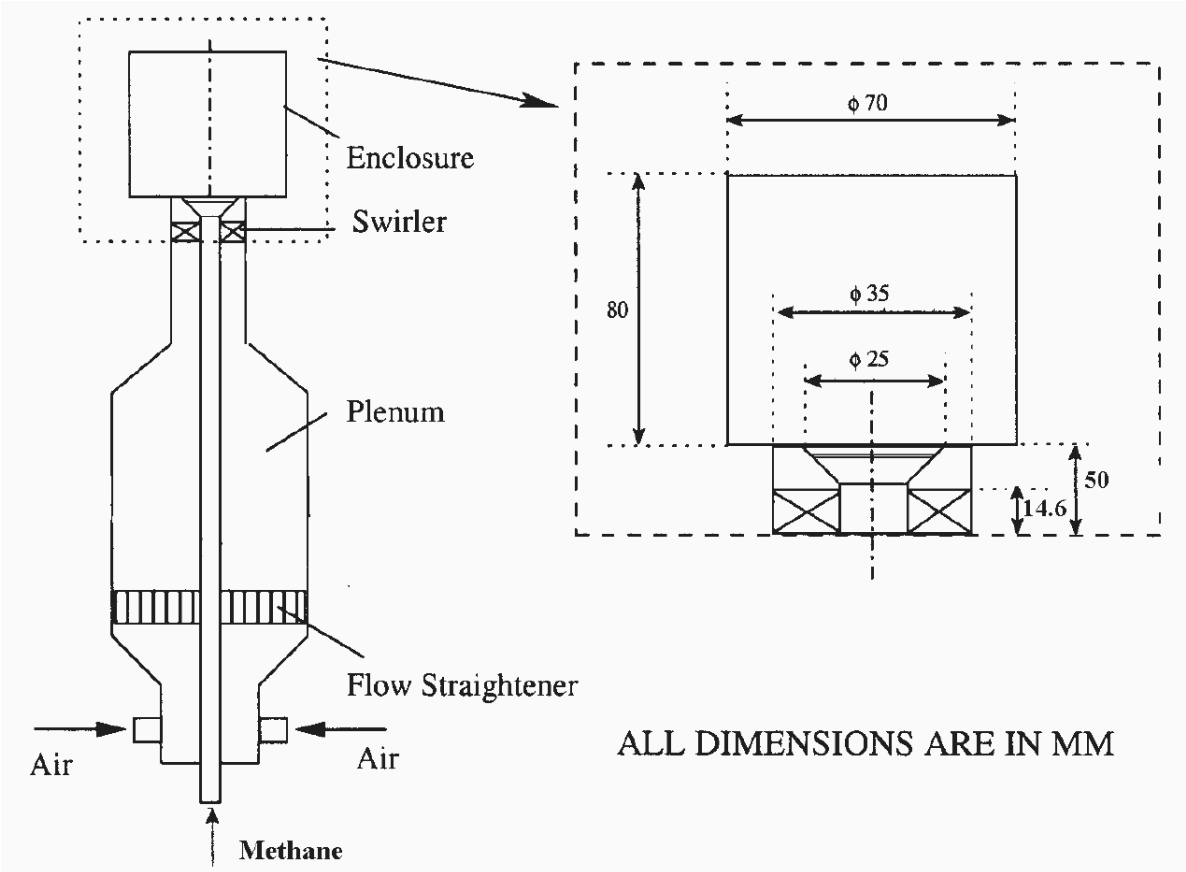

Figure 4.1: Schematic diagram of Cambridge experimental setup [3]

4.1 Experimental burner description

The target experiment chosen for validating the LES results is the work done by Ahmed [3] of Cambridge University, UK. The simulated burner is displayed in Fig. 4.1, showing a schematic view of the experimental device. The enclosure marked in Fig. 4.1 constitutes the burner, which is transparent for optical access. The burner is radially symmetric and measures 70 mm in diameter. The direction of the flow is from bottom to top and the length of the burner section is 80 mm. The burner features a conical shaped bluff-body placed at the inlet section. The magnified view of the enclosure and the conical bluff-body can be seen in the right hand side of the Fig. 4.1. The reactants are fed from the bottom of the burner. The reactant supplying pipes are concentric, one carrying air (outer pipe) and another carrying pure methane (inner pipe) and are attached to the burner inlet. The inner pipe, carrying methane, diverges out near the burner inlet, which forms the conical shaped bluff body. The flow emerges through the outer pipe and thus creates an annular region, through which air is injected into the burner. The inner pipe is closed at the top and the fuel is diverted and injected radially on the axially flowing air stream. The injection point of fuel is 2 mm below the inlet of the burner, thus the mixture is partially premixed at the burner inlet near the bluff-body lip. The diameter of the methane carrying inner pipe is 6 mm. The diameter of the bluff-body is 25 mm and denoted

by D_b, which is the inner diameter of the annular gap. The annulus is 5 mm wide; *i.e.* the outer diameter of the annulus is 35 mm. The blockage ratio (as defined in chapter 2) for this bluff-body configuration is nearly 50 percent. The presence of burner enclosure makes the flow, a confined one. The confinement diameter ratio[1] (CDR) of this experimental configuration is 35 %.

The air and methane are fed from the bottom of the concentric pipes, as shown in Fig. 4.1. The air is allowed to pass through a plenum chamber, which also contains a flow straightener to streamline the flow. The experimental case studies include swirling and non-swirling flow, and in experiments, swirling was accomplished via a swirler placed slightly upstream of the burner inlet, as seen in Fig. 4.1. However, only non-swirling case is considered and taken as the reference for validating the LES results, as the results provided for non-swirling case included very detailed measurement of flow and mixing fields (*i.e.* case B discussed in [3, 4]).

The Laser Doppler Velocimetry (LDV) method was used in experiment to measure the velocity fields. Five axial locations at regular intervals were chosen along the axial flow direction when the radial profiles of mean axial velocity (U_{av}) and radial velocity (R_{av}) were measured. The radial profiles of turbulent fluctuations were also measured in the same axial positions. The experimental mixture fraction measurements were done using acetone Planar Laser Induced Fluorescence (PLIF) with a resolution of 45 μm. In the ignition experiments, the development of the ignition kernel was tracked by fast camera images captured at a rate of 100 kHz. The development of the reaction zone of the flame was also recorded using OH PLIF. The luminosity of the flame during the period of kernel development with respect to time was recorded using a photo-multiplier tube.

4.1.1 Schematic of experimental flow field

As detailed in chapter 2, the bluff-body features a recirculating wake zone at the downstream side. The schematic picture of the time averaged flow field behind the Cambridge burner is shown in Fig. 4.2. The flow is stabilised behind this conical bluff body, with a central re-circulation zone. The two counter rotating recirculating bubbles are visible anchored immediately downstream of the bluff-body, they are referred as central recirculation zone (CRZ). The axial velocity at the burner axis inside the CRZ is negative and thus towards the bluff-body. The presence of recirculating bubbles also deviates the main jet away from the burner axis, and the core jet thus envelopes the CRZ. The point of zero axial velocity located at the burner axis (at the top of the CRZ) is known as rearward stagnation point. The distance of rearward stagnation point from the burner inlet is the length of CRZ. The presence of confinement also induces a weak side recirculation zone, which can be seen in Fig. 4.2. At far downstream, the core jets reattaches again beyond the rearward stagnation point, and then the region beyond this exhibits the characters of a normal round jet (*i. e.* the axial velocity is either positive or zero).

The bulk velocity U_b of the air in the experiment was 10 m/s. The Reynolds number (Re) for this flow configuration is calculated using the hydraulic mean diameter ($D_{hydraulic}$)

[1] CDR is defined as the ratio between the bluff-body diameter to the diameter of the confinement.

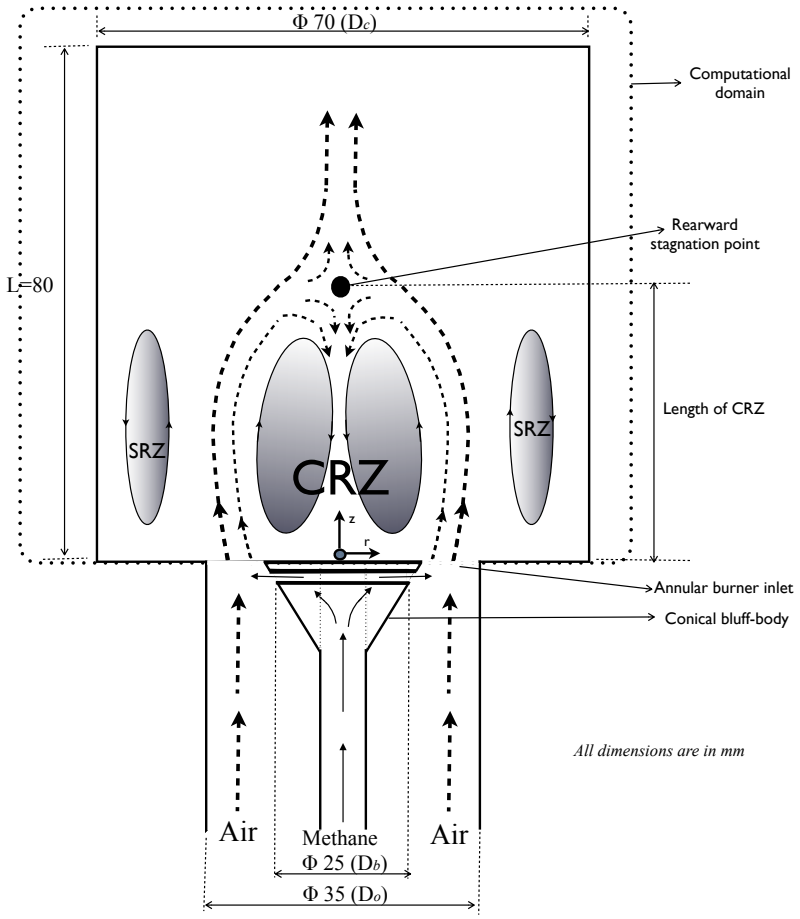

Figure 4.2: Schematic diagram showing the wake zone and the recirculating bubbles. The rearward stagnation point located at the burner axis is marked as a black dot. The streamlines starting from different annular regions are also marked.

as follows [143].

$$D_{hydraulic} = \frac{\text{Cross sectional area}}{\text{Wetted perimeter}} = \frac{\frac{\pi}{4}(D_0^2 - D_b^2)}{\frac{\pi}{4}(D_0 + D_b)} = (D_0 - D_b) = 10\ mm \tag{4.1}$$

$$Re = \frac{U_b D_{hydraulic}}{\nu} = \frac{10 \times 10 \times 10^{-3}}{1.57 \times 10^{-5}} \approx 6400 \tag{4.2}$$

The kinematic viscosity of air at 300K was taken as 1.57×10^{-5} in the above calculation. For annular jets, the flow is considered to be fully turbulent beyond a Re of 2000 [143]. Indeed, the turbulent fluctuations discussed in the later section of this chapter confirms that the flow is fully turbulent at this inlet conditions. The fuel injected through the fuel slit was at a flowrate of 0.0153 kg/s.

4.2 Details of the computations

Computations are performed with a finite volume formulation in a collocated grid using the LES nonpremixed turbulent flame methodology proposed by Domingo *e*t al. [42] using SiTCom solver, which is based on tabulated detailed chemistry and presumed sub-grid scale (SGS) probability density functions, coupled with the solving of the fully compressible form of the Navier-Stokes balance equations of mass, momentum and energy. The computational domain constitutes the enclosure (*i.e.* burner, which is in the downstream side of the bluff-body) marked in Fig. 4.2. The experimental enclosure is cylindrical in size, however the computational domain considered in this study is a rectangular box, whose dimensions are 80 $mm \times 70$ $mm \times$ 70 mm. As the coordinate system used in this study was Cartesian, it is difficult to treat curved boundary. Immersed boundary condition is one feasible option to accommodate curved surfaces in a Cartesian domain, however it was not implemented in the solver version used at the beginning of the present study. It is pointed by the experimentalist that the effect of the curved enclosure surface (*i.e.* confinement) has negligible effect on the flow field behind the bluff-body with this CDR which thus can be considered as an open flow [3]. This is indeed verified by the computation, and is confirmed by comparing the simulation statistics with measurements, in the upcoming sections. Hence, the presence of curved boundary is neglected in this study.

The solver version used in this simulation study is vectorized and optmized so as to be used in vector computers. Most of the computations reported in this thesis are done in NEC SX-8 vector machine, available in IDRIS, Paris. Few computations are done in scalar IBM cluster available in CRIHAN, Saint Etienne du Rouvray. A maximum of 8 processors can be reserved for one computation with a maximum CPU time of 10 hr per calculation. A typical cold-flow computation would take 10 hr of CPU time to cumulate the statistics for obtaining mean flow and mixing fields.

The domain is sliced in to 8 equal pieces, by cutting 4 pieces in Z direction and 2 pieces in Y direction. The computational domain is discretized over 1,764,000 grid points; $90 \times 140 \times 140$ finite volume cells in X, Y and Z directions respectively. The grid is uniform in spanwise direction and slightly stretched in the streamwise direction near the inlet, to capture the flow in the intense turbulence region near the bluff body lip. The typical cell size $\Delta = (\Delta_1 \Delta_2 \Delta_3)^{1/3}$ is about 0.5 mm, however it varies within a narrow band due to the stretching of the mesh in X direction. The boundary condition imposed are given in Table. 4.1.

As the burner is radially symmetric, it is convenient to represent the coordinate positions in YZ plane in circular coordinate, *i.e.* radial position (r), θ instead of Y and Z (The flow is orthogonal to the YZ plane and directed along X axis). The reported measurement of radial profiles of mean and turbulent fluctuations are given in polar coordinates and so the coordinate conversion is needed while comparing the computed results with experiments. Referring Fig. 4.3, the radial position of an arbitrary point A in YZ plane can be found as follows.

$$\vec{r} = Y sin\theta + Z cos\theta \tag{4.3}$$

The inlet boundary ($Xmin$), consists of open annulus between the radius 12.5 $mm > r >$ 17.5 mm and adiabatic wall in all other radial positions. An initial axial velocity profile is fitted using a tanh (hyperbolic tangent) equation and imposed at the inlet plane between these radius. As the conical shaped bluff body deviates the axial air stream, the initial velocity in lateral direction of the flow *i.e.* in Y and Z directions are not zero. Also, the radially injected

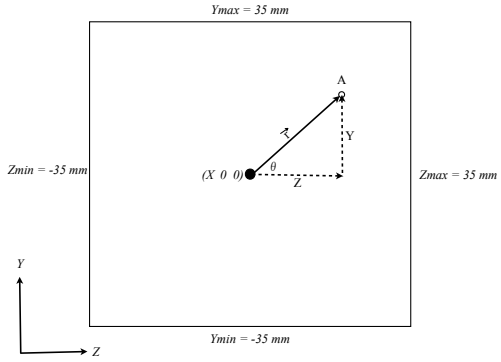

Figure 4.3: Coordinate transformation from Cartesian to polar. The X axis is normal to the paper.

Boundary	Coordinate	Condition
X_{min}	$(0, Y, Z)$	Inlet
X_{max}	$(80,\ Y,\ Z)$	Outlet
Y_{min}	$(X,\ -35,\ Z)$	Symmetric
Y_{max}	$(X,\ 35,\ Z)$	Symmetric
Z_{min}	$(X,\ Y,\ -35)$	Symmetric
Z_{max}	$(X,\ Y,\ 35)$	Symmetric

Table 4.1: Boundary conditions used in this computation. The coordinate positions are given in mm. The origin of the computational domain is located at the top of the bluff-body and at the burner axis.

fuel jet tries to deviate the flow. In the experimental result, measurement at first plane close to the inlet shows that there exists a strong radial component of velocity in the burner inlet. To account for this, the velocity components in Y and Z directions are initialized with proper projection of radial velocity in the respective directions (i.e after converting the values from polar to rectangular co-ordinates using the coordinate transformation discussed before).

The velocity profiles at the inlet was not known in prior. So, a suitable profile was assumed at the inlet and fed to the inlet. Different inlet axial velocity profiles were tested with varying jet boundary layer thickness and axisymmetry, while maintaining the bulk flow rate of 10 m/s. Satisfactory results were obtained with a stiff axial profile with a maximum jet velocity of 11 m/s (refer figure 4.4). The tanh formula used to initialise the velocity is shown in Equation (4.4).

$$U = -U_{max} \tanh \left[w_a C_n \left(\frac{2\,|R_m - r|}{w_a} - \frac{w_a}{2\,|r - R_m|} \right) \right] \tag{4.4}$$

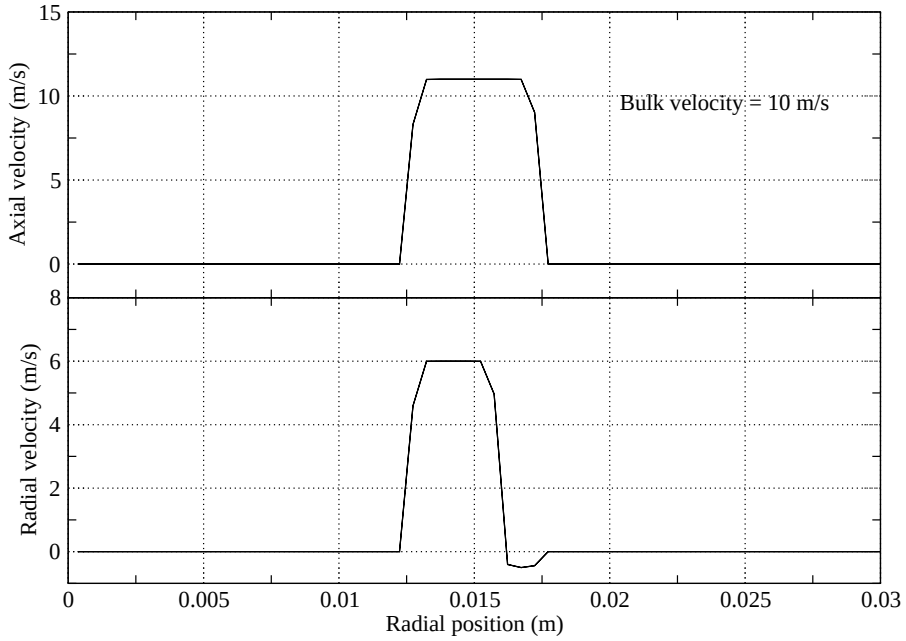

Figure 4.4: Imposed axial and radial velocity at the inlet boundary

where,
U_{max} is the maximum centreline jet velocity,
w_a is the width of the annular gap (5mm),
C_n = a constant, which could be tuned to vary the stiffness of the profile, and
R_m is the mean radius of the annular gap (15 mm).

The radial velocity is initialized with a help of two tanh equations (Eq. (4.4)), which takes a form shown in figure 4.4. The pseudo turbulence is injected at the boundary layers of the jet, calculated from the velocity gradients of the imposed inlet profiles. The maximum intensity of turbulence is taken equal to 40% of U_{bulk}, and the integral length scale for correlation (as discussed in Klein's method in chapter 3) is taken as $2\Delta \approx 1\ mm$.

The bluff-body boundary at the inlet ($0\ mm > r > 12.5\ mm$) and the radius beyond $r > 17.5\ mm$ are considered as adiabatic wall. Zero gradient of velocity, temperature and pressure are imposed in these regions. NSCBC formulation is used in both inlet and outlet boundaries. The lateral boundaries normal to main flow directions are treated with symmetric boundary conditions. The primitive variables at the inlet plane was copied throughout the domain (in all YZ planes along flow direction) while initializing the computation. The atmospheric pressure and temperature values are used while initialising the thermodynamic state of the whole domain.

Transport by unresolved velocity fluctuations are expressed using a sub-grid scale eddy viscosity hypothesis and different expressions have been tested for the cold flow simulations, viz. Smagorinsky [146], Filtered structure function [44] and Wall Adapted Local Eddy (WALE) viscosity [115]. The results were found to be almost similar due to the fact that the flow is quite well resolved, while eddy viscosity values are of the same order with laminar viscosity, in most of the burner region (This is will be demonstrated while discussing the results of turbulent eddy viscosity). Classical Smagorinsky' s formulation [146] is then retained for the cold-flow and sparking analysis, due to it's simplicity and wide usage. The Smagorinsky constant (C_s) is taken as 0.1.

Laminar viscosity (μ) response to temperature (T) is calculated using Sutherland's law as given below.

$$\mu = \mu_{ref} \left(\frac{T}{T_{ref}} \right)^{3/2} \frac{T_{ref} + S}{T + S} \tag{4.5}$$

where, $\mu_{ref} = 1.711 \times 10^{-5}$ is the viscosity at reference temperature T_{ref}, which is 273.15 K. S is Sutherland temperature, which is equal to 110.4 K. The laminar Prandlt number is taken as 0.72, while turbulent Prandlt number is assumed equal to 0.9.

As the main focus of this study is on flame kernel development, till the complete flame establishment, the temperature and species compositions strongly vary with space and time. Realistic thermochemical effects are included by considering the specific heat capacity as a function of temperature as well as composition. The species mass fractions (N_2, CH_4, O_2, CO_2, H_2O, CO, H_2, OH) are needed to obtain a correct estimation of the temperature [68]. The choice of the above species set was done based on relative contributions of the species to the mass budget. Chemistry tabulation gives access to major product species concentration, through which, specific heat capacity at constant volume C_v is constructed as follows

$$C_v = \sum Y_i C_{vi} \tag{4.6}$$

$$C_{vi} = A_i T^2 + B_i T + C_i \tag{4.7}$$

where, Y_i are the mass fraction of the species considered, C_{vi} their respective specific heat capacities, T is the temperature and the constants A_i, B_i, C_i are temperature coefficients of species read from JANAF table. The specific heat capacity is calculated at every time steps during the calculation, and used while calculating the temperature from the internal energy. As mentioned before, the internal energy is calculated from the total energy, for which, a transport equation is solved in SiTCom.

4.2.1 Cold flow test cases

In the experiments, the cold flow velocity and turbulent fluctuations measurements are done with only air injection due to safety reasons. The cold flow measurements of fuel/air mixing were performed by injecting only air through the annulus and closing the fuel inlet [3, 4]. It was found that injection of fuel does not significantly alter the velocity profile close to the inlet of the burner, due to the fact that the overall ratio of fuel to air flow rate is as small as 0.055 (thus the overall mixture condition being stoichiometric). Although the cold-flow measurements without fuel injection is considered equal to the flow field even with fuel injection due to the above mentioned fact, this characterisation may be questionable due to the difference in Reynolds

numbers of fuel and air streams [3]. In LES computations, this point is carefully studied by analyzing both cases, with and without injecting the fuel.

4.3 Cold flow results

4.3.1 Mean axial and radial velocity fields

Results of cold flow test cases are discussed first. The computation is started with initialised field and allowed to run for at least 3 times the *characteristic computation time*[2] before collecting the statistics for comparison. This ensures that any artificial effect of initialisation has disappeared and the jet then evolves naturally with the imposed boundary conditions and becomes statistically steady.

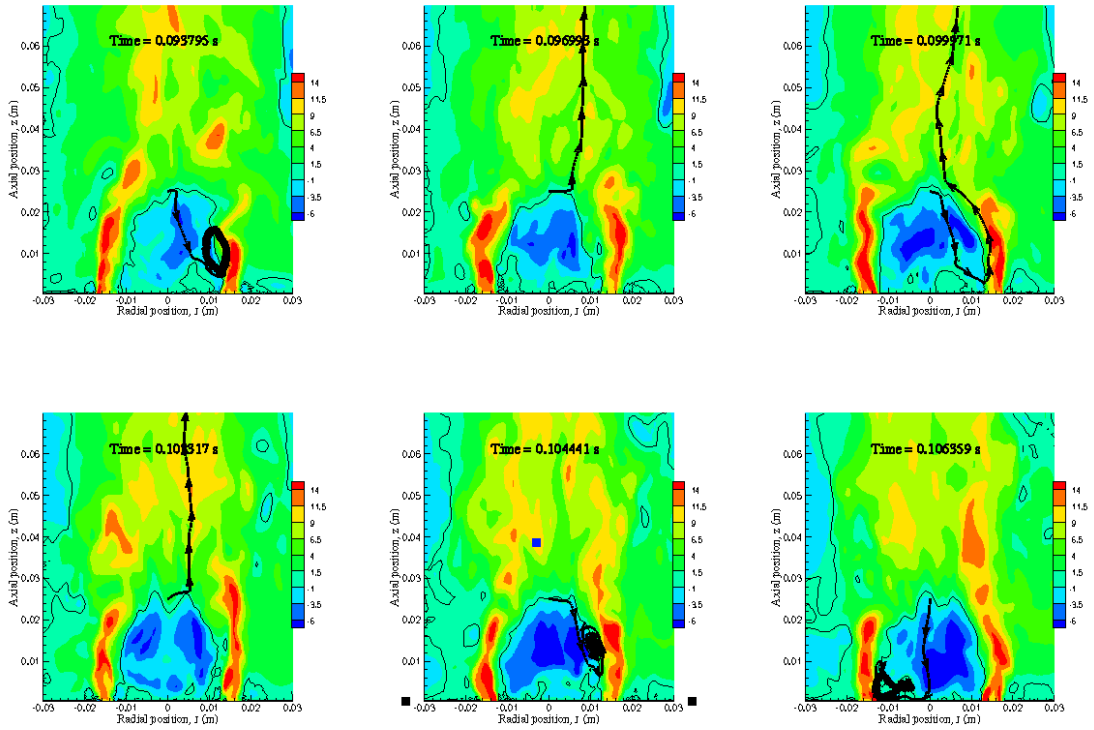

Figure 4.5: Instantaneous axial velocity in a mid-plane passing through burner axis at arbitrary time instances for the LES test-case of both air and methane injection. The thin black lines denote the instantaneous lines of zero axial velocity. The thick black lines denote streamlines starting from a point located at 25 *mm* downstream position on the burner axis.

The two-dimensional view of instantaneous LES resolved axial velocity field at a series of arbitrary time instants can be found in Fig. 4.5. The iso-zero velocity line is also marked in

[2]The characteristic computation time here refers to the time which the core jet takes to cross the computational domain in the main stream direction with the velocity equal to the bulk velocity.

the time series figure. The flapping associated with the flow can be found in the snapshots of velocity, indicating the prevailing strong turbulence. The iso-zero axial velocity, which marks the boundary of the CRZ, is undergoing changes in it's dimension, due to the interaction of the recirculating bubbles. Particularly, the height of the CRZ is fluctuating between the axial positions of $z = 20\ mm$ and $z = 25\ mm$. Any fluid parcel in the burner axis between these axial positions may experience either an advection towards downstream side or get captured within the CRZ and move towards the bluff-body depending on the time instants. For instance, the streamlines are shown for a point at an axial position of 25 mm, located on the burner axis, which confirm that there is a strong variability about the fluid particle trajectory at this location. The two counter rotating bubbles are distinctly visible at some time instances (for instance, at Time = 0.0999 s and 0.0101 s, shown in Fig. 4.5) and eventually are collapsing with each other. These bubbles continuously trap energy from the annular core jet and keep itself alive.

Statistics are collected and averaged in time for about $\tau_m = 4\,(L/U_{bulk})$ seconds, where L is the dimension of the domain in streamwise direction and U_{bulk} is the bulk velocity at inlet plane; τ_m was found large enough to ensure proper convergence of the results.The time averaged velocity and fluctuations are then azimuthally averaged (*i.e.* over the azimuthal direction) to increase the size of the statistics sample, which is compared against the ensemble averaged experimental measurements. In experiment, these frozen flow mixing measurements have been performed with only air injection and no fuel [4]. As mentioned before, to assess the eventual impact on momentum of methane density, both LES predictions with only air injection and both air and fuel injection are plotted against the experimental results. Figure 4.6 shows radial profiles of time averaged streamwise and radial velocity components taken at different axial positions of the burner. Here z refers to the axial positions along X direction *i.e.* the core jet direction.

Considering the case with only air injection (dashed line in Fig. 4.6), at a streamwise position $z = 5.5$ mm, the core jet region is visible and it spreads out radially further downstream. On the axis, a negative streamwise velocity representative of flow recirculation is observed at $z = 15.5$ mm and $z = 25$ mm, both amplitude and location of the corresponding recirculation zones are in agreement with measurements; this is not the case with fuel injection.

Far downstream ($z \geq 35$ mm), not much difference is found between the simulations with only air and air plus fuel. However, there is a significant impact noticed in the region of the recirculation zone, between $z = 15.5$ mm and 25 mm (Fig. 4.6). The width of recirculation zone is mostly unaltered whereas its length has reduced of about 10%, from 25 mm with only air, to 20 mm with fuel, thus shifting upstream the stagnation point when fuel is injected. Figure 4.7 shows a time averaged view of the recirculation zones obtained with and without fuel injection. The streamlines emanating from the core jet region, therefore exiting of the annular gap, which envelopes the recirculating bubbles are specifically indicated. With air injection (Fig. 4.7), as in the experiments, the rearward stagnation point, identifying the length of the CRZ is located on the burner axis at a distance of 25 mm from the burner, which equals D_f the bluff-body diameter. The width of the CRZ is also about D_f. This result falls inline with reported observation in studies on conical bluff-body flows [51, 52], where the length of the recirculation behind a conical bluff body is found to be in the range of 1 to $1.2D_f$, the width being $1D_f$. The accurate prediction of the dimension of the CRZ is of central importance in such burners, as the CRZ plays a key role in flame stabilisation.

The differences between cases with and without fuel can easily be explained. The experi-

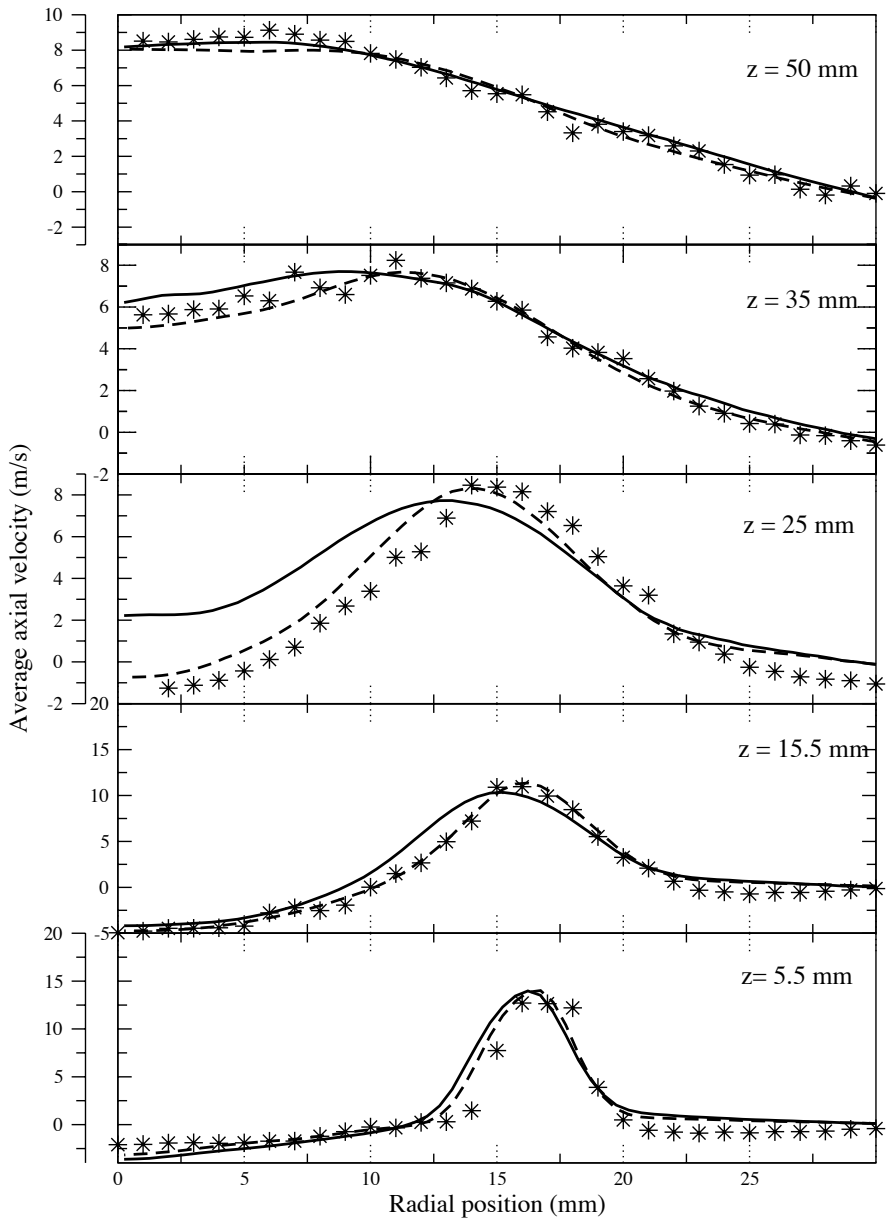

Figure 4.6: Radial profiles of time averaged axial velocities at different streamwise locations. Symbol: Measurements. Dashed line: LES with only air injection. Solid line: LES with air and methane injection.

mentalist mentioned that there existed no difference in the mean velocity profile at the inlet, for the cases with and without fuel injection. Even simulation confirms this behaviour, as the radial trends of two LES cases are more or less indifferent at the axial position of $z = 5.5\ mm$. But, the difference gets magnified in the downstream side. As the fuel is injected along the inner edge of the annular gap, a large amount of fuel gets trapped inside the CRZ. This is because the fuel injection is at the inner edge of the annular jet where the boundary layer effects

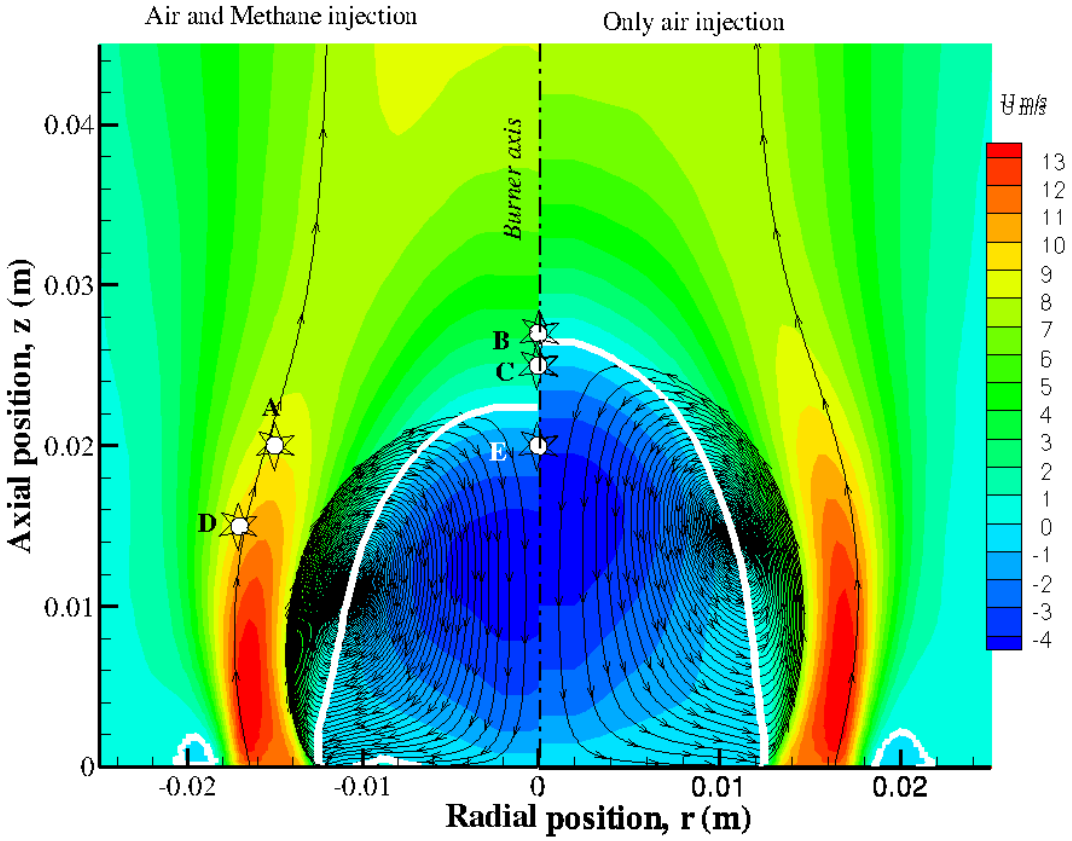

Figure 4.7: Average axial velocity contour. White line: Iso-line of zero axial velocity. Right: LES with only air injection. Left: LES with both air and methane injection. The small white sparklets indicate the ignition spots discussed in the forthcoming chapters.

are strong and thus the downstream convection is relatively slow. The turbulence prevailing in the boundary layer also mixes the fuel. The fuel stream also encounters the recirculating bubbles in the immediate downstream-side and so substantial amount of injected fuel get into the CRZ. The mixture fraction data discussed in the upcoming section confirms the presence of a rich mixture inside the CRZ. The fuel (roughly 8% in mass) inside the recirculation zone alters the density of the mixture of the CRZ and thus the momentum of the recirculating bubbles, which deviates the incoming jet. The present observation and the assessment could be confirmed by comparing the results with experimental measurements done with both air and fuel, which are, for the moment, not available. More supporting arguments can be made to reinforce the aforementioned observation, by comparing the experimental probability maps of kernel initiation and flame development. This will be highlighted in appropriate place while discussing kernel evolution in hot flow simulation in chapter 5.

The mean radial velocity profiles at different burner axial locations are shown in Fig. 4.8, where the predictions without fuel injection are also closer to experimental measurements.

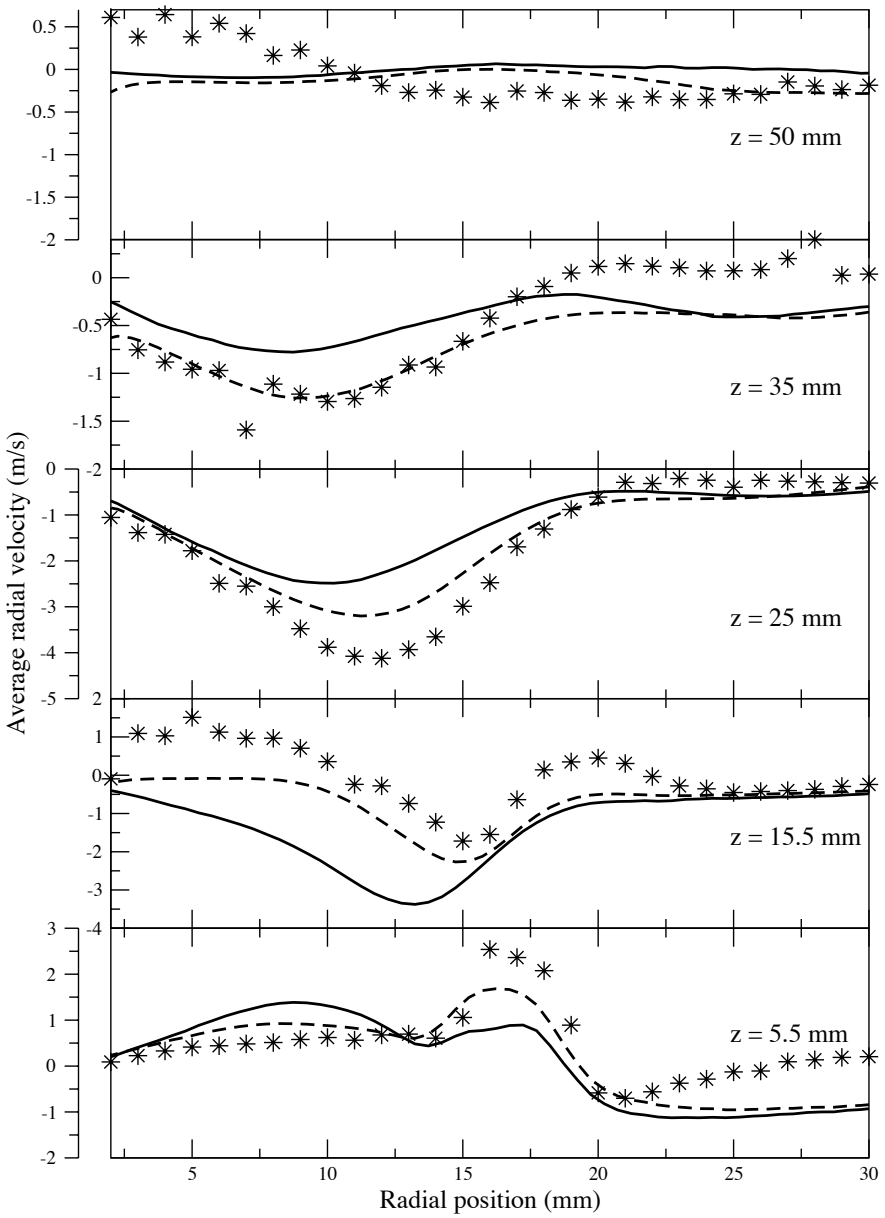

Figure 4.8: Radial profiles of time averaged radial velocities at different streamwise locations. Symbol: Measurements. Dashed line: LES with only air injection. Solid line: LES with air and methane injection.

The radial velocity is calculated by projecting the velocity components of V and W in polar coordinates as discussed in the previous section. From the sign convention used here, positive radial velocity denotes radially outward flow and negative velocity is representative of flow oriented towards the burner axis. In the experimental device, the flow is globally composed of an inner part, where the mixture recirculates, and an outer part, surrounding the inner part away from the central axis. The details of the properties of the outer part depends on the

burner enclosure and is driven by slow flow motions interacting with walls; the exact description of this outer part is out of the scope of the present LES, because it has low impact on the ignition burner properties, which will be discussed in the next chapter. Further, as mentioned before, the CDR of the burner configuration studied here is about 35% and so the external confinement should not have any impact on the central part of the flow examined below when sparking. Indeed, in Ahmed's experiment, it was shown that the confinement has little effect on the CRZ until the CDR is less than 50% [3]. The effect on the simulations of the outer recirculation zone can be seen at the axial position of 5.5 mm, where the velocity is slightly under-predicted in the vicinity of the wall (radial position of 30 mm). Some more discrepancies, nonetheless still acceptable, are also noted between computations and experimental results at 15.5 mm. Further downstream, the results reproduce the experimental observations, with still some departure observed at $z = 50\ mm$; but overall, radial velocity results are inline with what can be expected from LES of such flows with actual SGS modeling [84, 131, 158].

4.3.2 Turbulent kinetic energy

While calculating RMS of velocity fluctuations, both the resolved part and SGS (Sub Grid Scale) part are considered. The SGS part of the RMS is reconstructed from the SGS kinetic energy budget (k_{SGS}) [139], using Yoshizawa model equation as given below:

$$k_{SGS} = \frac{{\nu_t}^2}{(C_m \Delta)^2} \tag{4.8}$$

with ν_t the SGS eddy viscosity, Δ is the characteristic LES mesh size and the constant C_m is defined as

$$C_m = \sqrt{\frac{2}{3}} \frac{A}{\pi K_0^{3/2}} \tag{4.9}$$

Here, K_0 is Kolmogorov's constant and A is Kraichnan's Test Field Model (TFM) constant [139]. The assumption of directional homogeneity is applied while reconstructing the components of unresolved fluctuations from the sub-grid kinetic energy. The rigorous applicability of the above equation is clearly questionable, which is empirical in nature and developed from specific backgrounds. However, it roughly quantifies the unresolved SGS kinetic energy level, the k_{SGS}, which gives an informative picture relative to resolved energy levels, even-though the numbers are not exact. Further, it also helps to assess the quality of the LES as discussed further. Here, the sub-grid scale kinetic energy is directly linked to SGS eddy viscosity, which is, of course logical. Using Smagorinsky formulation, the calculated ratio of SGS eddy viscosity (ν_t) to laminar viscosity (ν_l) is shown in Fig. 4.9. As expected, the eddy viscosity is quite intense in the inner and outer boundary layer of annular jet. The centre-line region, close to the rearward stagnation point also experiences strong shear and thus more eddy viscosity, which is due to the interaction of the recirculating bubbles. In general, the eddy viscosity stays more or less in the same order that of laminar viscosity in most of the burner regime, which indicates that the flow is very well resolved.

4.3.3 Turbulence resolution parameter

The approximation given by Eq. (4.8) for sub-grid scale kinetic energy is also useful for assessing the quality of the LES, for instance via the turbulence resolution parameter (M) defined as

follows [129]:

$$M\left(\underline{x},t\right)=\frac{\langle k_{SGS}\left(\underline{x},t\right)\rangle}{K\left(\underline{x},t\right)+\langle k_{SGS}\left(\underline{x},t\right)\rangle} \tag{4.10}$$

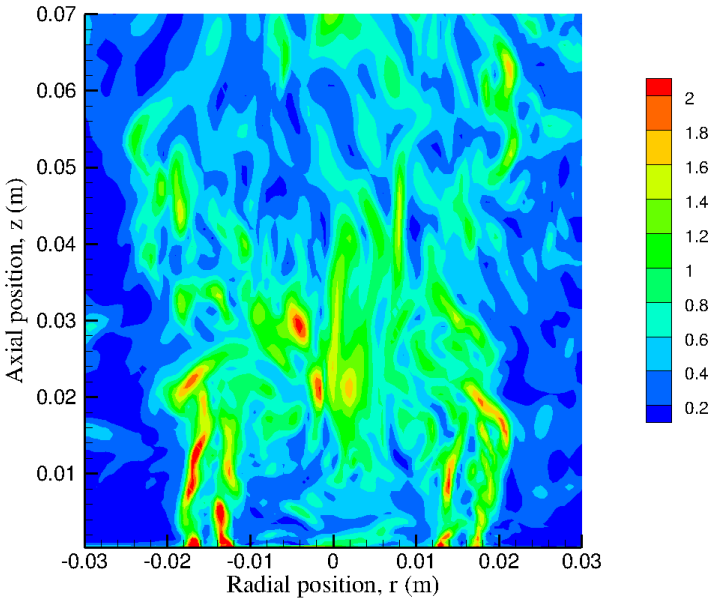

Figure 4.9: Ratio of turbulent to laminar viscosity calculated using Smagorinsky formula ($\frac{\nu_t}{\nu_l}$).

Here, $K\left(x,t\right)$ corresponds to resolved kinetic energy and $\langle\cdot\rangle$ indicates time averaging. By definition, M = 1 corresponds to RANS and M = 0 would be obtained in DNS. According to Pope [129], $M \leq 0.2$ characterises well resolved LES in which at least 80% of the energy of turbulence is resolved. In this computation, the turbulence resolution parameter is well below 0.2 except at the shear layer of the core jet region close to inlet, which can be seen in Fig. 4.10.

4.3.4 RMS of axial and radial velocities

The Root Mean Square (RMS) of velocity fluctuations are shown in Fig 4.11 and 4.12 for axial (U_{rms}) and radial component (R_{rms}) of velocities respectively, for the case with only air injection. In Fig. 4.11, the level of fluctuations inside the CRZ is well reproduced. Along the jet axis, the radial RMS fluctuations, R_{rms}, are superior to their streamwise counterpart, except at $z = 5.5$ mm; at the rearward stagnation point located at $z = 25$ mm, the radial peak value is also considerably higher than U_{rms}, which is typical for such a flow configuration [117]. Both axial and radial RMS fluctuations are considerably high and quite uniform inside the central recirculation zone. It can be recalled here that the flow is found fully turbulent with the prevailing level of turbulent axial and radial fluctuations. In Fig. 4.11, the resolved fluctuations completed with SGS fluctuations provides the best approximation of experiments, especially at the shear layer of the jet and in the recirculation zone, where the turbulent intensity is high. However, even when SGS contribution is added, the double peaks observed in U_{rms}

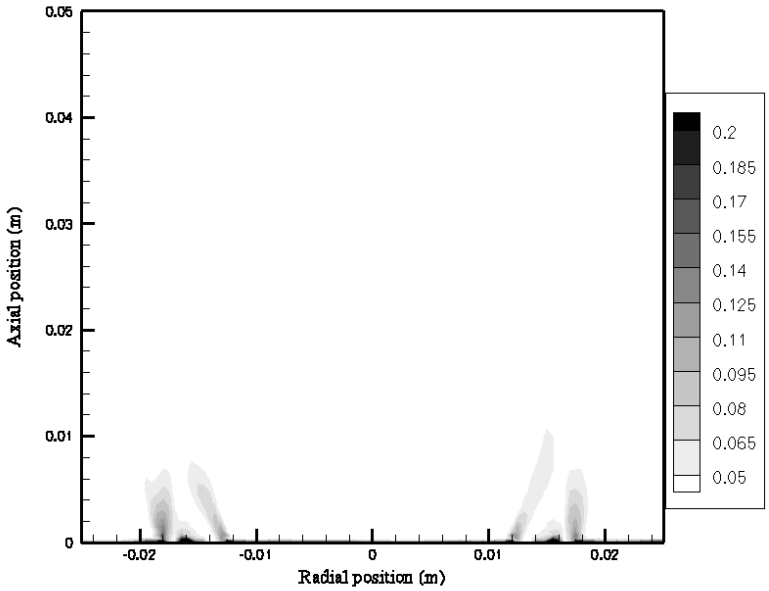

Figure 4.10: Turbulence resolution parameter M (calculated according to Eq. (4.10)).

profile of experimental measurement are still under-predicted in computations. In this LES, equal intensity of pseudo turbulence is forced in the inlet plane at inner and outer edges of the annular gap for both axial and azimuthal velocity components. In reality, the presence of sharp bluff body lip may induce non uniform flow instabilities between the outer and inner edges of the jet and also in axial and radial velocity components. An auxiliary simulation of the burner interior could be performed to provide refined inlet conditions; nevertheless, the spreading rate of fluctuations and its levels are arguably well predicted in Fig. 4.11 with the simplified inlet approximation used in this study. LES of similar flow configuration has been recently investigated by Triantafyllidis *et al* [158] by extending the computational domain until 25 mm upstream to the bluff-body and obtained similar quality results. Once again, at far downstream, $z \approx 30$ mm, and near the lateral boundary, the predictions are degraded due to the lack of fine description of the outer zone, and similar results were observed in DNS of burners [64]. As alluded above, this region is far away from the sparking locations of interest, and will have no impact on the ignition kernel dynamics in and around the CRZ; velocity results are then adopted and the mixture field is now discussed.

4.3.5 Mixing field

In experiments, the fuel was injected $2mm$ before the burner inlet. The fuel was mixed and the maximum mixture fraction (fuel mass concentration) at the inlet was nearly 0.2. A flat profile with 0.2 maximum mixture fraction is used in computation at the inlet boundary, and the injection takes place near the inner edge of the bluff-body. The area of fuel injection is adjusted to ensure that the fuel mass flow rate matches with the experimental fuel flow rate. The computed mixing field results are compared with the experimental acetone PLIF

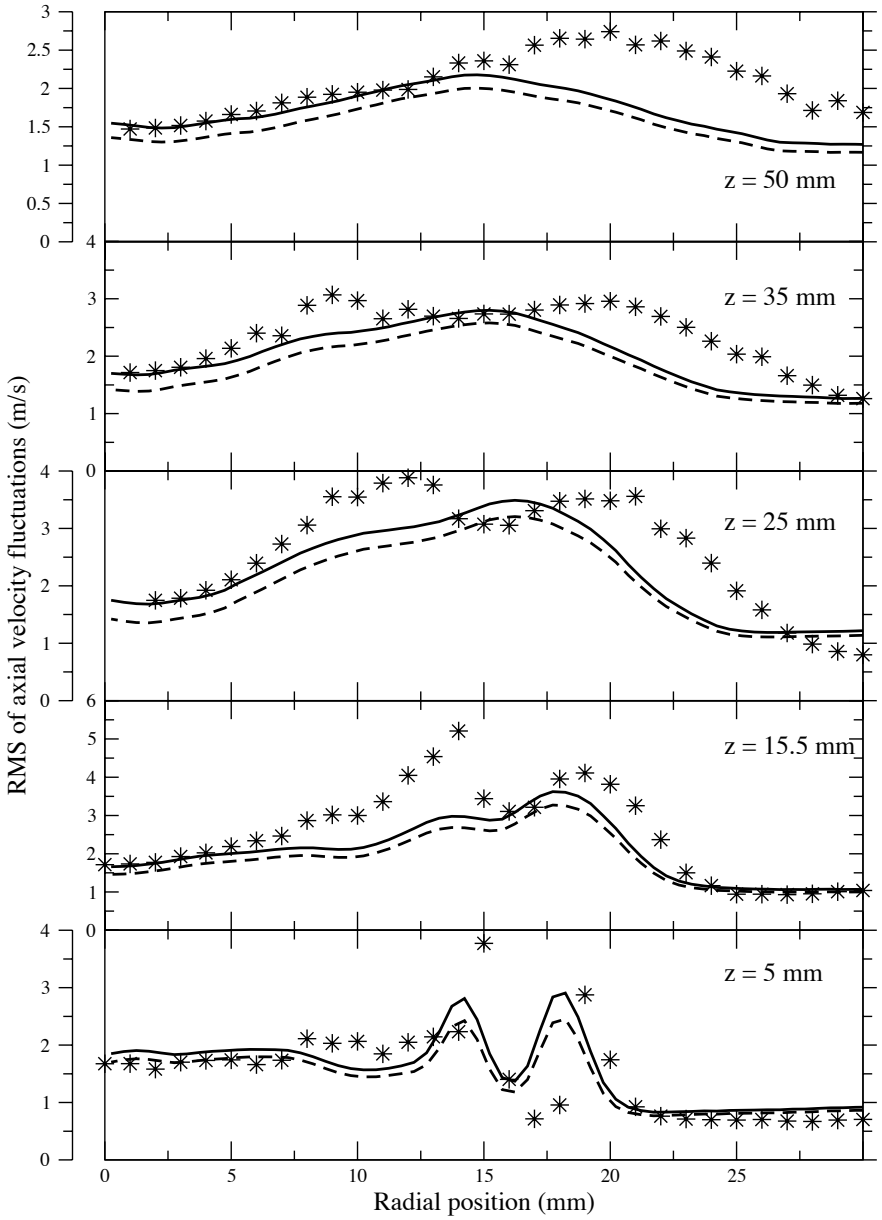

Figure 4.11: Radial profiles of axial RMS fluctuations at different streamwise locations. Symbol: Measurements. Dashed line: LES resolved. Solid line: LES resolved + SGS.

measurements. The computed results are of LES case with both air and fuel injection.

Mean mixing field

The time and spatially averaged averaged 2D mixture fraction contour can be seen in Fig. 4.13. The iso-line of flammability limits can be seen in the mixture fraction 2D plane. The mean mixture fraction fraction at a region surrounding the rearward stagnation point stays more

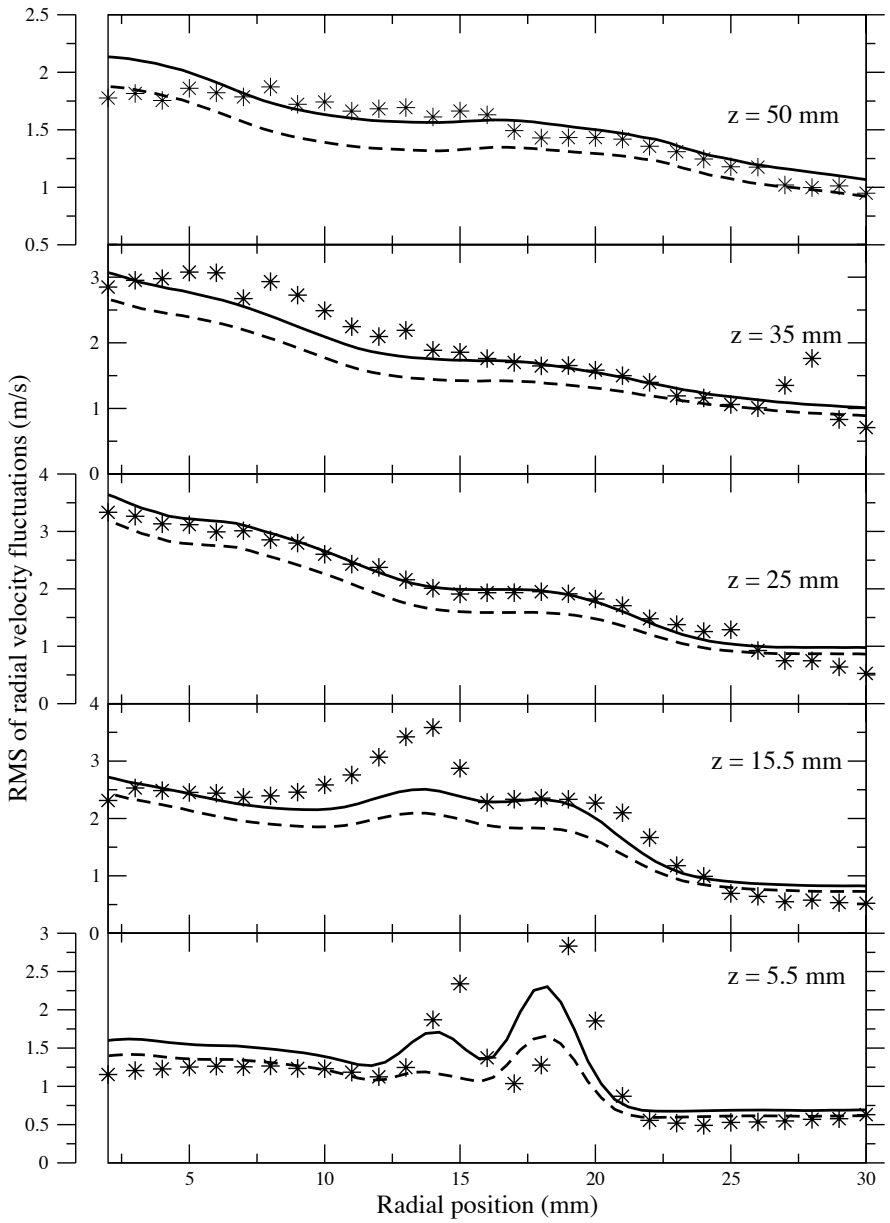

Figure 4.12: Radial profiles of radial RMS fluctuations at different streamwise locations. Symbol: Measurements. Dashed line: LES resolved. Solid line: LES resolved + SGS.

or less stoichiometric. One could expect, based on the statistical mixing field, the preferable region for sparking to be around the rearward stagnation point. However, there are many other factors influencing the ignition characteristics of burner regimes, which will be explored in detail, in the next chapter. The 2D planar contour of Fig. 4.13 can be compared against Fig. 9b of [4].

The time and spatially averaged 2D contour of mixture fraction fluctuations can be seen in Fig. 4.14, for which, the experimental counterpart can be seen in Fig. 9c of [4]. The fluctuation

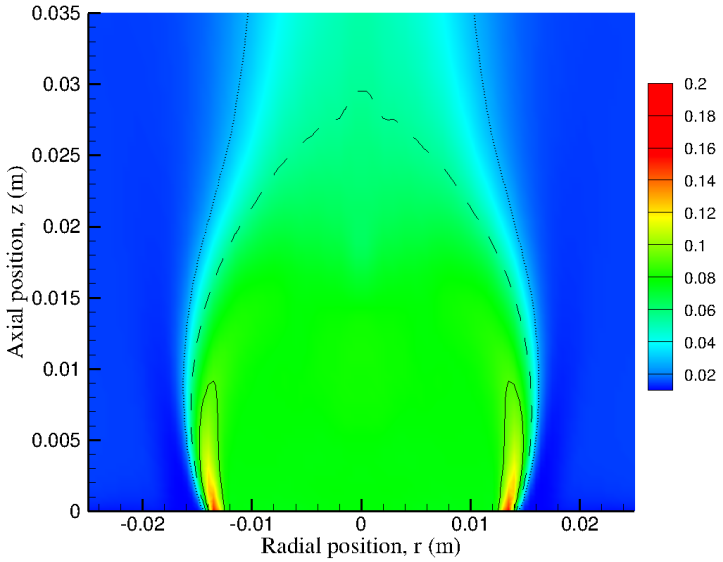

Figure 4.13: Two-dimensional view of LES resolved mean mixture fraction. Continuous black line: Isoline of rich flammability limit (Z_{rich}), Dotted black line: Isoline of lean flammability limit (Z_{lean}), Dashed black line: Iso-stoichiometric line (Z_s).

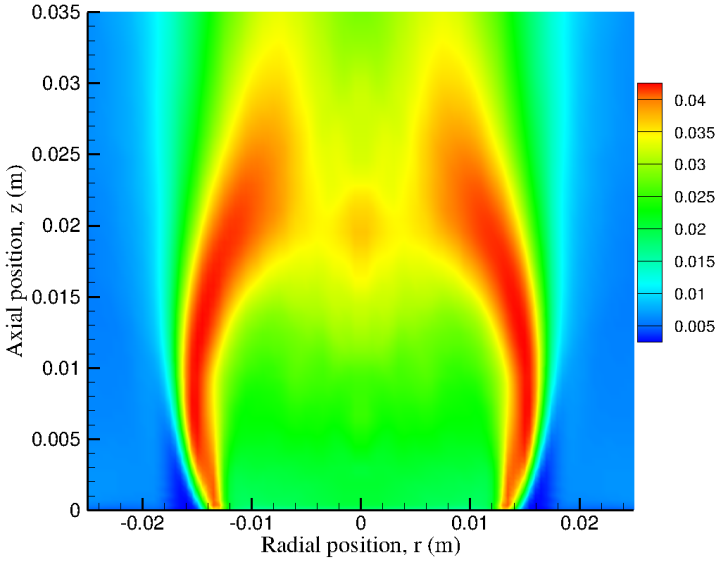

Figure 4.14: 2-dimensional view of RMS of mixture fraction (Resolved+SGS contributions).

shown here accounts for both resolved and unresolved components.

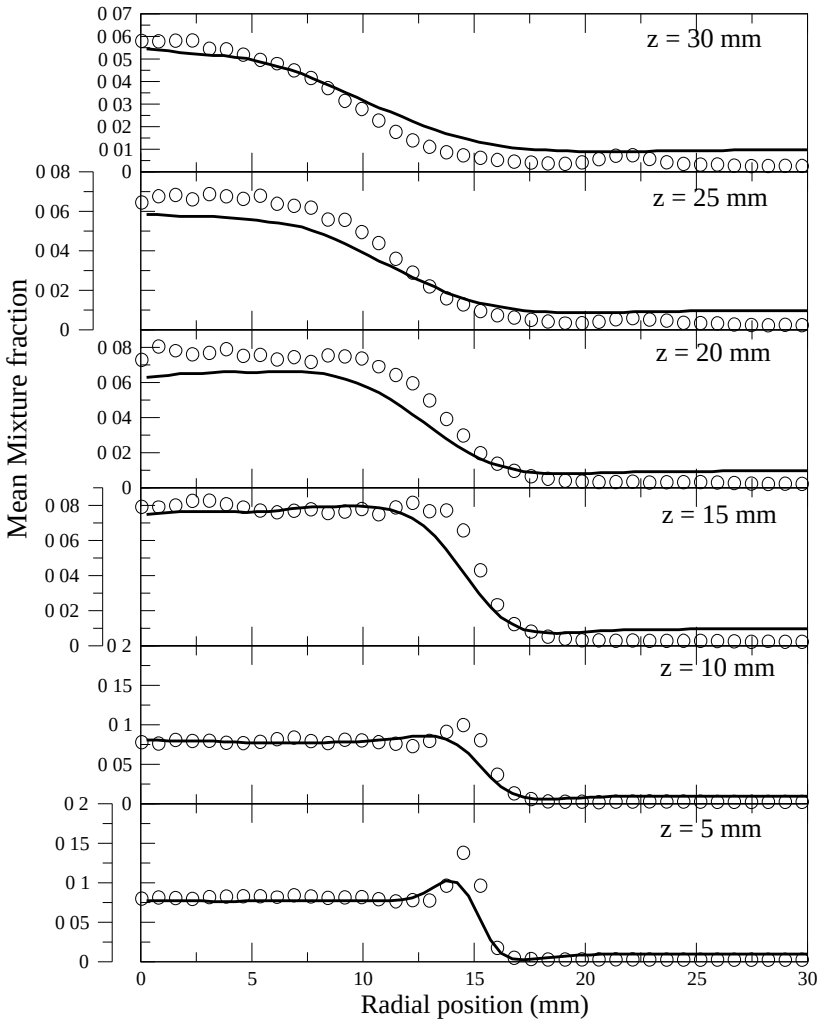

Figure 4.15: Radial profiles of time averaged velocities at different streamwise locations. Symbol: Measurements. Dashed line: LES with only air injection. Solid line: LES with air and methane injection.

Figure 4.15 shows the radial profiles of mean mixture fraction at six equi-distant axial locations along the burner axis. The symbols in Fig. 4.15 correspond to experimental PLIF measurements done with fuel seeded with 10% acetone[3] [4]. The mean mixture fraction is fairly

[3]The presence of acetone vapour could change the effective density of methane and it's diffusive properties,

well predicted at all axial locations; at 5 mm downstream of injection, the peak value near the radius of 15 mm is, however, slightly underpredicted, this could be due to an insufficient mesh resolution in this zone. Further downstream, the spreading of computed mixture fraction seems to be a little faster than in experiments. At a distance of 30 mm from inlet, where the region is beyond the rearward stagnation point, the mixture fraction seems to be slightly over-predicted at larger radius. According to the experimentalists [4], the PLIF signal in this zone is very weak and measurements uncertainties become large. Nevertheless, the overall radial trends are in fairly good agreement at all axial positions.

The mixture fraction values inside the CRZ is almost uniform and is well predicted in the computation. Notice that the mixture fraction value here is close to 0.08, which means that the mixture is quite rich (equivalence ratio of about 1.6) and thus appreciably affecting the mixture density inside the CRZ for the case with methane injection. It can be recalled that the change in the dimension of CRZ could possibly be due to this low density mixture, which is trapped inside the CRZ.

Fig. 4.16 shows the RMS fluctuations of mixture fraction compared with their experimental counterpart, with and without considering the subgrid scale contribution. The mixture fraction PLIF measurements have been performed with a resolution $\Delta_{PLIF} \approx \Delta/10$, where Δ is the LES filter size. Therefore, the amplitude of the measured fluctuations must be between the resolved LES fluctuations and the resolved LES fluctuations to which the SGS contribution is added [68]. This SGS part is known after solving a balance equation for $Z_v = \widetilde{ZZ} - \widetilde{Z}\,\widetilde{Z}$ [42]. Figure 4.16 confirms this expected distribution of mixture fraction fluctuations. Again, little discrepancies are noticed at the $z = 5$ mm downstream position. As mentioned before, the scalar dissipation rate term in the Z_v equation was closed by linear relaxation of variance [42], which assumes that the scalar mixing time is proportional to the SGS turbulent characteristic time [80]. This links the SGS kinetic energy levels with the SGS scalar variance, which means, any error in SGS kinetic energy will be reflected in scalar variance. Local mesh refinement near the bluff body lip could probably improve the prediction in this region. Fig. 4.17 depicts a 2D slice showing contour of LES resolved instantaneous mixture fraction at an arbitrary instant in time. Large scale structures at the stoichiometric line are visualised as well as the well-mixed mixture inside the CRZ. At the rearward stagnation point (*i.e.* z = 20 mm and r = 0), although the mean mixture fraction stays close to stoichiometric, the instantaneous mixture fraction can be sometimes extremely rich, or lean, due to the entrainment of air and fuel from the top of the CRZ. The lean packet of entrained air can be clearly seen in Fig. 4.17, which will eventually mix well within the CRZ due to the strong turbulence.

Overall, all measured trends are captured by the present LES. Certainly, the agreement between averaged LES and measurements could be improved by adjusting inlet conditions and refining the mesh [18], but it will be shown in the coming chapter that this description is sufficient to fully reproduce and analyze the transient ignition behavior and, more importantly, its statistical variability. Many simulations are needed to check this last point and the effort is therefore oriented in this direction, rather than fine tuning of the averaged values.

however, this effect was neglected in experimental measurements [3].

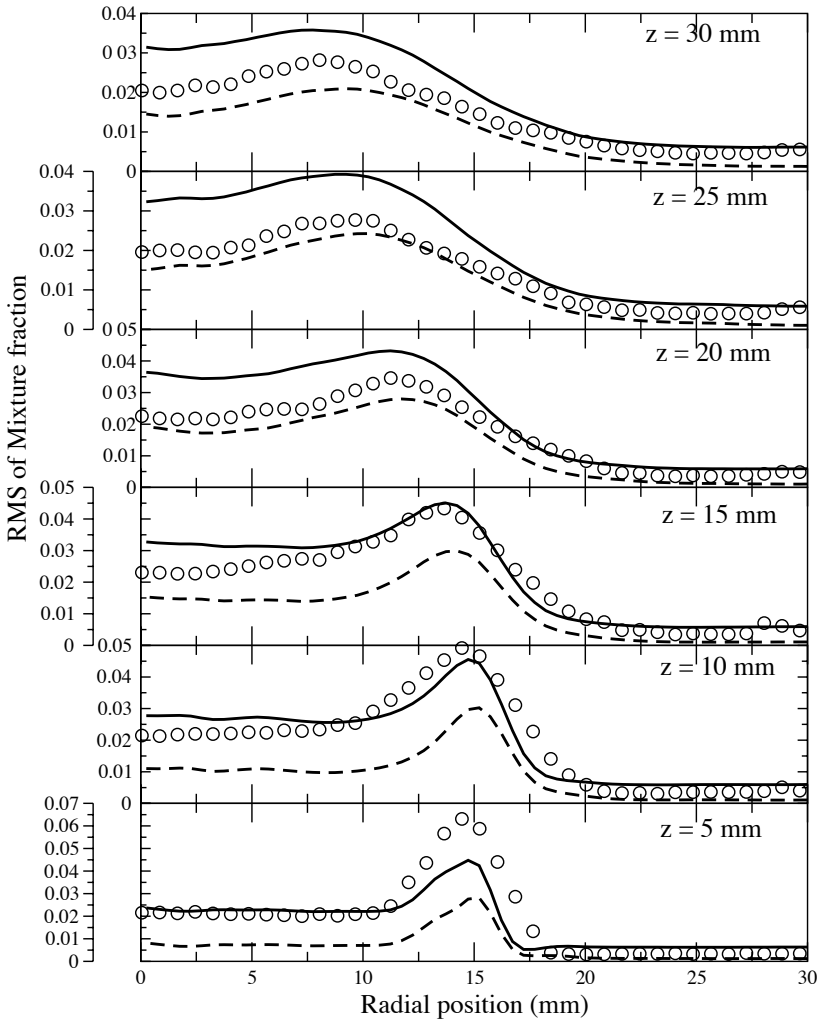

Figure 4.16: Radial profiles of time averaged velocities at different streamwise locations. Symbol: Measurements. Dashed line: LES with only air injection. Solid line: LES with air and methane injection.

4.3.6 Flammability factor

In turbulent fuel-air mixtures, the success of ignition at a given location is not just a function of mean flow and mixture properties, it also depends heavily on the instantaneous flow field values at the sparking moment and the following time histories of the same. Before obtaining a successful primary ignition, which completely lighten the burner, the spark has to locally

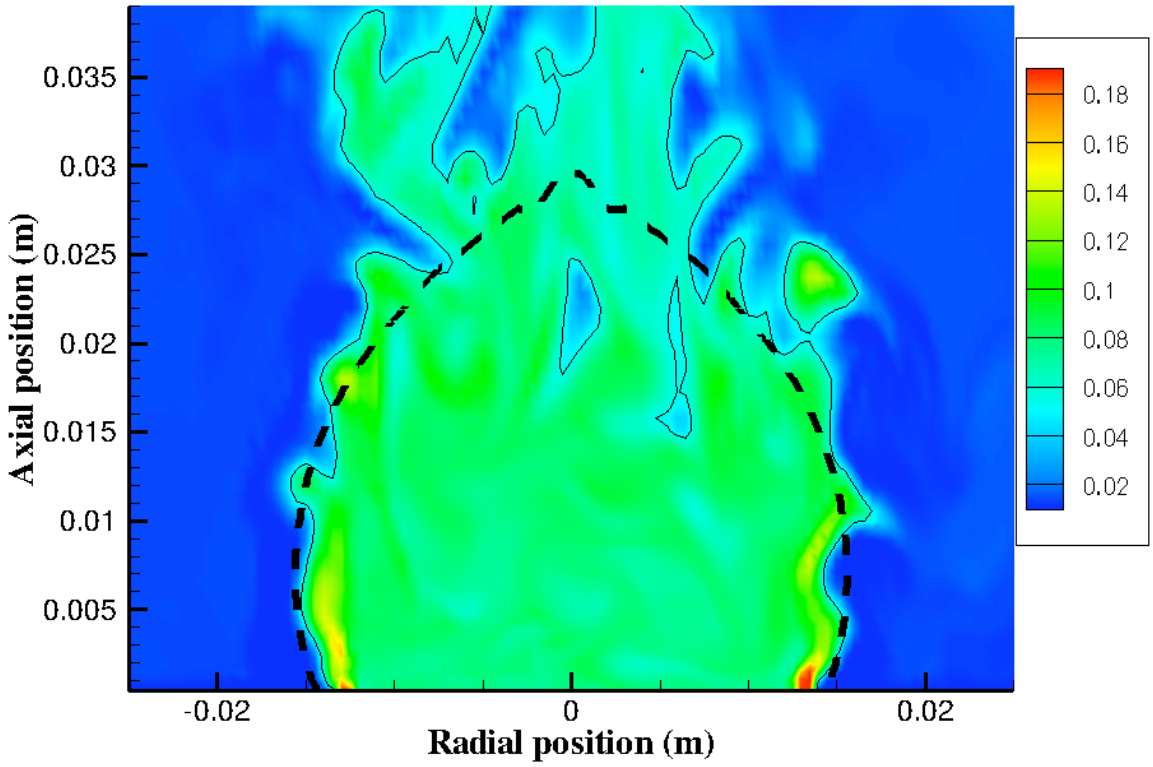

Figure 4.17: LES resolved instantaneous mixture fraction distribution. Black line: LES resolved instantaneous stoichiometric line. Dashed line: averaged stoichiometric line.

ignite the mixture, then the sparking zone should either possess ignitable mixture during the sparking moment, or ignitable flow should be transported from a very nearby location before substantial diffusion of deposited energy. In a first approximation, the success of ignition at the exact sparking location can thus be related to the statistics of local mixture conditions [5]. The probability density function (pdf) of the LES resolved mixture fraction, $P(\widetilde{Z};\underline{x})$, calculated from the time history of the mixture fraction field is a possible ingredient to start quantifying the local ignitability [8]. The flammability factor $F(\underline{x})$ [4, 5, 17], is defined as the probability to find the mixture fraction within the static limits of flammability. In other words, Flammability Factor (FF) is defined as the cumulative probability of a potentially flammable mixture occurring at a given point. Hence, at a given location, the ignition flammability factor is defined as:

$$F(\underline{x}) = \int_{Z_l}^{Z_r} P(\overline{Z}^*;\underline{x})\, d\overline{Z}^* \tag{4.11}$$

where $Z_l = 0.028$ and $Z_r = 0.089$, denote the chosen lean and rich flammability limits of the methane-air mixture. (By definition, a unity flammability factor corresponds to a zone which always possesses ignitable mixture). This FF was was initially formulated in experimental context, trying to characterise the ignition behaviour of a turbulent free jet [17]. There exists a critical surface in turbulent jet, which separats the region into two ignition regimes; one exhibits a local ignition with locally good flammability factor but the flame gets blown due to the advection and the other side of the surface, the flame packet propagates against the flow and 'light-back' the flame. Thus the flammability factor is found to be a measure of ignition success on a certain region of the flow, at least for a free jet. This could, however be not the same for annular jets which features unique flow characteristics like recirculation and reattachment.

LES provides access to the flammability factor, based on the resolved mixture fraction by cumulating in time, at each node, a sample of the resolved mixture fraction field. Mixture fraction probability density functions are shown in Fig. 4.18 for some selected points, see similar probability density functions in Fig. 13 of [4]. Along the burner axis, for the points $r = 0$ mm, $z = 20$ mm and $r = 0$ mm, $z = 30$ mm, the mixture fraction pdf displays a near Gaussian distribution. These points are part of those selected for systematic comparison with the sparking experimental results, which will be discussed in the next chapter. The point $r = 0$ mm, $z = 20$ mm is located inside the recirculation zone and frequently faces rich mixtures due to the interaction of the rotating recirculating bubbles with the injected fuel stream. Part of the pdf then lies outside the flammability limit in a quite rich zone. The location $r = 0$ mm, $z = 30$ mm is behind the rearward stagnation point, where the turbulence intensity is quite high. The mixture in this region is always within the flammability limits, suggesting facilitated ignition. The pdfs extracted from LES are very similar to those extracted from experiment (Fig. 13 of [4]).

The points $r = 15$ mm, $z = 25$ mm and $z = 20$ mm are located within the envelope of the central recirculation zone. The flow in this region is highly intermittent, which leads to a non-Gaussian mixture pdf. As seen in Fig. 4.18, $P(\widetilde{Z};\underline{x})$ is positively skewed toward the zero mixture fraction, resulting in a low flammability factor. Nevertheless, the chance of getting a mixture within the flammability limits is non zero. Such $P(\widetilde{Z};\underline{x})$ has been constructed at all points in a plane cutting the burner axis, using Eq. ((4.11)). The flammability factor can then be evaluated for every point of a central plane passing through the burner axis, and is shown in Fig. 4.19. Qualitatively, F computed from the LES is the same as that of the experiments, showing a high flammability zone centered on the burner axis, with a large base of the width of the bluff body, but narrowing slightly when progressing downstream (see Fig. 22(c) of [4]). Quantitatively, in the details, F extracted from LES shows some departure from its experimental counterpart, where the non zero flammability zone is narrower; showing that having quite similar time averaged basic statistics (Figs. 4.16 and 4.15) does not ensure fully similar flammability factor.

Also in the experiment, the highest probability of ignition, as reported from sparking attempts, is maximum for a radial position located between 15 and 18 mm (for $13 < z < 17$ mm), a location with an experimental flammability factor that is very small or null. In the LES, for the same zone, the flammability factor is small (below 25%) but mostly larger than in the experiment. Hence, for this zone, the LES flammability factor would better anticipate the real ignition behavior. Nonetheless, locations can also be found in the LES where F is null and the real probability of ignition is high. One of these locations will be presented in the next

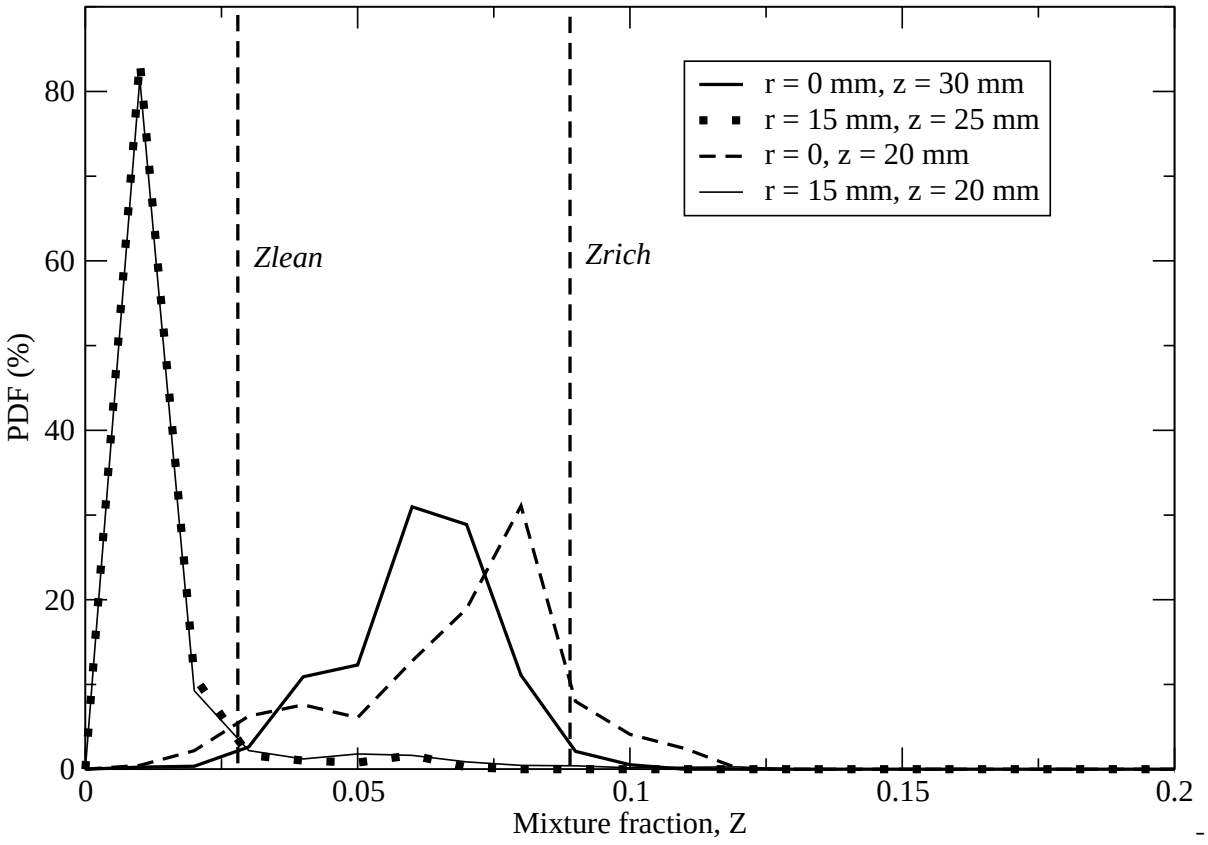

Figure 4.18: Pdf of $\tilde{Z}$ at a few selected locations in the burner.

chapter, while discussing spark ignition. It is therefore difficult, at this stage, to really conclude on the exact validity of the flammability factor for anticipating, from cold flow analysis, the probability of ignition success; clearly more information is needed.

4.4 Summary of cold flow results

In this chapter, the results of cold flow velocity and mixing fields are compared against the experimental measurements. The predictions of mean fields are fairly good, at least in and around the central recirculation zone (CRZ), which is the region of interest while analysing ignition in the forthcoming chapter. Injecting fuel has a non-negligible effect on the dimension of the CRZ, which of course impacted the radial profiles in the upstream axial locations. This point necessitates the need to perform the cold-flow velocity measurements with actual inlet conditions (*i.e.* with fuel injection) to correlate the cold-flow data while analysing ignition. Otherwise, this could be misleading while interpreting the ignition behaviour along with the cold-flow measurements done with mocked inlet conditions.

Apart from the mean and fluctuations of mixture fraction, the flammability map was constructed from the resolved probability density function (PDF) of mixture fraction and com-

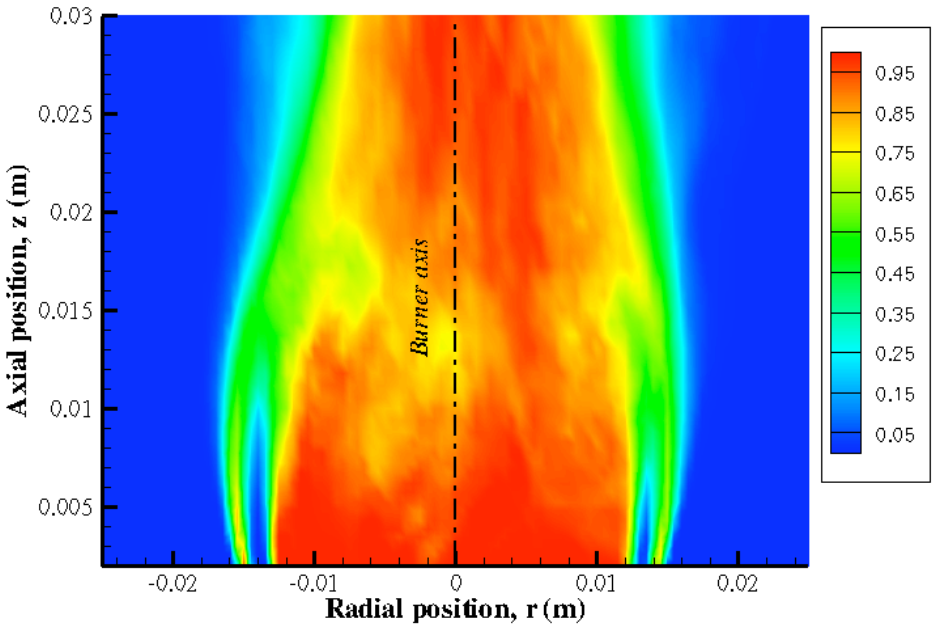

Figure 4.19: Flammability contour based on the resolved mixture fraction pdf (cut in the central plane).

pared against the measurement. Although, few discrepancies are noticed in the flammability factor (FF) of computation, the qualitative picture of the FF is same as the one obtained in the experiment.

In the coming chapter, results of hot flow simulation will be discussed for few locations, chosen based on the above information, by depositing spark energy and the ignition behaviour will be explored. The different ignition spots retained are marked on the mean axial velocity contour shown in Fig. 4.7 and their characteristics will be summarised in the first section of the chapter 5. These points are taken in and around the CRZ region, with low and high flammability factors, and, high and low probability of providing a whole flame ignition. A detailed analysis of the flame development at these locations will be given in chapter 5.

CHAPTER 5

Hot flow simulation

Contents

The simulation of reacting cases are discussed in this chapter. All the test cases discussed here and in the forthcoming chapter are done with LES case considering air plus fuel injection. The conventional PCM-FPI method was used in this simulation, where the table was prepared based on laminar unstrained premixed flamelet calculations, as discussed in section 3.4. The modelling of spark is detailed in the first section. The spark model is applied on different zones of the burner featuring different flow and mixing patterns. The success and failure of ignition kernel are observed in these ignition spots and the correlation between the ignition success or failure and the velocities and mixing fields are explored in detail. The difference between flammability factor, probability of ignition kernel initiation and the probability of successful burner lightening are analysed.

5.1 Initial flame kernel / spark modeling

The modeling of the flame kernel resulting from sparking is now discussed first. As detailed in section 2.3, sparking is a process of ionising gas molecules by rapid deposition of energy in a small space between the spark electrodes. Rigourous modelling of spark ignition is quite complicated, as the mechanism involves plasma formation under extremely high temperature/pressure

conditions with very small time and length scales [156, 157]. Neither the detailed combustion chemical scheme used in this work nor the conventional thermochemical relations are applicable in such an environment. In the experiment, the spark energy deposit always generates a small kernel of hot gases, and, it is the subsequent time development of this initial flame kernel that determines the ignition success or failure of the overall burner [4]. A simplified modelling procedure is thus adopted in this study to reproduce only the macroscopic effect of spark promoting flame kernel initiation.

The spark energy deposited is mimicked by a source term in the energy equation, a general procedure followed in many earlier works [25, 77, 81, 116]. The modelled source term takes a Gaussian distribution in space, centred at the spark location. The spark source also follows gaussian distribution in time, to better match with the energy deposition schedule obtained in the experiment, which could be inferred from the ignition current profile [3]. Accordingly, the spark energy source term is cast in [116]:

$$\dot{\omega}_s = \dot{\omega}_s^o \exp\left[-\left(\frac{t-t_0}{2\sigma_t}\right)^2 - \left(\frac{x-x_0}{2\sigma_x}\right)^2 - \left(\frac{y-y_0}{2\sigma_y}\right)^2 - \left(\frac{z-z_0}{2\sigma_z}\right)^2\right] \tag{5.1}$$

with

$$\dot{\omega}_s^o = \frac{E_s}{V_s \delta_{ts}} \tag{5.2}$$

where, t_o is the sparking instant in time; x_o, y_o and z_o are the spark coordinates. E_s is the net spark energy chosen in such a way that the maximum local temperature is below the maximum allowable temperature ($T_{max} = 2500$ K), for which the conventional thermochemical relations are applicable, typically E_s is of the order of 60 mJ. The initial spark kernel volume $V_s = (4/3)\pi R_s^3$ is with the radius $R_s = 0.5$ mm, as suggested in former studies [101, 155], and the spark duration of the experiment is used $\delta_{ts} = 400$ μs [4]. The time and space relaxation parameters in Eq. ((5.1)) are set as: $\sigma_t = 0.2$ ms and $\sigma_x = \sigma_y = \sigma_z = 1$ mm.

In the experiment, the spark energy deposit leads to temperature levels well above $\widetilde{T}^{Eq}$, the filtered chemical equilibrium temperature of the mixture; the thermal energy diffuses away from the initial spark kernel and a flame is formed; however, the amount of energy transferred from the sparking device to the flow stays small compared to the heat released by combustion once initiated. To mimic this thermal process, the increase of local temperature that follows energy deposit is continuously monitored and compared with the local chemical equilibrium temperature. As soon as the temperature exceeds $\widetilde{T}^{Eq}$, the local composition is adjusted to the tabulated chemical equilibrium composition, thus initiating combustion. The equilibrium temperature overshoot is only transitory and, in all cases studied, it is not observed for more than 1 ms after sparking has vanished. The main parameters of this simplified numerical sparking procedure have been varied, without significant change in the reproduction of the ignition probability map.

5.2 Choice of ignition spots for LES analysis

In experiments, ignition probability map was built based on 50 ignition experiments at every ignition spots. The complete burner region was mapped with 25×25 matrix points across and along the burner, thus making the total number of ignition spots analysed to be 625. It is merely impossible to analyse all these ignition spots in LES simulation, as the time needed for

performing one ignition calculation would be normally several CPU hours. Rather, few ignition spots are chosen for LES analysis, distributed along the burner regime. These locations are marked in Fig. 4.7, and for convenience, named using alphabets. As the burner is radially symmetric, the radially eccentric ignition spots discussed here are chosen to be on the left side of the burner axis in the two-dimensional view shown in the figure. The list of ignition spots analysed in this chapter and in the forthcoming chapter are given in Table. 5.1 along with their corresponding coordinate positions[1]. The mean axial velocity, radial velocity and mixture fraction of these ignition spots are listed in Table. 5.1. The flammability factor calculated based on Eq. (4.11) for each ignition spot are also given in Table. 5.1. As seen in the table the spots chosen for ignition analysis feature different set of velocity, mixing and flammability factor combinations.

Table 5.1: Ignition spots with time averaged flow field and mixing field informations

Ignition spot	U_m	R_m	Z_m	F
Index - [z, r]	m/s	m/s		%
A - [20, 15]	7.03	-1.04	0.010	6
B - [27, 0]	3.28	0	0.054	85
C - [25, 0]	2.13	0	0.058	87
D - [15, 17]	4.93	-0.54	0.0067	0.3
E - [20, 0]	-1.70	0	0.07	85

z: Axial downstream position (mm), r: Radial position (mm), U_m: Mean axial velocity, R_m: Mean radial velocity, Z_m: Mean mixture fraction, F: Flammability factor.

5.3 Choice of ignition timing

Energy was deposited in the selected ignition spots at a time instance chosen based on the flow and mixing history. This is done by probing the velocity field values and mixture fraction at every ignition spot over a period of time from frozen flow simulation. The complete instantaneous three dimensional field data (storing all primitive variables in *bloc-files*) are also stored at a definite time interval, which enable us to rewind and start the simulation from any particular time instant. The history of axial velocity, radial velocity and mixture fraction is used to choose a particular time instance to analyse ignition. From the frozen flow data stock, the closest *bloc-file* is chosen to restart the simulation, which is then done with chemistry.

Apart from the mean flow and mixing variables, the instantaneous field play a major role in driving the event to end up in either successful or failed ignition, which will be discussed in forthcoming sections. The flow and mixing instabilities, as will be seen further, could make it difficult to foresee the possibility of the ignition kernel to lighten the burner only based on the mean quantities. Thus, in order to delineate the transient effects of flow and mixing, the instantaneous value of axial, radial velocities and mixture fraction are averaged over spark

[1]Following same notations used in chapter 4, z here refers to the streamwise location of the ignition spot from burner inlet and r refers to the radial distance of the ignition spot from the burner axis.

duration[2] for every spark instance analysed for all ignition spots. Table. 5.2 lists these values of velocity and mixing field for successful and failed ignition events for the ignition spots, which will be discussed in following sections.

Table 5.2: Ignition spots with velocities and mixture fraction time averaged over the sparking time duration

Ignition spot Index - [z, r]	Burner ignition	Time instant s	U_m^s m/s	R_m^s m/s	Z_m^s
A - [20, 15]	Failed	0.09379	6.9	-0.28	0.004
A - [20, 15]	Success	0.09486	3.6	-3.9	0.003
B - [27, 0]	Failed	0.1534	4.23	-3.26	0.032
B - [27, 0]	Success	0.1393	0.54	-0.98	0.043
C - [25, 0]	Success	0.13765	1.54	-1.176	0.052
D - [15, 17]	Success	0.09379	10.26	0.06	0.008

z: Axial downstream position (mm), r: Radial position (mm), U_m^s: Mean axial velocity, R_m^s: Mean radial velocity, Z_m^s: Mean mixture fraction, upperscript s indicates averaging over the sparking time.

5.4 Point A: z = 20,r = 15

This point located outside the CRZ, has a flammability factor of 6%. The experiment [4] has shown that the probability to contribute to successful flame kernel initiation after sparking at point A is close to 50% and the probability of whole burner ignition is of the order of 25%.

As mentioned before, the success of an ignition kernel to establish a stable flame does not depend only on local flow and fuel distribution at sparking time, but also on the time history of field variables experienced by the developing kernel. One experimental observation is that a spot favourable for local ignition is not necessarily a successful spot for getting a fully developed flame at every time. On the other hand, a zone with a small local flammability could be a relatively better spot for successfully lightening the flame. The advection and unsteady nature of the flow make these differences. The spot A, which exhibits strong flow intermittence, is retained to analyze these effects with LES. The time histories of velocities and mixture fraction were recorded for a given duration. The kernel development was tested at two different instants selected from this time history ($t_s = 0.09380$ s and $t_s = 0.09486$ s).

Figure 5.1 shows the time history of axial velocity, radial velocity and mixture fraction at the spot A of Table 5.1. Most of the time, this region faces a high axial velocity. The radial velocity is generally negative and thus towards the CRZ. The fluctuations of both radial and axial velocities are high (Figs 4.11 and 4.12), which indicates quite strong flow intermittency at this point. The mixture fraction is small and presents high fluctuations (Figs 4.16 and

[2]It is to be noted that the energy deposition via spark lasts for 400 microsecond, and so the instantaneous values are averaged over this period of time to better represent the flow and mixing field ahead of the ignition kernel, right after sparking.

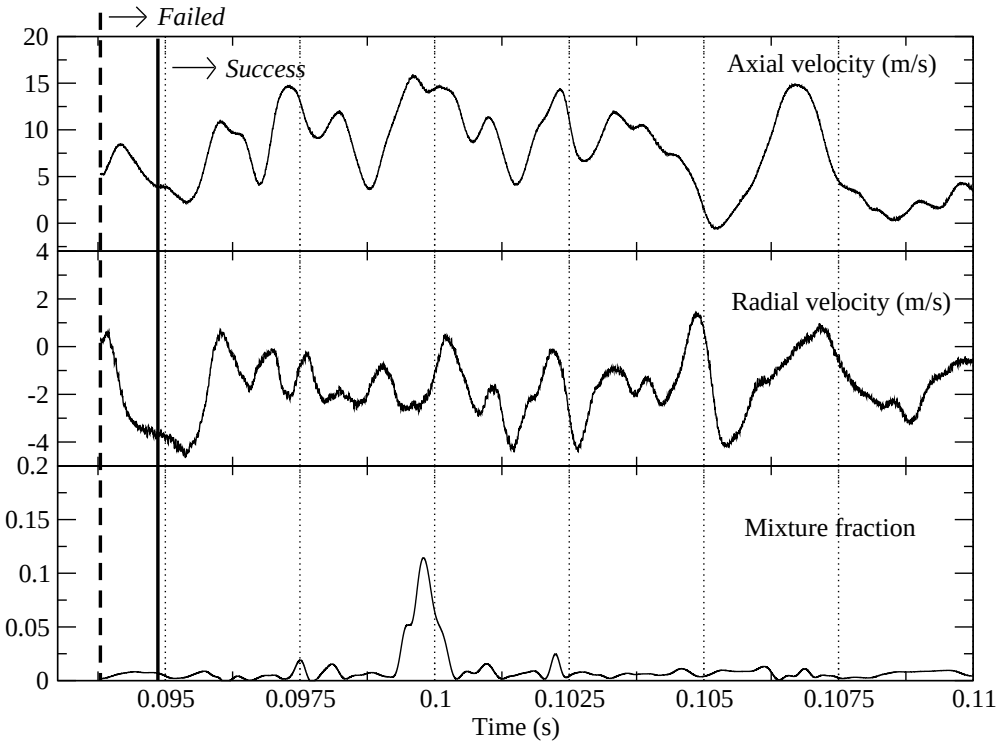

Figure 5.1: Time history of velocities and mixture fraction at spot A (z = 20 mm, r = 15 mm). Continuous line: Favourable time instant. Dashed line: Non-favourable time instant.

5.1), varying from nearly zero to an extremely rich value beyond the flammability limits. This could be verified from the pdf of the resolved mixture fraction field shown in Fig. 4.18. The flammability factor in this region is small, suggesting that local ignition is less probable, Table 5.1 summarizes the time averaged velocities, mixture fraction and flammability factor for this zone.

5.4.1 Failed ignition

Ignition was tested at two instants in time giving rise respectively to a failed and a successful ignition case, which are indicated in Fig. 5.1 in dashed and continuous lines. The velocities and fuel mass fraction averaged during the sparking duration (400 μs) are given in Table 5.2 for each sparking attempt. At a time instant of $t_s = 0.09379$ s, the deposited energy initiates an ignition kernel, which fails to lighten the burner. For this particular time instant, the histograms of axial velocity, radial velocity and mixture fraction, constructed from their respective time history recorded during the spark duration, are shown in Fig. 5.2.

Referring to Figs. 5.1 and 5.2a, the averaged axial velocity during the spark duration is of

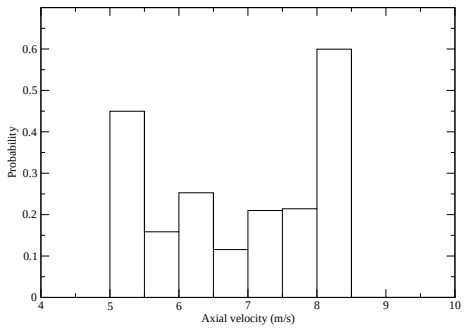

(a) Axial velocity

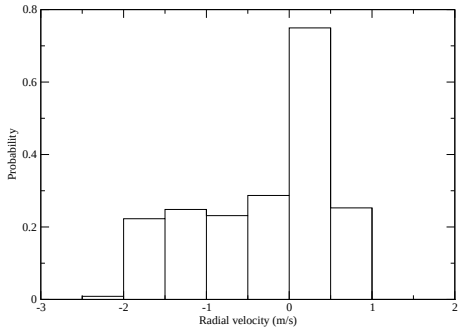

(b) Radial velocity

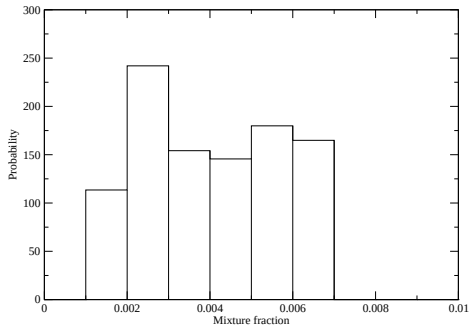

(c) Mixture fraction

Figure 5.2: PDF of velocity and mixture fraction at spot A (z = 20 mm, r = 15 mm), during the sparking moment. Sparking time = 0.09379 s.

the order of 6.9 m/s, which is quite high for this flow, while the averaged radial velocity stays almost zero, which means that the kernel is not experiencing any radial movement while being convected downstream.

The mixture fraction is far away from flammability limits, however, as this region is quite close to the iso-stoichiometric surface (Fig. 4.7), the deposited energy can diffuse toward the flammable region in the close vicinity of this ignition spot and a burning kernel is first created as already observed in [135]. The behaviour of this kernel is displayed in Fig. 5.3, which shows the snapshots of temperature, tracked in series of time instants, following ignition. The envelope of iso-stoichiometric surface is within 2 mm from the ignition spot at the beginning of ignition (taken as $t = 0$ for the discussion). The streamline (based on LES resolved instantaneous axial and radial velocities) at the ignition spot is also plotted at the start of ignition. This streamline is more or less parallel to the burner axis, showing that the kernel is going to experience an axial transport without much deviation in its radial position. The near spherical spark kernel, observed after $t = 0.15$ ms, is undisturbed by turbulence; a phenomenon also reported in the experimental observation of spark ignition [140]. At a time of 1 ms after sparking, the kernel become big and is stretched axially by the flow. After 3 ms, the kernel is enlarged, but has been

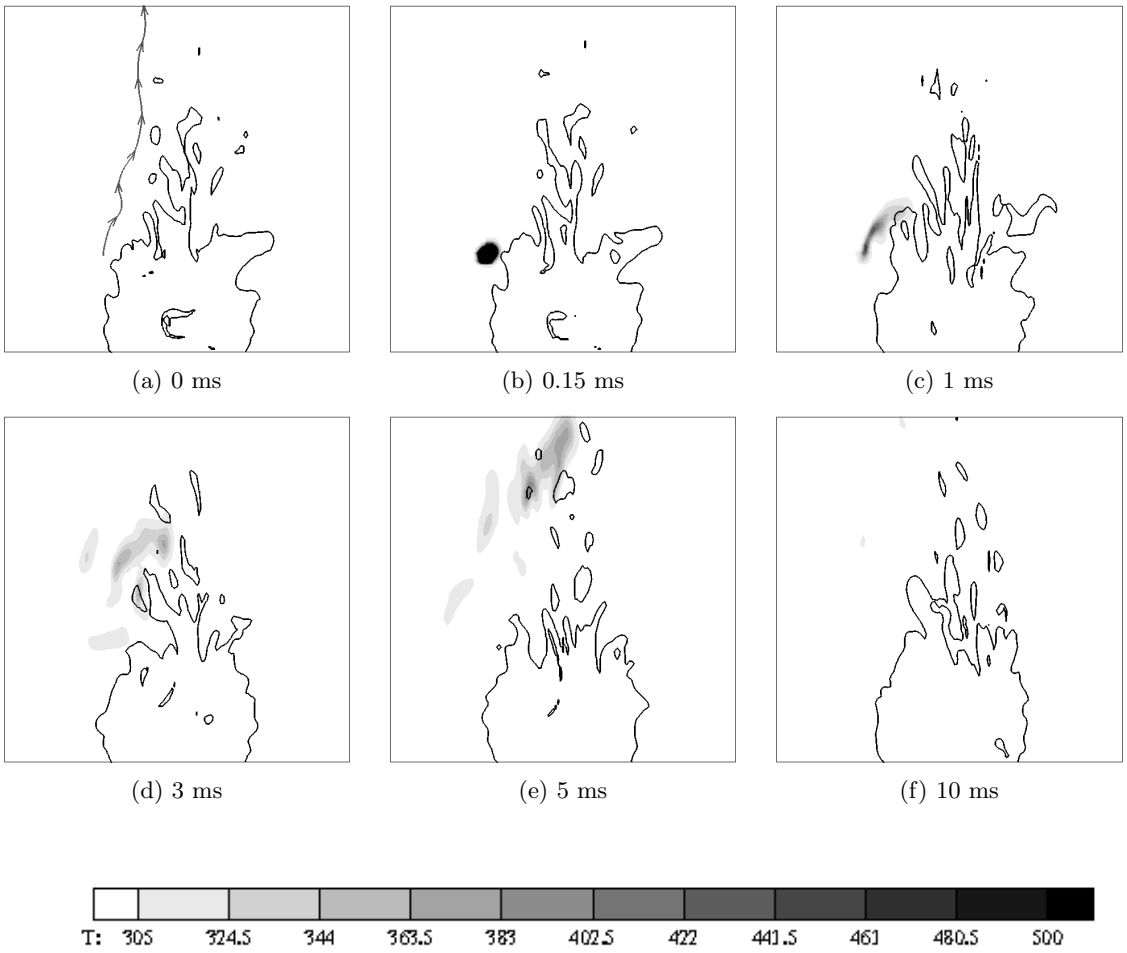

(a) 0 ms (b) 0.15 ms (c) 1 ms

(d) 3 ms (e) 5 ms (f) 10 ms

Figure 5.3: LES resolved instantaneous snapshots of temperature after sparking at Spot A (z = 20 mm, r = 15 mm). Spark time = 0.09379 s, (in Fig. 5.1), in caption the relative time after the ignition event. Solid black line: Iso-line of stoichiometric mixture fraction. Image covers the domain dimension of 70 x 70 mm.

also scattered, the burnt gases pocket then reaches the zone beyond the rearward stagnation point, where the flow is only positive in all radial positions (Fig.4.6). Later in time the kernel is still growing, but it is transported further downstream to get finally completely blown. In the experiment, this spot was identified to have a high probability of successful kernel initiation, but a relatively small probability to lighten the burner (see Fig. 22(a) and (b) in [4]). The difference between these two probabilities arises due to the transport of the burning kernel, which is driven by the instantaneous flow field.

5.4.2 Successful ignition

A spark at a latter instant (t_s = 0.09486 s) featuring different conditions has also been tried resulting in successful ignition of the burner, thus LES captures burner ignition variability for

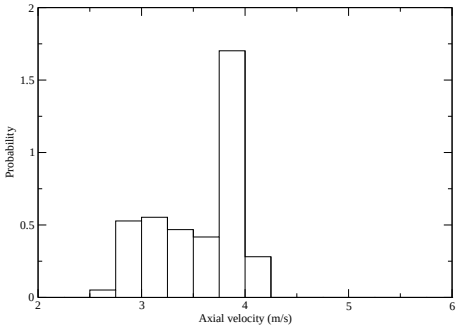

(a) Axial velocity

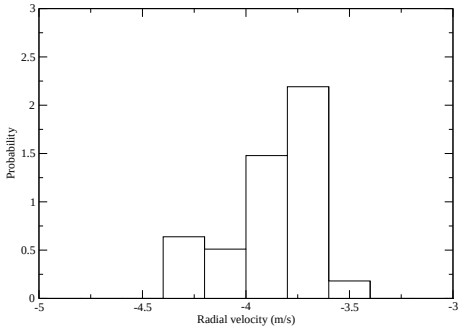

(b) Radial velocity

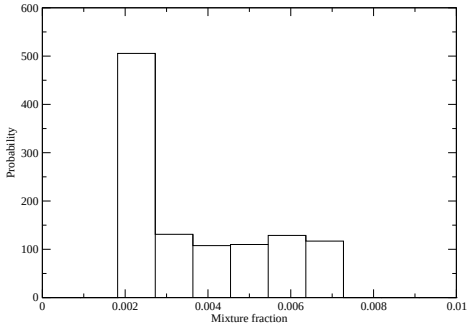

(c) Mixture fraction

Figure 5.4: Pdf of velocity and mixture fraction at Spot A (z = 20 mm, r = 15 mm), during the sparking moment. Sparking time = 0.09486 s.

this point. Figure 5.4a shows the histogram of axial velocity during the energy deposition period at this spot. The axial velocity is relatively low, about 3.6 m/s, compared to 6.9 m/s at the previous instant, and it helps the kernel to grow before getting convected too far downstream. At the same time, the radial velocity shows a negative trend (Fig. 5.4b), thus transporting substantial amount of deposited energy towards the CRZ, with favourable mixture fraction during the travel of the kernel, giving rise to a successful local ignition.

The development of flame kernel from the sparking moment is shown in Fig. 5.5, which depicts shot by shot temperature distribution. The streamline issued from the spark location at $t_s = 0.09486$ s presents a slight radial inclination towards the burner axis, due to the negative radial velocity prevailing at this time instant and gets very close to the stoichiometric line. A near spherical kernel is observed at $t = 0.16$ ms, immediately following ignition. The kernel gets advected downstream by the axial component of velocity and also spreads out radially, as seen at $t = 1$ ms in Fig. 5.5. The intense burning core region is advected by the strong axial velocity. In the meantime, a part of the developing kernel is taken within the recirculation zone, and, this portion experiences a flow reversal and travels towards the bluff body. At $t = 10$ ms, the initial intense core region has been completely convected away from the domain, whereas

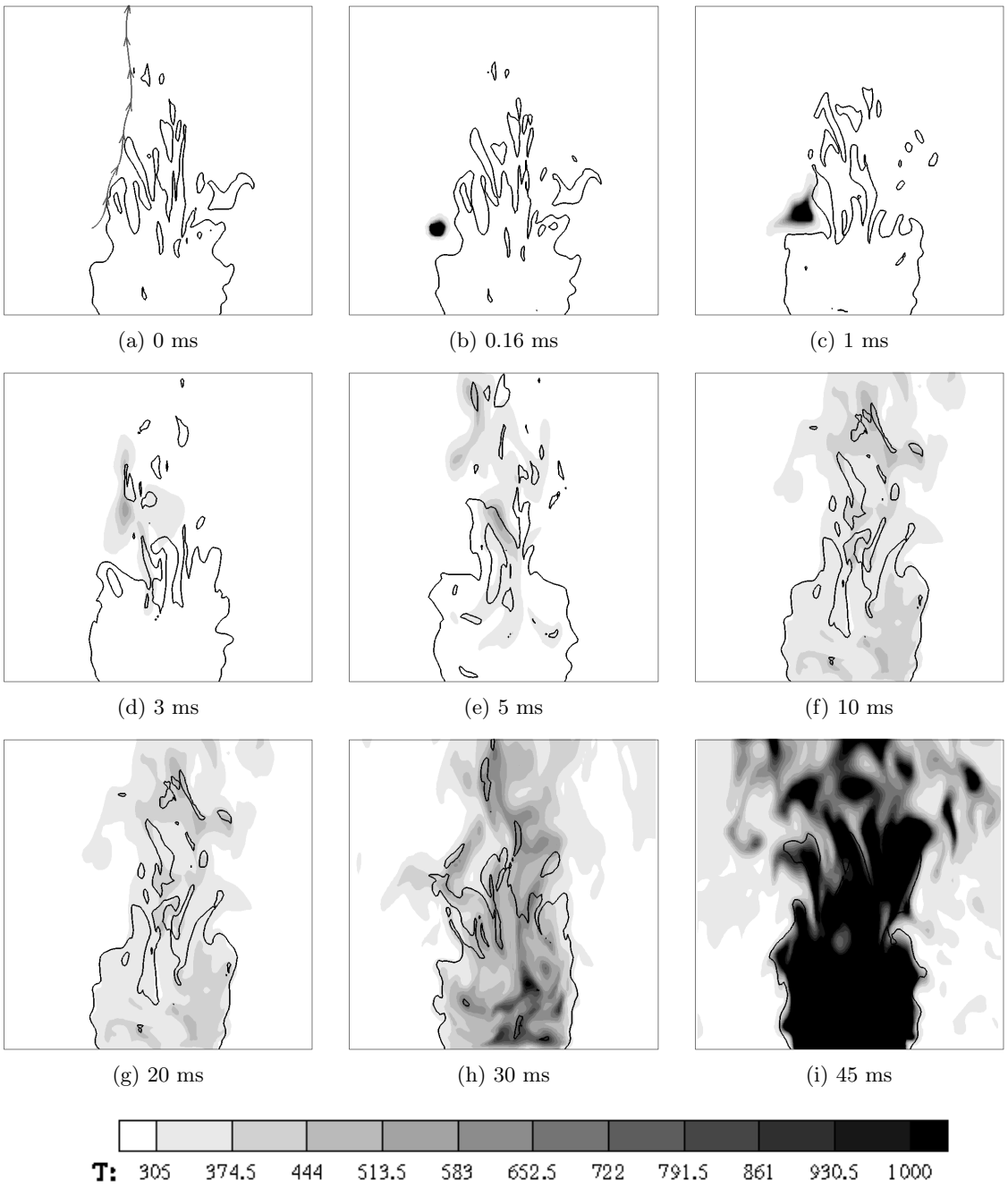

Figure 5.5: LES resolved instantaneous snapshots of temperature after sparking at spot A (z = 20 mm, r = 15 mm). Sparking time 0.09486 s (in Fig. 5.1), in caption the relative time after the ignition event. Solid black line: Iso-line of stoichiometric mixture fraction. Image covers the domain dimension of 70 x 70 mm.

the flame starts developing inside the CRZ from the trapped part of the kernel. Inside the CRZ, the recirculating bubbles transport the reaction zone radially outwards and thus ignites

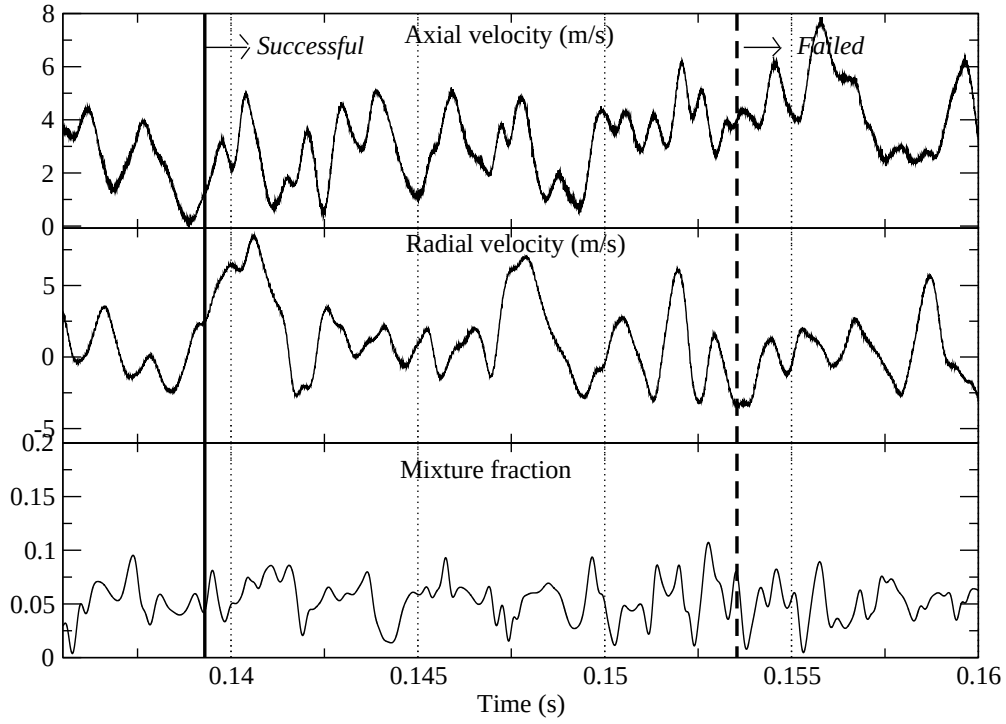

Figure 5.6: Time history of velocities and Mixture fraction at spot B (z = 27 mm, r = 0 mm). Continuous line: Favourable time instant, Dashed line: Non-favourable time instant.

the iso-stoichiometric surface. Between 10 and 45 ms after sparking, the flame develops inside the CRZ. At $t = 45$ ms, a stable flame is obtained. The time taken by the ignition kernel from the sparking moment to establish a fully developed flame is about 45 ms for this ignition spot, which is the same duration as the one reported in the experimental results (see Fig. 14 in [4]).

5.5 Point B: z = 27 mm, r = 0 mm

This point is located downstream of the CRZ, at a location where the flammability factor is high (85%). In the experiment, while the probability of getting a successful kernel is found high (over 30%), the probability of getting an established flame is low (below 10%). Table 5.1 gives the time averaged flow and mixing field values of this ignition spot. The flow here is relatively less intermittent, at least compared to the previously discussed ignition position. The mean axial and radial velocities are also small (Figs. 4.6 and 4.8), which should be favourable for the development of the ignition kernel. The velocity at this point is under the influence of the time evolution of the CRZ; this makes the kernel to experience advection towards or away from the CRZ, leading to a successful or a failed ignition event, respectively. Figure 5.6 shows the time

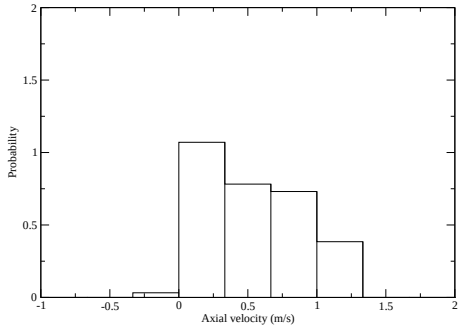

(a) Axial velocity

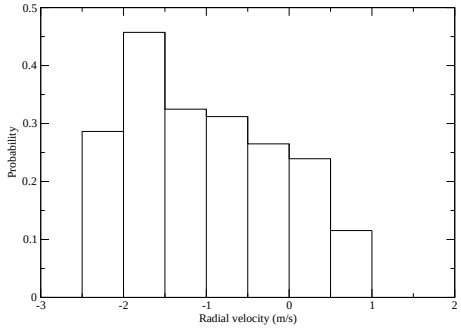

(b) Radial velocity

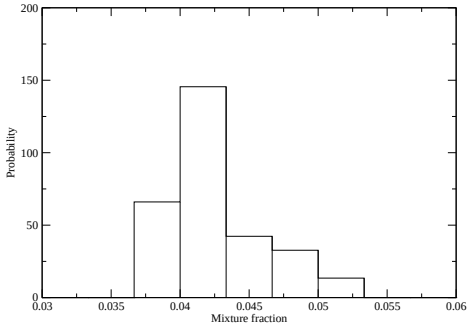

(c) Mixture fraction

Figure 5.7: PDF of velocity and Mixture fraction at Spot z = 27 mm, r = 0 mm, during the sparking moment. Spark time = 0.1393 s

history of velocities and mixture fraction at this ignition spot. The axial velocity is always positive in this region, as this zone is located downstream relative to the rearward stagnation point. Beside the time averaged radial component is nearly zero, the LES resolved instantaneous radial velocity shows an oscillating trend ranging from negative to positive values due to the interactions of recirculating bubbles. The mixture fraction stays close to the stoichiometric value of 0.055, suggesting that most of the sparking attempt will result in a successful kernel. The time instants analysed are $t_s = 0.1393$ s and $t_s = 0.1534$ s, which respectively resulted in successful and failed ignition, as marked in Fig. 5.6.

5.5.1 Successful ignition

From the time history of flow variables, it is observed that if this ignition spot always faces positive axial velocity, there are also few instances where the axial velocity is very close to zero. Hence, only when the spark is imposed when the axial velocity vanishes, the kernel has a chance to produce an established flame before getting blown. One of such time instant is

t_s = 0.1393 s. The axial velocity averaged during the spark duration (400 μ s) stays small (see Table 5.2), close to the premixed flame propagating velocity at stoichiometry (0.4 m/s).

Fig. 5.7 shows the velocity and mixture fraction PDF during the sparking duration, reinforcing the low advection and favourable ignition of this spot at this time instant.The kernel evolution from $t_s = 0.1393$ s is shown in Fig. 5.8. The local streamline issued from the spark location indicates that the kernel movement is perpendicular to the burner axis, allowing the kernel to grow in an almost stoichiometric region. At 0.16 ms after sparking, the kernel has maintained its spherical shape centered at the spot B ($z = 27$ mm, $r = 0$ mm). After 0.7 ms, the kernel has moved from the ignition spot, though facing a positive axial velocity. As the mixture is almost stoichimetric here, the burning velocity is high enough to help the kernel to propagate against the flow. The flow advection and kernel propagation result in an 'edge-flame' like structure with a burning tail oriented downstream. After 3 ms, a part of the kernel has reached the rearward stagnation point and is subsequently taken inside the CRZ, where the flow is axially negative. After 5 ms, the trapped part of kernel inside the recirculation zone is developing, but with a lesser intensity as the mixture here is close to rich flammability limit. In the subsequent time instants, the strong turbulence inside the CRZ stirs and distributes the reaction zone and thus results in complete lightening of the flame.

5.5.2 Failed ignition

This location turned out to be an unsuccessful ignition spot at a different time instant, $t_s = 0.1534$ s. Fig. 5.9 shows the PDF of axial, radial velocities and mixture fraction during the sparking moment. The mixture fraction is well within the flammability limit, ensuring local ignition. On the other hand, the axial velocity shows a strong positive value, which stays close to 4 m/s during the sparking instance (Fig. 5.6). The close to stoichiometry mixture fraction combined with the high axial velocity (see Table 5.2) suggest that the spark will generate a developing kernel but that this kernel will get blown away. This is indeed what is observed in Fig. 5.10 showing the evolution of the flame kernel after ignition. At 1 ms after ignition, the flame kernel has already moved approximately 3 mm towards downstream from the ignition spot. The kernel axially propagates against the flow and takes an elliptical shape. However, the kernel fails to reach the stagnation point, as it does not possess enough propagation speed to face the increasing axial velocity. After $t = 3$ ms, the kernel while still growing in size, is further carried downstream by the flow. In successive time instants (see $t = 10$ ms and 20 ms in Fig. 5.10) the flow convects the flame away and finally a failed ignition procedure is achieved.

5.6 Point C: z = 25 mm, r = 0 mm

The two previous cases so far discussed were in the region enveloping the iso-stoichiometric surface as well as CRZ, where the time averaged axial velocity always stays positive. It would be interesting to see the kernel behaviour of a zone at the top of the CRZ when the axial velocity is negative. Spot $z = 25\ mm, r = 0\ mm$ is the ignition spot chosen for this, where detailed experimental investigation was carried and reported in [4]. This ignition spot is located on the burner axis, just ahead of the rearward stagnation point. As observed in Fig. 4.6 and 4.8, the mean axial velocity is positive with a zero mean radial velocity at this spot. Though the time averaged axial velocity in this spot is positive, this ignition spot also experiences

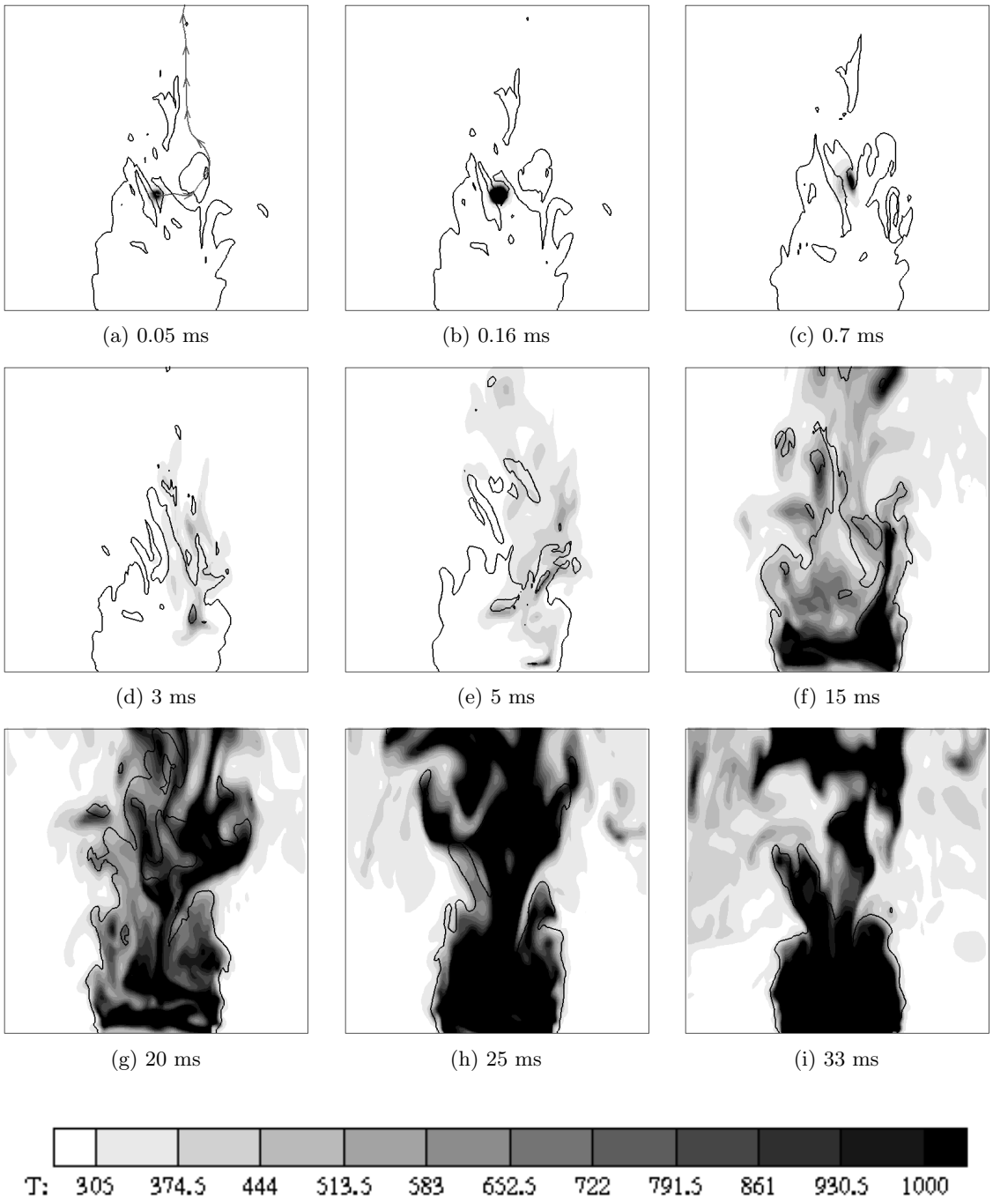

Figure 5.8: LES resolved instantaneous snapshots of temperature after sparking at spot B (z = 27 mm, r = 0 mm). Sparking time = 0.1393 s (in Fig. 5.6), in caption the relative time after the ignition event. Solid black line: Iso-line of stoichiometric mixture fraction. Image covers the domain dimension of 70 x 70 mm.

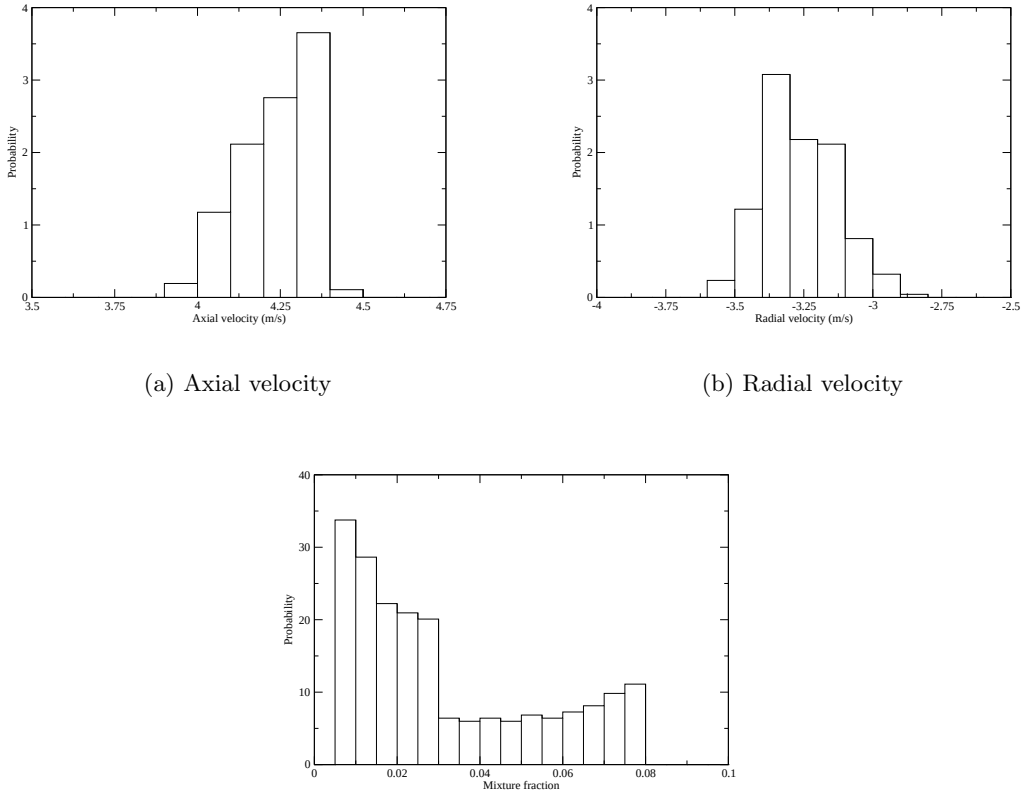

(a) Axial velocity

(b) Radial velocity

(c) Mixture fraction

Figure 5.9: PDF of velocity and Mixture fraction at Spot z = 27 mm, r = 0 mm, during the sparking moment. Spark time = 0.1534 s

negative axial velocity due to the axial fluctuations (refer Fig. 4.11) associated with rearward stagnation point. The mixture fraction here is more favourable for local ignition as same as the spot $z = 27\ mm, r = 0\ mm$, along with higher level of fluctuations in the radial component of velocity.

Like point B, point C is outside of the CRZ zone. At this location, a 87% flammability factor is found both in experiment and LES. Among the ignitions spots analysed so far, this spots features the maximum flammability factor, as seen from Table. 5.1. The experiment evidences a probability to get a successful flame kernel close to 40%, as observed at the point B, but the probability of full burner ignition is higher (20%) than at point B. Because axial velocities close to zero or negative are more probable at point C than B (see time history of flow variables in Fig. 5.11), the chances of getting full ignition are higher independently of the local mixture fraction, which is roughly the same at both locations.

As mentioned before, in experiments, two probability maps are reported. The first one is the probability of obtaining successful ignition kernel; which depends on flammable mixture availability between the spark electrodes or in the nearby vicinity. Only then, the energy deposited through spark can promote local ignition, which subsequently can lead to flame

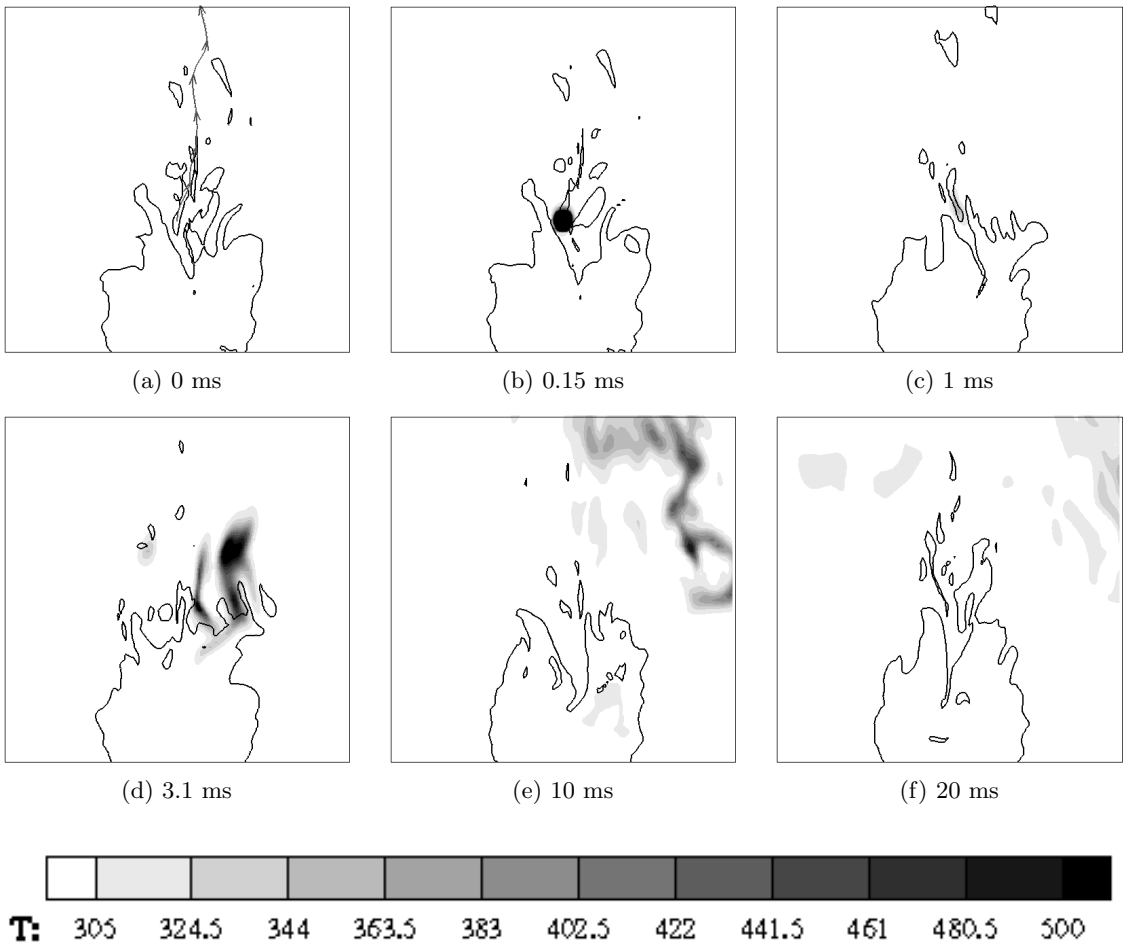

Figure 5.10: LES resolved instantaneous snapshots of temperature after sparking at spot B (z = 27 mm, r = 0 mm). Spark time = 0.1534 s (in Fig. 5.6). Solid black line: Iso-line of stoichiometric mixture fraction. Image shows the domain dimension of 70 x 70 mm.

spreading by flame propagation as well as flow advection. If the deposited energy finds no flammable mixture, then the spark energy will dissipate immediately and no visible flame can be noticed. The first probability map reported by Ahmed [4] quantifies the probability of creating a successful burning pocket. However, this local ignition needs not lead to complete burner lightening. The local convection could carry away the burning flame element towards downstream and finally may lead to blow-out. Only, if the axial downstream convection is not very strong, then the local ignition can lead to complete burner ignition. The second probability map reported in experiment, quantifies the probability of complete burner lightening. The difference between these two probability maps can be seen as the effect of axial convection on the ignition kernel. This can be easily verified by comparing the figures 22(a) and (b) of [4]. Within the central recirculation zone, the axial velocity is always negative and thus it plays a positive role in burner lightening. So, the sparks promoting local ignition can eventually grow and lighten the burner, which means that the probability of successful burner ignition is the probability of creating a locally burning pocket. The probability maps should be ideally

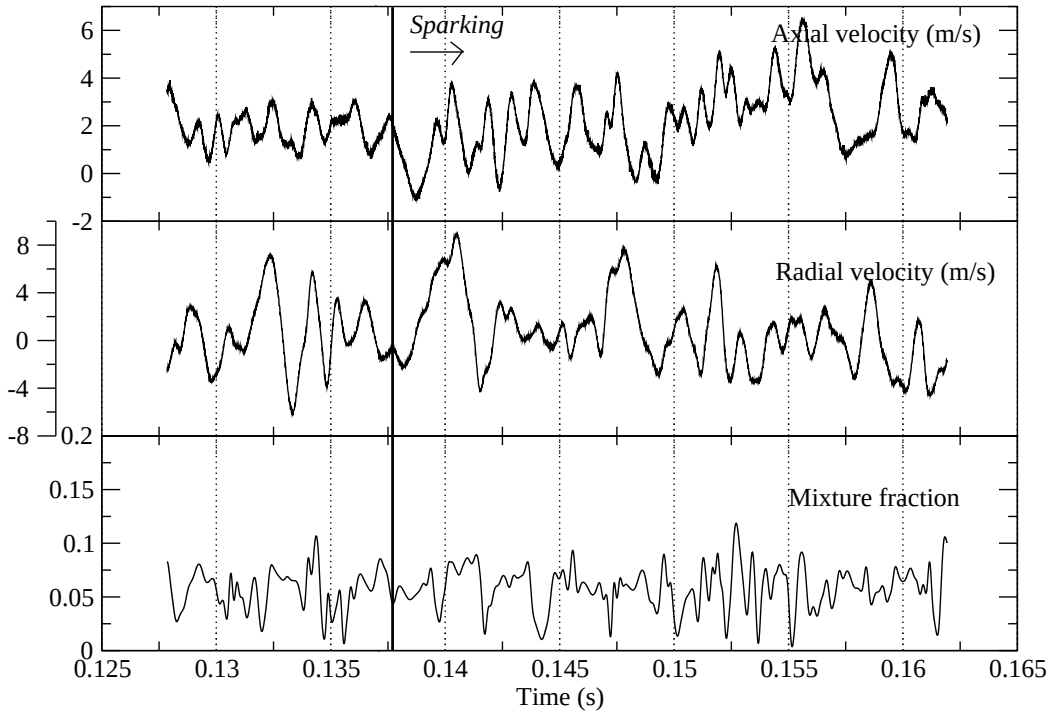

Figure 5.11: Time history of velocities and Mixture fraction at spot C (z = 25 mm, r = 0 mm). Continuous line: Favourable time instant.

same, which is what is observed in the experiment. While moving along the burner axis in the downstream direction, at a certain point, differences started appearing between the two probability maps. This can be regarded as the zone beyond the rearward stagnation point, where the axial velocity is positive, and it's role on kernel development is thus negative. At a downstream position of 25 mm, (i. e. at ignition spot C), the probability of complete burner lightening is 20%; one half of the probability of successful kernel initiation. This is due to the fact that, spot C faces a positive mean axial velocity (ref Fig. 4.6). It can be recalled that, the measurement with only air injection finds the spot C to be within the CRZ, however, with fuel injection this zone becomes exterior to the CRZ, due to the change of dimension of the CRZ. The flow measurement with only air injection could be misleading, if it is used to explain the observed ignition probability maps, which pin points the necessity to perform the cold flow analysis with actual fuel injection, instead of mocked inlet conditions.

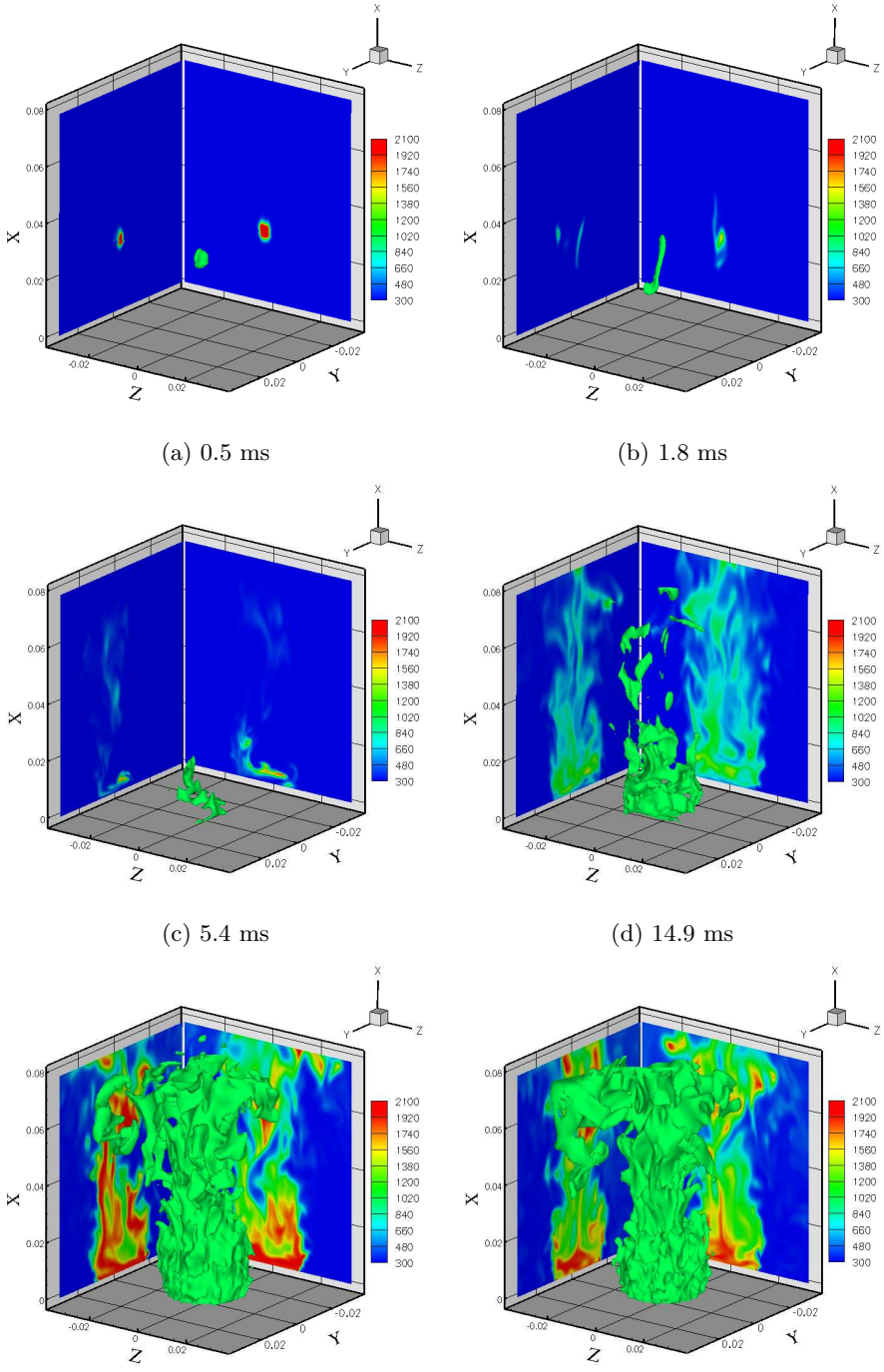

(a) 0.5 ms

(b) 1.8 ms

(c) 5.4 ms

(d) 14.9 ms

(e) 25.4 ms

(f) 45.5 ms

Figure 5.12: LES resolved instantaneous snapshots of temperature after sparking at spot C (z = 25 mm, r = 0 mm). The iso-surface corresponds to 1000 K. The planar views are in two orthogonal planes including the burner axis (X axis on the figure). Image shows the domain dimension of 70 x 70 mm, in caption the relative time after the ignition event.

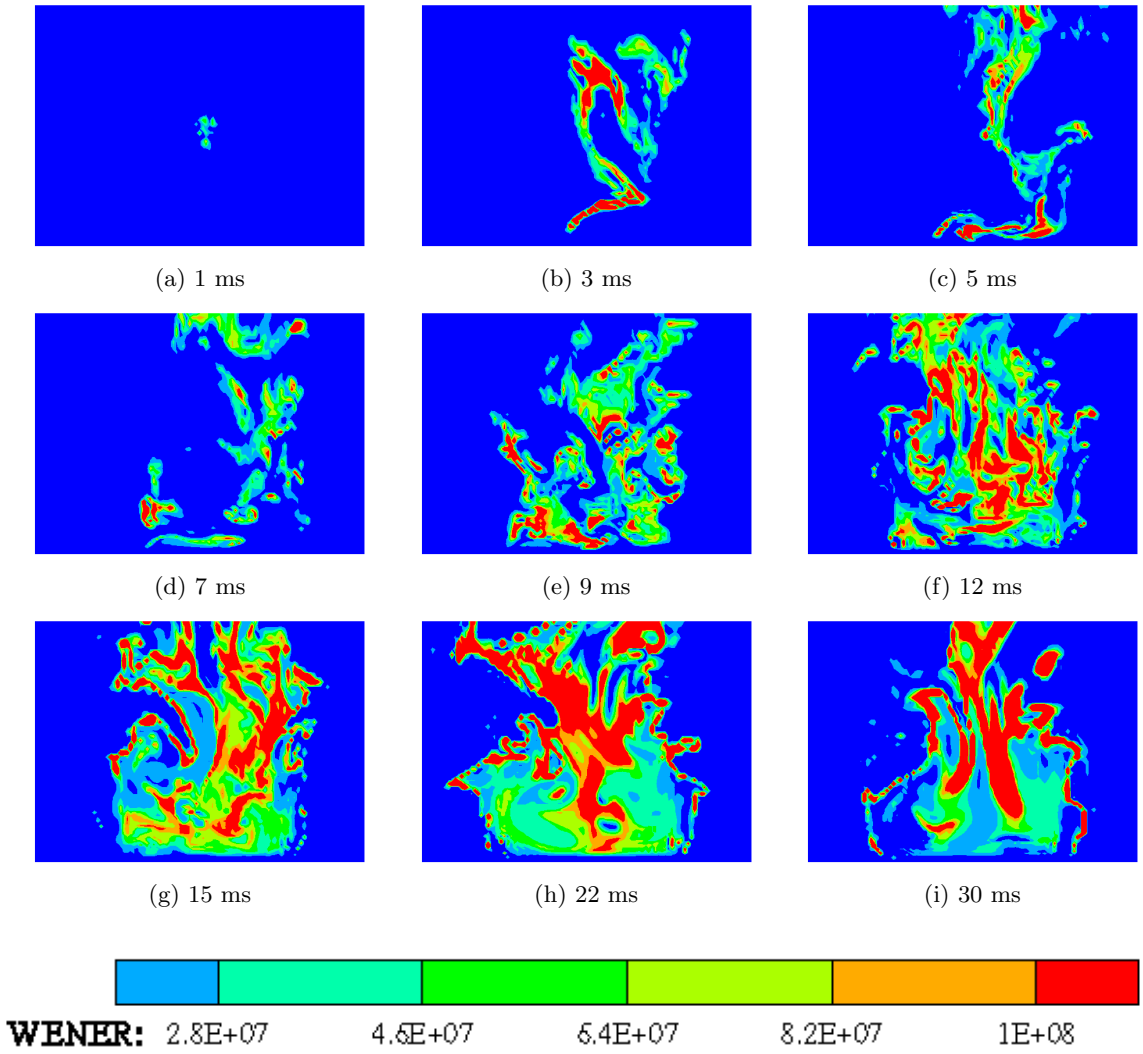

Figure 5.13: LES resolved instantaneous snapshots of reaction zone after sparking at spot C (z = 25 mm, r = 0 mm). Image shows the domain dimension of 70 x 50 mm.

5.6.1 Successful ignition

Figure 5.12 shows the planar and three dimensional contours of temperature, displaying the behaviour of ignition kernel at this spot, while sparking at $t_s = 0.13765$ s, a time instant where the axial velocity is negative. A quite large portion of the kernel is first convected towards the bluff body ($t = 1.8$ ms), with a first increasing and then decreasing negative axial velocity. The development of the burning kernel during this advection is relatively slow, because it faces a mixture which becomes progressively rich. Nevertheless, an important deformation of the kernel is observed in the three spatial directions. At about $t = 5$ ms, the kernel is carried close to the bluff body and also radially away from the burner axis by the counter rotating recirculating bubbles. At about 10 to 15 ms, the flame starts appearing at the edges of the CRZ, burning along the iso-surface of stoichiometric mixture fraction. At 14.9 ms, the flame base is

established at the bottom of the CRZ. At 25 ms after sparking, the flame is fully established and will not globally change at latter times (shown for 45.5 ms). The temperature iso-surface allows for observing the flame surface wrinkling induced by the high turbulence level. The global path of flame development reported here is inline with the observations made in the experimental work, which could be verified from the high-speed camera frames shown in Fig. 15 of [4]. Apart from the fast camera images, OH PLIF (Planar Laser Induced Fluorescence) images at closer time instants are also reported by the experimentalist, to visualise the flame structure during ignition kernel evolution; in the simulations, intense reaction zone is characterized with the strong heat release. Figure 5.13 shows the evolution of the source term of energy equation, which could be compared against OH PLIF image of experiment given in Fig. 18 of [4]. After 1 ms, the kernel which has hardly moved from its initial position appears distorted by the strong turbulence prevailing at the top of the CRZ. The flame kernel experiences acceleration ($t = 3$ ms) followed by deceleration ($t = 5$ ms) along the burner axis during its travel towards bluff body. At $t = 7$ ms, the kernel reachs the region close to the bluff body, where the axial velocity is almost zero. The flame stays then at the same axial position, but starts spreading in azimuthal direction by igniting the stoichiometric mixture found close to the bluff body lip ($t = 9$ ms). At further time, the main stream carries the burning flame pockets downstream, while a part stays entangled into the CRZ. At $t = 22$ ms, the reaction zone exhibits a patchy distribution, which is spreading inside CRZ as well as in the region beyond the rearward stagnation zone. At $t = 30$ ms, the reaction zone is active mostly at the downstream edge of the main flow, whereas within the CRZ it is diminished, as the CRZ contains mostly the recirculated burnt products at this stage. The computed LES resolved instantaneous flame evolution during the first stage of its development appears to be faster than the evolution observed in the experimental work (though rigourous qualitative comparison of instantaneous frames is not feasible). These simulations are done with unstrained premixed flamelet table, thus neglecting strain rate effects in the description of the chemical response of the young kernel, this may explain part of the discrepancy, this point is discussed in the following chapter. Also in the experiment, the introduction of a sparking device in this sensitive zone may also have non negligible effect on the flow dynamics. Apart from the little discrepancies noticed in the initial stage, the global flame evolution is satisfactorily reproduced by the simulation, considering the complexity of the phenomena involved in the overall process. Failed ignition cases occurring for positive axial velocity at the sparking time are not discussed in detail, since they are similar to point B (Fig. 5.10).

5.7 Point D: z = 15 mm, r = 17 mm

The ignition spots discussed so far cover the regions with either low flammability factor or considerably high flammability factor. But there are also certain burner regions where the flammability factor in the experiment is zero, whereas the probability of burner ignition is non zero. Interestingly, as per the experimental findings, these regions are found to be the most suitable ignition spots for complete lightening of the burner. The region covered by $z = 11$ to 18 mm and $r = 14$ to 18 mm, is the one with peak probability of ignition success (see Fig. 22(a) of [4]). Referring to Fig. 4.7, this region envelops the iso-stoichiometric surface of mixture fraction featuring strong axial velocity and turbulence. It can also be seen that the streamlines (based on average axial and radial velocities) issuing from this zone (Fig. 4.7) are

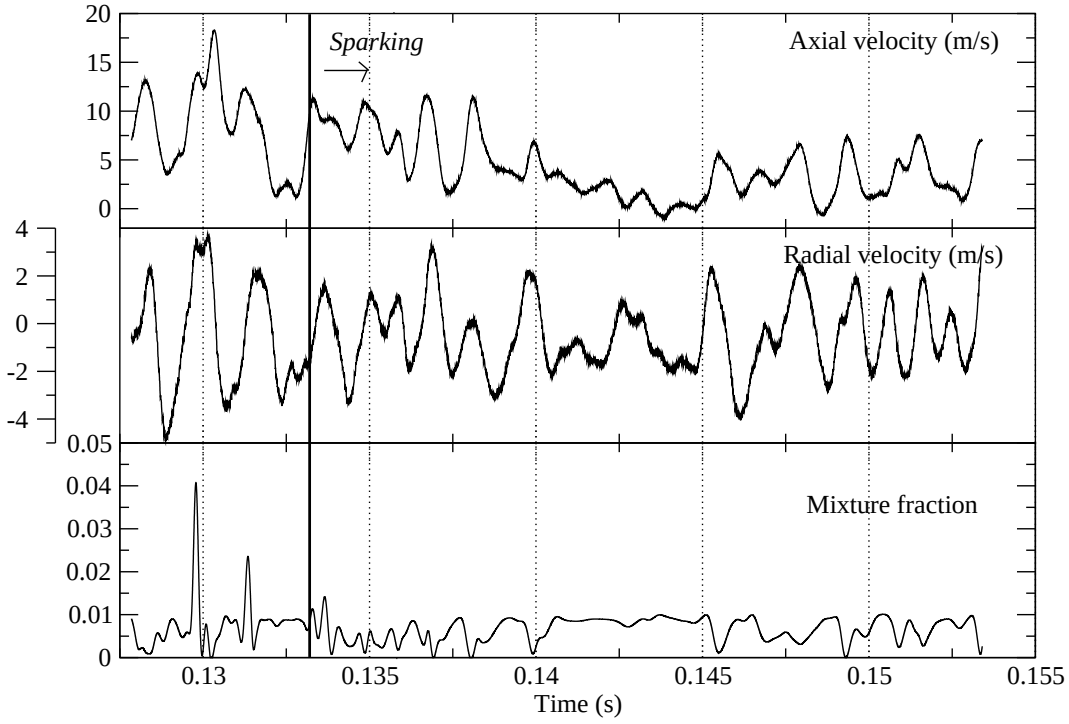

Figure 5.14: Time history of velocities and Mixture fraction at spot D (z = 15 mm, r = 17 mm).

bent toward the CRZ and the stoichiometric line. This indicates that the energy deposited there, has a great probability to enter a near to stoichiometry zone and then to get trapped into the CRZ, once the flame kernel has begun to grow. On the opposite, spark deposits inside the zone delimited by the stoichiometric surface have a lesser probability to ignite the burner, since the energy will be directly sent in a rich mixture environment without encountering very favourable stoichiometric mixtures on their trajectory.

Spot D (z = 15 mm, r = 17 mm) is one point with zero flammability and a non-zero probability of full burner ignition. Figure 5.14 shows the velocity and mixture fraction history of this ignition spot. The mean axial velocity features a positive value, which sometimes spikes to very high levels, as one is looking here at the outer shear layer of the annular jet. The mean radial velocity is almost zero, with considerable fluctuations due to the flapping associated with the flow instabilities developing at the shear layer of the jet. The mixture fraction is very small, with a mean value of about 0.0067 (Table. 5.1), which is far away from the lean flammability limit, and thus the flammability factor is nearly null (0.3 %) at this location. Nevertheless, the probability of getting a fully established flame, or a successful flame initiation, is around 70% in the experiment.

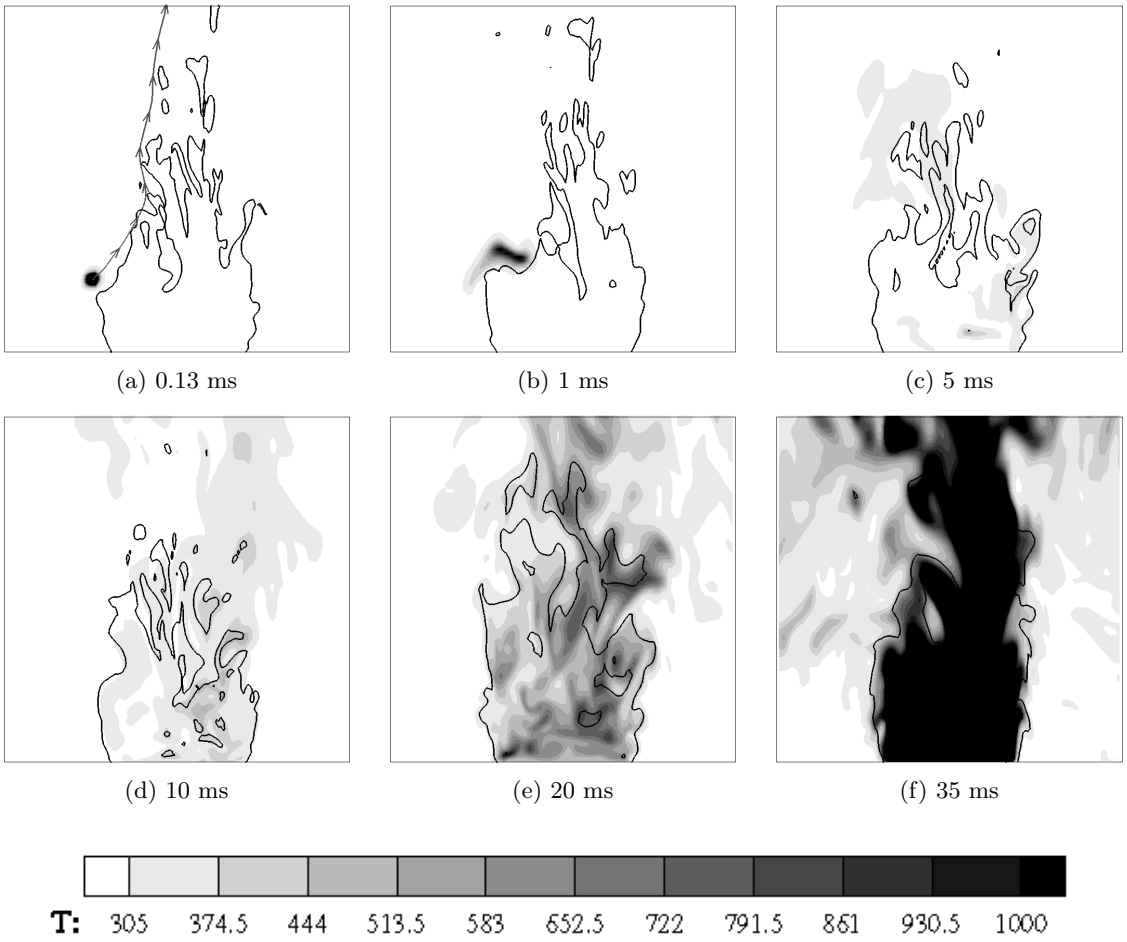

Figure 5.15: LES resolved instantaneous snapshots of temperature after sparking at spot D (z = 15 mm, r = 17 mm). Sparkng time = 0.1330 s. Solid black line: Iso-line of stoichiometric mixture fraction. Image shows the domain dimension of 70 x 70 mm, in caption the relative time after the ignition event.

5.7.1 Successful ignition

The evolution of the ignition kernel at a typical time instance (t_s = 0.133 s) has been investigated with LES. The time averaged velocities and mixture fraction over the spark duration (Table 5.2) shows that the axial velocity is high (10.26 m/s in average) and that the radial velocity is very small on average (0.06 m/s), while the mixture fraction remains well below flammability limit. In Fig. 5.15, it is observed that the streamline based on LES resolved instantaneous axial and radial velocities, 0.14 ms after spark, is oriented toward the stoichiometric region. Though the kernel at t = 0.13 s is still spherical, the strong axial transport has already started convecting the deposited energy. After 1 ms, the kernel has moved axially of about 3 to 5 mm and has grown bigger due to axial convection as well as diffusion. The radial velocity in this region is negative, towards the burner axis, and thus the kernel can ignite a substantial portion of the isostoichiometric mixture fraction surface. At further time instants, the

flame propagates rapidly following the stoichiometric mixture fraction surface and a portion of it gets trapped inside the CRZ. Further development of the flame is similar to the development discussed for successful ignition case at the spot A ($z = 20$ mm, $r = 15$ mm) after 10 ms (in Fig. 5.5); however, there is a key difference on the role played by the transport effect between these locations. In the spot A, as the flammability factor is non zero, the spark can locally initiate combustion, which is then further promoted by convection. Whereas, in the present spot D ($z = 15$ mm, $r = 17$ mm), the spark does not find immediately ignitable mixture, as the flammability factor is zero between the electrodes. The spark energy has first to be carried by the flow toward the iso-stoichiometric surface to lighten the burner, this obviously delays the total time needed to get a fully establish flame for this ignition spot, when compared to point A.

At the instant which has been probed, the axial velocity averaged over the spark time is twice its converged time averaged value; the averaged radial velocity over the spark time is slightly positive, while the converged one is negative. The time instant tested therefore presents conditions less favourable to a successful ignition than other time instants. This is clearly shown in Fig. 5.14, where instants figuring a quite low axial velocity and a negative radial velocity are much more probable. In consequence, if a spark at $t_s = 0.133$ s has been able to ignite the whole burner despite high axial velocity and vanishing radial one, at most other time instants having better velocity conditions, sparking will lead to a successful ignition and it is indeed what is observed in the experiment (70% probability of success).

Combustion also affects the geometry of the backflow region. The volumetric expansion caused by the chemical heat release causes an increase in the recirculation zone length and crossflow area, hence the residence time is further increased and the mass and heat transfer across the shear layer are reduced due to the heat release effects (reduced density and turbulent intensity). Fig. 5.16 depicts this effect; showing the ratio of eddy viscosity to laminar viscosity ratio variation during ignition event. Right after sparking, the local gas viscosity increases by several folds, which is clearly visible at 0.13 ms after sparking. The inner and outer shear layers are clearly visible at this time instance at the lip of the bluff body. The instantaneous shape of the CRZ can be noticed from the iso-line of zero axial velocity, and the CRZ contains strong shear layers arising due to the interaction of vortex bubbles. In the subsequent time instants, the flame starts spreading inside the CRZ and increases the temperature inside the CRZ and thus viscosity and thus wipes out the turbulence inside the CRZ. Once the flame is established, the CRZ contains hot burnt products and the size of the CRZ become big, as seen in Fig. 5.16 at 35 ms.

5.8 Other locations

Others characteristic sparking regions inside the CRZ ($z < 10$ mm) have been simulated; in these locations, the equivalence ratio is quite rich (around $Z = 0.08$ for equivalence ratio 1.6), the axial velocity is negative and the turbulence level is high. Sparking close to the wall, as in the experiment, the ignition probability is close to zero in LES; the initiated kernel has a slow development due to the rich mixture, it is easily torn and scattered by turbulence and quickly transported toward the bluff body, which is a cold boundary condition that quenches the flame.

Sparking within CZR, but not close to wall, simulations lead to ignition for most of the

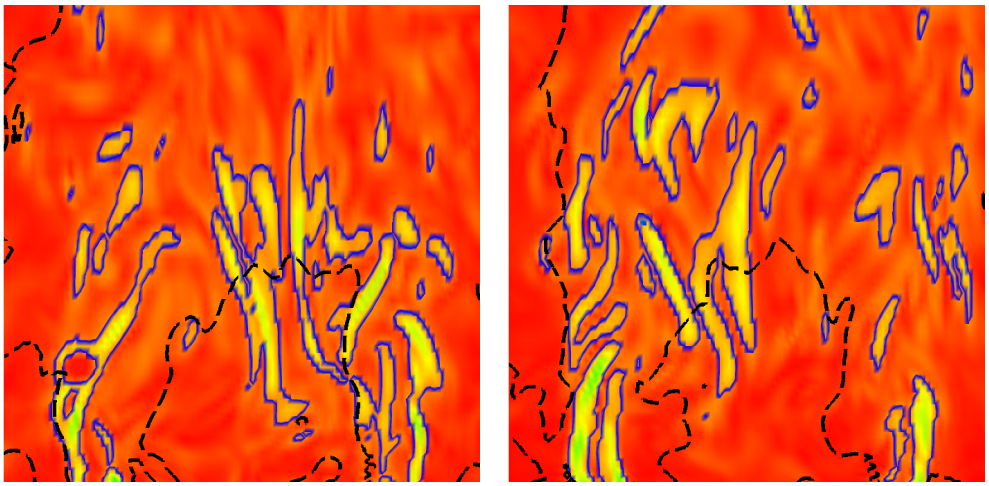

(a) 0.13 ms (b) 10 ms

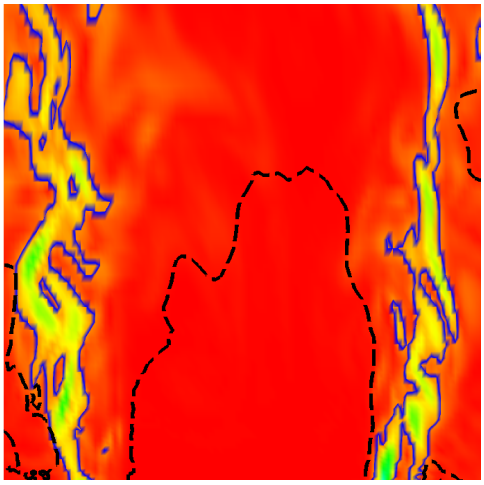

(c) 35 ms

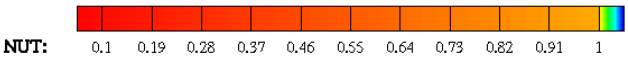

Figure 5.16: Snapshots of ratio of eddy viscosity to laminar viscosity after sparking at spot D (z = 15 mm, r = 17 mm). Sparking time = 0.1330 s. Dashed black line: Iso-line of zero axial velocity. Image shows the domain dimension of 50 x 50 mm, in caption the relative time after the ignition event.

locations, a result in contradiction with experiment. From the measurements, it was concluded that the high level of turbulence and the closeness to the rich flammability limit provides an hostile environment for the flame kernel, which becomes then very sensitive to stretch. This latter ingredient was not explicitly included in simulations discussed so far. This point will be discussed in more detail in the following chapter where the impact of the stretch rate correction in the modeling is presented.

5.9 Summary of hot flow results

Forced ignition was verified in selected ignition spots featuring different flow and mixing patterns. The results here can be compared against the results presented in [4]. Although, strict comparison between the instantaneous snapshots of experiments and simulation cannot be done, the global kernel development can be verified from the simulation results. The time varying flow field is demonstrated to play a significant role in determining the success of ignition, with a same spot being successful ignition spot in certain time instants and become unsuccessful in others. The information from flammability factor is clearly not sufficient in such kind of burners which exhibits a highly transient flow and mixing field with a recirculating wake zone. For the ignition to be successful, the spark should be introduced in a stoichiometric mixture region where the local axial convection is not too strong. Also the preferable ignition spot should be axially located before the rearward stagnation point, as the flow ahead of this point is positive in all radial location and so will convect away the spark kernel. This could enable the spark kernel to get into the recirculation zone during the development and experience a flow reversal and further develop and lighten the burner.

The cold flow analysis needed to be done with actual air and fuel inlet conditions rather than mocked inlet condition. Because, the central recirculation zone (CRZ) is quite sensitive to inlet condition and any change in the fuel or air flow rate could possibly alter the location of rearward stagnation point. To establish a clear relation between the ignition probability and the flow/mixing conditions, it is imperative to have a better representative flow and mixing field data.

Sparking within CZR, but not close to wall, simulations lead to ignition for most of the locations, a result in contradiction with experiment. The velocity field always play a positive role within the CRZ. The high flammability factor always favours a successful initiation of kernel, which developes and lighten the burner. However, in experiments, the kernel was observed to quench at many occasion leading to low probability of ignition (for both successful flame initiation and burner lightening). From the measurements, it was concluded that the high level of turbulence and the closeness to the rich flammability limit provides an hostile environment for the flame kernel, which becomes then very sensitive to stretch. This latter ingredient is not explicitly included in conventional PCM-FPI tabulation method discussed so far, which is built with unstrained laminar flamelets.

CHAPTER 6

Accounting strain effects in PCM-FPI method

Contents

This chapter is devoted to the development of new model to account for strain rate effects on developing ignition kernel. A general introduction is first given on the topic of kernel turbulence interaction. The need for including strain is detailed followed by the development of the correction factor proposed to account for strain induced effects in PCM-FPI technique. Simulation results are then presented to demonstrate the impact of the new correction factor and compared against the results of conventional PCM-FPI method. Finally, a fine LES computation results are presented to analyse the mesh dependency of the results presented so far.

6.1 Background

The conventional PCM-FPI method is observed to predict the development of ignition kernel in the zone in and around CRZ. The trajectory of developing flame kernel dictated by the local transient flow and mixing field are well captured by the conventional tabulation technique and compared with the parallel observation made in experiment. The difference between the probability maps (for obtaining a successful local ignition and for complete burner lightening) and inference from the flammability factor on bluff-body burner ignition were analysed in detail. Aside from obvious equivalence ratio considerations, the local velocity field is found to be the major determining factor for the fate of the ignition kernel; by either successfully igniting the burner or getting blown out. Two main types of failures are reported in the experiments.

- Kernel blow-out due to flow advection. This happens while introducing spark in a region where local instantaneous axial velocity is strong. Strong convection enhances the heat transfer to the spark plug electrodes and reduces the energy transfer to gases during the sparking process. After energy deposition, the kernel, although it was growing in size, gets advected by the flow and thus fails to lighten the burner. This is a commonly reported failure in the core jet region.

- Kernel quenching due to intense turbulence. This happens when the spark is introduced in a region where the local turbulence is strong, for instance in the central recirculation zone. This failure is a function of local mixture fraction, as the kernel response to local turbulence in dictated by the local burning velocity of the mixture. Here the kernel never grows in its size and exhibits serious shrinkage following spark and subsequently disappears.

The conventional PCM-FPI tabulation technique is first tried in this simulation to reproduce the experimentally observed kernel failure/success. The success and failure due to flow and mixing instabilities are fairly well reproduced, tested around the zone covering the central recirculation zone. Nevertheless, the CRZ remained as a challenge for this method. Inside the CRZ, as seen in mixing field data, the mixture is well within the flammability limits, though it is close to rich flammability limit. The flammability maps shown in Experiment (Fig. 22 (c) of [4]) and in the simulation (Fig. 4.19) verify a peak flammability factor of around 90% inside the CRZ. The velocity field in central recirculating wake region is always supportive for kernel development, with a negative axial velocity. One would clearly expect, the central recirculation zone to be the ideal ignition spot for obtaining successful ignition based on the velocity and mixing field. However, interestingly, in Ahmed's experiment, it is found that the CRZ is a zone with less probability of ignition. Both the probabilities, i.e. the probability of successful kernel initiation as well as complete burner ignition (Fig. 22(a) and (b) of [4]) are the same[1] and between 10 to 20%. The reason attributed to this behaviour, according to Ahmed *et al* [4] is the kernel quenching due to the intense turbulence prevailing inside the CRZ. The rich mixture trapped inside the CRZ features a weak laminar burning velocity and would be more sensitive to the turbulent flow field and thus can be easily quenched when exposed to strong velocity fluctuations.

[1] This is again due to the positive role of convection, which is always negative and thus toward the bluff-body. So, the successful kernel initiation would always end up in complete burner ignition without kernel blow-out.

This kernel quenching behaviour is not observed in simulations while using classical PCM-FPI closure. As the main ingredient for capturing this phenomenon is the flame stretch, which is completely missing in the chemistry tabulation. The central assumption on the FPI method is the consideration of flamelets to be laminar and unstrained. Thus the ignition characteristics obtained with this method within the central recirculation zone show a departure from experimental observation, mainly because the effect of aerodynamic strain is completely neglected in chemistry tabulation. The failure due to strong aerodynamic strain are thus, not reproducible in simulation, which is a limitation of the classical PCM-FPI method.

6.2 Literature on flame turbulence interaction

The concept of flame stretch was first introduced by Karlovitz *et al* in 1951 [82] with their studies related to extinction of turbulent flames. The work of Markstein during 1964 [104] shed more light on response of turbulent flames to flame stretching and flame stabilization. After these pioneering works on stretched flame propagation, plenty of studies were carried out in late 1980s and 90s [1, 2, 31].

It was Williams [170] who first proposed a generalised definition for flame stretch, which is even popularly used these days. It reads:

$$\text{Flame stretch} = K = \frac{1}{A}\frac{dA}{dt} \tag{6.1}$$

Where the flame stretch is defined as the fractional change of the flame surface area (A) to it's original surface area. The inherent assumption here is that the flame is infinitesimally thin and considered to be a material surface, which can be elongated or compressed. Later, De Goey *et al* [37] have extended this formulation for a modified definition based on mass, which is more rigourous and can even be suited for thick flames. Accordingly, the stretch is defined as the fractional change of elemental flame mass to the original mass.

$$K = \frac{1}{m}\frac{dm}{dt} \tag{6.2}$$

The Karlovitz number Ka introduced in chapter 2 is also sometimes referred as non-dimensional stretch and can be written as

$$Ka = \frac{K}{S_L/\delta_L} \tag{6.3}$$

The definitions given here and in Eq. (2.8) are, in principle, the same. The implication here is that the flame stretch can also be regarded as the inverse of the flow time scale. The sensitivity of the flame to stretch is quantified using another non-dimensional number called Markstein number Ma. It is defined as

$$Ma = \frac{\mathcal{L}}{\delta_L} \tag{6.4}$$

Where $\mathcal{L}$ is called Markstein length, which is function of Lewis number (Le) of the mixture.

6.2.1 Asymptotic theory of stretched flame

The important quantity of interest in the turbulent strained flame is the turbulent burning velocity (or turbulent burning rate), which is a function of Karlovitz number and Markstein

number. Asymptotic analysis [33] of stretched flame formulated a relation between the unstretched burning velocity and the stretched burning velocity, which reads,

$$S_L = S_L^0(1 - KaMa) \tag{6.5}$$

where S_L is the stretched burning velocity and S_L^0 is the unstretched burning velocity. This linear relation was verified through numerical analysis [19, 20, 27] as well as experiments[74, 145].

In general, the turbulent eddies influence the flame in two ways, which are contradictory to each other. They are:

- The turbulent eddies wrinkle the flame front and increases the surface area of the flame. This results in increased consumption rate of reactions and thus, the turbulent burning velocity increases.
- On contrary to the first effect, the turbulent eddies also disturbs the preflame zone (and even the reaction zone, if the turbulence is intense) and thus reduces the reaction rate so does the turbulent burning velocity.

The first effect will be normally present in the flow field when the turbulent length scale is bigger than flame thickness, *i.e.* when the Re is low. The second effect becomes dominant when the scales of the turbulent flow field are comparable with flame length scale. This effect is dominating with high flow Re and ultimately could lead to flame quenching if the turbulence increases beyond the quenching limit[2].

6.2.2 Turbulent burning rate

It was the first experimental finding reported by Abdel Gayed and Bradley [1, 2] regarding the quenching of turbulent propagating premixed flame due to flame straining effects. They observed the *bending effect*[3] of turbulent burning velocity with increasing turbulence. Based on their experimental results, they come-up with a set of empirical relations for quenching of turbulent flames in two different turbulent Re regime.

$$\frac{u'}{u_l} \geq 0.71 R_L^{0.5} \quad \text{for} \quad R_L < 300 \tag{6.6}$$

$$\frac{u'}{u_l} \geq 3.1 \left(\frac{R_L}{Le^2}\right)^{0.25} \quad \text{for} \quad R_L > 300 \tag{6.7}$$

where u' is the RMS fluctuation, u_l is the laminar burning speed, R_L is the turbulent Reynolds number based on based on u' and integral length scale, Le is the Lewis number.

[2] In turbulent flame terminology, the quenching limit would be normally expressed in terms of scalar dissipation rate; for premixed flame it is the scalar dissipation rate of progress variable (χ_{Y_c}) and for non-premixed flame it is the scalar dissipation rate of mixture fraction (χ_Z). In premixed flame context, it is sometimes even expressed in-terms of strain rate called as "quenching limit strain rate (a_q)". Note that all these terms have the dimension $1/s$, which is the dimension of the stretch.

[3] The ratio of turbulent burning velocity to laminar burning velocity variation with increasing Re exhibited a quasi-linear increase for low Re, and then decrease in high Re, which further resulted in flame quenching. This effect is popularly known as bending effect of turbulent flames.

Bradley *et al* [20] formulated a relation for mean volumetric heat release rate source term of strained laminar premixed flamelets, which, in RANS context reads as below:

$$\overline{q}_t = \int_{-\infty}^{\infty} \int_0^1 \int_0^1 q_l(c, Z, K) p(c, Z, K) dc \; dZ \; dK \tag{6.8}$$

Where, q_l is the strained laminar heat release source term, c is the reaction progress variable, Z is the mixture fraction and K is the stretch. The PDF $p(c, Z, K)$ is the joint probability density function of c, Z and K.

6.2.3 Distribution of tangential strain and curvature

Stretch defined by Eq. (6.1) can be decomposed into tangential strain and curvature term [24]. Both the terms can take values varying from positive to negative depending on the local turbulence field. Jenkins *et al* [79] studied the effect of contributions of stretch terms on the propagation of spherical flame kernel in the thin-rection zone regime using single step DNS calculations. They found that the tangential strain rate PDF shows a probability of finding positive strain rate that is much higher than negative strain rate, thus the mean tangential strain being positive.

Chen *et al* [27] performed two dimensional DNS of lean turbulent premixed methane/air flame. They analysed the contribution of curvature and aerodynamic strain on total stretch. One interesting observation from this study is that the linear relation derived for stretched burning rate is an excellent approximation for even for large Ka i.e. $Ka \sim \mathcal{O}(1)$, although the relation was formally derived for $Ka \ll 1$. Moreover, for given turbulence parameters, over a statistically relevant stretch range, the response of flame to tangential stretch rate is much larger than the curvature.

Bradley developed a relation to express the averaged stretched burning rate in-terms of unstretched burning rate and PDF of stretch [22]. Bradley pointed out the uncertainty associated effect of negative stretch on turbulent burning velocity. He analyzed the influence of curvature and flame straining effects on turbulent burning velocity and found that the contribution of former surpasses the later, especially in a non-local sense. This is due to the fact that the effect of positive and negative value of curvature tends to cancel each other, and thus the mean burning rate is insensitive to curvature contribution.

Hag *et al* [74] also reinforced this fact through their experimental study and concluded that the PDF of curvature exhibited a Gaussian distribution around the mean, especially when the turbulence was strong. They too found that the curvature has significant influence on local flame structure; however the global parameters are not influenced by curvature mainly due to the symmetrical distribution of curvature PDF.

Meneveau and Poinsot [108] performed a DNS study flame-vortex interaction and quenching of flamelets by a pair of eddies. They proposed a model called intermittent turbulent net flame stretch (INTFS) model, which incorporates the effect of stretch intermittence, viscous, transient and curvature effects. They concluded that the Klimov-William criterion exaggerates the effect of flame stretch, thus, the validity of flamelet regime in Borghi diagram even extends beyond the limit defined by $Ka \leq 1$. The results also indicated that the large eddies are more efficient at stretching the flame than small eddies, which is the same conclusion drawn by Filatyev *et al* [59] through their experimental results.

6.2.4 Effect of Lewis number

Hassan *et al* [75] conducted experimental as well as theoretical analysis to find flame/stretch interactions of laminar premixed methane/air flames and to analyse the effect of preferential diffusion. The measurements and predictions indicated that the methane air flames are generally stable with respect to preferential-diffusion effects, at-least at low pressure range. However, at high pressure of 4 bar, the flames exhibited diffusional instability. The Lewis number effects of premixed stretched flames are experimentally studied by Lee *et al* [92] for hydrogen/air, methane/air and propane/air flames. The non-unity *Le* number of hydrogen flames was linked to its strong response to flame curvature, whereas the methane air ($\phi = 0.8$) flame shows very weak response. This study also concluded that the local flame curvature may strongly influence the flame structure of non unity *Le* number flames , however, the mean burning rate is nearly unaltered due to flame curvature.

6.3 Development of new closure for strain correction on rate of kernel development

It was reported in Ahmed's experiments that the ignition kernel could get quenched by local flow fluctuations. Typically, inside the central recirculation zone where the mixture is relatively rich, there exists a considerable difference between the flammability map and the ignition probability map. Inside the CRZ, the axial velocity always plays a positive role by transporting the kernel in the negative axial direction, but still the ignition kernel fails to develop and fully lighten the burner. This peculiar flame behavior, as intermittency in ignition success, was attributed to strain rate effects acting on flame propagation in a fuel rich mixture zone ($Z > 0.08$, equivalence ratio slightly above 1.6), thus for conditions at which flame speed is quite sensitive to burning reduction induced by strain rate. Referring to Figs. 4.11 and 4.12, the velocity fluctuations inside the CRZ are quite intense. The premixed flame propagation speed in the rich mixture prevailing inside the CRZ, is several times smaller than the stoichiometric mixture, making the kernel more sensitive to the local turbulence, which can eventually quench the small burning zone, as attributed by the experimental findings. For example, referring Fig. 4.12, the fluctuations (u') at a point inside CRZ ($z = 15.5\ mm,\ r = 0\ mm$) is in the order of 3 m/s. From Fig. 4.15 the mean mixture fraction here is 0.08, for which the laminar burning speed S_L is approximately 0.003 m/s [93]. This corresponds to a u'/S_L ratio of 1000, which is considered to produce a strong straining effect on flame. This required a model to account for flame straining effects in LES, which is done as explained in this section.

In LES, the filtered conditional mean is given as:

$$\left(\overline{\varphi \mid Z^*;\underline{x},t}\right) = \int_0^1 \int_{K-}^{K+} \varphi^{FPI}(Z^*,c^*,K^*)\overline{P}(c^*;\underline{x},t)\overline{P}(K^*;\underline{x},t)\,dc^*dK^* \tag{6.9}$$

where, φ^{FPI} is a scalar or a source term arising from the flamelets calculations and $\overline{P}(c^*;\underline{x},t)$ is the filtered probability density function of normalised progress of reaction, which is also presumed to follow a Beta distribution. $\overline{P}(K^*;\underline{x},t)$ is the flame stretch pdf [19, 20, 23] whose statistical space covers $[K-,K+]$; in a first analysis c and K can be assumed statistically independent [20].

The stretch here is accounted for in a global manner; the starting point is observations by Bradley *et al.* [20], who have reported that the premixed flame response used to tabulate chemistry, as, $\dot{\omega}_q(Z,c,K)$, the volumetric heat release rate at a stretch rate, K, can be related to $\dot{\omega}_q^o(Z,c)$, the value at zero stretch rate:

$$\dot{\omega}_q(Z,c,K) = f(K)\dot{\omega}_q^o(Z,c) \tag{6.10}$$

where $f(K)$ is a flame stretch factor. A relation that is applied to every equivalence ratio and in the context of Eq. ((6.9)), this would read:

$$\left(\overline{\dot{\omega}_q|Z^*}\right) = \left(\overline{\dot{\omega}_q^o|Z^*}\right) P_b \tag{6.11}$$

with

$$P_b = \int_{K-}^{K+} f(K^*)\overline{P}(K^*;\underline{x},t)dK^* \tag{6.12}$$

A careful analysis of $f(K)$ and of the burning rate factor P_b, is given in [19], where it is shown that it behaves as

$$f(K) = 1 - \sigma K \tag{6.13}$$

where σ combines various flame properties, as the Markstein length, the flame thickness and flame speed. In Reynolds averaging context and assuming a gaussian distribution for $\overline{P}(K^*;\underline{x},t)$, the burning probability factor, P_b, response versus stretch is non-linear [19]. This is transposed to LES with three observations; Direct Numerical Simulation (DNS) have shown that the highest rate of strain and flame curvature result from large eddies [124], which are mostly resolved in LES; second, the zones where flame stretch impacts on ignition probability have been reported in Ahmed *et al.* [3] experiment to be mainly fuel rich, flamelets in the rich zone have low flame speed levels, high sensitivity to stretch and are quenched for much smaller K levels than under stoichiometric conditions; third, laminar flame analysis demonstrates a first order linear flame response of a scaled mass burning rate versus stretch [31, 32]. From these observations, only the first order linear part is kept to correct the flamelet response to LES resolved stretch, $P_b \approx \left(1 - K(\widetilde{Z})\right)$ and Eq. ((6.11)) is cast in:

$$\left(\overline{\dot{\omega}_q|Z^*}\right) = \left(\overline{\dot{\omega}_q^o|Z^*}\right)\left(1 - K(\widetilde{Z})\right) \tag{6.14}$$

to globally correct the conditional burning rate, according to flame response to stretch, with $K(\widetilde{Z})$ remaining to be defined.

The steady premixed laminar flamelets equation may be written:

$$\frac{\partial \rho u \varphi}{\partial \xi} = \frac{\partial}{\partial \xi}\left(\rho D_\varphi \frac{\partial \varphi}{\partial \xi}\right) + \rho\dot{\omega}_\varphi + \rho\dot{S}_{K_\varphi} \tag{6.15}$$

where u is the velocity, D_φ is the diffusion coefficient of φ and $\dot{\omega}_\varphi$ is the chemical source. The coordinate in the direction normal to the flame front is ξ and $\dot{S}_{K_\varphi}$ is a stretch leakage term that cumulates budgets of fluxes occuring along the flame surface, thus representative of transverse convection and diffusion resulting from straining and curvature of the flamelet surface; the case of a freely propagating one-dimensional unstrained premixed corresponds to $\dot{S}_{k_\varphi} = 0$.

Laminar flame analyses [31, 32, 36, 38, 39] have reported that the mass flux burning rate $\rho(\xi_o)u(\xi_o)$, determined at the position ξ_o on the burnt gas side of the flame, where the burning rate is of the order of 10% of its maximum level, relates to the unstretched flame speed $S_L^o(Z)$:

$$\rho(\xi_o, Z)u(\xi_o, Z) = \rho_o(Z)S_L^o(Z)(1 - Ka(Z)) \tag{6.16}$$

with Ka the Karlovitz integral value:

$$Ka(Z) = \frac{1}{\rho_o(Z)S_L^o(Z)} \int_{-\infty}^{+\infty} \rho(Z;\xi)K(Z;\xi)c(Z;\xi)\, d\xi \tag{6.17}$$

where the relation has been generalized to every equivalence ratio (or mixture fraction) within flammability limits. Integrating Eq. ((6.15)) in the direction normal to an unstretched flamelet ($\dot{S}_{k_\varphi} = 0$) and for $\varphi = c$, gives the relation between the unstrained flame speed and the integral of the burning rate through the flame:

$$\rho_o(Z)S_L^o(Z) = \int_{-\infty}^{+\infty} \rho(Z;\xi)\dot{\omega}_c^o(Z;\xi)d\xi = \int_0^1 \rho(Z, c^*)\frac{\dot{\omega}_c^o(Z, c^*)}{|\nabla_\xi c^*|}dc^* \tag{6.18}$$

while it may be written, in the case of stretched flamelet integrated from fresh gases up to ξ_o,

$$\rho(\xi_o, Z)u(\xi_o, Z)c(\xi_o, Z) = \int_{-\infty}^{\xi_o} \rho(Z;\xi)\dot{\omega}_c(Z;\xi)d\xi + \int_{-\infty}^{\xi_o} \rho(Z;\xi)\dot{S}_{K_c}(Z;\xi)d\xi \tag{6.19}$$

Combining relations ((6.16)), ((6.18)) and ((6.19)):

$$\begin{aligned} c(\xi_o, Z)\,(1 - Ka(Z)) \int_{-\infty}^{+\infty} \rho(Z;\xi)\dot{\omega}_c^o(Z,\xi)d\xi \quad - \quad & \int_{-\infty}^{\xi_o} \rho(Z;\xi)\dot{S}_{K_c}(Z;\xi)d\xi = \\ & \int_{-\infty}^{\xi_o} \rho(Z;\xi)\dot{\omega}_c(Z;\xi)d\xi \end{aligned} \tag{6.20}$$

Assuming that ξ_o is close to fully burnt gases and that the $\dot{S}_{K_c}$ integral is not a leading order term in Eq. ((6.20)):

$$\int_{-\infty}^{+\infty} \rho(Z;\xi)\dot{\omega}_c(Z;\xi)d\xi = (1 - Ka(Z)) \int_{-\infty}^{+\infty} \rho(Z;\xi)\dot{\omega}_c^o(Z;\xi)d\xi \tag{6.21}$$

Arguing that flame integrated and filtered burning rates behave similarly versus stretch, this last relation may be written for the energy source:

$$\left(\overline{\dot{\omega}_q|Z^*}\right) = (1 - Ka(Z^*))\left(\overline{\dot{\omega}_q^o|Z^*}\right) \tag{6.22}$$

which is similar to Eq. ((6.14)), but obtained in a slightly different context. Furthermore, assuming that there exists a stretch measure Ψ_K so that

$$\int_{-\infty}^{+\infty} \rho(Z;\xi)K(Z;\xi)c(Z;\xi)\,d\xi = \Psi_K I_c(Z) \tag{6.23}$$

with

$$I_c(Z) = \int_{-\infty}^{+\infty} \rho(Z,\xi)c(Z,\xi)d\xi \tag{6.24}$$

the relations ((6.14)), ((6.17)), ((6.22)) and ((6.23)) lead to:

$$K(\widetilde{Z}) = \frac{I_c(\widetilde{Z})}{\rho_o(\widetilde{Z})S_L(\widetilde{Z})}\Psi_K \tag{6.25}$$

with $I_c(\widetilde{Z})$ computed from the flamelet database. The stretch measure Ψ_K, may then be seen as the resolved part of the normalized time evolution of the flame surface density[4] [125]:

$$\Psi_K = \nabla\cdot\widetilde{\mathbf{u}} - \mathbf{n}n{:}\nabla\widetilde{\mathbf{u}} + S_L\nabla\cdot\mathbf{n} \tag{6.26}$$

with $\mathbf{n} = -\nabla\overline{c}/|\nabla\overline{c}|$, simulations have been performed with and without the curvature term $S_L\nabla\cdot\mathbf{n}$ in Ψ_K, without much net impact on burner ignition probability. Equation ((6.14)) then reads:

$$\left(\overline{\dot{\omega}_q|Z^*}\right) = \left(\overline{\dot{\omega}_q^o|Z^*}\right)\left(1-\zeta(\widetilde{Z})\Psi_K\right) \tag{6.27}$$

with the following options for ζ:

- with $\zeta = 0$, simulations are performed without any attempt to include stretch effects on laminar flamelet speed, as it was done so far in PCM modeling [42, 68];
- with

$$\zeta(\widetilde{Z}) = \frac{I_c(\widetilde{Z})}{\rho_o(\widetilde{Z})S_L(\widetilde{Z})} \tag{6.28}$$

  which is a fixed distribution computed from the flamelet database, simulations are performed including an approximate stretch correction. $\zeta(\widetilde{Z})$ is plotted in Fig. 6.1, its minimum is found close to stoichiometry for slightly rich mixtures, to rapidly increase in both fuel lean and rich sides. For moderate stretch levels, this first order linear attenuation has almost no impact on stoichiometric mixtures, but a non-negligible one for fuel lean and rich conditions; for example at $Z \approx 0.08$, the rich sparking condition considered in the simulations, $\zeta^{-1} = 200$ s^{-1}.

It should be mentioned here that the Lewis number effect has been neglected in this model considering the fact that the methane air mixtures has near unity Lewis number (unless the

[4] In the relations ((6.14)) and ((6.25)), Ψ_K is introduced to include response of local flame speed to stretch only, SGS flame wrinkling effects are accounted for with the presumed pdfs of mixture fraction and progress of reaction in Eqs. ((3.39)) and ((6.9)); leading to different needs compared to SGS models fully relying on flame surface density, where SGS stretch cannot be neglected [134].

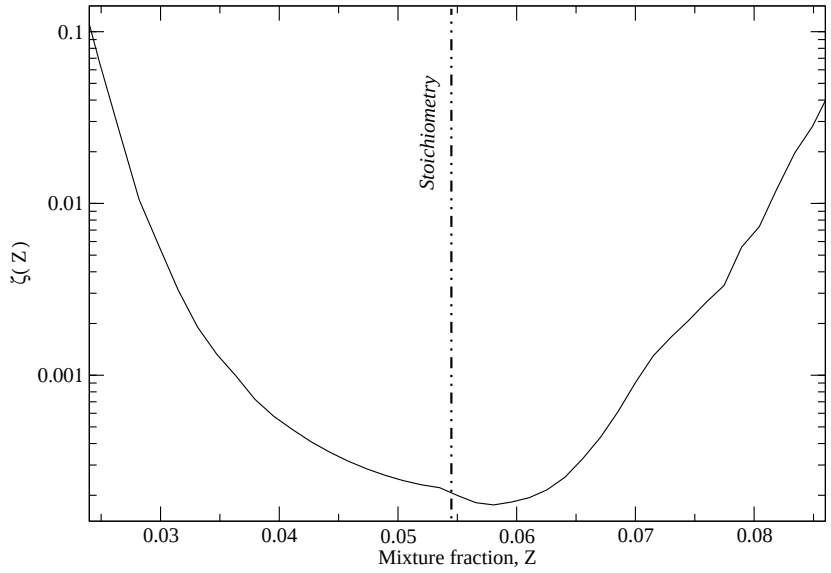

Figure 6.1: $\zeta(Z)$ as defined in Eq. ((6.28)).

mixture is extremely lean). This point also has been discussed by de Goey et al [38], where the effect of preferential diffusion on mass burning rate is negligible for methane air flame ($\phi = 0.8$), due to near unity lewis number of methane air mixtures. There is no adhoc constant or parameter introduced in this stretch correction, since ζ is computed from the flamelet library with Eq. ((6.28)); transposing the detailed analysis by Bradley *et al.* [19], quenching would be assumed when $\Psi_K > \zeta(\widetilde{Z})^{-1}$, it is also postulated that the inherent instability of a flame to negative stretch might cause it to reorient toward positive stretch rate [19]. As expected from experimental results, it is reported that fuel rich flow locations, with high velocity fluctuations, need to be addressed with non-zero ζ to reproduce ignition variability; nevertheless, the stretch correction was not found to modify ignition probability at other locations. In addition, considering a single fuel rich location, the stretch correction does not always prevent ignition at this point, depending on turbulence time history; hence, ensuring that the included strain rate effect does not behave as an artificially high damping of the energy source, that would prevent burner ignition always for rich sparking locations.

6.3.1 Point E: z = 20 mm, r = 0 mm

The first spot (referred here after as point E) selected to analyse the proposed strain correction is located in a region inside the CRZ, where the flammability is high (larger than 85%), the axial velocity is negative and the mixture is quite rich (see Table 5.1). In the experiment, it was found that the ignition probability and the probability of successful flame kernel initiation were identical at this location. In other words, when the sparking results in the generation of

Table 6.1: Ignition spots with velocities and mixture fraction time averaged over the sparking time duration

Ignition spot Index - [z, r]	Burner ignition	Time instant s	U_m^s m/s	R_m^s m/s	Z_m^s
E - [20, 0]	Failed	0.1321	-1.95	3.3	0.081
E - [20, 0]	Success	0.13765	-2.816	-1.09	0.07
D - [15, 17]	Success	0.09379	10.26	0.06	0.008

z: Axial downstream position (mm), r: Radial position (mm), U_m^s: Mean axial velocity, R_m^s: Mean radial velocity, Z_m^s: Mean mixture fraction, upperscript s indicates averaging over the sparking time.

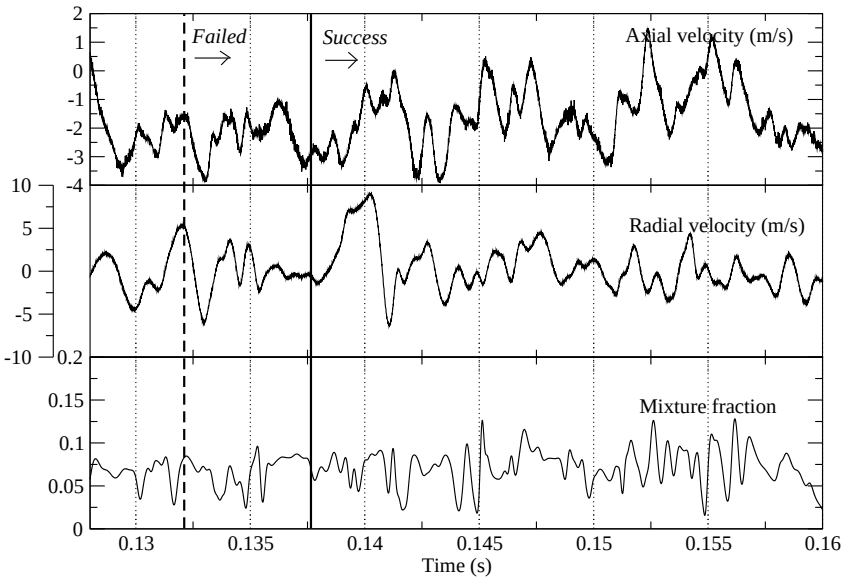

Figure 6.2: Time history of velocities and Mixture fraction at spot E (z = 20 mm, r = 0 mm).

a visible burning region that can survive long enough, then the full ignition turns out to be successful, because the ignition kernel is never convected downstream by the axial component of velocity. In contrary, when the flame kernel is quenched for the same sparking point, it happens at the very first stages of its development, when its diameter is still less than 3 mm [4].

The time history for this ignition spot (Fig. 6.2) confirms that in the LES, the conditions are favourable for ignition and kernel development at most of the time instants. The two time instants analysed in this case are $t_s = 0.1321$ s and $t_s = 0.13765$ s, which resulted in a quenched kernel and a successful ignition, respectively. The velocity and mixture fraction

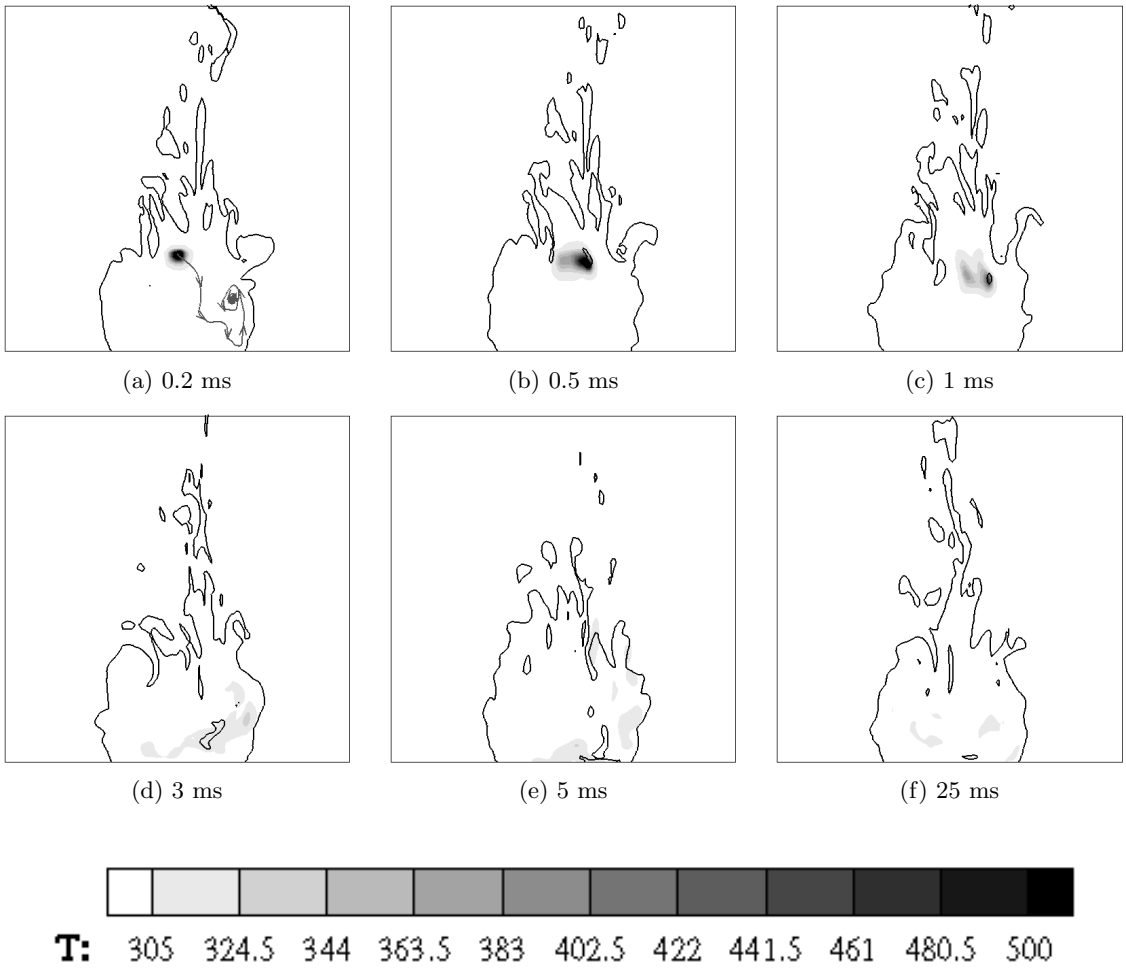

(a) 0.2 ms (b) 0.5 ms (c) 1 ms

(d) 3 ms (e) 5 ms (f) 25 ms

Figure 6.3: LES resolved instantaneous snapshots of temperature after sparking at spot E (z = 20 mm, r = 0 mm), showing kernel quenching. Sparking time = 0.1321 s. Solid black line: Iso-line of stoichiometric mixture fraction. Image shows the domain dimension of 70 x 70 mm. Time is the relative time after the ignition event.

during the spark duration are given in Table 6.1. It is to be noted that the mixture fraction during both of these time instants is relatively rich, even though it is within the flammability limit.

Figure 6.3 shows the evolution of the flame kernel during the unsuccessful time instance, resulting in kernel quenching. The streamline issued from the spark location confirms that the tendency of the kernel will be to travel toward the bluff-body. This is what is observed, the spark develops first into a round kernel (0.2 ms), which gets displaced through the CRZ, where the mixture remains appreciably rich with a mean mixture fraction value of about 0.08. The correction factor, $\zeta(\widetilde{Z})$, applied to the filtered burning rate is quite high for this equivalence ratio (Fig. 6.1). This high value of $\zeta(\widetilde{Z})$ combined with the high stretch rate, Ψ_K, induced by local turbulence, has a negative impact on the kernel development. From Fig. 6.3, it can be observed that at 1 ms after sparking, the kernel has shrunk in its size due to local high

turbulence. After 5 ms, the kernel is quenched with no more sign of positive development. It is to be noted here that the observed displacement of the flame kernel is only due to the flow advection and not due to flame propagation. (The kernel would have disappeared remaining in the same position, if the time averaged velocities would have been zero.)

Figure 6.4 shows the successful evolution of an ignition kernel at the same point E, but at a different time instant as marked in Fig. 6.2. The streamline emanating from the ignition spot is not very different from the previous case, where the kernel got quenched. However, the local mixture fraction during the sparking moment is about 0.07, which is leaner than the previous case; the reduction in burning rate due to flow straining is then 10 times smaller than for $Z = 0.08$ (Fig. 6.1). From Fig. 6.4, after 1 ms, the spark kernel appears much bigger, although the local strain rate correction is still applied to the source terms (Eq. ((6.22))).

The experimental reporting are thus reproduced, where the kernel exhibits a serious reduction in size after 1 ms, in the cases where quenching is observed. In the experiment, for the successful test cases, after 1 ms, the kernel size remains either the same, or sometimes slightly bigger (Fig. 23 of [4]). The same behaviour is observed in this LES in Figs. 6.3 and 6.4. The further global evolution of the kernel for the successful time instance is very similar to what is obtained at point C, because the convective field in the CRZ is similar; though, there is a definite reduction of the rate of the kernel growth due to the introduction of the strain correction, which increases the time taken by the kernel to fully lighten the burner.

To quantify the complete flame establishment duration, the time evolution of the volume averaged source term of energy is introduced. This quantity is displayed in Fig. 6.5 for point E. For the successful case, the volume averaged source term shows a linear and slow growth until 25 ms. Between 20 and 30 ms, strong reaction zones are visible near the iso-stoichiometric surface (Fig. 6.4), which eventually accelerates the burning. Meanwhile, the temperature inside the CRZ increases, viscosity also increases and thus damps the fluctuations, thereby accelerating the burning rate. Between 25 to 50 ms, the burning rate shows a steep increase due to the tangential flame spreading through the stoichiometric mixture, noticed by the stiff slope of the evolution of total energy source term, as seen in Fig. 6.5. The kernel evolution observed in this case closely matches with the experimental finding in a spot inside the CRZ (Fig. 15 of [4]). The time taken for complete lightening of the burner for this case was found to be around 50 ms, in close agreement with the experiment. Fig. 6.5 also shows the source term evolution of the quenched case at this same ignition spot, due to local flow straining. The very quick disappearance of the flame kernel is clearly observed, only the peak corresponding to the energy deposited by the spark is visible. The volume averaged source term of energy is also plotted for a spark at the same instant ($t_s = 0.1321$ s), when the original PCM-FPI approach is employed without accounting for stretch correction. It is observed (Fig. 6.5 bottom) that a full lightening of the burner is obtained with this closure. More, in the simulations featuring the original approach ($\zeta = 0$ in Eq. (6.27)), it has proved impossible to obtain a quenched kernel at Point E, whatever the time instant tested and the corresponding local conditions.

6.3.2 Strain rate effects on flame establishment time

According to results discussed above, the stretch rate correction (Eq. ((6.22))) captures the reduction in the flame kernel development and the variability of ignition, as it was shown for point E, where both ignition or quenching can be found with this correction. It has also been verified on all previously tested points (A to D) and sparking time instants, that the success

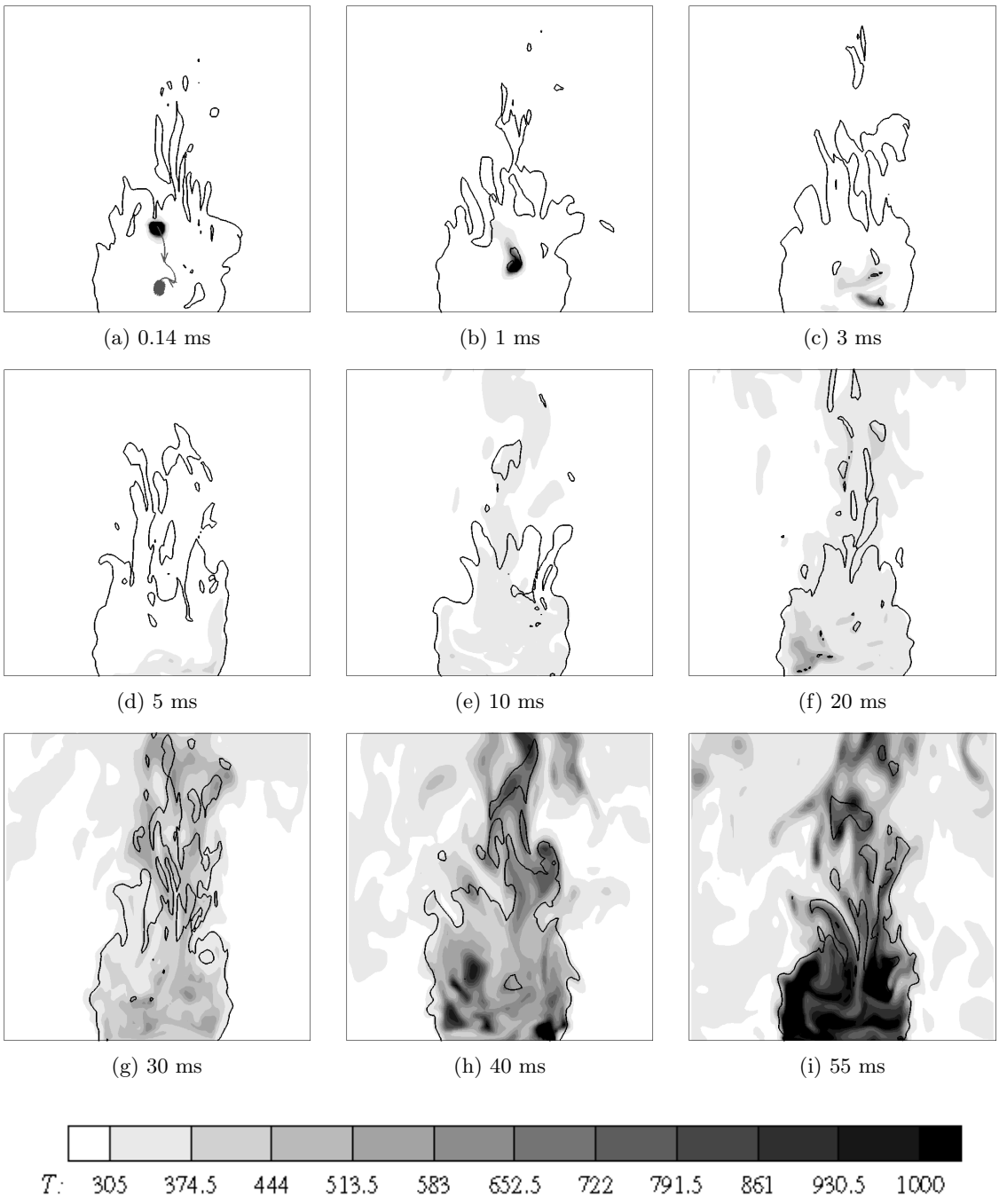

(a) 0.14 ms (b) 1 ms (c) 3 ms

(d) 5 ms (e) 10 ms (f) 20 ms

(g) 30 ms (h) 40 ms (i) 55 ms

Figure 6.4: LES resolved instantaneous snapshots of temperature after sparking at spot E (z = 20 mm, r = 0 mm), showing positive kernel development. Sparking time = 0.13765 s. Solid black line: Iso-line of stoichiometric mixture fraction. Image shows the domain dimension of 70 x 70 mm, in caption the relative time after the ignition event.

or failure of the spark to ignite the burner is not affected by the improved model. This is

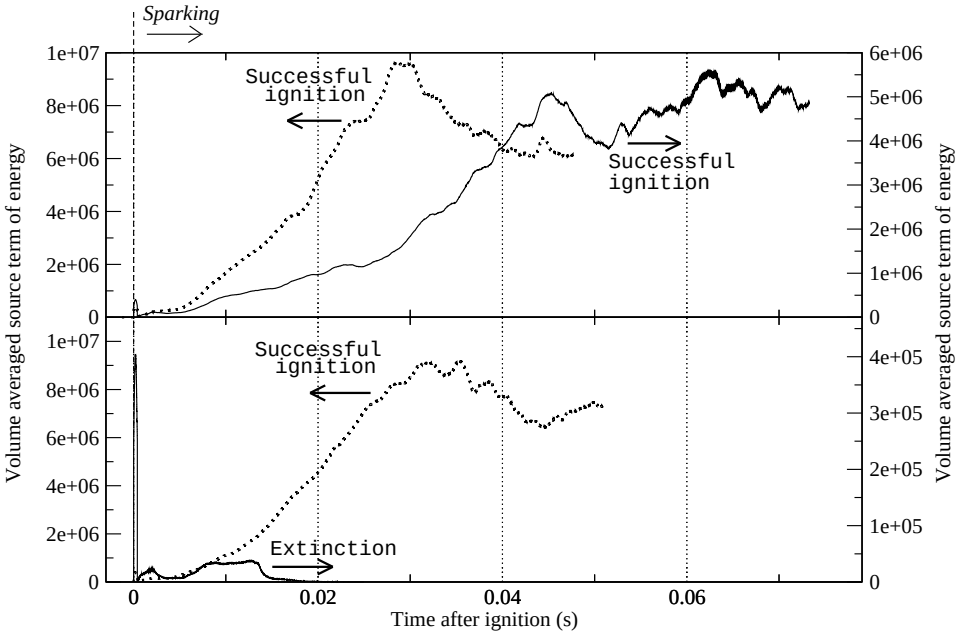

Figure 6.5: Time evolution of volume averaged energy source term for both successful and unsuccessful case for spot E (z = 20 mm, r = 0 mm). Time shows the relative time after sparking instance. Black dotted line: Conventional PCM-FPI closure without accounting for flow straining effects, Black solid line: New closure for accounting flow straining effects.

expected since the correction brought by Eq. ((6.22)) stays negligible for flame development arising mostly over stoichiometric mixture.

In some cases, there is a non negligible difference in the rate of flame kernel development, between the simulations with and without flow straining effects. To illustrate the reduction in burning rate, two simulations with $\zeta = 0$ (no stretch effect) and non-zero ζ (stretch as given by Eq. ((6.22))) are performed from the same initial conditions for the ignition spots D ($z =$ 15 mm, $r = 17$ mm) and E ($z = 20$ mm, $r = 0$ mm) at time instants where ignition is successful for both approaches. The time evolution of the integrated energy source term is displayed in Fig. 6.6 at point D, starting from the sparking instant. Without accounting for strain, intense burning starts rapidly after the spark, the total establishment time is about 30 to 40 ms. Accounting for flow straining effects, the flame establishment duration is between 55 to 70 ms. This difference predominantly arises from the initial part of the kernel development period, which is much slower in the case accounting for strain effects, the reduction in burning rate attributed to the flow straining is thus dominant for young flame kernel. A similar lengthening of the flame establishment time is observed for point E in Fig. 6.5 top. This is the reason why the kernels are often quenched when the sparking is inside the CRZ (for instance point E discussed before), since at this location, they face high turbulence levels while being of small size. A parallel can be made with experimental observations, which concluded that a young kernel is more prone to quench compared to a developed one, for the same turbulence intensity [105]. Therefore, if an ignition kernel can sufficiently grow before being inducted into highly strained and rich mixtures within the CRZ, it is not quenched. This has been observed for spot ignition D, when the kernel has grown substantially by spreading through

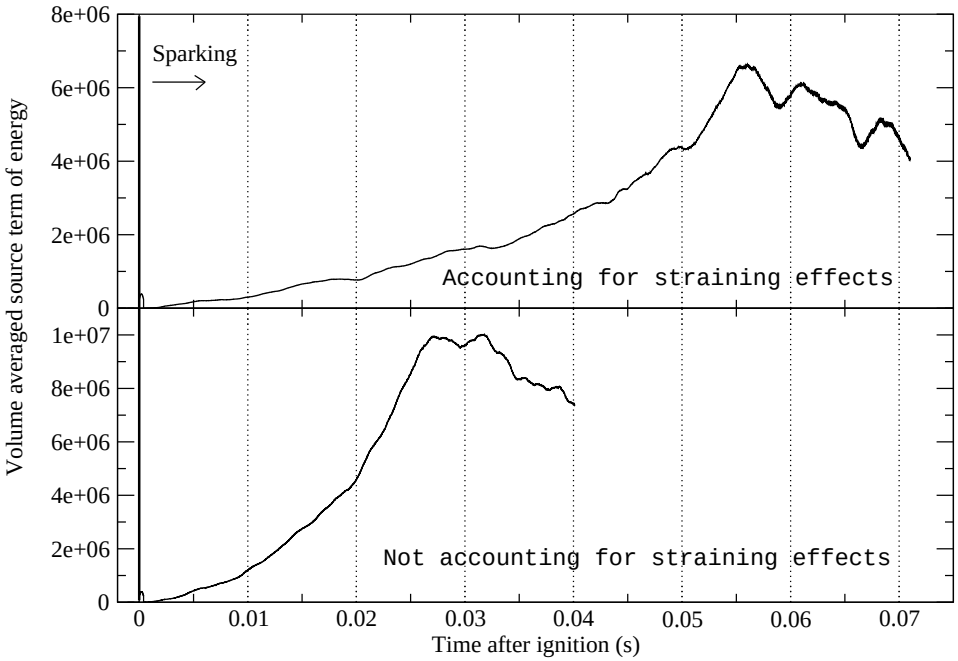

Figure 6.6: Time evolution of volume averaged source term with and without accounting for flow straining effects. The ignition spot D (z = 15 mm, r = 17 mm) is located on iso stoichiometric surface. Time is the relative time after sparking instance

the stoichiometric surface, before entering the recirculation zone to promote full ignition of the burner.

6.4 Fine LES calculation and mesh dependency study

No complete conclusion can be drawn based on numerical simulation without analyzing the mesh dependency of the results. Ignoring the mesh dependency could often result in embarrassment in modeling business. The choice of computational grid, and thus mesh size is normally dictated by the available computational resources. Minimum number of grid points are usually preferred, especially when the computation power is limited. In such situation, the results exhibits strong mesh dependency, which is inevitable. In simulation, models used for representing the physical process involved is developed based on specific circumstances, by invoking certain hypotheses and assumptions. For instance, in LES, the sub-grid scale models are developed based on the assumptions that the filter size[5] falls in the inertial scale range of turbulent spectrum. In implicit LES, if very coarse mesh is used, then this condition is clearly violated leading to unphysical results. Thus, it is imperative to perform a quality cross check on computational results to make sure that the results are untainted. The accepted convention to check the mesh dependence of numerical results is through performing simulations with successively increased mesh resolution (by often halving the mesh size) and see the convergence of the results.

[5]It should be recalled that in implicit LES, the grid functions as a filter.

A more refined LES computation is performed to verify the quality of the LES results presented so far. The number of grid points used are augmented from $90 \times 140 \times 140$ to $130 \times 200 \times 200$, thus the total number of finite volume cells are increased from 1.76 millions to 5.2 millions, thus increasing the computational overhead by nearly 3 times. The typical mesh size of fine the LES grid is around 0.35 mm. The cold flow fields mean flow and mixing fields are compared to see the effect of mesh resolution and it's impact. The cold flow comparison shown here are done with both air and fuel injection, in both LES cases. The experimental velocity profiles are also plotted here for reference purpose, and care should be taken while comparing the experimental velocity profiles with the LES results. It can be recalled that the experimental velocity measurements are done with only air injection. Quantitative comparison between hot flow results are not possible between instantaneous field of two LES computations. Care should be taken while interpreting the results of reactive flow LES cases presented below. In the following discussions, coarse mesh results refer to the LES results done with 1.76 M grids and fine mesh results refers to 5.2 M grids LES results.

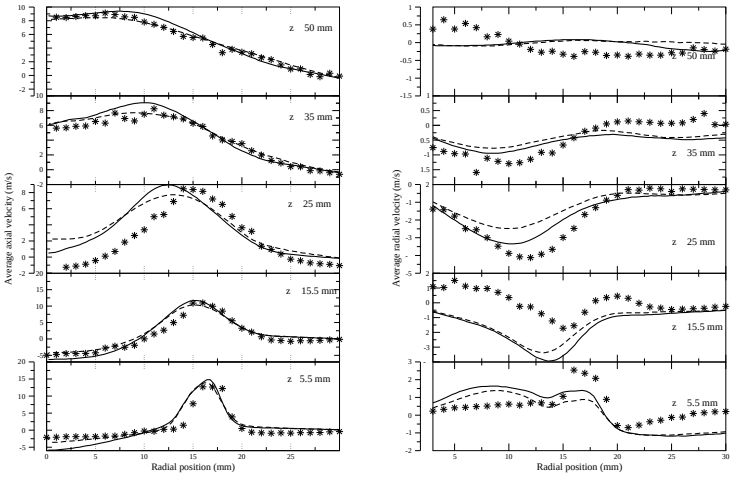

(a) Axial velocity (b) Radial velocity

Figure 6.7: Radial profiles of time averaged velocities at different streamwise locations. Symbol: Measurements. Dashed line: LES with coarse mesh (1.76M grids). Solid line: LES with fine mesh (5.2M grids).

The results of coarse mesh and fine mesh on mean average axial and radial velocity can be seen in Fig. 6.7a and 6.7b. At 5.5 mm downstream side, the fine slightly overpredicts the negative axial velocity. This could be due to the fact the this axial position is close to the inlet where wall boundary condition are imposed (i. e. at the bluff-body), and the mesh resolution near the wall has a direct impact on the velocity fields. At large radius, these difference completely vanishes away and both LES results are very close to eachother. It can be noted that even coarse LES results quantitatively differ from the measurements at the CRZ (i. e. at z = 25 mm), where the coarse LES also exhibited the same order of difference. In further downstream region, the radial trends of two LES show close agreement. Similar observation can be made from mean radial velocity, which show more or less the trend in all axial locations.

The results of RMS fluctuations can be seen in Fig. 6.8a and 6.8b. The double peak in

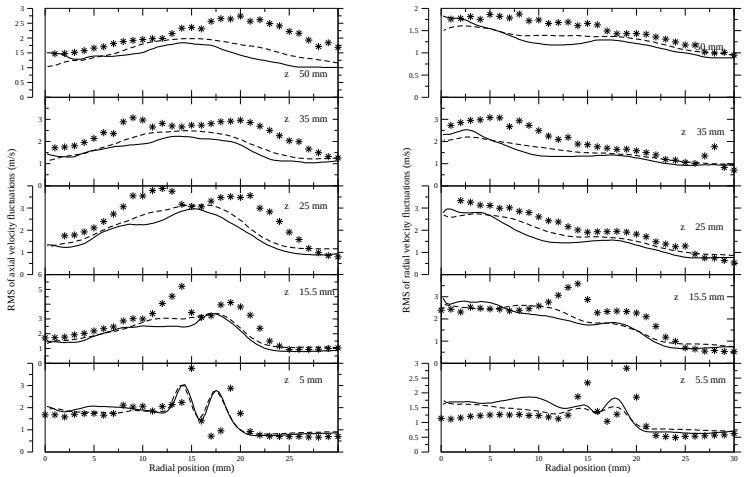

(a) Axial component (b) Radial component

Figure 6.8: Radial profiles of RMS velocity fluctuations at different streamwise locations. Symbol: Measurements. Dashed line: LES with coarse mesh (1.76M grids). Solid line: LES with fine mesh (5.2M grids).

the shear layer of the annular gap in both computation are very similar. As mentioned in chapter 4, this is due to strong anisotropy of the turbulence in the regime close to the burner inlet. The fine mesh seems to preserve this anisotropy little more than the coarse LES, as could be observed from the little cusp seen in RMS profile at z = 15.5 mm. No big difference is observed in the mean fluctuation profiles, both in axial and radial components. However, the coarse mesh LES results seems to be little better than fine LES results, at-least in axial RMS distribution. Similar results are observed in LES simulations by Triantafyllidis *et al* [158] done for the same configuration, with different mesh resolution. It should be remembered that the measurement reported in experiments are done with only air injection and thus, it cannot be considered as the datum reference for the LES validations shown here. The presence of fuel inside the CRZ would considerably modify the flow field inside the burner as seen before, which is the reason for the quantitative difference observed between the measurements and LES results presented here.

The mean mixture fraction and fluctuation of mixture fraction can be seen in Fig. 6.9a and Fig. 6.9b. The fluctuation here comprises of sum of resolved and sub-grid scale fluctuations. Unlike the mesh dependency of the mixing field reported in [158], both the LES show overall similar results. The fuel jet break-up is thus well predicted even with the coarse mesh used in this computation. In the fluctuations, noticeable difference can be seen between the coarse and fine LES results, especially at downstream region, where fine LES results are little better than the coarse LES results as expected.

The direct impact of mesh refinement can be seen by comparing the unresolved SGS energy, which can be inferred from sub-grid scale eddy viscosity following Pope's criterion. Fig 6.10 compares the viscosity ratio for coarse mesh and fine mesh. The eddy viscosity value of fine LES computation is less that the laminar viscosity at most of the burner region, showing that the scales of the flow are very well resolved in this computation. More fine mixing scales are

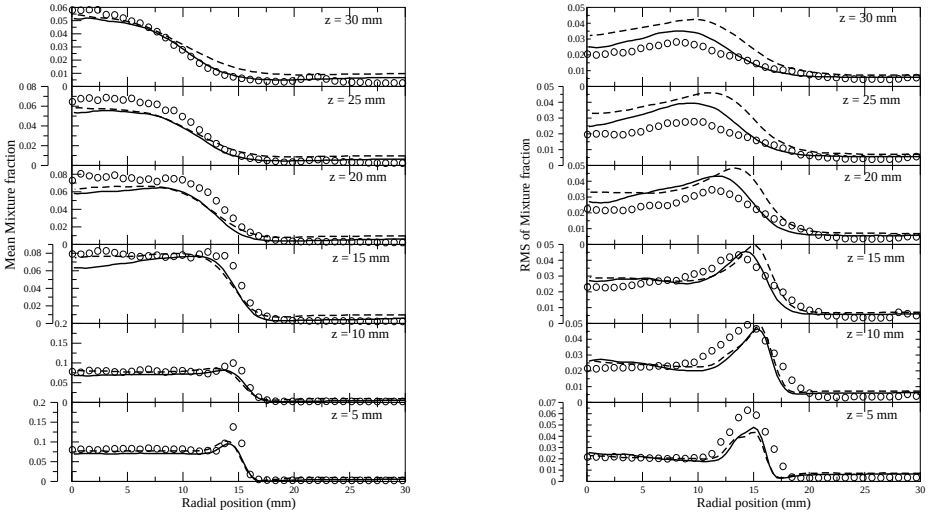

(a) Mean Mixture fraction

(b) RMS fluctuations of Mixture fraction, Resolved + SGS contribution.

Figure 6.9: Radial profiles of mixture fraction and RMS of mixture fraction fluctuations at different streamwise locations. Symbol: Measurements. Dashed line: LES with coarse mesh (1.76M grids). Solid line: LES with fine mesh (5.2M grids).

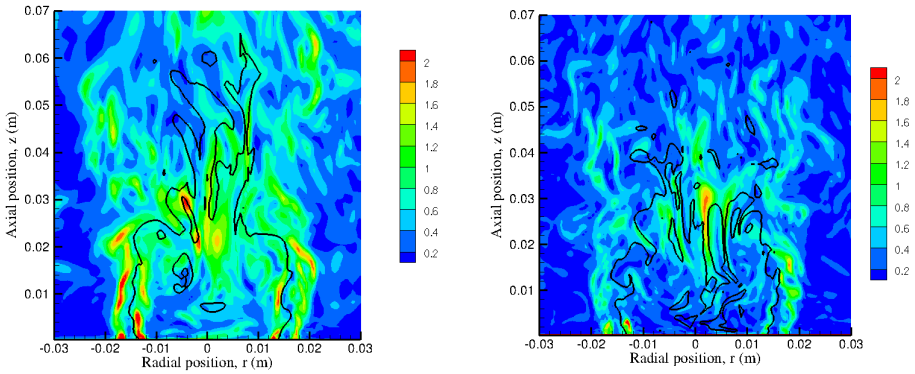

(a) Coarse mesh

(b) Fine mesh

Figure 6.10: Ratio of eddy viscosity to laminar viscosity with two different LES mesh. Left: Coarse mesh with 1.76 m grids. Right: Fine mesh with 5.2 M grids. Black line: Iso-line of stoichiometric mixture fraction.

resolved in the fine LES computation, which can be seen by observing the iso-stoichiometric line of the fine LES computation.

One set of reactive case computation was done with fine LES mesh on spot E, to characterize

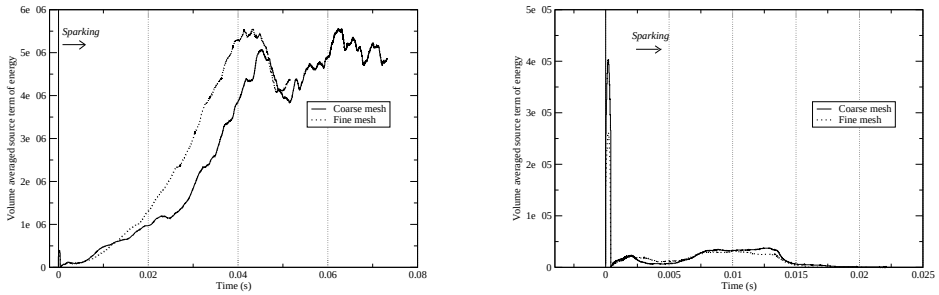

(a) Successful ignition (b) Failed ignition

Figure 6.11: Time evolution of volume averaged energy source term for both successful and unsuccessful case for spot E (z = 20 mm, r = 0 mm). Time shows the relative time after sparking instance. Black dotted line: Coarse LES with 1.76 M grid, Black solid line: Fine mesh with 5.2 M grids.

the difference in the flame establishment period between the two LES computations. One successful and one failed case simulation were performed and Fig. 6.11 shows the volume averaged source term evolution of coarse and fine LES for both successful and failed case ignition for spot E, compared against the results obtained from coarse LES simulation. The little differences observed between the two LES simulations are possibly due to the difference in the initial conditions at the beginning of the ignition. The total time take by the kernel to develop and lighten flame or be quenched by the intense turbulence is almost similar in both LES test cases. This verifies the validity of the results presented in this chapter and the previous chapters done with 1.76 M grid points.

6.5 Summary

A way to account for aerodynamic strain in the conventional PCM-FPI closure is presented and tested at a ignition spot within the central recirculation zone (CRZ). The CRZ features a unique ignition characteristics with kernel getting quenched due to local turbulence, a phenomenon which cannot be reproduced with the traditional PCM-FPI method. The first order strain correction function proposed here is the direct manifestation of strained laminar flamelet equation, which does not contain any model constant. The correction factor is calculated beforehand and a distribution function is used in the computation. The correction function mimics the reduction in burning rate based on local LES resolved strain rate, which is also a function of local mixture strength. This correction factor is applied to the PCM-FPI method and simulations are performed to describe the ignition kernel behavior with-in the central recirculation zone. The kernel quenching due to local turbulence is better reproduced with the new model. Successful ignition event are also observed with the proposed correction factor ensuring that the new model is not artificially over-dampening. The inclusion of strain correction has altered the rate of kernel development, as the flame development period was increased by nearly 30% compared to the conventional unstrained PCM-FPI technique. How-

ever, it has not altered the ignition prospects of zone where the local strain is not strong and the mixture is near stoichiometric. Complete burner mapping could be possible with the new model when used along with PCM-FPI technique, which is very handy and needs no big extra computational overhead.

The quality of the LES results are cross checked by performing a mesh dependency analysis, performed with a more refined LES mesh. The results of both LES are, in general similar, proving the reliability of the LES results presented in this thesis.

CHAPTER 7

Conclusions and recommendations for future work

Contents

Turbulent combustion modeling has been widely applied to steady state process due to the limitations posed by the computational resources and difficulties associated with the model developments, although, in most of the practical situations, the processes involve are unsteady. Large-eddy simulation has emerged as an viable option in the recent days to tackle the transient modeling problems. This computational study focussed on LES modelling of forced ignition and flame spreading of an annular bluff-body burner, experimentally investigated in Cambridge university, UK. The chemistry part of this simulation is dealt using tabulated detailed chemistry approach, known as PCM-FPI (presumed conditional moment - Flamelet prolongation of ILDM) method. The important findings of this numerical study are elaborated in this chapter. This thesis closes with an end note of recommendations to extend this work for future research.

7.1 Conclusions

Large-Eddy Simulation of forced ignition of an annular bluff-body burner has been conducted; the objective was to estimate the prediction capabilities of LES with tabulated detailed chem-

istry for a fully transient phenomenon, which also features strong variability of its statistical properties. Attempt has been made to bring-out the correlation between the success/failure of the ignition kernel and the turbulent flow field variables. Prior to any hot flow simulations, the detailed cold flow simulation has been performed and result are compared against the available experimental measurements. This is done to cross check the prediction capabilities of LES in such kind of flow scenario. Based on the cold flow analysis, the following conclusions are made.

7.1.1 Cold flow simulation

1) The predictions of mean velocity in both radial and axial component shows agreement with the measurement reported. The central recirculation zone (CRZ) was captured in correct size and stretch, proving the prediction capability of LES in flow involving vortex shedding and flow separation. The length and width of CRZ are of same order than that of the bluff-body diameter analysed here.

2) The turbulent fluctuation trends in most of the burner region show fair agreement with the experimental values. The predictions of turbulent RMS fluctuations in the annular shear layer and in the zone surrounding the rearward stagnation points are appreciably good. From the level of turbulence prevailing inside the CRZ of this burner, the flow configuration analysed here can be considered as fully turbulent.

3) The mixing field characterised by the mean mixture fraction and the fluctuation of mixture fraction are also in good agreement with the measurement counterpart. Substantial amount of injected fuel gets trapped inside the CRZ, as the fuel is injected near the inner shear layer of the annular jet. The mixture trapped inside the CRZ is well mixed and so the mixture fraction is nearly homogeneous due to the strong stirring velocity field present inside the CRZ.

4) The cold flow velocity fields with only air injection is very different from the velocity field with both air and fuel injection, although the overall mass flow ratio of fuel to air is close to just 5.5 %. The flow immediately behind the bluff-body wake highly depends on the thermodynamic properties of the mixture trapped inside the CRZ; thus with fuel injection, the density of the mixture inside the CRZ changes considerable leading to a change in dimension of the CRZ. The measurements reported from experiment found no change in the mean velocity field within few mm downstream of the bluff-body with fuel injection, which is in-fact verified even in simulation. However, at the further downstream side, there exists a non negligible impact in the velocity field due to fuel injection. The analysis based only air injection could be misleading while analysing effect of local advection on ignition kernel evolution. Thus, care should be taken while interpreting the results done with mocked inlet conditions. It is rather preferred to perform measurements with actual inlet conditions to precisely analyse and relation between the turbulent flow fields and ignition kernel development.

5) The predictions of probability density function (PDF) of mixture fraction and flammability factor (FF) contour characterising the local ignitability of different burner regimes show good qualitative agreement with the measured values. The CRZ is found to be the region with high local ignititability as the mixture is the CRZ is well within the static

flammability limits and nearly homogeneous. However, the flammability factor is found to be a misleading indicator of ignition probability of the the burner analysed, which exhibits relatively complex flow field.

7.1.2 Ignition test cases

Based on the available information from cold flow LES analysis, few spots are chosen to analyse spark ignition and subsequent flame development. The bluff-body character of the flow makes it complex, at least compared to sparking in a simple jet where the birthing flame can only move upstream or downstream. In the bluff-body having unsteady recirculation zones, four major scenarios are observed with LES, when sparking in a zone where the fuel/air mixture is close to flammability limits:

1) Persisting high streamwise velocity levels right after sparking, will transport the flame kernel away from the recirculation zone and full ignition of the burner cannot be reached. However, the region with high flow intermittency can be a successful ignition spot at certain time instants when the local convection is not strong, although the time averaged velocity field features high advection. Again, the ignition probability is determined based on the relative location of these spots with respect to rearward stagnation point, beyond which, the flow behaves like a normal round jet.

Convection by radial velocity towards the center recirculation zone or sparking directly in this zone is an important ingredient for the flame kernel to develop, however, two limitations exist:

2) close to the bluff-body wall, the flame may be quenched.

3) high strain rates encountered by small size kernels in too rich areas of the central recirculation zone may jeopardize the full ignition process. The mere availability of flammable mixture and low convection velocity fields need not always result in positive flame development. The local Karlovitz number (Ka) has a definite impact in the kernel dynamics, with high Ka quenches the flame, especially if the mixture is far from stoichoimetry. However, if the kernel is not quenched in it's initial development period, the ignition inside CRZ always resulted in successful burner lightening, as the CRZ features a negative axial convection and thus plays positive role in transporting the flame.

and finally:

4) the highest probability for full ignition of the burner is reached for a flame initiated from sparking in the very vicinity of the stoichiometric zone, on the lean side outside the main recirculation zone and axially located on the half bottom of the recirculating bubble. Convected towards the burner axis, this flame kernel enters the recirculation zone, after crossing the stoichiometric line. The flame kernel is then sufficiently developed and is much less sensitive to strain when facing the central recirculation zone rich mixture and high turbulence level. The implications from FF and ignition probability infer that this region need not possess good local ignition characteristics, as the spark energy can diffuse and ignite the flammable mixture in near vicinity. The local advection should be supportive in carrying the deposited energy towards flammable mixture, thus promoting local ignition, which then developes following the isostoichiometric surface.

These observations globally agree with available experiment measurements. It has also been shown that strain rate effects need to be included in the modeling of the filtered burning rate; an ingredient which is missing in the conventional PCM-FPI technique. A burning rate correction to the usual presumed probability density function modeling associated with tabulated chemistry has been discussed, which is based on the local LES resolved strain. The results are validated against experimental observation to address the improvements brought by accounting for strain rate in LES filtered burning rate. This model can be extended for other gaseous fuels too, provided the chemical schemes are available. The use of liquid fuel could seriously complicate these scenarios of ignition, since fuel spray combustion features specific properties [103, 174].

7.2 Recommendations for future work

Turbulent combustion modeling is a ever-growing subject. The complexity of simulating a highly transient ignition phenomenon and flame development has been studied in this work, however with some simplifications. The enormous rise in the computing facility directs the work towards better understanding from day to day. The models presented here can be still improved with sound physical background and in this way, the experimentally observed phenomenon are better captured and the physics behind it becomes more understandable. This work has been done as a first step for better capturing the observed phenomenon, and has been more or less successful in achieving it. Nevertheless, refinements can still be done in the frame of this work; which are summarized below.

- Immersed boundary conditions can be used to treat the curved boundaries at the lateral directions of the flow. Although, as seen in the results, the effect of confinement is negligible for this flow configuration, the scenario would be different with different bluff-body geometry and inlet conditions. In such situations, the immersed boundary treatment could clearly help improving the predictions at the large radius of the burner.

- The cold flow and mixing predictions can be further improved by including the region upstream to the burner inlet, where fuel injection takes place. Otherwise, as mentioned in the manuscript, an auxiliary simulation can be performed to verify the imposed inlet conditions, which would possibly enhance the quality of the cold flow mean field predictions and turbulent fluctuations.

- A quite simplified approach has been used in this modeling study to mimic the spark. More sophisticated models can be used to represent the spark, which may probably improve the predictions of kernel evolution, at least in the initial development periods. An auxiliary table can be generated accounting for plasma physics to handle the high temperature thermodynamics during sparking and can be smoothly coupled with the chemistry table generated using GRI mechanism. The total energy budget during sparking and the electrode heat losses can thus be accounted quantitatively, which would be a significant improvement in this frame work.

- The chemistry tabulation can be done considering the partial premixing of the mixture, instead of premixed flamelet library. A multi-dimensional flamelet manifold (MFM) [114] method can be employed to generate such a chemistry tabulation. This could be a

remarkable value addition, especially while simulating the test cases with strong mixture non-homogenity, for instance, the test case C of the Cambridge experiment.

- The stretch correction function developed during the coarse of this work can be rigorously validated by performing a direct numerical simulation (DNS) study. The complete experimental geometry can be scaled down for such a study and then can be conveniently handled in DNS. The validity of the assumptions such as linear correlation between stretch and burning rate reduction and the distribution of stretch along the flame front could thus be verified using the DNS results.

Part II

Archival Publications

PAPER 1

Subramanian V., Domingo P., Vervisch L. Large eddy simulation of forced ignition of an annular bluff-body burner, *Combustion and Flame*, **157(3)**: (2010) 579-601

Combustion and Flame 157 (2010) 579–601

Contents lists available at ScienceDirect

Combustion and Flame

journal homepage: www.elsevier.com/locate/combustflame

Large eddy simulation of forced ignition of an annular bluff-body burner

V. Subramanian, P. Domingo *, L. Vervisch

CORIA-CNRS and INSA de Rouen, Technopole du Madrillet, BP 8, 76801 Saint-Etienne-du-Rouvray, France

ARTICLE INFO

Article history:
Received 29 June 2009
Received in revised form 8 August 2009
Accepted 21 September 2009
Available online 4 November 2009

Keywords:
Large eddy simulation
Spark ignition
Laminar flamelets
Turbulent flames

ABSTRACT

The optimization of the ignition process is a crucial issue in the design of many combustion systems. Large eddy simulation (LES) of a conical shaped bluff body turbulent nonpremixed burner has been performed to study the impact of spark location on ignition success. This burner was experimentally investigated by Ahmed et al. [Combust. Flame 151 (2007) 366–385]. The present work focuses on the case without swirl, for which detailed measurements are available. First, cold flow measurements of velocities and mixture fractions are compared with their LES counterparts, to assess the prediction capabilities of simulations in terms of flow and turbulent mixing. Time histories of velocities and mixture fractions are recorded at selected spots, to probe the resolved probability density function (pdf) of flow variables, in an attempt to reproduce, from the knowledge of LES resolved instantaneous flow conditions, the experimentally observed reasons for success or failure of spark ignition. A flammability map is also constructed from the resolved mixture fraction pdf and compared with its experimental counterpart. LES of forced ignition is then performed using flamelet fully detailed tabulated chemistry combined with presumed pdfs. Various scenarios of flame kernel development are analyzed and correlated with typical flow conditions observed in this burner. The correlations between, velocities and mixture fraction values at the sparking time and the success or failure of ignition, are then further discussed and analyzed.

1. Introduction

Many gas turbine burners adopt a bluff body configuration to improve flame stabilization [1], sometimes termed as 'bluff body stabilization'. This comes under geometrical flame holding mechanisms, where a recirculation zone, created in the wake behind the bluff body, anchors the flame [2,3]. The introduction of blockage in the flowing combustion mixture stream increases the turbulence level due to vortex shedding and flow separation, which enhances the mixing. Furthermore, the combustion products trapped inside the recirculation zone may serve as a burning source by continuously igniting the incoming fuel–air mixture. In an axisymmetric bluff body burner, the flow emerges out of an annular gap formed by the intrusion of a bluff body into the main stream flow. The jet injected via this annular gap deviates slightly radially outward and envelops the central recirculating bubble, which continuously traps energy from the main streams and maintains the turbulence level. Farther downstream, the flow behaves similar to a fully established round jet [4]. The unique aerodynamics and flow field properties of such bluff body configurations have motivated several research studies, both experimental and numerical [5,6,1,7,4,8–10]. Many of the reported numerical works concentrated on aerodynamics and cold flow mixing in bluff body burners; simulation of such complex aerodynamical configuration demands on unsteady numerical technique, such as large eddy simulation (LES), for fair description [11–13,4,14].

Recently, Raman and Pitsch [15] and Kempf et al. [16] performed LES of the Sydney bluff body burner [17,18], featuring central fuel injection surrounded by coflowing air. The steady flamelet model used in those works captures the correct species and temperature distribution in most of the burner regions, particularly where the velocity components and the mixture fraction are in close agreement with the experimental results. Both authors reported the importance of mesh resolution requirements for capturing the flow field properties, which also further influences the reactive case predictions. El Asrag and Menon [3] also reproduced most of the major species and temperature profiles in a bluff body stabilized swirled nonpremixed flame.

Forced ignition modeling is not new, as numerous studies have focused on forced ignition in internal combustion engines [19–23]. However, few have considered spark ignition of nonpremixed burners [24–26], mainly because these burners, like those found in gas turbines, operate in combustion regimes that are, overall, steady. Nevertheless, the growing interest in optimization of aeronautical engine relight of high altitude motivates studies of nonpremixed burner forced ignition [27]. Very recently, numerical simulation of spark ignited lifted jet flames with global step chemistry [28] and bluff body flames with complex chemistry [29] has been reported.

* Corresponding author.
E-mail address: domingo@coria.fr (P. Domingo).

0010-2180/$ - see front matter © 2009 The Combustion Institute. Published by Elsevier Inc. All rights reserved.
doi:10.1016/j.combustflame.2009.09.014

It is becoming increasingly common to operate gas turbines under fuel lean or diluted operating conditions, due to stringent emission regulations and efficiency concerns; thus combustion is more susceptible to instabilities and blow off. This demands more careful design of ignition devices and their placement in the combustion chamber, to ensure reliable and faster relighting in case of flame blow out. The forced ignition phenomena observed in such burners are highly transient in nature. Various factors influence the development of spark kernels from the moment of spark deposit until complete flame establishment. The most favorable ignition spots for sparking in these burners are influenced not just by local equivalence ratio, but also by the time history of the velocity fluctuations, which will transport the flame kernel away from the ignition spot. The success of the spark in initiating the flame and the rate of flame development thus become a complex function of all flow field variables. An unsteady three dimensional numerical simulation could fairly describe the associated physics and give insight into the experimentally observed phenomenon. Such an attempt has been made in this study, which is motivated by a recent experimental work done by Ahmed et al. [27].

Large eddy simulation (LES) of flame ignition is performed with flamelet modeling associated in the presumed probability density function (pdf) (called PCM FPI [30] in this context). The aim is to reproduce the main features of the ignition probability map determined experimentally [27] and to explore it in the light of information extracted from LES. The experimentalists have reported that local strain rate acting on the growing flame kernel, could play a major role in the central recirculation zone (CRZ). To account for this effect, a strain rate correction to unstrained flamelets with presumed pdf modeling has been developed from previous works on flame response to stretch, and it is tested in this context.

In the first part of the paper, the methodology and the experimental setup are presented. Cold flow results are first discussed and compared with experiments, the subsequent section concerns the burning simulations, showing the flame development after forced ignition for representative spark locations. How the resolved flow field characteristics, in terms of velocity and mixture fraction, relate to the success of the ignition is further examined to illuminate some of the previously observed experimental behavior of the primary flame kernel. For comparison, simulations are performed with and without accounting for strain rate effects on flame subgrid scale chemistry; LES is found to reproduce most of the experimental observations.

2. Burner description

The simulated burner was designed by Ahmed et al. [27] for studying forced ignition. Two concentric pipes, one carrying air (outer pipe) and another carrying pure methane (inner pipe), are attached to the burner inlet. The inner pipe, carrying methane, diverges out to form a conical shaped bluff body at the inlet of the burner, which creates an annular region, through which air enters the burner. The fuel is injected radially on the axially flowing air stream, near the bluff body lip, thus forming a partially premixed mixture at the burner inlet. The flow is stabilized behind this conical bluff body, with a central recirculation zone. The bulk velocity of the air in the experiment was 10 m/s, which corresponds to a Reynolds number of around 6000 based on the annular width of 5 mm. As discussed in [31], this kind of annular jet can be considered fully turbulent for Reynolds numbers over 2000. Though, the experimental work by Ahmed et al. reports cases with and without swirl, only the nonswirling case is investigated in this computational study, because detailed cold flow measurements are available for it. Ahmed et al. have discussed the impact of spark location on ignition behavior from three burner maps: (i) a flammability factor map, based on mixture fraction measurements in frozen flow mixing; (ii) a map of successful flame kernel initiation probability; and (iii) a map of successfully established combustion probability. Selecting the most representative points, to cover all the experimentally observed types of ignition failure or success, the forced ignition behavior of this burner is now discussed with LES.

3. Numerics and subgrid-scale modeling

3.1. Flow solver

Computations are performed with a finite volume formulation in a collocated grid using the LES nonpremixed turbulent flame methodology proposed by Domingo et al. [30], which is based on tabulated detailed chemistry and presumed subgrid scale (SGS) probability density functions, coupled with the solving of the fully compressible form of the Navier–Stokes balance equations of mass, momentum, and energy. The domain, corresponding to the enclosure, measures 70 mm in spanwise direction and 80 mm in streamwise direction; it is discretized over 1,764,000 grid points. The grid is uniform in the spanwise direction and slightly stretched in the streamwise direction near the inlet, to capture the flow in the intense turbulence region near the bluff body lip. Implicit filtering is used in this LES and the characteristic size of the LES mesh is on the order of 0.4 mm. More refined LES could be performed for this burner; here it was chosen to limit the number of grid points to favor the treatment of numerous cases. A series of 20 simulations with different sparking cases have been completed and analyzed. A fourth order skew symmetric like scheme [32] is adopted for convective terms, while a fourth order centered scheme is employed for diffusive flux calculations. Time marching is done within explicit minimum storage Runge–Kutta scheme of order 3 [33]. The annular inflows of air and fuel are constructed from hyperbolic tangent profiles at the inlet plane, matching the corresponding experimental mass flow rates.

In the experiments, the cold flow velocity and turbulent fluctuation measurements are done with only air injection, thus neglecting the density difference between fuel and air. It was found that this replacement does not significantly alter the velocity profile close to the inlet of the burner, due to the fact that the overall ratio of fuel to air flow rate is as small as 0.055 (the overall mixture condition thus being stoichiometric) [34]. In LES computations, this point is carefully studied by analyzing both cases, with and without considering the density difference between fuel and air. The cold flow measurements of fuel/air mixing were performed by injecting fuel seeded with acetone [27,34], to better represent the mixing field experienced by the spark.

The inflow mean velocities are superimposed with synthetic turbulence, generated from the procedure proposed by Klein et al. [35]. Symmetric boundary conditions are applied at the spanwise boundaries (there is a wall enclosure in the experiment far from the axis of symmetry of the burner), and a nonreflecting subsonic outflow boundary condition is used at the outlet boundary. Acoustic waves traveling in and out of the computational domain were treated based on the Navier–Stokes characteristic boundary condition (NSCBC) [36].

Transport by unresolved velocity fluctuations is expressed using a subgrid scale eddy viscosity hypothesis and different expressions have been tested for the cold flow simulations, viz. Smagorinsky [37]. The filtered structure function [38], and wall adapted local eddy (WALE) viscosity [39]. The results were found to be almost similar due to the fact that the flow is quite well resolved, with a maximum eddy viscosity that never exceeds 20 times the molecular viscosity. The classical Smagorinsky's formulation [37] is then

retained for the sparking analysis, due to its simplicity and wide usage. A laminar viscosity response to temperature is calculated using Sutherland's law. The laminar Prandlt number is taken as 0.72, while the turbulent Prandlt number is assumed equal to 0.9. As the main focus of this study is on flame kernel development, until complete flame establishment, the temperature and species compositions vary strongly with space and time. Realistic thermo chemical effects are included by considering the specific heat capacity as a function of temperature as well as composition. The species mass fractions (N_2, CH_4, O_2, CO_2, H_2O, CO, H_2, OH) needed to obtain a correct estimation of the temperature [40] are tabu lated in PCM FPI, as now discussed.

3.2. SGS combustion modeling

Various methods have been proposed to tabulate the high com plexity of combustion chemistry, to keep LES computing require ments sufficiently low. One approach consists of considering canonical laminar combustion model problems, so called flam elets, which are filtered with presumed pdfs to account for unre solved subgrid scale fluctuations; it is named here PCM FPI [41,42]. Details concerning the background of this modeling ap proach applied to LES may be found in [30,40,43,44]. Two versions of SGS modeling are discussed in this paper; the first one does not account for the impact of flame stretching on the burning rate of the reference flamelets; the second includes a stretch correction. Premixed laminar flamelets are considered, mainly for three rea sons: (i) the turbulent mixing rate is high in this burner and spark ing occurs in already mixed reactants; (ii) once the burning kernel forms after energy deposit, partially premixed flame propagation may play some role in flame spreading; (iii) it was shown in previ ous studies, that most of nonpremixed combustion properties in terms of energy release are reproduced by premixed flamelet tab ulation, at least for equivalence ratios below 1.8 [30,45].

Space filtered quantities are denoted $\overline{\varphi}(\underline{x},t)$; the mass weighted filtered scalars and chemical source terms read

$$\overline{\rho}\widetilde{\varphi} \quad \overline{\rho\varphi} \quad \overline{\rho}\int_0^1 \left(\overline{\varphi|Z^*;\underline{x},t}\right)\widetilde{P}(Z^*;\underline{x},t)\,dZ^*, \tag{1}$$

where ρ is the density and $(\overline{\varphi|Z^*;\underline{x},t})$ is the filtered conditional mean of φ, estimated for the mixture fraction value $Z \quad Z^*$ (a pas sive scalar verifying $Z \quad 0$ in air and $Z \quad 1$ in fuel jet). $\widetilde{P}(Z^*;\underline{x},t)$ is the mass weighted filtered probability density function of mixture fraction Z, presumed to take a beta shape. The chemistry evolution is projected in a low dimensional composition space, which is here reduced to two variables, Z and a reaction progress variable Y_c, built from the sum of CO and CO_2 mass fractions, ensuring one to one correspondence between Y_c and species concentrations and sources [46,47]. A normalized progress variable is also defined, as Y_c nor malized by its equilibrium value $c \quad Y_c/Y_c^{Eq}$, where Y_c^{Eq} is deter mined with EQUIL software [48]. The filtered conditional mean is then given as

$$\left(\overline{\varphi|Z^*;\underline{x},t}\right) \quad \int_0^1\int_K^{K+} \varphi^{FPI}(Z^*,c^*,K^*)\overline{P}(c^*;\underline{x},t)\overline{P}(K^*;\underline{x},t)\,dc^*dK^*, \tag{2}$$

where φ^{FPI} is a scalar or a source term arising from the flamelets cal culations and $\overline{P}(c^*;\underline{x},t)$ is the filtered probability density function of normalised progress of reaction, which is also presumed to follow a Beta distribution. $\overline{P}(K^*;\underline{x},t)$ is the flame stretch pdf [49 51] whose statistical space covers $[K \quad ,K+]$; in a first analysis c and K can be assumed to be statistically independent [51]. The two marginal pdfs, $\widetilde{P}(Z^*;\underline{x},t)$ and $\overline{P}(c^*;\underline{x},t)$, are presumed from $\widetilde{Z},Z_v \quad \widetilde{ZZ}$ $\widetilde{Z}\widetilde{Z},\widetilde{Y}_c$, and $\widetilde{Y_cY_c}$ for which balance equations are solved [30]. The hypothesis of statistical independence between Z and c (not Y_c) was previously discussed [41,30]. $\widetilde{Y_c^2}$ is solved instead of the SGS variance for numerical reasons, to avoid transporting the energy of the resolved field $\widetilde{Y_c}^2$ within the SGS variance [43,52].

Scalar dissipation rates appear in the equations for Z_v and $\widetilde{Y_cY_c}$ [30]; they measure the SGS turbulent mixing rate and are decom posed into their resolved and SGS parts,

$$\overline{\rho}\widetilde{\chi}_\varphi \quad \overline{\rho\mathscr{D}|\nabla\varphi|^2} \quad \overline{\rho}\mathscr{D}|\nabla\widetilde{\varphi}| + \overline{s}_{\chi_\varphi}, \tag{3}$$

where $\mathscr{D}$ is the molecular diffusivity of φ. The SGS mixture fraction dissipation rate appearing in the Z_v balance equation is expressed using a linear relaxation closure,

$$\overline{s}_{\chi_Z} \quad \frac{\overline{\rho}Z_v}{\Delta^2/\nu_T}, \tag{4}$$

with Δ the local filter size and ν_T the SGS eddy viscosity. For Y_c, the progress of reaction, the dissipation rate expression that accounts for the presence of thin flame fronts is used [30],

$$\overline{s}_{\chi_{Y_c}} \quad (1 \quad S_c)\frac{\overline{\rho}\left(\widetilde{Y^2} \quad \widetilde{Y}^2\right)}{\Delta^2/\nu_T} + S_c\left(\overline{\rho}\mathscr{D}|\nabla\widetilde{Y}_c|^2 + \overline{Y_c\dot{\omega}_{Yc}} + \overline{Y_c^{Eq}\dot{\omega}_{Yc}}/2\right), \tag{5}$$

with $S_c \quad \left(\overline{c^2} \quad \overline{c}^2\right)/(\overline{c}(1 \quad \overline{c}))$, the unmixedness of the progress var iable ($S_c \in [0,1]$); $\dot{\omega}_{Y_c}$ denotes the chemical source of Y_c. The first term in Eq. (5) accounts for low unmixedness levels, corresponding to quasi Gaussian SGS pdfs, the second results from the BML theory [49], where the flame is seen as a thin interface separating fresh and burnt gases, with bimodal pdfs. Once $\varphi^{FPI}(Z,c,K)$ and $\overline{P}(K^*;\underline{x},t)$ have been prescribed, all relevant thermochemical quantities and filtered sources are computed from Eq. (1), which is tabulated as functions of $\widetilde{Z},S_Z \quad Z_v/\left(\widetilde{Z}\left(1 \quad \widetilde{Z}\right)\right),\widetilde{Y}_c$ and S_c, over a nonuniform grid of $100\times20\times100\times20$ points, clustered around the stoichiometric surface.

As alluded to above, in the experiment by Ahmed et al. [27] some peculiar flame behavior, such as a strong intermittency in ignition success in the central recirculation zone, was attributed to strain rate effects acting on flame propagation in a fuel rich mix ture zone ($Z > 0.08$, equivalence ratio slightly above 1.6), thus for conditions under which flame speed is quite sensitive to burning reduction induced by strain rate. To further examine this point, two kinds of simulations are performed, with and without account ing for the impact of flame stretch on SGS tabulated chemistry. In the first, the stretch effect is neglected and $\varphi^{FPI}(Z,c,K) \quad \varphi^o(Z,c)$ is built from a collection of freely propagating unstrained premixed flamelets, computed with the PREMIX software [48] and the GRI methane air detailed mechanism [53] with complex transport properties, as in previous LES using similar SGS modeling [30,40]. In the second, the stretch is accounted for in a global manner; the starting point is based on observations by Bradley et al. [51], who have reported that the premixed flame response used to tab ulate chemistry, such as, $\dot{\omega}_q(Z,c,K)$, the volumetric heat release rate at a stretch rate K, can be related to $\dot{\omega}_q^o(Z,c)$, the value at zero stretch rate as:

$$\dot{\omega}_q(Z,c,K) \quad f(K)\dot{\omega}_q^o(Z,c), \tag{6}$$

where $f(K)$ is a flame stretch factor. A relation which is applied to every equivalence ratio and in the context of Eq. (2), this would read

$$\left(\overline{\dot{\omega}_q|Z^*}\right) \quad \left(\overline{\dot{\omega}_q^o|Z^*}\right)P_b, \tag{7}$$

with

$$P_b \quad \int_K^{K+} f(K^*)\overline{P}(K^*;\underline{x},t)dK^*. \tag{8}$$

A thorough analysis of $f(K)$ and of the burning rate factor P_b is given in [50], where it is shown that it behaves as

$$f(K) \quad 1 \quad \sigma K, \tag{9}$$

where σ combines various flame properties, such as the Markstein length, the flame thickness, and the flame speed. In, Reynolds, averaging context and assuming a Gaussian distribution for $\overline{P}(K^*;\underline{x},t)$, the burning probability factor, P_b, response versus stretch is nonlinear [50]. This is transposed to LES with three observations; first, direct numerical simulation (DNS) has shown that the highest rate of strain and flame curvature result from large eddies [54], which are mostly resolved in LES; second, the zones where flame stretch is likely to impact on ignition probability have been reported in the Ahmed experiment [34] to be mainly fuel rich, and flamelets in the rich zone have low flame speed levels, and high sensitivity to stretch and they are quenched for much smaller K levels than under stoichiometric conditions; third, laminar flame analysis demonstrates a first order linear flame response of a scaled mass burning rate versus stretch [55,56]. From these observations, only the first order linear part is kept to correct the flamelet response to LES resolved stretch, $P_b \approx (1 \quad \mathscr{K}(\widetilde{Z}))$, and Eq. (7) is cast in

$$\left(\overline{\dot{\omega}_q|Z^*}\right) \quad \left(\overline{\dot{\omega}_q^o|Z^*}\right)\left(1 \quad \mathscr{K}(\widetilde{Z})\right) \tag{10}$$

to globally correct the conditional burning rate, according to flame response to stretch, where $\mathscr{K}(\widetilde{Z})$ remains to be defined. An estimation of $\mathscr{K}(\widetilde{Z})$ is now discussed.

The steady premixed laminar flamelets equation may be written

$$\frac{\partial \rho u \varphi}{\partial \xi} \quad \frac{\partial}{\partial \xi}\left(\rho \mathscr{D}_\varphi \frac{\partial \varphi}{\partial \xi}\right) + \rho \dot{\omega}_\varphi \quad \rho \dot{S}_{K_\varphi} \tag{11}$$

where u is the velocity, $\mathscr{D}_\varphi$ is the diffusion coefficient of φ, and $\dot{\omega}_\varphi$ is the chemical source. The coordinate in the direction normal to the flame front is ξ, and $\dot{S}_{K_\varphi}$ is a stretch leakage term that includes all fluxes occurring along the flame surface, and thus representative of transverse convection and diffusion resulting from straining and curvature of the flamelet surface; the case of a freely propagating one dimensional unstrained premixed flame corresponds to $\dot{S}_{K_\varphi} \quad 0$.

Integrating Eq. (11) in the direction normal to an unstretched flamelet ($\dot{S}_{K_\varphi} \quad 0$) and for $\varphi \quad c$ gives the relation between the unstrained flame speed S_L^o and the integral of the burning rate through the flame,

$$\rho_o(Z)S_L^o(Z) \quad \rho_b^o(Z)u_b^o(Z) \quad \int_\infty^{+\infty} \rho(Z;\xi)\dot{\omega}_c^o(Z;\xi)d\xi \quad \int_0^1 \rho(Z,c^*)\frac{\dot{\omega}_c^o(Z,c^*)}{|\nabla_\xi c^*|}dc^*, \tag{12}$$

where ρ_o is the density in the fresh gases, and, ρ_b^o and u_b^o denote the density and velocity of burned gases in the unstretched flamelet. A similar integration of Eq. (11) is done for the stretched flame, assuming a linear dependance between the stretch leakage term and the local stretch measure [55 59], $\dot{S}_{K_c} \quad Kc$, thus

$$\rho_b(Z)u_b(Z) \quad \int_\infty^{+\infty} \rho(Z;\xi)\dot{\omega}_c(Z;\xi)d\xi \quad \int_\infty^{+\infty} \rho(Z;\xi)c(Z;\xi)K(Z;\xi)d\xi \tag{13}$$

In a more detailed analysis (see for instance [57]), the mass flux burning rate is determined at the position ξ_o on the burnt gas side of the flame. The LHS of Eq. (13) becomes $\rho(Z;\xi_o)u(Z;\xi_o)$, with ξ_o the position where the burning rate is of the order of 10% of its maximum level, to demonstrate that $\rho_b(Z)u_b(Z) \approx \rho(Z;\xi_o)u(Z;\xi_o)$ [57], mainly because the remaining contribution in burned gases remains small compared to the flame one in the range $\xi \in [0,\xi_o]$.

We further assume that the unstretched burning rate and progress variable profiles can be used also in the integrals of the stretched relation (13), combining Eqs. (12) and (13),

$$\rho_b(Z)u_b(Z) \quad \rho_o(Z)S_L^o(Z)\left(1 \quad \frac{1}{\rho_o(Z)S_L^o(Z)}\int_\infty^{+\infty} \rho(Z;\xi)c(Z;\xi)K(Z;\xi)\right)d\xi, \tag{14}$$

which may be written

$$\rho_b(Z)u_b(Z) \quad \rho_o(Z)S_L^o(Z)(1 \quad Ka(Z)), \tag{15}$$

with Ka the Karlovitz integral value computed from unstretched profiles:

$$Ka(Z) \quad \frac{1}{\rho_o(Z)S_L^o(Z)}\int_\infty^{+\infty} \rho(Z;\xi)K(Z;\xi)c(Z;\xi)\,d\xi. \tag{16}$$

From the above relations, one may then write

$$\int_\infty^{+\infty} \rho(Z;\xi)\dot{\omega}_c(Z;\xi)\,d\xi \quad (1 \quad Ka(Z))\int_\infty^{+\infty} \rho(Z;\xi)\dot{\omega}_c^o(Z;\xi)\,d\xi. \tag{17}$$

Arguing that flame integrated and filtered burning rates behave similarly versus stretch, this last relation may be written for the energy source

$$\left(\overline{\dot{\omega}_q|Z^*}\right) \quad (1 \quad Ka(Z^*))\left(\overline{\dot{\omega}_q^o|Z^*}\right), \tag{18}$$

which is similar to Eq. (10), but obtained in a slightly different context. Furthermore, assuming that there exists a stretch measure Ψ_K such that

$$\int_\infty^{+\infty} \rho(Z;\xi)K(Z;\xi)c(Z;\xi)\,d\xi \quad \Psi_K \mathscr{I}_c(Z) \tag{19}$$

with

$$\mathscr{I}_c(Z) \quad \int_\infty^{+\infty} \rho(Z,\xi)c(Z,\xi)\,d\xi, \tag{20}$$

the relations (10), (16), (18) and (19) lead to

$$\mathscr{K}(\widetilde{Z}) \quad \frac{\mathscr{I}_c(\widetilde{Z})}{\rho_o(\widetilde{Z})S_L(\widetilde{Z})}\Psi_K, \tag{21}$$

with $\mathscr{I}_c(\widetilde{Z})$ computed from the flamelet database. The stretch measure Ψ_K, may then be seen as the resolved part of the normalized time evolution of the flame surface density [60],[1]

$$\Psi_K \quad \nabla\cdot\widetilde{\mathbf{u}} \quad \mathbf{nn}:\nabla\widetilde{\mathbf{u}} + S_L\nabla\cdot\mathbf{n}, \tag{22}$$

with $\mathbf{n} \quad \nabla\overline{c}/|\nabla\overline{c}|$. Simulations have been performed with and without the curvature term $S_L\nabla \quad \mathbf{n}$ in Ψ_K, without much net impact on burner ignition probability; therefore presented results are without the curvature term, which overall has a small impact on the global burning rate compared to strain rate, as previously reported [61 64]. Eq. (10) then reads

$$\left(\overline{\dot{\omega}_q|Z^*}\right) \quad \left(\overline{\dot{\omega}_q^o|Z^*}\right)\left(1 \quad \zeta(\widetilde{Z})\Psi_K\right) \tag{23}$$

with the following options for ζ:

- With $\zeta \quad 0$, simulations are performed without any attempt to include stretch effects on laminar flamelet speed, as it was done so far in PCM modeling [30,40];

[1] In the relations (10) and (21), Ψ_K is introduced to include response of local burning rate and flame speed to stretch only, SGS flame-wrinkling effects are accounted for with the presumed pdfs of mixture fraction and progress of reaction in Eqs. (1) and (2), leading to different needs compared to SGS models fully relying on flame surface density, where SGS stretch cannot be neglected [21].

• With

$$\zeta(\widetilde{Z}) \quad \frac{\mathscr{I}_c(\widetilde{Z})}{\rho_o(\widetilde{Z})S_L(\widetilde{Z})}, \tag{24}$$

which is a fixed distribution computed from the flamelet database, simulations are performed including an approximate stretch correc tion. $\zeta(\widetilde{Z})$ is plotted in Fig. 1, its minimum is found close to stoichi ometry for slightly rich mixtures, and it rapidly increases in both fuel lean and rich sides. For moderate stretch levels, this first order linear attenuation has almost no impact on stoichiometric mixtures, but a non negligible one for fuel lean and rich conditions; for example at $Z \approx 0.08$, the rich sparking condition considered in the simulations, ζ 1 200 s 1.

There is no ad hoc constant or parameter introduced in this stretch correction, since ζ is computed from the flamelet library with Eq. (24); transposing the detailed analysis by Bradley et al. [50], quenching would be assumed when $\Psi_K > \zeta(\widetilde{Z})$ 1. It is also postulated that the inherent instability of a flame to negative stretch might cause it to reorientate toward positive stretch rate [50]. Simulations are performed at first for all cases with ζ 0; then additional simulations are conducted to evaluate the impact of the stretch correction. As expected from experimental results, it is reported thereafter that fuel rich flow locations, with high velocity fluctuations, need to be addressed with nonzero ζ to repro duce ignition variability; nevertheless, the stretch correction was not found to modify ignition probability at other locations. In addi tion, considering a single fuel rich location, the stretch correction does not always prevent ignition at this point, depending on turbu lence properties' time history; hence it is ensured that the included strain rate effect does not behave as an artificially high damping of the energy source, which would prevent burner ignition always for rich sparking locations. Other modeling approaches for stretch effects on flame speed in LES context may be found in [65 67]. In this first order modeling of the flame stretch rate, Lewis number effects have not been explicitly included. Lewis number effects on growing ignition kernels have been demonstrated for mixtures of hydrogen and propane in air at elevated pressures in [68]. For methane air flame, it was shown that the effect of preferential diffusion on mass burning rate is globally negligible [57], due to near unity Lewis number of the mixture. The modeling of the flame kernel resulting from sparking is now discussed.

3.3. Initial flame kernel and spark modeling

Rigorous modeling of spark ignition is quite complicated, as the mechanism involves plasma formation under extremely high tem perature/pressure conditions with very small time and length scales [69,70]. Neither the detailed combustion chemical scheme used in this work nor the conventional thermochemical relations are applicable in such an environment. In the experiment, the spark energy deposit always generates a small kernel of hot gases, and, it is the subsequent time development of this initial flame ker nel that determines the ignition success or failure of the overall burner [27]. A simplified modeling procedure is thus adopted in this study to reproduce only the macroscopic effect of sparks pro moting flame kernel initiation.

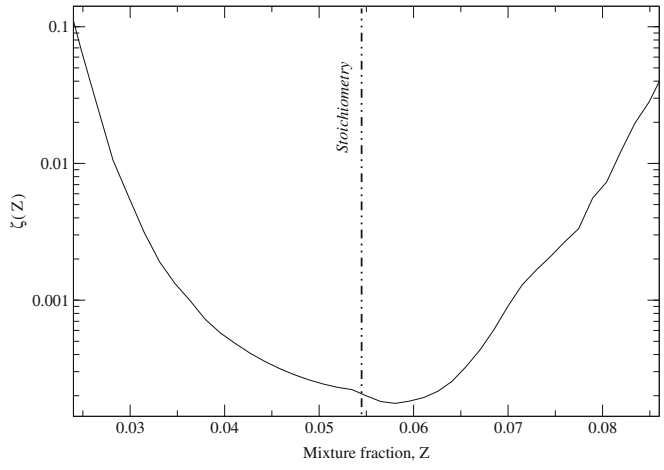

Fig. 1. $\zeta(Z)$ as defined in Eq. (24).

The spark energy deposited is mimicked by a source term in the energy equation, a general procedure followed in many earlier works [25,71 73]. The modeled source term takes a Gaussian dis tribution in space, centred at the spark location. The spark source also follows a Gaussian distribution in time, to better match with the energy deposition schedule obtained in the experiment, which could be inferred from the ignition current profile [34]. Accord ingly, the spark energy source term is cast in [71],

$$\dot{\omega}_s \quad \dot{\omega}_s^o \exp\left[\left(\frac{t \quad t_0}{2\sigma_t}\right)^2 \quad \left(\frac{x \quad x_0}{2\sigma_x}\right)^2 \quad \left(\frac{y \quad y_0}{2\sigma_y}\right)^2 \quad \left(\frac{z \quad z_0}{2\sigma_z}\right)^2 \right] \tag{25}$$

with

$$\dot{\omega}_s^o \quad \frac{E_s}{V_s \delta_{ts}}, \tag{26}$$

where t_o is the sparking instant in time, and x_o, y_o and z_o are the spark coordinates. E_s is the net spark energy, chosen in such a way that the maximum local temperature is below the maximum allowable temperature (T_{max} = 2500 K), for which the conventional thermochemical relations are applicable; typically E_s is on the order of 60 mJ. The initial spark kernel volume $V_s \quad (4/3)\pi R_s^3$ is with ra dius R_s = 0.5 mm, as suggested in former studies [22,74], and the spark duration of the experiment is $\delta_{ts} \quad 400$ μs [27]. The time and space relaxation parameters in Eq. (25) are set as $\sigma_t \quad 0.2$ ms and $\sigma_x \quad \sigma_y \quad \sigma_z \quad 1$ mm.

In the experiment, the spark energy deposit leads to tempera ture levels well above $\widetilde{T}^{Eq}$, the filtered chemical equilibrium tem perature of the mixture obtained from the lookup table including SGS mixture fraction fluctuation effects. The thermal energy dif fuses away from the initial spark kernel and a flame is formed. However, the amount of energy transferred from the sparking de vice to the flow stays small compared to the heat released by com bustion once initiated. To mimic this thermal process, the increase of local temperature that follows energy deposit is continuously monitored and compared with the local chemical equilibrium tem perature. As soon as the temperature exceeds $\widetilde{T}^{Eq}$, the local compo sition is adjusted to the tabulated chemical equilibrium composition, thus initiating combustion. The equilibrium temper ature overshoot is only transitory and, in all cases studied, it is not observed for more than 1 ms after sparking has vanished. Sim ilar observations were made in DNS of forced ignition of laminar H_2/air stratified mixtures [75], where the transient spark effect dis sipates in less than 0.18 ms. The main parameters of this simplified numerical sparking procedure have been varied, without signifi cant change in the reproduction of the ignition probability map.

4. Cold flow results

4.1. Velocity field and fluctuations

Results of cold flow test cases are discussed first. Statistics are collected and averaged in time for about $\tau_m \quad 4(L/U_m)$ s, where L is the dimension of the domain in the streamwise direction and U_m is the bulk velocity at inlet plane; τ_m was found large enough

to ensure proper convergence of the results. The time averaged velocity and fluctuations are then radially averaged (i.e. over the azimuthal direction) to increase the size of the statistical sample, which is compared against the ensemble averaged experimental measurements. These frozen flow mixing measurements have been performed with fuel injection replaced by air seeded with acetone [27]. As noted above, to assess the eventual impact of methane density on momentum, both LES predictions with the fuel replaced by air and with real fuel injection are plotted against the experi mental results. Fig. 2a shows radial profiles of time averaged streamwise and radial velocity components taken at different axial positions of the burner.

Considering the case with only air injection (dashed line in Fig. 2a), at a streamwise position z 5.5 mm, the core jet region is visible and it spreads out radially further downstream. On the axis, a negative streamwise velocity representative of flow recircu lation is observed at z 15.5 mm and z 25 mm. Both amplitude and location of the corresponding recirculation zones are in agree ment with measurements; this is not the case with fuel injection.

Far downstream ($z \geqslant 35$ mm), not much difference is found be tween the simulations with only air and air plus fuel. However, there is a significant impact noticed in the region of the recircula tion zone, between z = 15.5 mm and 25 mm (Fig. 2a). The width of the recirculation zone is mostly unaltered, whereas its length has decreased by about 10%, from 25 mm with only air, to 20 mm with fuel, thus shifting the stagnation point upstream when fuel is in jected. Fig. 3 shows a time averaged view of the recirculation zones obtained with and without fuel. The streamlines emanating from the core jet region, therefore exiting from the annular gap, which envelops the recirculating bubbles are specifically indicated. With air injection (Fig. 3), as in the experiments, the rearward stagnation point identifying the length of the CRZ is located on the burner axis at a distance of 25 mm from the burner, which equals D_f, the bluff body diameter. The width of the CRZ is also about D_f. This result falls in line with reported observation in studies on conical bluff body flows [6,1], where the length of the recirculation behind a conical bluff body is found to be in the range of 1 1.2D_f, the width being 1D_f. The accurate prediction of the dimension of the CRZ is of central importance in such burners, as the CRZ plays a key role in flame stabilization.

The differences between cases with and without fuel can easily be explained. As the fuel is injected along the inner edge of the annular gap, a large amount of fuel gets trapped inside the CRZ. The mixture fraction data discussed in the upcoming section con firms the presence of a rich mixture inside the CRZ. The fuel (roughly 8% in mass) inside the recirculation zone alters the density of the mixture of the CRZ and thus the momentum of the recirculating bubbles, which deviates the incoming jet.

The mean radial velocity profiles at different burner axial loca tions are shown in Fig. 2b, where the predictions without fuel injection are also closer to experimental measurements. From the sign convention used here, positive radial velocity denotes radially outward flow and negative velocity is representative of flow ori ented toward the burner axis. In the experimental device, the flow is globally composed of an inner part, where the mixture recircu lates, and an outer part, surrounding the inner part away from the central axis. The details of the properties of the outer part de pend on the burner enclosure and are driven by slow flow motions

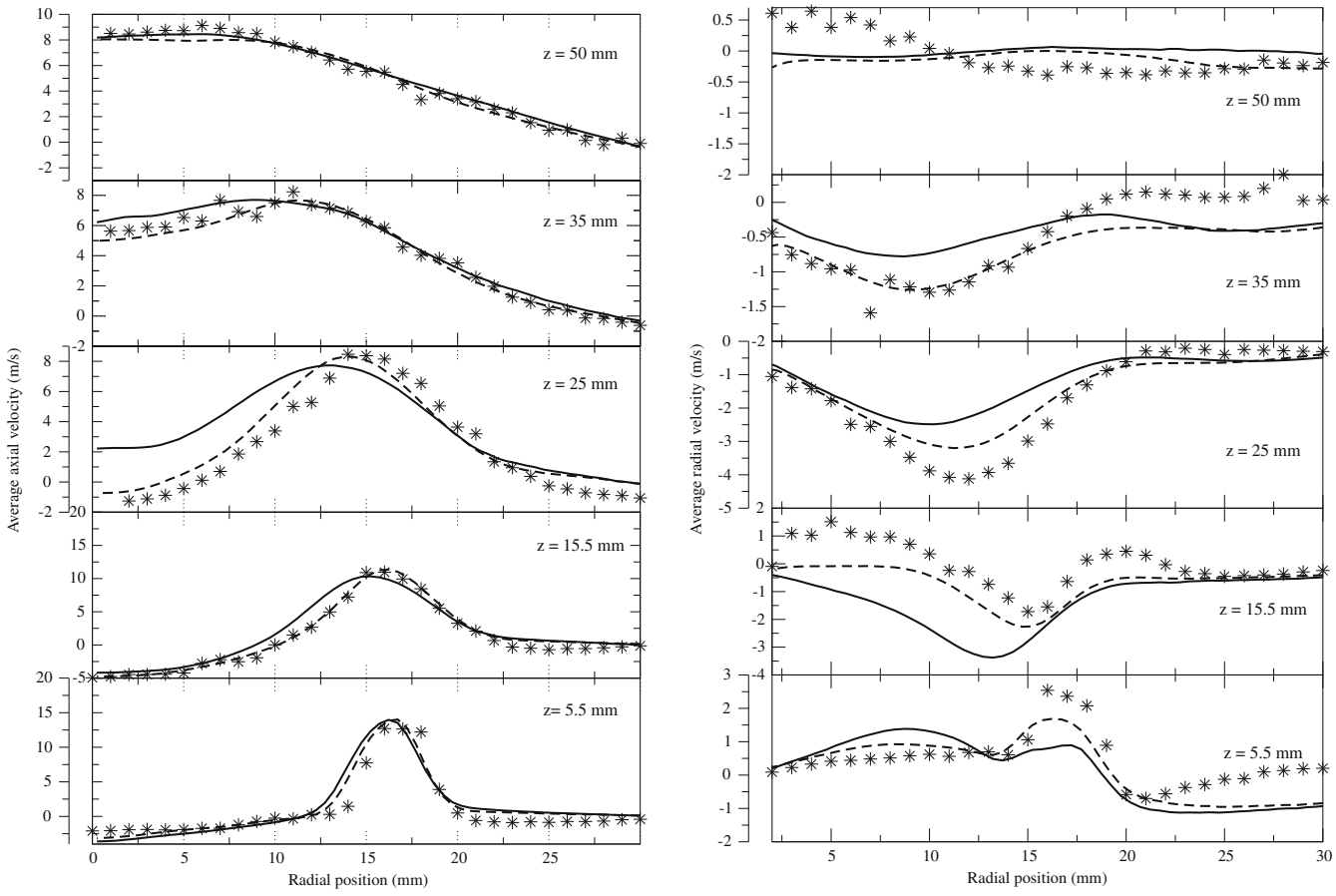

Fig. 2. Radial profiles of time-averaged velocities at different streamwise locations. Symbol: measurements. Dashed line: LES with only air injection. Solid line: LES with air and methane injection.

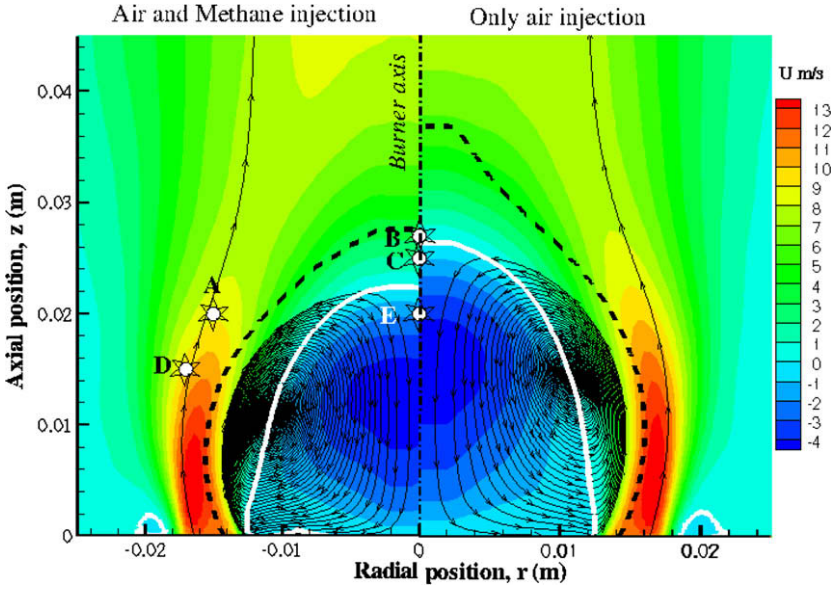

Fig. 3. Average axial velocity contour. White line: Isoline of zero axial velocity. Black dashed line: isoline of stoichiometric mixture fraction. Right: LES with only air injection. Left: LES with both air and methane injection. The small white sparklets indicate the ignition spots discussed in Section 4.3 (Tables 1 and 2).

interacting with walls; the exact description of this outer part is out of the scope of the present LES, because it has little impact on the ignition burner properties studied below. Indeed, experiments have shown that the confinement has little effect on the CRZ until the confinement diameter ratio (CDR = D_b/D_f, D_b being the burner diameter) is less than 50% [34]. The CDR of the burner

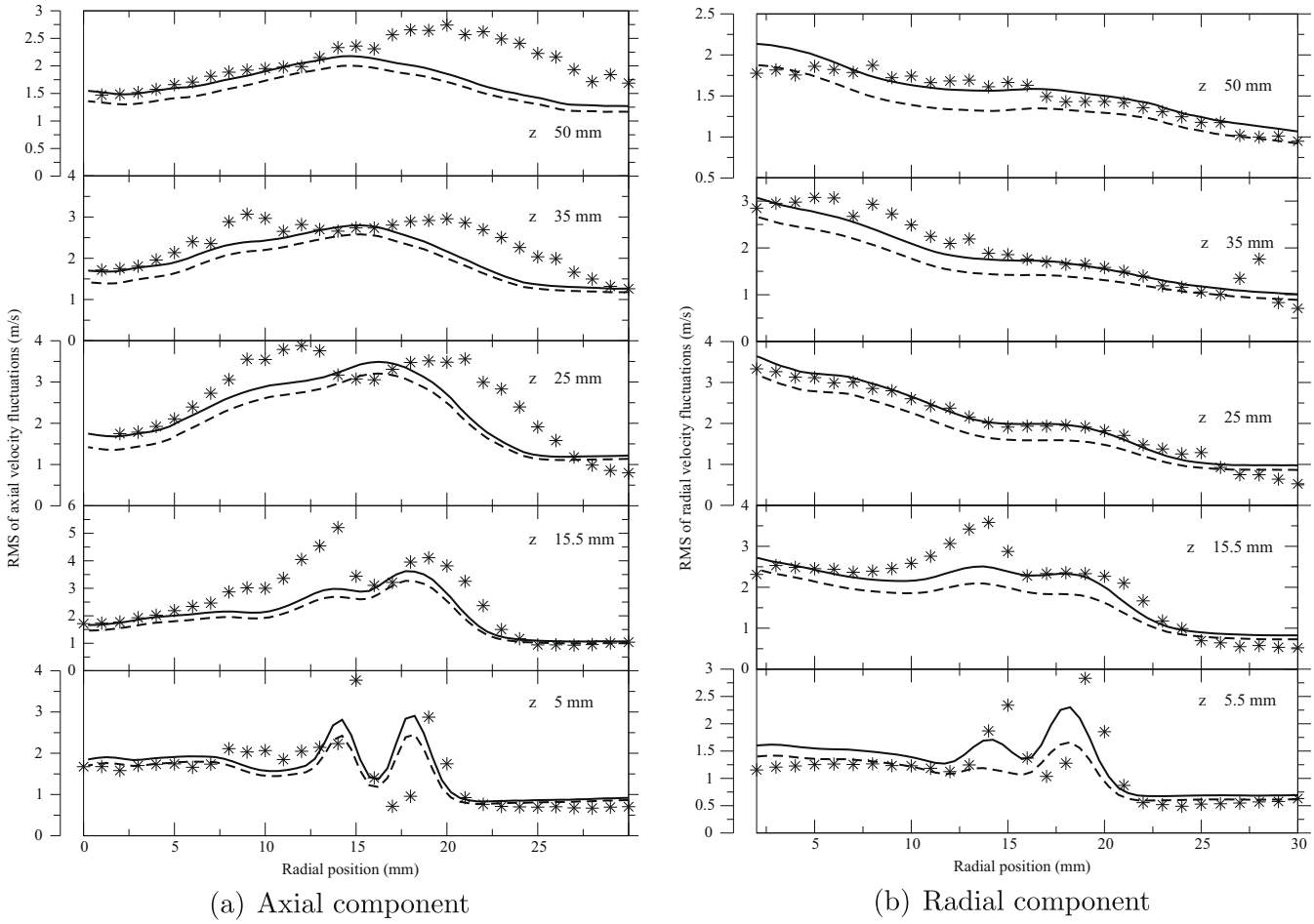

Fig. 4. Radial profiles of RMS velocity fluctuations at different streamwise locations. Symbol: measurements. Line: LES resolved + SGS. Dashed line: LES resolved.

configuration studied here is about 35% and so the external con finement should not have any impact on the central part of the flow examined below when sparking. The effect on the simulations of the outer recirculation zone can be seen at the axial position of 5.5 mm, where the velocity is slightly underpredicted in the vicin ity of the wall (radial position of 30 mm). Some more discrepan cies, nonetheless still acceptable, are also noted between computations and experimental results at 15.5 mm. Further down stream, the results reproduce the experimental observations, with some departure still observed at z 50 mm; but overall, radial velocity results are in line with what can be expected from LES of such flows with actual SGS modeling.

The root mean square (RMS) of velocity fluctuations is shown in Fig. 4a and b for axial (U_{rms}) and radial components (R_{rms}) of veloc ities, respectively, for the case with only air injection. While calcu lating RMS of velocity fluctuations, both the resolved part and the SGS (subgrid scale) part are considered. The SGS part of the RMS is reconstructed from the SGS kinetic energy budget (k_{SGS}) [76], de rived from

$$k_{SGS} \quad \frac{v_t^2}{(C_m \Delta)^2}, \tag{27}$$

with v_t the SGS eddy viscosity, Δ the characteristic LES mesh size, and the constant C_m defined as

$$C_m \quad \sqrt{\frac{2}{3}\frac{A}{\pi K_0^{3/2}}} \tag{28}$$

Here, K_0 is Kolmogrov's constant and A is Kraichnan's Test Field Model (TFM) constant [76]. This approximation of the kinetic sub grid energy is also useful for assessing the quality of the LES, for in stance via the turbulence resolution parameter (M), defined as follows [77]:

$$M(\underline{x}, t) \quad \frac{\langle k_{SGS}(\underline{x}, t)\rangle}{K(\underline{x}, t) + \langle k_{SGS}(\underline{x}, t)\rangle}. \tag{29}$$

Here, $K(x, t)$ corresponds to resolved kinetic energy and $\langle\ \rangle$ indicates time averaging. By definition, $M = 1$ corresponds to RANS and $M = 0$ would be obtained in DNS. According to Pope [77], $M \leqslant 0.2$ charac terizes well resolved LES in which at least 80% of the energy of tur bulence is resolved. In this computation, the turbulence resolution parameter is well below 0.2 except at the shear layer of the core jet region close to the inlet.

In Fig. 4a, the level of fluctuations inside the CRZ is well repro duced. Along the jet axis, the radial RMS fluctuations, R_{rms}, are superior to their streamwise counterpart, except at z 5.5 mm; at the rearward stagnation point located at z 25 mm, the radial peak value is also considerably higher than U_{rms}, which is typical for such a flow configuration [5]. Both axial and radial RMS fluctu ations are high and quite uniform inside the central recirculation zone. In Fig. 4a, the resolved fluctuations completed with SGS

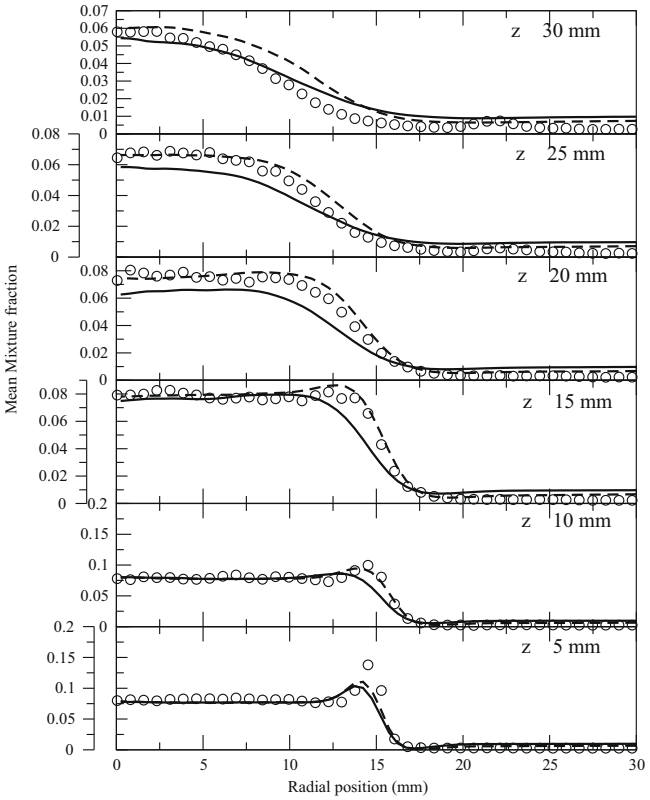

(a) Mean Mixture fraction. Solid line: LES with both air and methane injection. Dashed line: LES with only air injection

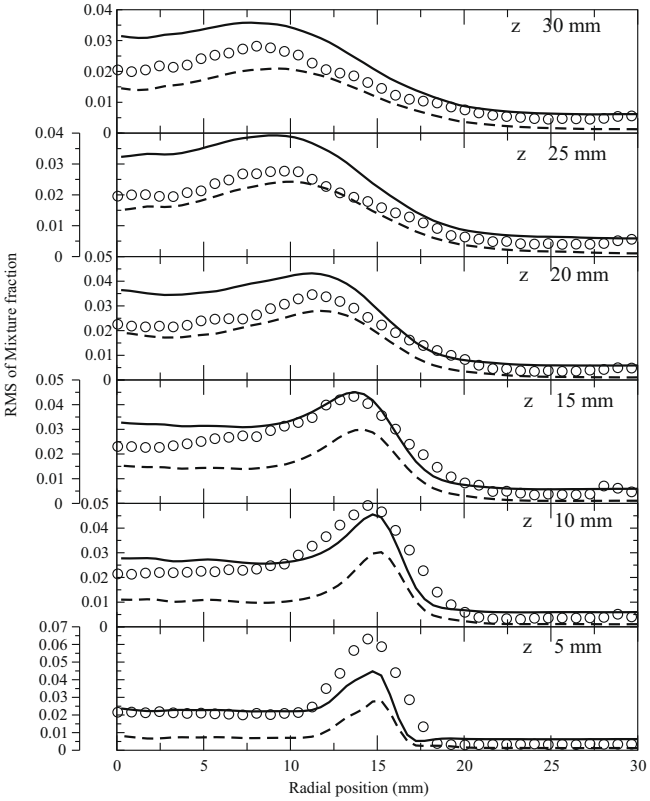

(b) RMS fluctuations of Mixture fraction (methane injection). Solid line: Resolved + SGS contribution, Dashed line: Resolved.

Fig. 5. Radial profiles of mixture fraction and RMS of mixture fraction fluctuations at different streamwise locations.

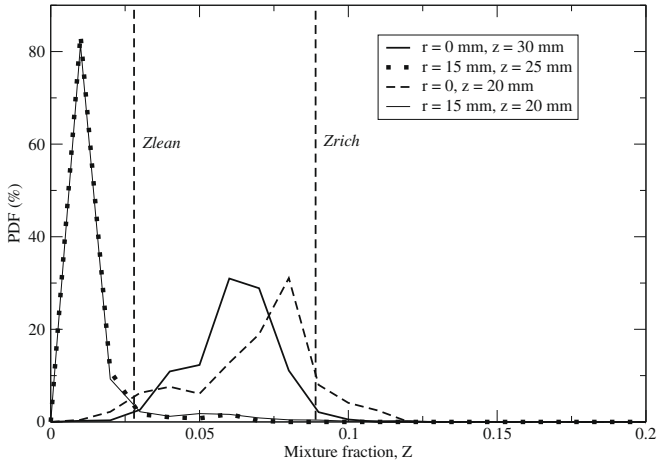

Fig. 6. Pdf of $\widetilde{Z}$ at a few selected locations in the burner.

Table 1
Ignition spots with time-averaged flow field and mixing field information.

Ignition spot index – [z,r]	U_m (m/s)	R_m (m/s)	Z_m	F (%)
A – [20,15]	7.03	−1.04	0.010	6
B – [27,0]	3.28	0	0.054	85
C – [25,0]	2.13	0	0.058	87
D – [15,17]	4.93	−0.54	0.0067	0.3
E – [20,0]	−1.70	0	0.07	85

Notes: z, axial downstream position (mm); r, radial position (mm); U_m, mean axial velocity; R_m, mean radial velocity; Z_m, mean mixture fraction; F, flammability factor.

fluctuations provides the best approximation of experiments, espe cially at the shear layer of the jet and in the recirculation zone, where the turbulent intensity is high. However, even when the SGS contribution is added, the double peaks observed in the U_{rms} profile of experimental measurement are still underpredicted in computations. In this LES, equal intensity of pseudo turbulence is forced in the inlet plane at inner and outer edges of the annular gap for both axial and azimuthal velocity components. In reality, the presence of a sharp bluff body lip may induce nonuniform flow instabilities between the outer and inner edges of the jet and also in axial and radial velocity components. An auxiliary simulation of the burner interior could be performed to provide refined inlet conditions; nevertheless, the spreading rate of fluctuations and its levels are arguably well predicted in Fig. 4a with the simplified inlet approximation used in this study. Once again, far down stream, $z \approx 30$ mm, and near the lateral boundary, the predictions are degraded due to the lack of fine description of the outer zone, and similar results were observed in DNS of burners [10]. As al luded above, this region is far away from the sparking locations of interest, where the focus is on the ignition kernel dynamics in and around the CRZ; velocity results are then adopted and the mix ture field is now discussed.

4.2. Mixture fraction field and fluctuations

Fig. 5 shows the radial profiles of mean mixture fraction at six locations along the burner axis. The symbols in Fig. 5 correspond to experimental PLIF measurements done with fuel seeded with 10% acetone [27]. Two LES computations are done, one with only air injection and another with both air and fuel injection. The mean mixture fraction is well predicted at all axial locations; 5 mm downstream of injection, the peak value near the radius of 15 mm is, however, slightly underpredicted. This could be due to an insufficient mesh resolution in this zone. Further downstream, the predictions based on an air only injection are very close to the experimental results. Only at a distance of 30 mm from the in let, where the region is beyond the rearward stagnation point, the mixture fraction seems to be a little over predicted. According to the experimentalists [27], the PLIF signal in this zone is very weak and measurement uncertainties become large.

The mixture fraction values inside the first half of the CRZ are almost the same for both LES cases. Notice that the mixture frac tion value here is close to 0.08, which means that the mixture is quite rich (equivalence ratio of about 1.6) and thus appreciably affecting the mixture density inside the CRZ for the case with methane injection. A difference is observed between the two LES cases first at the shear layer of the 15 mm location; downstream of this point, this difference is observed all over the radial profiles. The iso stoichiometric lines shown in Fig. 3 highlight the difference between the two LES calculations done with and without account ing for fuel density induced effects.

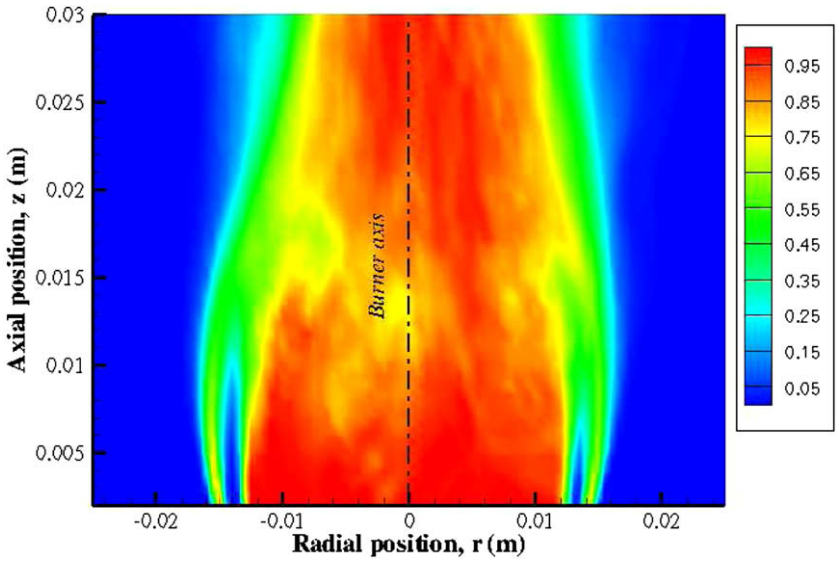

Fig. 7. Flammability contour based on the resolved mixture fraction pdf (cut in the central plane).

Table 2
Ignition spots with velocities and mixture fractions time-averaged over the sparking time duration.

Ignition spot index – [z,r]	Burner ignition	Time instant (s)	U^s_m (m/s)	R^s_m (m/s)	Z^s_m
A – [20, 15]	Failed	0.09379	6.9	−0.28	0.004
A – [20, 15]	Success	0.09486	3.6	−3.9	0.003
B – [27, 0]	Failed	0.1534	4.23	−3.26	0.032
B – [27, 0]	Success	0.1393	0.54	−0.98	0.043
C – [25, 0]	Success	0.13765	1.54	−1.176	0.052
D – [15, 17]	Success	0.09379	10.26	0.06	0.008
E – [20, 0]	Failed	0.1321	−1.95	3.3	0.081
E – [20, 0]	Success	0.13765	−2.816	−1.09	0.07

Notes: z, axial downstream position (mm); r, radial position (mm); U^s_m, mean axial velocity; R^s_m, mean radial velocity; Z^s_m, mean mixture fraction – superscript s indicates averaging over the sparking time.

Fig. 5 shows the RMS fluctuations of mixture fraction compared with their experimental counterpart, with and without considering the subgrid scale contribution. The mixture fraction LIF measurements have been performed with a resolution $\Delta_{LIF} \approx \Delta/10$, where Δ is the LES filter size. Therefore, the amplitude of the measured fluctuations must be between the resolved LES fluctuations and the resolved LES fluctuations to which the SGS contribution is added [40]. This SGS part is known after solving a balance equation for Z_v $\widetilde{Z}\widetilde{Z}$ $\widetilde{Z}\,\widetilde{Z}$ [30]. Fig. 5 confirms this expected distribution of mixture fraction fluctuations. Again, small discrepancies are noticed at the z 5 mm downstream position. As mentioned before, the scalar dissipation rate term in the Z_v equation was closed by linear relaxation of variance [30], which assumes that the scalar mixing time is proportional to the SGS turbulent characteristic time [78]. This links the SGS kinetic energy levels with the SGS scalar variance, which means that any error in SGS kinetic energy will be reflected in scalar variance. Local mesh refinement near the bluff body lip could probably improve the prediction in this region.

Overall, all measured trends are captured by the present LES. Certainly, the agreement between averaged LES and measurements could be improved by adjusting inlet conditions and refining the mesh [79], but it is shown thereafter that this description is sufficient to fully reproduce and analyze the transient ignition behavior and, more importantly, its statistical variability. Many simulations are needed to check this last point and the effort is therefore oriented in this direction, rather that fine tuning of the averaged values.

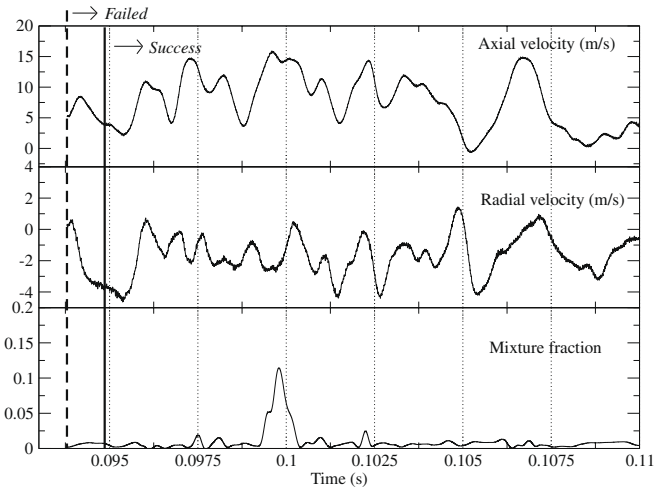

Fig. 8. Time history of velocities and mixture fractions at spot A (z = 20 mm, r = 15 mm). Continuous line: favorable time instant. Dashed line: nonfavorable time instant.

4.3. Flammability factor

In turbulent fuel air mixtures, the success of ignition at a given location is not just a function of mean flow and mixture properties; it also depends heavily on the instantaneous flow field values at the sparking moment and the following time histories of the same. Before a successful primary ignition is obtained, which completely lights the burner, the spark has to locally ignite the mixture, thus either the sparking zone should possess an ignitable mixture during the sparking moment, or ignitable flow should be transported from a very nearby location before substantial diffusion of deposited energy. In a first approximation, the success of ignition at the exact sparking location can thus be related to the statistics of local mixture conditions [80]. The probability density function (pdf) of the LES resolved mixture fraction, $P(\widetilde{Z};\underline{x})$, calculated from the time history of the mixture fraction field is a possible ingredient to start quantifying the local ignitability [81]. The flammability factor $F(\underline{x})$ [27,80], is defined as the probability of finding the mixture fraction within the static limits of flammability. Hence, at a given location, the ignition flammability factor is defined as

$$F(\underline{x}) \quad \int_{Z_l}^{Z_r} P(\overline{Z}^*;\underline{x})\, d\overline{Z}^*, \tag{30}$$

where Z_l 0.028 and Z_r 0.089, denote the chosen lean and rich flammability limits of the methane air mixture. (By definition, a unity flammability factor corresponds to a zone that always possesses an ignitable mixture.)

LES provides access to the flammability factor, based on the resolved mixture fraction by cumulating in time, at each node, a sample of the resolved mixture fraction field. Mixture fraction probability density functions are shown in Fig. 6 for some selected points; see similar probability density functions in Fig. 13 of [27]. Along the burner axis, for the points r 0 mm, z 20 mm and r 0 mm, z 30 mm, the mixture fraction pdf displays a near Gaussian distribution. These points are part of those selected for systematic comparison with the sparking experimental results (Table 1). The point r 0 mm, z 20 mm is located inside the recirculation zone and frequently faces rich mixtures due to the interaction of the rotating recirculating bubbles with the injected fuel stream. Part of the pdf then lies outside the flammability limit in a quite rich zone. The location r 0 mm, z 30 mm is behind the rearward stagnation point, where the turbulence intensity is quite high. The mixture in this region is always within the flammability limits, suggesting facilitated ignition. The pdfs extracted from LES are similar to those extracted from experiment (Fig. 13 of [27]).

The points r 15 mm, z 25 mm, and z 20 mm are located within the envelope of the central recirculation zone. The flow in this region is highly intermittent, which leads to a non Gaussian mixture pdf. As seen in Fig. 6, $P(\widetilde{Z};\underline{x})$ is positively skewed toward

the zero mixture fraction, resulting in a low flammability factor. Nevertheless, the chance of getting a mixture within the flamma bility limits is nonzero. Such $P(\widetilde{Z};\underline{x})$ has been constructed at all points in a plane cutting the burner axis, using Eq. (30). The flam mability factor can then be evaluated for every point of a central plane passing through the burner axis, and is shown in Fig. 7. Qual itatively, F computed from the LES is the same as that of the exper iments, showing a high flammability zone centered on the burner axis, with a large base of the width of the bluff body, but narrow ing slightly when progressing downstream (see Fig. 22 of [27]). Quantitatively, in the details, F extracted from LES shows some departure from its experimental counterpart, where the nonzero flammability zone is narrower; showing that having quite similar time averaged basic statistics (Figs. 5b and a) does not ensure fully similar flammability factor.

Also in the experiment, the highest probability of ignition, as re ported from sparking attempts, is maximum for a radial position located between 15 and 18 mm (for $13 < z < 17$ mm), a location with an experimental flamability factor that is very small or null. In the LES, for the same zone, the flammability factor is small (be low 25%), but mostly larger than in the experiment. Hence, for this zone, the LES flammability factor would better anticipate the real ignition behavior. Nonetheless, locations can also be found in the LES where F is null and the real probability of ignition is high. One of these locations will be presented in the next section. It is therefore difficult, at this stage, to really conclude on the exact validity of the flammability factor for anticipating, from cold flow analysis, the probability of ignition success; clearly more informa tion is needed.

A few locations have been chosen, based on the above informa tion, to deposit the spark energy. The different ignition spots re tained are marked on the mean axial velocity contour shown in Fig. 3 and their characteristics are summarized in Table 2. These points are taken in and out of the CRZ, with low and high flamma bility factor, and high and low probabilities of providing whole flame ignition. A detailed analysis of the flame development at these locations is proposed in the next section.

5. Flame kernel development

In this section, the modeling discussed above is used without including stretch effects on chemistry tabulation (ζ 0 in Eq. (23)) to reproduce a large part of the ignition probability map. The modifications and improvements brought by the model including stretched flames ($\zeta \neq 0$) will then be discussed in the next section.

5.1. Point A: z = 20 mm, r = 15 mm

This point, located outside the CRZ, has a flammability factor of 6%. The experiment [27] has shown that the probability of contrib uting to successful flame kernel initiation after sparking at point A is close to 50% and the probability of whole burner ignition is of the order of 25%.

As mentioned before, the success of an ignition kernel in estab lishing a stable flame does not depend only on local flow and fuel distribution at sparking time, but also on the time history of field variables experienced by the developing kernel. One experimental observation is that a spot favorable for local ignition is not neces sarily a successful spot for getting a fully developed flame at every time. On the other hand, a zone with a small local flammability could be a relatively better spot for successfully lighting the flame. The advection and unsteady nature of the flow make these differ ences. The spot A, which exhibits strong flow intermittence, is re tained to analyze these effects with LES. The time histories of velocities and mixture fraction were recorded for a given duration. The kernel development was tested at two different instants se lected from this time history (t_s = 0.09380 s and t_s = 0.09486 s).

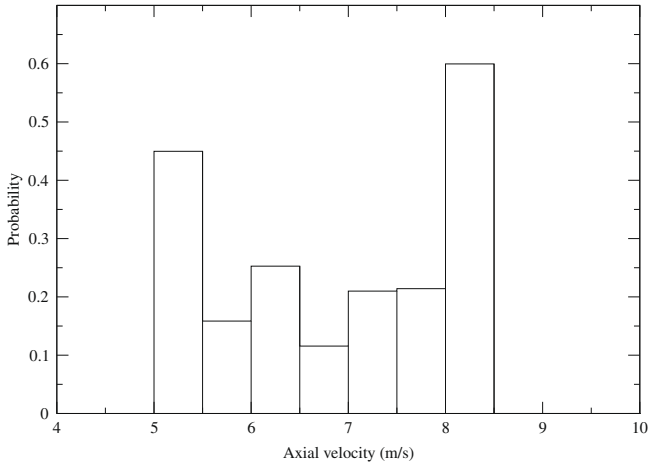

(a) Axial velocity

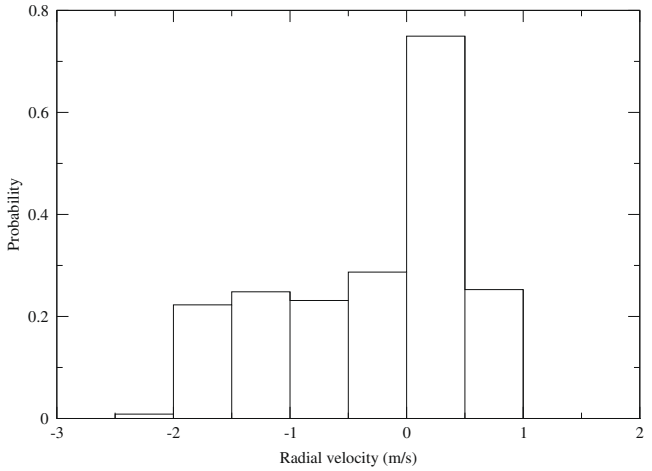

(b) Radial velocity

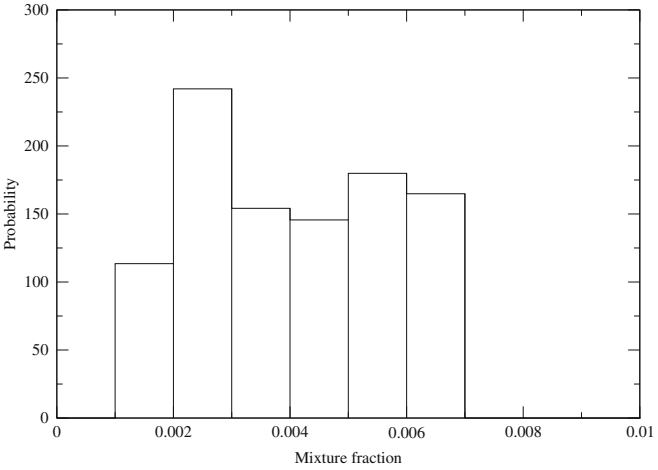

(c) Mixture fraction

Fig. 9. Pdf of velocity and mixture fraction at spot A (z = 20 mm, r = 15 mm), during the sparking moment. Sparking time = 0.09379 s.

Fig. 8 shows the time history of axial velocity, radial velocity, and mixture fraction at the spot A of Table 1. Most of the time, this region faces a high axial velocity. The radial velocity is generally negative and thus toward the CRZ. The fluctuations of both radial and axial velocities are high (Fig. 4a and b), which indicates quite strong flow intermittency at this point. The mixture fraction is small and presents high fluctuations (Figs. 5 and 8), varying from nearly zero to an extremely rich value beyond the flammability limits. This could be verified from the pdf of the resolved mixture fraction field shown in Fig. 6. The flammability factor in this region is small, suggesting that local ignition is less probable, Table 1 summarizes the time averaged velocities, mixture fraction, and flammability factor for this zone.

Ignition was tested at two instants in time, giving rise, respec tively, to a failed and a successful ignition case, which are indicated in Fig. 8 in dashed and continuous lines. The velocities and fuel mass fraction averaged during the sparking duration (400 μs) are given in Table 2 for each sparking attempt. At a time instant of t_s 0.09379 s, the deposited energy initiates an ignition kernel, which fails to light the burner. For this particular time instant, the histograms of axial velocity, radial velocity, and mixture frac tion, constructed from their respective time histories recorded dur ing the spark duration, are shown in Fig. 9. Referring to Figs. 8 and 9a, the averaged axial velocity during the spark duration is on the order of 6.9 m/s, which is quite high for this flow, while the aver aged radial velocity stays almost zero, which means that the kernel is not experiencing any radial movement while being convected downstream. The mixture fraction is far away from flammability limits; however, as this region is quite close to the isostoichiomet ric surface (Fig. 3), the deposited energy can diffuse toward the flammable region in the close vicinity of this ignition spot and a burning kernel is first created as already observed in [24]. The behavior of this kernel is displayed in Fig. 10, which shows snap shots of temperature, tracked in series of time instants, following ignition. The envelope of the isostoichiometric surface is within 2 mm from the ignition spot at the beginning of ignition (taken as t 0 for the discussion). The streamline (based on LES resolved instantaneous axial and radial velocities) at the ignition spot is also plotted at the start of ignition. This streamline is more or less par allel to the burner axis, showing that the kernel is going to experi ence axial transport without much deviation in its radial position. The near spherical spark kernel, observed after t = 0.15 ms, is undisturbed by turbulence, a phenomenon also reported in the experimental observation of spark ignition [82]. At a time of 1 ms after sparking, the kernel grows in size and is stretched axi ally by the flow. After 3 ms, the kernel is enlarged, but has been also scattered, the burnt gases pocket then reaches the zone be yond the rearward stagnation point, where the flow is only positive in all radial positions (Fig. 2a). Later in time the kernel is still grow ing, but it is transported further downstream to get finally com pletely blown. In the experiment, this spot was identified to have a high probability of successful kernel initiation, but a relatively small probability of lighting the burner (see Fig. 22a and b in [27]). The difference between these two probabilities arises due to the transport of the burning kernel, which is driven by the instantaneous flow field.

A spark at a later instant (t_s = 0.09486 s) featuring different con ditions has also been tried resulting in successful ignition of the burner; thus LES captures burner ignition variability for this point. Fig. 11 shows the histogram of axial velocity during the energy deposition period at this spot. The axial velocity is relatively low, about 3.6 m/s, compared to 6.9 m/s at the previous instant, and it helps the kernel to grow before getting convected too far down stream. At the same time, the radial velocity shows a negative trend (Fig. 11b), thus transporting a substantial amount of depos ited energy toward the CRZ, with a favorable mixture fraction dur ing the travel of the kernel, giving rise to successful local ignition.

The development of the flame kernel from the sparking moment is shown in Fig. 12, which depicts shot by shot temperature distri bution. The streamline issued from the spark location at t_s = 0.09486 s presents a slight radial inclination toward the burner axis, due to the negative radial velocity prevailing at this time in stant, and gets very close to the stoichiometric line. A near spher ical kernel is observed at t 0.16 ms, immediately following

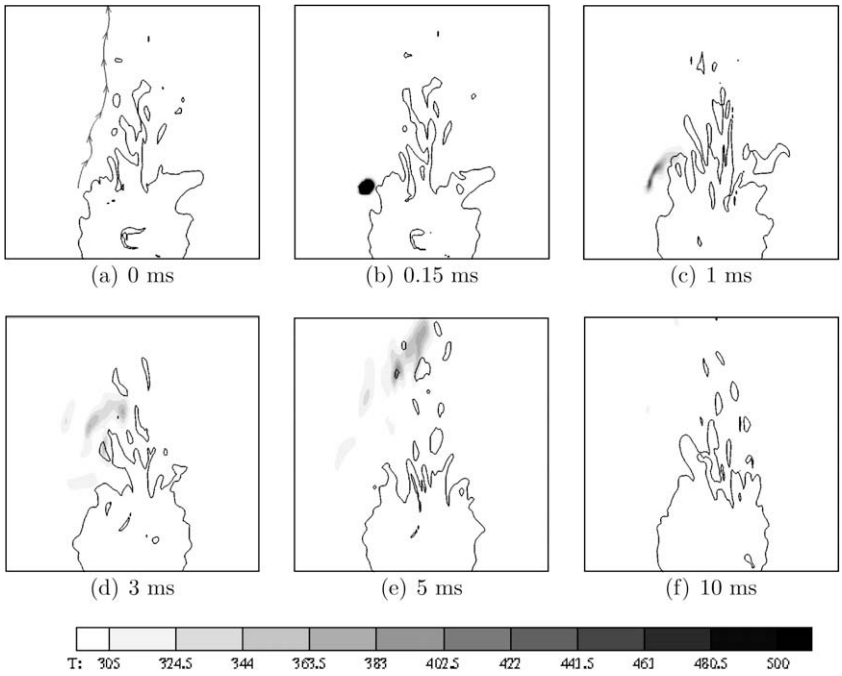

Fig. 10. LES-resolved instantaneous snapshots of temperature after sparking at spot A (z = 20 mm, r = 15 mm). Spark time = 0.09379 s, (in Fig. 8). The relative time after the ignition event. Solid black line: isoline of stoichiometric mixture fraction. Image covers the domain dimension of 70 × 70 mm.

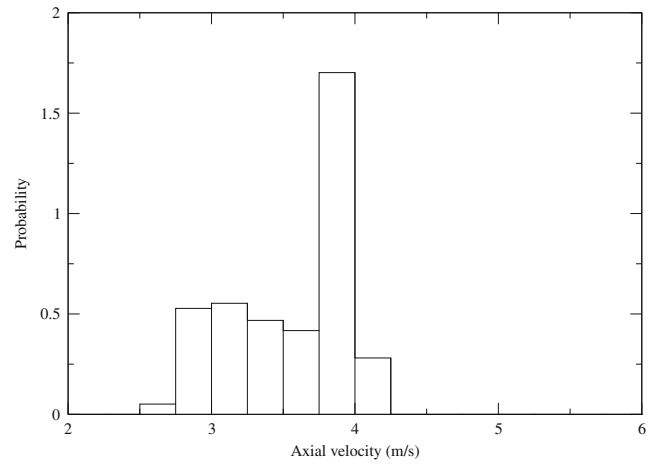

(a) Axial velocity

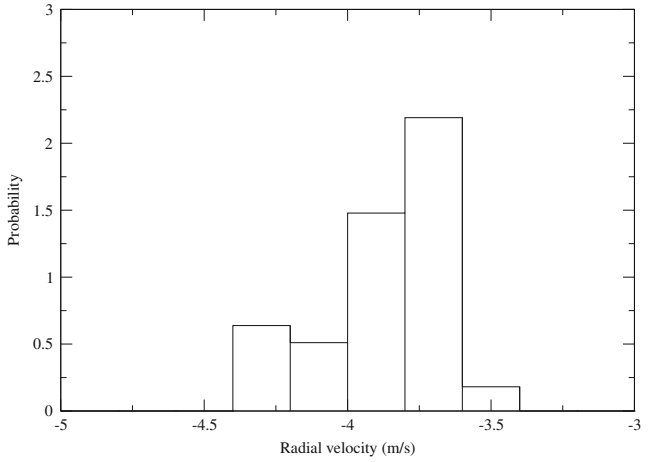

(b) Radial velocity

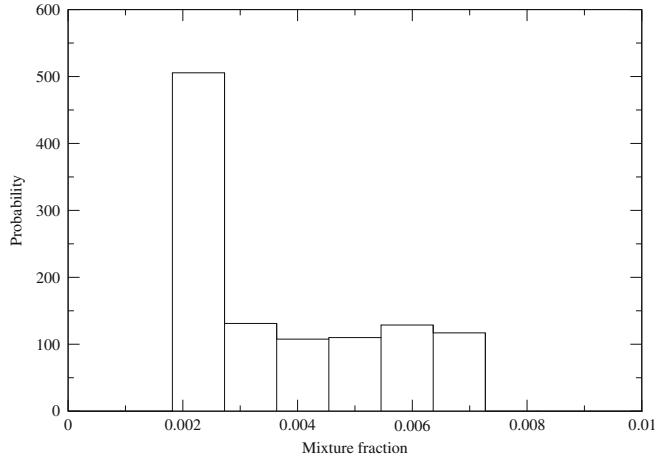

(c) Mixture fraction

Fig. 11. Pdf of velocity and mixture fraction at spot A ($z = 20$ mm, $r = 15$ mm), during the sparking moment. Sparking time = 0.09486 s.

ignition. The kernel gets advected downstream by the axial component of velocity and also spreads out radially, as seen at t 1 ms in Fig. 12. The intense burning core region is advected by the strong axial velocity. In the meantime, a part of the developing kernel is taken within the recirculation zone, and this portion experiences a flow reversal and travels toward the bluff body. At t 10 ms, the initial intense core region has been completely convected away from the domain, whereas the flame starts developing inside the CRZ from the trapped part of the kernel. Inside the CRZ, the recirculating bubbles transport the reaction zone radially outward and thus ignite the isostoichiometric surface. Between 10 and 45 ms after sparking, the flame develops inside the CRZ. At t 45 ms, a stable flame is obtained. The time taken by the ignition kernel from the sparking moment to establish a fully developed flame is about 45 ms for this ignition spot, which is the same duration as the one reported in the experimental results (see Fig. 14 in [27]).

5.2. Point B: $z = 27$ mm, $r = 0$ mm

This point is located downstream of the CRZ, at a location where the flammability factor is high (85%). In the experiment, while the probability of getting a successful kernel is high (over 30%), the probability of getting an established flame is low (below 10%). Table 1 gives the time averaged flow and mixing field values of this ignition spot. The flow here is relatively less intermittent, at least compared to the previously discussed ignition position. The mean axial and radial velocities are also small (Fig. 2a and b), which should be favorable for the development of the ignition kernel. The velocity at this point is under the influence of the time evolution of the CRZ; this makes the kernel to experience advection toward or away from the CRZ, leading to a successful or a failed ignition event, respectively. Fig. 13 shows the time history of velocities and mixture fraction at this ignition spot. The axial velocity is always positive in this region, as this zone is located downstream relative to the rearward stagnation point. Beside the time averaged radial component is nearly zero, the LES resolved instantaneous radial velocity shows an oscillating trend ranging from negative to positive values due to the interactions with recirculating bubbles. The mixture fraction stays close to the stoichiometric value of 0.055, suggesting that most of the sparking attempt will result in a successful kernel. The time instants analyzed are t_s 0.1393 s and t_s 0.1534 s, which, respectively, resulted in successful and failed ignition, as marked in Fig. 13.

From the time history of flow variables, it is observed that if this ignition spot always faces positive axial velocity, there are also few instances where the axial velocity is very close to zero. Hence, only when the spark is imposed when the axial velocity vanishes, the kernel has a chance to produce an established flame before getting blown out. One of such time instants is t_s 0.1393 s. The axial velocity averaged during the spark duration (400 μs) stays small (see Table 2), close to the premixed flame propagating velocity at stoichiometry (0.4 m/s).

The kernel evolution from $t_s = 0.1393$ s is shown in Fig. 14. The local streamline issued from the spark location indicates that the kernel movement is perpendicular to the burner axis, allowing the kernel to grow in an almost stoichiometric region. At 0.16 ms after sparking, the kernel has maintained its spherical shape, centered at the spot B (z 27 mm, r 0 mm). After 0.7 ms, the kernel has moved from the ignition spot, though facing a positive axial velocity. As the mixture is almost stoichiometric here, the burning velocity is high enough to help the kernel propagate against the flow. The flow advection and kernel propagation result in an edge flame like structure with a burning tail oriented downstream. After 3 ms, a part of the kernel has reached the rearward stagnation point and is subsequently taken inside the CRZ, where the flow is axially negative. After 5 ms, the trapped part of the kernel inside the recirculation zone is developing, but with a lesser intensity, as the mixture here is close to the rich flammability limit. In the subsequent time instants, the strong turbulence inside the CRZ stirs and distributes the reaction zone and thus results in complete lighting of the flame.

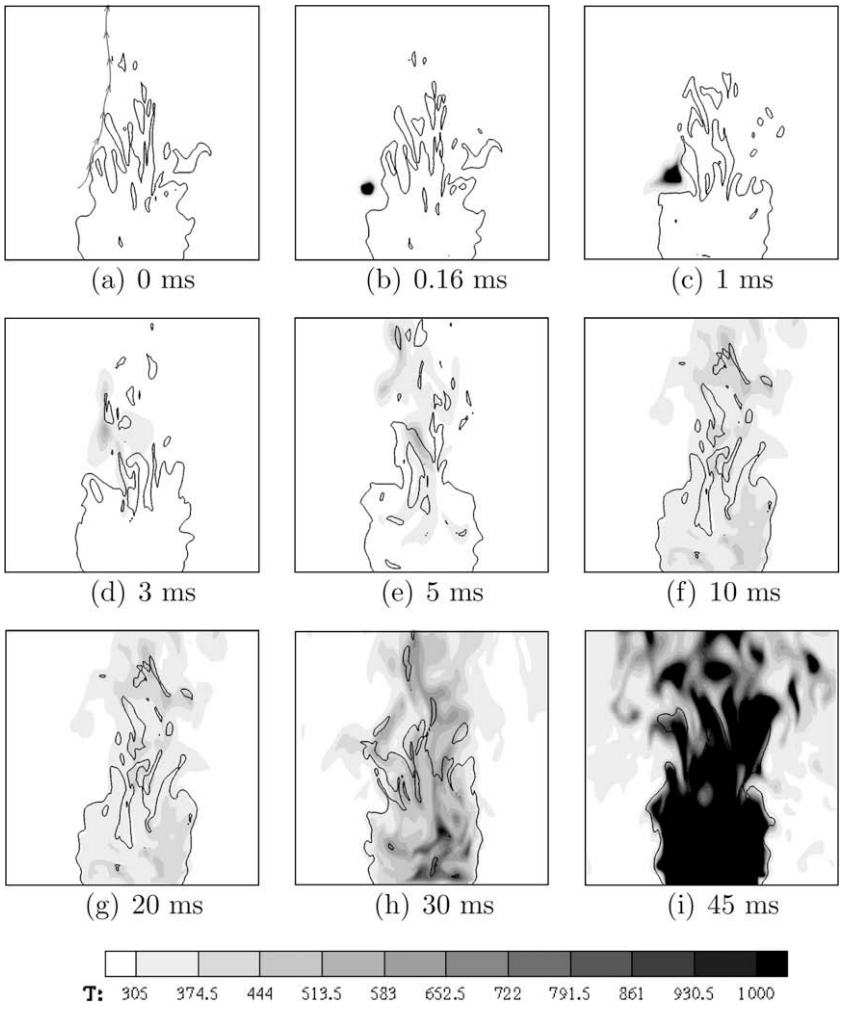

Fig. 12. LES-resolved instantaneous snapshots of temperature after sparking at spot A (z = 20 mm, r = 15 mm). Sparking time 0.09486 s (in Fig. 8), in caption the relative time after the ignition event. Solid black line: isoline of stoichiometric mixture fraction. Image covers the domain dimension of 70 × 70 mm.

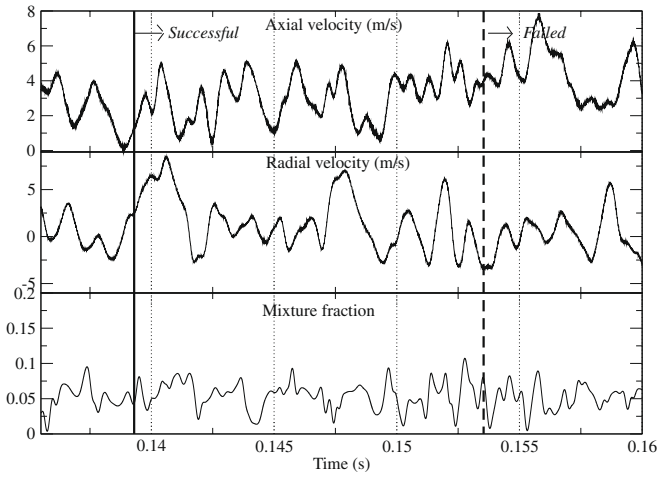

Fig. 13. Time history of velocities and mixture fraction at spot B (z = 27 mm, r = 0 mm). Continuous line: favorable time instant. Dashed line: nonfavorable time instant.

This location turned out to be an unsuccessful ignition spot at a different time instant, t_s = 0.1534 s. There, the mixture fraction is well within the flammability limit, ensuring local ignition. On the other hand, the axial velocity shows a strong positive value, which stays close to 4 m/s during the sparking instant (Fig. 13). The close to stoichiometry mixture fraction combined with the high axial velocity (see Table 2) suggests that the spark will generate a devel oping kernel but that this kernel will get blown away. This is in deed what is observed in Fig. 15, showing the evolution of the flame kernel after ignition. At 1 ms after ignition, the flame kernel has already moved approximately 3 mm downstream from the ignition spot. The kernel axially propagates against the flow and takes an elliptical shape. However, the kernel fails to reach the stagnation point, as it does not possess enough propagation speed to face the increasing axial velocity. After t 3 ms, the kernel while still growing in size, is further carried downstream by the flow. In successive time instants (see t 10 ms and 20 ms in Fig. 15) the flow convects the flame away and finally a failed igni tion procedure is achieved.

5.3. Point C: z = 25 mm, r = 0 mm

Like point B, point C is outside of the CRZ zone. At this loca tion, an 85% flammability factor is found both in experiment and in LES. The experiment evidences a probability of a successful flame kernel close to 40%, as observed at the point B, but the probability of full burner ignition is higher (20%) than at point B. Because axial velocities close to zero or negative are more probable at point C than at point B (see time history of flow

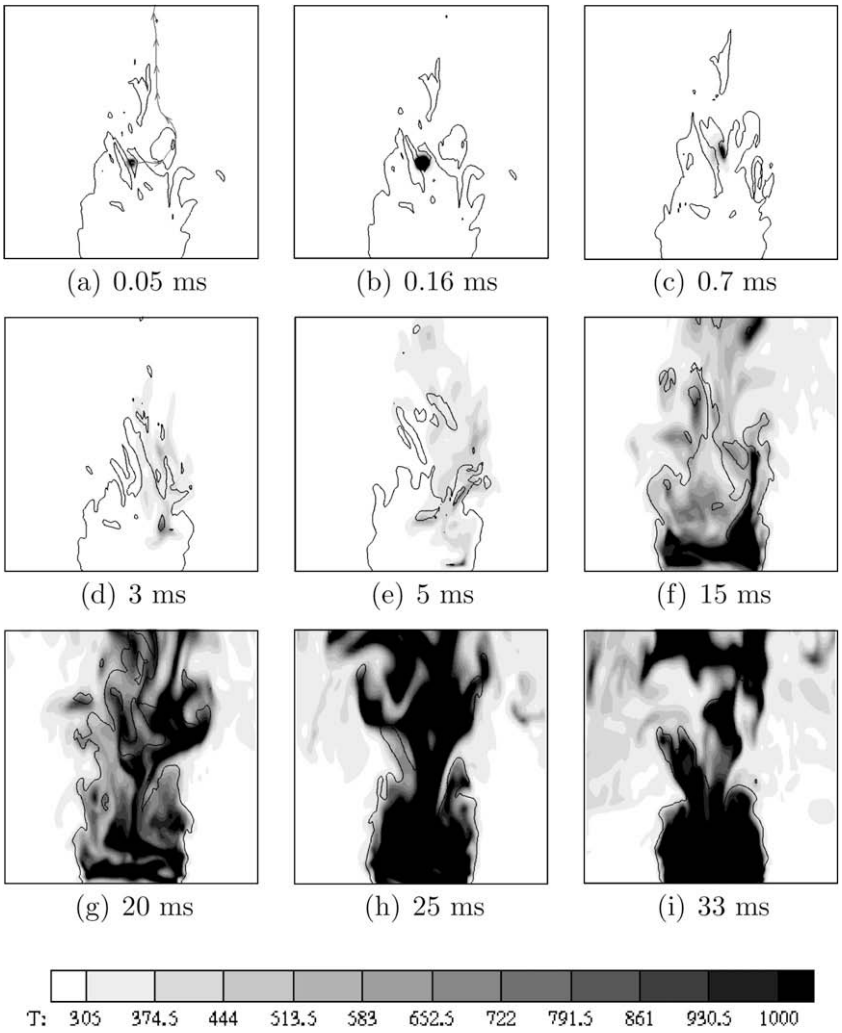

Fig. 14. LES-resolved instantaneous snapshots of temperature after sparking at spot B (z = 27 mm, r = 0 mm). Sparking time = 0.1393 s (in Fig. 13), the relative time after the ignition event. Solid black line: isoline of stoichiometric mixture fraction. Image covers the domain dimension of 70 × 70 mm.

variables in Fig. 16), the chances of getting ignition are higher independent of the local mixture fraction, which is roughly the same at both locations.

Fig. 17 shows the planar and three dimensional contours of temperature, displaying the behavior of the ignition kernel at this spot, while sparking at t_s = 0.13765 s, a time instant where the axial velocity is negative. A quite large portion of the kernel is first convected toward the bluff body (t 1.8 ms), with a first increasing and then decreasing negative axial velocity. The devel opment of the burning kernel during this advection is relatively slow, because it faces a mixture that becomes progressively rich. Nevertheless, an important deformation of the kernel is observed in the three spatial directions. At about t 5 ms, the kernel is carried close to the bluff body and also radially away from the burner axis by the counterrotating recirculating bubbles. At about 10 15 ms, the flame starts appearing at the edges of the CRZ, burning along the isosurface of the stoichiometric mixture frac tion. At 14.9 ms, the flame base is established at the bottom of the CRZ. At 25 ms after sparking, the flame is fully established and will not globally change at latter times (shown for 45.5 ms). The temperature iso surface allows for observing the flame surface wrinkling induced by the high turbulence level. The global path of flame development reported here is in line with the observations made in the experimental work, which could be verified from the high speed camera frames shown in Fig. 15 of [27]. Apart from the fast camera images, OH PLIF (pla nar laser induced fluorescence) images at closer time instants are also reported by the experimentalist, to visualize the flame struc ture during ignition kernel evolution; in the simulations, the in tense reaction zone is characterized by strong heat release. Fig. 18 shows the evolution of the source term of the energy equation, which could be compared against the OH PLIF image of the experiment given in Fig. 18 of [27]. After 1 ms, the kernel, which has hardly moved from its initial position, appears dis torted by the strong turbulence prevailing at the top of the CRZ. The flame kernel experiences acceleration (t 3 ms) followed by deceleration (t 5 ms) along the burner axis during its travel toward the bluff body. At t 7 ms, the kernel reaches the region close to the bluff body, where the axial velocity is almost zero. The flame then stays at the same axial position, but starts spread ing in the azimuthal direction by igniting the stoichiometric mix ture found close to the bluff body lip (t 9 ms). At a further time, the main stream carries the burning flame pockets downstream, while a part stays entangled into the CRZ. At t 22 ms, the reac tion zone exhibits a patchy distribution, which is spreading inside the CRZ as well as in the region beyond the rearward stagnation zone. At t 30 ms, the reaction zone is active mostly at the downstream edge of the main flow, whereas within the CRZ it is diminished, as the CRZ contains mostly the recirculated burnt products at this stage. The computed LES resolved instantaneous

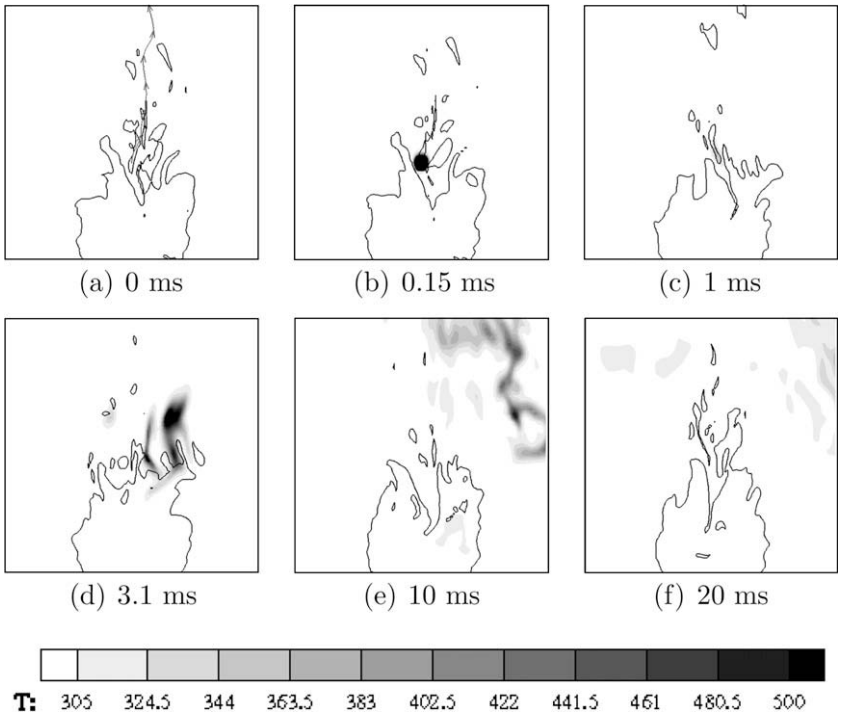

Fig. 15. LES-resolved instantaneous snapshots of temperature after sparking at spot B ($z = 27$ mm, $r = 0$ mm). Spark time = 0.1534 s (in Fig. 13). Solid black line: isoline of stoichiometric mixture fraction. Image shows the domain dimension of 70 × 70 mm.

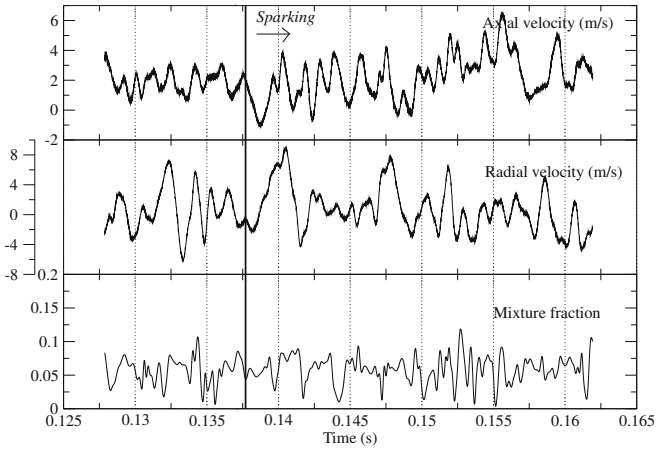

Fig. 16. Time history of velocities and mixture fractions at spot C ($z = 25$ mm, $r = 0$ mm). Continuous line: favorable time instant.

flame evolution during the first stage of its development appears to be faster than the evolution observed in the experimental work (though rigourous qualitative comparison of instantaneous frames is not feasible). These simulations are done with $\zeta = 0$ in Eq. (23), thus neglecting strain rate effects in the description of the chemical response of the young kernel, this may explain part of the discrepancy. This point is discussed in a following section. Also in the experiment, the introduction of a sparking device in this sensitive zone may also have a non negligible effect on the flow dynamics. Apart from the little discrepancies noticed in the initial stage, the global flame evolution is satisfactorily reproduced by the simulation, considering the complexity of the phenomena involved in the overall process. Failed ignition cases occurring for positive axial velocity at the sparking time are not discussed in detail, since they are similar to point B (Fig. 15).

5.4. Point D: $z = 15$ mm, $r = 17$ mm

The ignition spots discussed so far cover the regions with either low flammability factor or very high flammability factor. But there are also certain burner regions where the flammability factor in the experiment is zero, whereas the probability of burner ignition is nonzero. Interestingly, as per the experimental findings, these regions are found to be the most suitable ignition spots for complete lighting of the burner. The region covered by $z = 11$ 18 mm and $r = 14$ 18 mm is the one with peak probability of ignition success (see Fig. 22a of [27]). Referring to Fig. 3, this region envelops the iso stoichiometric surface of mixture fraction featuring strong axial velocity and turbulence. It can also be seen that the streamlines (based on average axial and radial velocities) issuing from this zone (Fig. 3) are bent toward the CRZ and the stoichiometric line. This indicates that the energy deposited there, has a great probability of entering a near to stoichiometry zone and then getting trapped in the CRZ, once the flame kernel has begun to grow. On the other hand, spark deposits inside the zone delimited by the stoichiometric surface have a lesser probability to ignite the burner, since the energy will be directly sent in a rich mixture environment without encountering very favorable stoichiometric mixtures on their trajectory.

Spot D ($z = 15$ mm, $r = 17$ mm) is one point with zero flammability and a nonzero probability of full burner ignition. Fig. 19 shows the velocity and mixture fraction history of this ignition spot. The mean axial velocity features a positive value, which sometimes spikes to very high levels, as one is looking here at the outer shear layer of the annular jet. The mean radial velocity is almost zero, with considerable fluctuations due to the flapping associated with the flow instabilities developing at the shear layer of the jet. The mixture fraction is very small, with a mean value of about 0.0067 (Table 1), which is far from the lean flammability limit, and thus the flammability factor is nearly null (0.3%) at this location. Nevertheless, the probability of getting a fully established

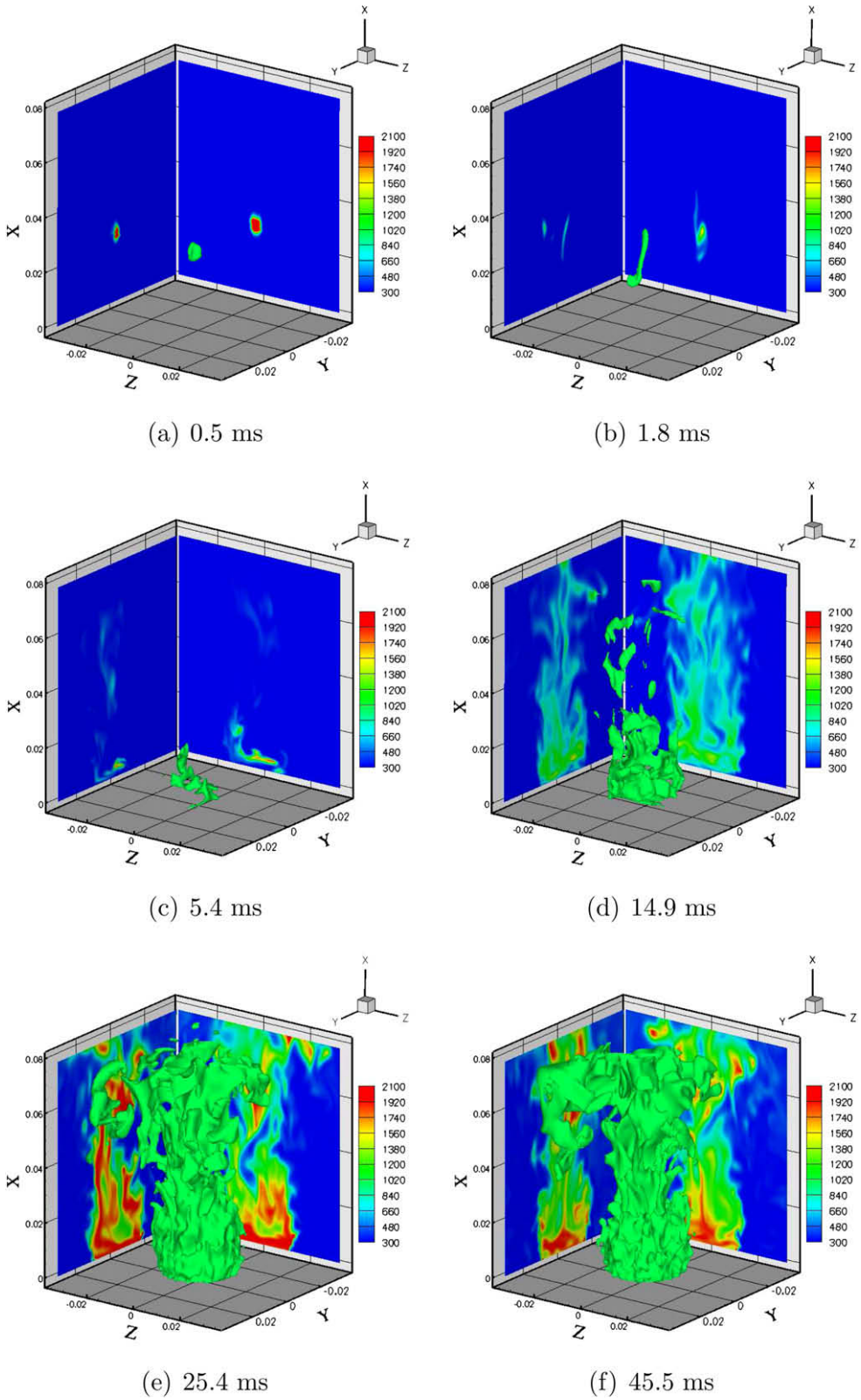

Fig. 17. LES-resolved instantaneous snapshots of temperature after sparking at spot C ($z = 25$ mm, $r = 0$ mm). The isosurface corresponds to 1000 K. The planar views are in two orthogonal planes including the burner axis (X axis on the figure). Image shows the domain dimension of 70 × 70 mm, in caption the relative time after the ignition event.

flame, or a successful flame initiation, is around 70% in the experiment. The evolution of the ignition kernel at a typical time instance (t_s 0.133 s) has been investigated with LES. The time averaged velocities and mixture fraction over the spark duration (Table 2) show that the axial velocity is high (10.26 m/s on average) and that the radial velocity is very small on average (0.06 m/s), while the mixture fraction remains well below flamma bility limit. In Fig. 20, it is observed that the streamline based on LES resolved instantaneous axial and radial velocities, 0.14 ms after spark, is oriented toward the stoichiometric region. Though

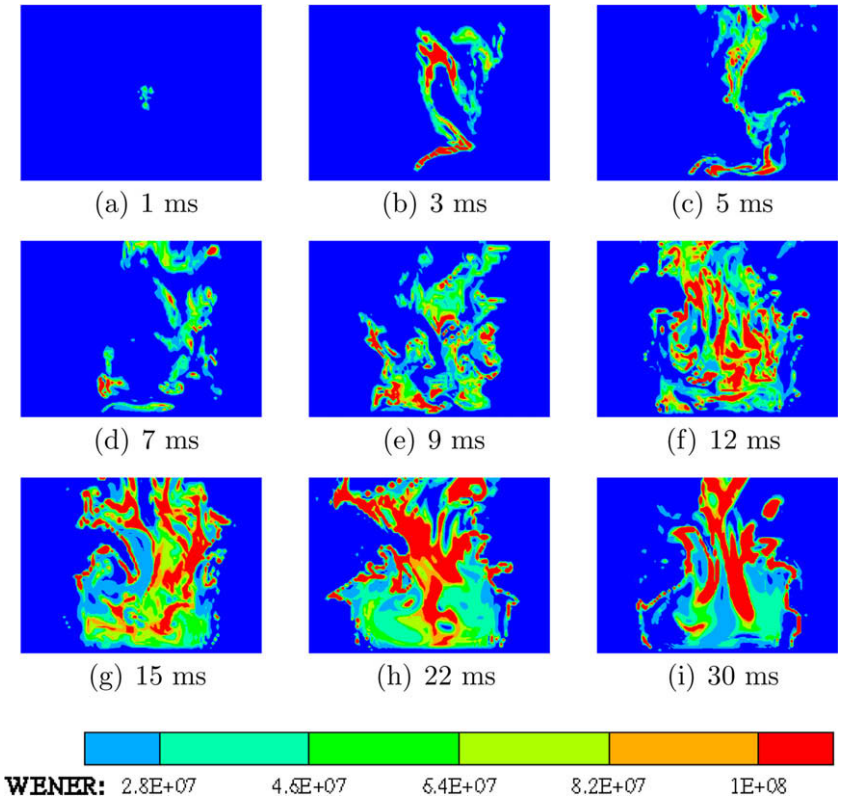

Fig. 18. LES-resolved instantaneous snapshots of reaction zone after sparking at spot C ($z = 25$ mm, $r = 0$ mm). Image shows the domain dimension of 70 × 50 mm (J/m^3).

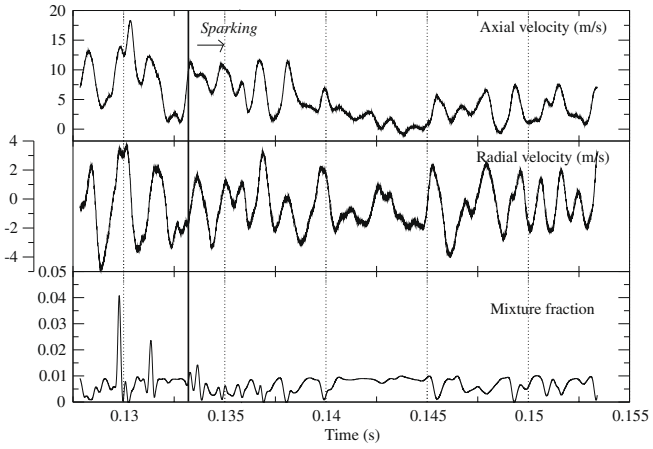

Fig. 19. Time history of velocities and mixture fractions at spot D ($z = 15$ mm, $r = 17$ mm).

the kernel at t 0.13 s is still spherical, the strong axial transport has already started convecting the deposited energy. After 1 ms, the kernel has moved axially of about 3 5 mm and has grown bigger due to axial convection as well as diffusion. The radial velocity in this region is negative, toward the burner axis, and thus the kernel can ignite a substantial portion of the iso stoichiometric mixture fraction surface. At further time instants, the flame propagates rapidly following the stoichiometric mixture fraction surface and a portion of it gets trapped inside the CRZ. Further development of the flame is similar to the development discussed for the successful ignition case at spot A (z 20 mm, r 15 mm) after 10 ms (in Fig. 12); however, there is a key difference on the role played by the transport effect between these locations. In the spot A, as the flammability factor is nonzero, the spark can locally initiate combustion, which is then further promoted by convection, whereas, in the present spot D (z 15 mm, r 17 mm), the spark does not find an immediately ignitable mixture, as the flammability factor is zero between the electrodes. The spark energy has first to be carried by the flow toward the isostoichiometric surface to light the burner. This obviously delays the total time needed to get a fully established flame for this ignition spot, when compared to point A.

At the instant which has been probed, the axial velocity averaged over the spark time is twice its converged time averaged value; the averaged radial velocity over the spark time is slightly positive, while the converged one is negative. The time instant tested therefore presents conditions less favorable to successful ignition than other time instants. This is clearly shown in Fig. 19, where instants figuring a quite low axial velocity and a negative radial velocity are much more probable. In consequence, if a spark at t_s 0.133 s has been able to ignite the whole burner despite high axial velocity and vanishing radial velocity, at most other time instants having better velocity conditions, sparking will lead to successful ignition and this indeed what is observed in the experiment (70% probability of success).

5.5. Other locations

Others characteristic sparking regions inside the CRZ ($z < 10$ mm) have been simulated; in these locations, the equivalence ratio is quite rich (around Z 0.08 for equivalence ratio 1.6), the axial velocity is negative, and the turbulence level is higher. Sparking close to the wall, as in the experiment, the ignition probability is close to zero in LES; the initiated kernel has a slow development due to the rich mixture; it is easily torn and scattered by turbulence and quickly transported toward the bluff body, which is a cold boundary condition that quenches the flame.

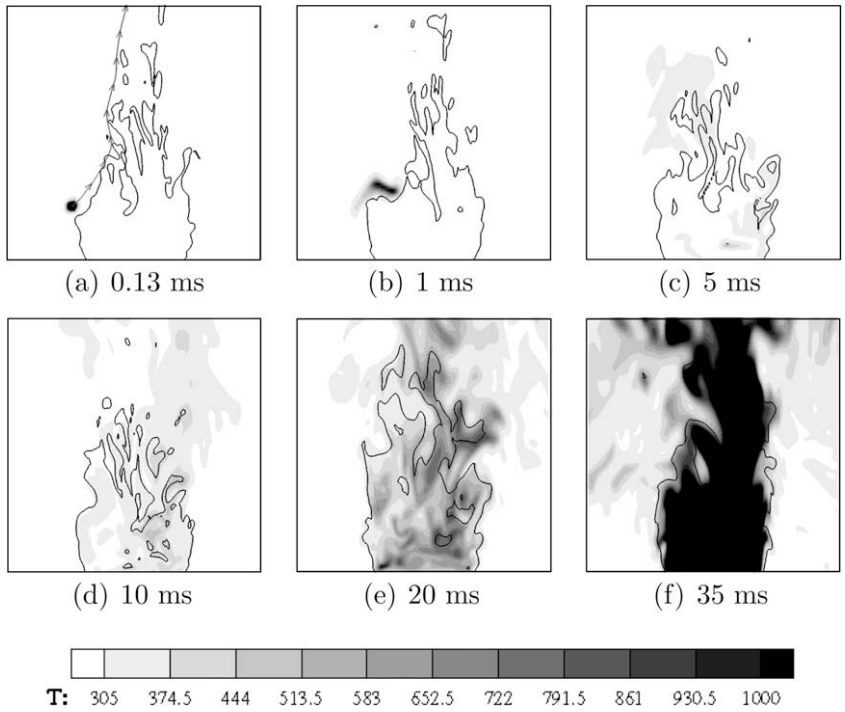

Fig. 20. LES-resolved instantaneous snapshots of temperature after sparking at spot D ($z = 15$ mm, $r = 17$ mm). Sparking time = 0.1330 s. Solid black line: isoline of stoichiometric mixture fraction. Image shows the domain dimension of 70 × 70 mm. The relative time after the ignition event.

Sparking within CZR, but not close to the wall, simulations lead to ignition for most of the locations, a result in contradiction with experiment. From the measurements, it was concluded that the high level of turbulence and the closeness to the rich flammability limit provide hostile environment for the flame kernel, which then becomes very sensitive to stretch. This latter ingredient was not explicitly included in simulations discussed so far (ζ 0 in Eq. (18)); in the next section, the impact of the stretch rate correction in the modeling is studied.

6. Ignition kernel development with inclusion of flow straining effects

It was reported in Ahmed's experiments that the ignition kernel could get quenched by local flow fluctuations. Typically, inside the central recirculation zone where the mixture is relatively rich, there exists a considerable difference between the flammability map and the ignition probability map. Inside the CRZ, the axial velocity always plays a positive role by transporting the kernel in the negative axial direction, but still the ignition kernel fails to develop and fully light the burner. Referring to Fig. 4a and b, the velocity fluctuations inside the CRZ are quite intense. The premixed flame propagation speed in the rich mixture prevailing inside the CRZ is several times lower than in the stoichiometric mixture, making the kernel more sensitive to the local turbulence, which can eventually quench the small burning zone, as evidenced by the experimental findings. The correction proposed in Eq. (18) for stretch is now activated with nonzero ζ and the LES response for various sparking points is analyzed.

6.1. Point E: z = 20 mm, r = 0 mm

The first spot (referred hereafter as point E) selected to analyze the proposed strain correction is located in a region inside the CRZ, where the flammability is high (higher than 85%), the axial velocity is negative, and the mixture is quite rich (see Table 1). In the experiment, it was found that the ignition probability and the probability of successful flame kernel initiation were identical at this location. In other words, when the sparking results in the generation of a visible burning region that can survive long enough, the full ignition turns out to be successful, because the ignition kernel is never convected downstream by the axial component of velocity. In contrast, when the flame kernel is quenched for the same sparking point, it happens at the very first stages of its development, when its diameter is still less than 3 mm [27].

The time history for this ignition spot (Fig. 21) confirms that in the LES, the conditions are favorable for ignition and kernel development at most of the time instants. The two time instants analyzed in this case are t_s 0.1321 s and t_s 0.13765 s, which resulted in a quenched kernel and a successful ignition, respectively. The velocity and mixture fraction during the spark duration are given in Table 2. It is to be noted that the mixture fraction dur

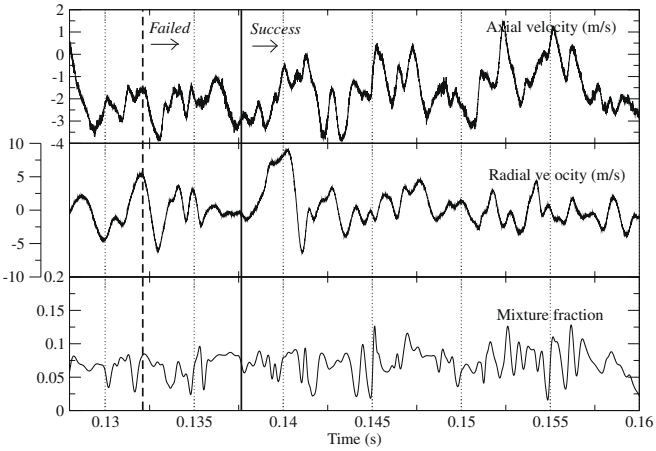

Fig. 21. Time history of velocities and mixture fractions at spot E ($z = 20$ mm, $r = 0$ mm).

ing both of these time instants is relatively rich, even though it is within the flammability limit.

Fig. 22 shows the evolution of the flame kernel during the unsuccessful time instants, resulting in kernel quenching. The streamline issued from the spark location confirms that the ten dency of the kernel will be to travel toward the bluff body. This is what is observed: the spark develops first into a round kernel (0.2 ms), which gets displaced through the CRZ, where the mixture remains appreciably rich, with a mean mixture fraction value of about 0.08. The correction factor, $\zeta(\tilde{Z})$, applied to the filtered burn ing rate is quite high for this equivalence ratio (Fig. 1). This high va lue of $\zeta(\tilde{Z})$ combined with the high stretch rate Ψ_K induced by local turbulence has a negative impact on the kernel. From Fig. 22, it can be observed that 1 ms after sparking, the kernel has shrunk in size due to local high turbulence. After 5 ms, the kernel is quenched with no more sign of positive development. It is to be noted here that the observed displacement of the flame kernel is only due to flow advection and not due to flame propagation. (The kernel would have disappeared remaining in the same position, if the time averaged velocities had been zero.)

Fig. 23 shows the successful evolution of an ignition kernel at the same point E, but at a different time instant, as marked in Fig. 21. The streamline emanating from that in the ignition spot is not very different from the previous case, where the kernel got quenched. However, the local mixture fraction during the sparking moment is about 0.07, which is leaner than in the previous case; the reduction in burning rate due to flow straining is then 10 times smaller than for Z 0.08 (Fig. 1). From Fig. 23, after 1 ms, the spark kernel appears much bigger, although the local strain rate correc tion is still applied to the source terms (Eq. (18)).

The experimental reporting is thus reproduced, where the ker nel exhibits a serious reduction in size after 1 ms, in the cases where quenching is observed. In the experiment, for the successful test cases, after 1 ms, the kernel size either remains the same, or sometimes slightly bigger (Fig. 23 of [27]). The same behavior is observed in this LES in Figs. 22 and 23. The further global evolution of the kernel for the successful time instants is very similar to what is obtained at point C, because the convective field in the CRZ is similar, though there is a definite reduction of the rate of kernel growth due to the introduction of the strain correction, which in creases the time taken by the kernel to fully light the burner.

To quantify the complete flame establishment duration, the time evolution of the volume averaged source term of energy is introduced. This quantity is displayed in Fig. 24 for point E. For the successful case, the volume averaged source term shows linear and slow growth until 25 ms. Between 20 and 30 ms, strong reac tion zones are visible near the isostoichiometric surface (Fig. 23), which eventually accelerates the burning. Meanwhile, the temper ature inside the CRZ increases, and viscosity also increases and thus damps the fluctuations, thereby accelerating the burning rate. Between 25 and 50 ms, the burning rate shows a steep increase due to the tangential flame spreading through the stoichiometric mixture, shown by the stiff slope of the evolution of total energy source term, as seen in Fig. 24. The kernel evolution observed in this case closely matches with the experimental finding in a spot inside the CRZ (Fig. 15 of [27]). The time taken for complete light ing of the burner for this case was found to be around 50 ms, in close agreement with the experiment. Fig. 24 also shows the source term evolution of the quenched case at this same ignition spot, due to local flow straining. The very quick disappearance of the flame kernel is clearly observed, only the peak corresponding to the energy deposited by the spark is visible. The volume aver aged source term of energy is also plotted for a spark at the same instant (t_s 0.1321 s), when the original PCM FPI approach is em ployed without accounting for stretch correction. It is observed (Fig. 24 bottom) that a full lighting of the burner is obtained with this closure. Further, in the simulations featuring the original ap proach (ζ 0 in Eq. (23)), it has proved impossible to obtain a quenched kernel at point E, whatever the time instant tested and the corresponding local conditions.

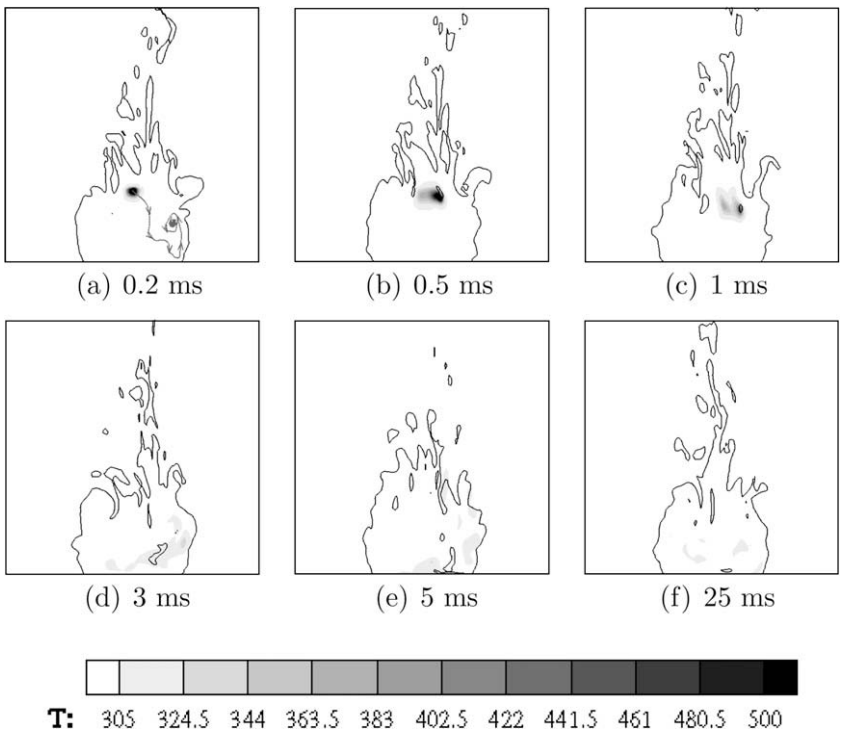

Fig. 22. LES-resolved instantaneous snapshots of temperature after sparking at spot E (z = 20 mm, r = 0 mm), showing kernel quenching. Sparking time = 0.1321 s. Solid black line: isoline of stoichiometric mixture fraction. Image shows the domain dimension of 70 × 70 mm. Time is the relative time after the ignition event.

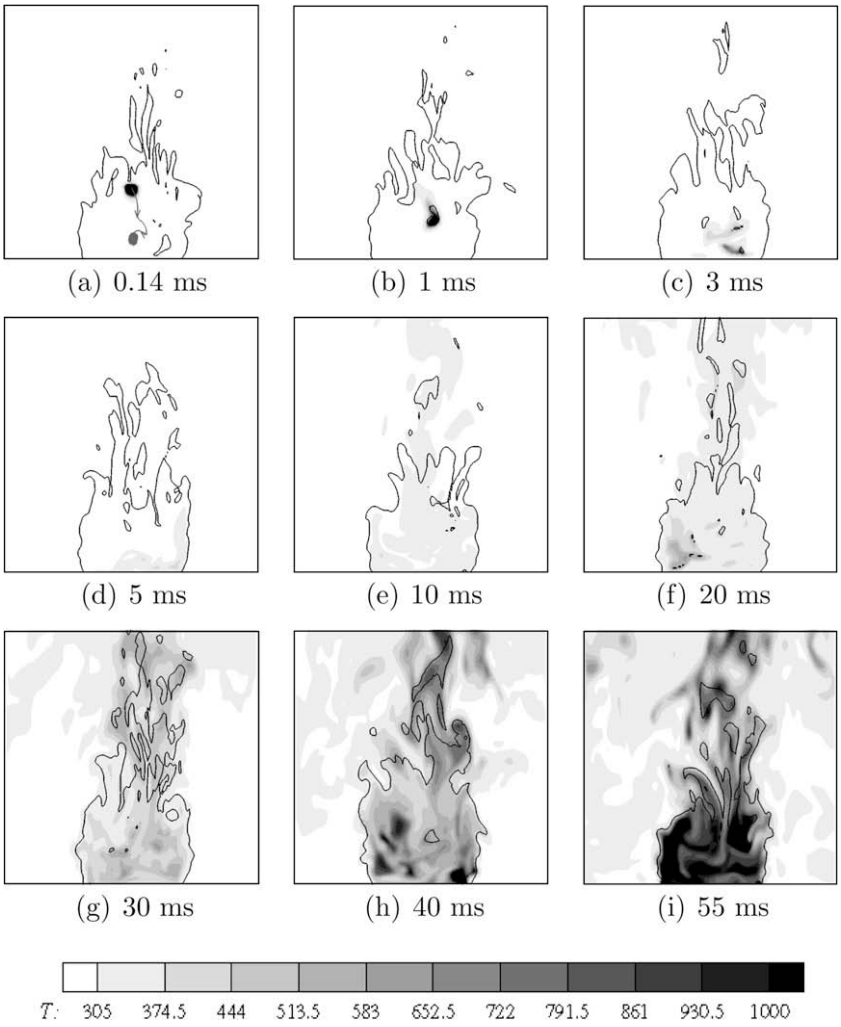

Fig. 23. LES-resolved instantaneous snapshots of temperature after sparking at spot E ($z = 20$ mm, $r = 0$ mm), showing positive kernel development. Sparking time = 0.13765 s. Solid black line: isoline of stoichiometric mixture fraction. Image shows the domain dimension of 70 × 70 mm, the relative time after the ignition event.

6.2. Strain rate effects on flame establishment time

According to results discussed above, the stretch rate correction (Eq. (18)) captures the slowdown of flame kernel development and the variability of ignition, as was shown for point E, where both ignition and quenching can be found with this correction. It has also been verified for all previously tested points (A D) and spark ing time instants, that the success or failure of the spark igniting the burner is not affected by the improved model. This is expected since the correction brought by Eq. (18) stays negligible for flame development, arising mostly over stoichiometric mixture.

In some cases, there is a non negligible difference in the rate of flame kernel development, between the simulations with and without flow straining effects. To illustrate the reduction in burn ing rate, two simulations with ζ 0 (no stretch effect) and nonzero ζ (stretch as given by Eq. (18)) are performed from the same initial conditions for the ignition spots D (z 15 mm, r 17 mm) and E (z 20 mm, r 0 mm) at time instants where ignition is success ful for both approaches. The time evolution of the integrated en ergy source term is displayed in Fig. 25 at point D, starting from the sparking instant. Without accounting for strain, intense burn ing starts rapidly after the spark; the total establishment time is about 30 40 ms. Accounting for flow straining effects, the flame establishment duration is between 55 and 70 ms. This difference predominantly arises from the initial part of the kernel develop ment period, which is much slower in the case accounting for strain effects, the reduction in burning rate attributed to the flow straining is thus dominant for young flame kernels. A similar lengthening of the flame establishment time is observed for point E in Fig. 24 top. This is the reason why the kernels are often quenched when the sparking is inside the CRZ (for instance, point E, discussed before), since at this location, they face high turbu lence levels while being of small size. A parallel can be made with experimental observations, which concluded that a young kernel is more prone to quench compared to a developed one, for the same turbulence intensity [83]. Therefore, if an ignition kernel can grow sufficiently before being inducted into highly strained and rich mixtures within the CRZ, it is not quenched. This has been ob served for spot ignition D, when the kernel has grown substantially by spreading through the stoichiometric surface, before entering the recirculation zone to promote full ignition of the burner.

7. Summary

Large eddy simulation of forced ignition of an annular bluff body burner has been conducted; the objective was to estimate the prediction capabilities of LES with tabulated detailed chemistry for a fully transient phenomenon, which also features strong vari ability of its statistical properties. The bluff body character of the flow makes it complex, at least compared to sparking in a simple

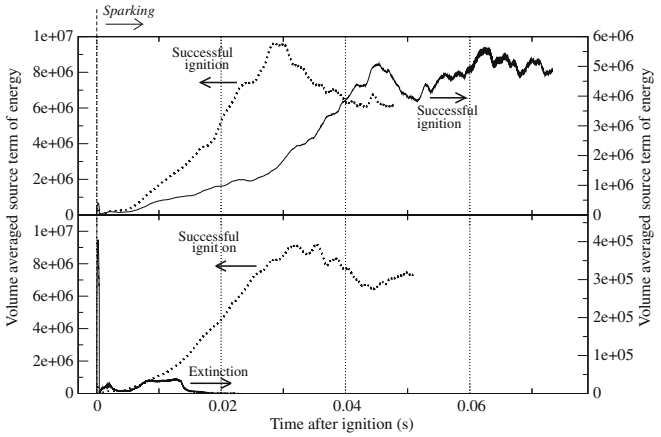

Fig. 24. Time evolution of volume-averaged energy source term for both successful and unsuccessful case for spot E ($z = 20$ mm, $r = 0$ mm). Time shows the relative time after the sparking instant. Black dotted line: conventional PCM-FPI closure without accounting for flow-straining effects. Black solid line: new closure accounting for flow-straining effects.

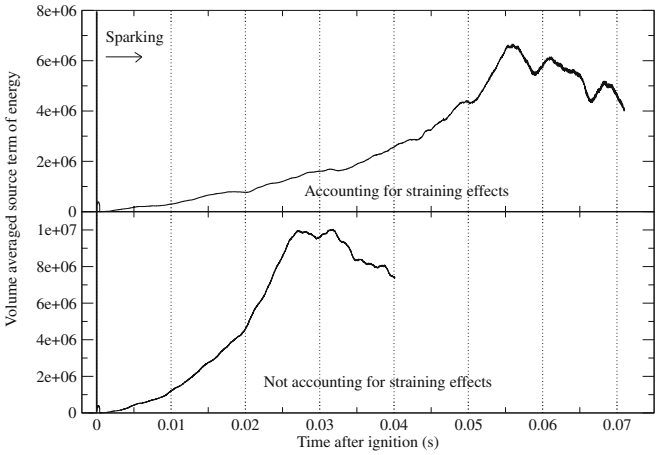

Fig. 25. Time evolution of volume-averaged source term with and without accounting for flow-straining effects. The ignition spot D ($z = 15$ mm, $r = 17$ mm) is located on the isostoichiometric surface. Time is relative time after sparking instant.

jet, where the birthing flame can only move upstream or downstream. In the bluff body having unsteady recirculation zones, four major scenarios are observed with LES, when sparking in a zone where the fuel/air mixture is close to flammability limits:

(1) Persisting high streamwise velocity levels right after sparking will transport the flame kernel away from the recirculation zone, and full ignition of the burner cannot be reached.

Convection by radial velocity toward the center recirculation zone or sparking directly in this zone are essential ingredients for the kernel to develop. However, two limitations exist:

(2) Close to the bluff body wall, the flame may be quenched.
(3) High strain rates encountered by small kernels in too rich areas of the central recirculation zone may jeopardize the full ignition process.

And finally

(4) The highest probability for full ignition of the burner is reached for a flame initiated from sparking in the very vicinity of the stoichiometric zone, on the lean side outside the main recirculation zone and axially located on the half bottom of the recirculating bubble. Convected toward the burner axis, this flame kernel enters the recirculation zone, after crossing the stoichiometric line. The flame kernel is then sufficiently developed and is much less sensitive to strain when facing the central recirculation zone's rich mixture and high turbulence level.

These observations globally agree with experiment, and comparisons with available measurements show that strain rate effects need to be included in the modeling of the filtered burning rate; a correction to the usual presumed probability density function modeling associated with tabulated chemistry has been discussed and validated to address this point. The use of liquid fuel could seriously complicate these scenarios of ignition, since fuel spray combustion features specific properties [84,85].

Acknowledgments

Financial support by the European Commission through the project "Toward Innovative Methods for Combustion Prediction in Aeronautic Engines" (TIMECOP AE, AST5 CT 2006 030828) is gratefully acknowledged. The authors extend their kind acknowledgement to Dr. Ahmed and Prof. Mastorakos of Cambridge University, UK, for providing the experimental data for comparison and for many fruitful discussions. The computational resources were provided by CRIHAN (Haute Normandie) and GENCI IDRIS (CNRS).

References

[1] I. Esquiva-Dano, D. Escudie, Combust. Flame 142 (2005) 299–302.
[2] I. Glassman, Combustion, second ed., Academic press Inc, 1987, 1987.
[3] H. El-Asrag, S. Menon, Proc. Combust. Inst. 31 (2007) 1747–1754.
[4] C.D. Taglia, L. Blum, J. Gass, Y. Ventikos, D. Poulikakos, J. Fluid Eng. 126 (2004) 375–384.
[5] B. Patte-Rouland, G. Lalizel, J. Moreau, E. Rouland, Meas. Sci. Technol. 12 (2001) 1404–1412.
[6] I. Esquiva-Dano, H.T. Nguyen, D. Escudie, Combust. Flame 127 (2001) 2167–2180.
[7] Andres A. Chaparro, Baki M. Cetegen, Combust. Flame 144 (2006) 318–335.
[8] Y. Fujimoto, N. Yamasaki, JSME Int. J. 49 (2006) 1125–1132.
[9] M. Garcia-Villalba, J. Frohlich, W. Rodi, in: Proceedings of the 4th International Symposium on Turbulence and Shear Flow Phenomena, Williamsburg, USA, 2005.
[10] M. Freitag, M. Klein, M. Gregor, D. Geyer, C. Schneider, A. Dreizler, J. Janicka, Int. J. Heat Fluid flow 27 (2006) 636–643.
[11] S.B. Pope, Turbulent Flows, Cambridge University Press, 2000.
[12] J. Janicka, A. Sadiki, Proc. Combust. Inst. 30 (1) (2005) 537–547.
[13] R.W. Bilger, S.B. Pope, K.N.C. Bray, J.F. Driscoll, Proc. Combust. Inst. 30 (2005) 21–42.
[14] H. Pitsch, Annu. Rev. Fluid Mech. 38 (2006) 453–482.
[15] V. Raman, H. Pitsch, Combust. Flame 142 (2005) 329–347.
[16] A. Kempf, R.P. Lindstedt, J. Janicka, Combust. Flame 144 (2006) 170–189.
[17] B.B. Dally, A.R. Masri, R.S. Barlow, G.J. Fiechtner, Combust. Flame 114 (2) (1998) 119–148.
[18] B.B. Dally, D.F. Fletcher, A.R. Masri, Combust. Theory Model. 2 (2) (1998) 193–219.
[19] Y.Z. Zhang, E.H. Kung, D.C. Haworth, Proc. Combust. Inst. 30 (2) (2005) 2763–2771.
[20] J.P. Szybist, A.L. Boehman, D.C. Haworth, H. Koga, Combust. Flame 149 (1/2) (2007) 112–128.
[21] S. Richard, O. Colin, O. Vermorel, A. Benkenida, C. Angelberger, D. Veynante, Proc. Combust. Inst. 31 (2007) 3059–3066.
[22] Z. Tan, R.D. Reitz, Combust. Flame 145 (2006) 1–15.
[23] R. Dahms, T.D. Fansler, M.C. Drake, T.W. Kuo, A.M. Lippert, N. Peters, Proc. Combust. Inst. 32 (2009) 2743–2750.
[24] E.S. Richardson, E. Mastorakos, Combust. Sci. Technol. 179 (2007) 21–37.
[25] N. Chakraborty, E. Mastorakos, R.S. Cant, Combust. Sci. Technol. 179 (2007) 293–317.
[26] M. Boileau, G. Staffelbach, B. Cuenot, T. Poinsot, C. Bérat, Combust. Flame 154 (1/2) (2008) 2–22.
[27] S.F. Ahmed, R. Balachandran, T. Marchione, E. Mastorakos, Combust. Flame 151 (2007) 366–385.

[28] G. Lacaze, E. Richardson, T. Poinsot, Combust. Flame 156 (10) (2009) 1993–2009.
[29] A. Triantafyllidis, E. Mastorakos, R.L.G.M. Eggels, Combust. Flame 156 (2009) 2328–2345.
[30] P. Domingo, L. Vervisch, D. Veynante, Combust. Flame 152 (2008) 415–432.
[31] H.J. Sheen, W.J. Chen, J.S.J. Wu, Fluid Mech. 350 (1997) 177–188.
[32] F. Ducros, F. Laporte, T. Souleres, V. Guinot, P. Moinat, B. Caruelle, J. Comput. Phys. 161 (2000) 114–139.
[33] A.A. Wray, Minimal storage time-advancement schemes for spectral methods, Computational Fluid Dynamics Branch, NASA Ames Research Centre, Moffett Field, CA, 1986.
[34] S.F. Ahmed, Spark ignition of turbulent non-premixed flames. Ph.D. thesis, University of Cambridge, September 2006.
[35] M. Klein, A. Sadiki, J. Janika, J. Comput. Phys. 186 (2003) 652–665.
[36] T.J. Poinsot, S.K. Lele, J. Comput. Phys. 101 (1992) 104–129.
[37] J. Smagorinsky, Mon. Weather Rev. 61 (1963) 99–164.
[38] F. Ducros, P. Comte, M.J. Lesieur, Fluid Mech. 326 (1996) 1–36.
[39] F. Nicoud, F. Ducros, Flow Turbul. Combust. 62 (1999) 183–200.
[40] J. Galpin, A. Naudin, L. Vervisch, C. Angelberger, O. Colin, P. Domingo, Combust. Flame 155 (2008) 247–266.
[41] L. Vervisch, P. Domingo, M. Rullaud, R. Hauguel, J. Turbul. 5 (2004) 1–36.
[42] B. Fiorina, O. Gicquel, L. Vervisch, S. Carpentier, N. Darabiha, Proc. Combust. Inst. 30 (2005) 867–874.
[43] P. Domingo, L. Vervisch, S. Payet, R. Hauguel, Combust. Flame 143 (2005) 566–586.
[44] A.W. Vreman, B.A. Albrecht, J.A. van Oijen, R.J.M. Bastiaans, Combust. Flame 153 (3) (2008) 394–416.
[45] B. Fiorina, O. Gicquel, L. Vervisch, S. Carpentier, N. Darabiha, Combust. Flame 140 (3) (2005) 147–160.
[46] O. Gicquel, N. Darabiha, D. Thevenin, Proc. Combust. Inst. 28 (2000) 1901–1908.
[47] J.A. van Oijen, F.A. Lammers, L.P.H. de Goey, Combust. Flame 127 (3) (2001) 2124–2134.
[48] R.J. Kee, J.F. Gracer, M.D. Smooke, J.A.A. Miller, Fortran program for modeling steady laminar one-dimensional premixed flames, Technical Report, Report No. SAND87-8248 UC-4, Sandia National Laboratories, 1990.
[49] K.N.C. Bray, Proc. Combust. Inst. 26 (1996) 1–26.
[50] D. Bradley, P.H. Gaskell, X.J. Gu, Twenty-Seventh Symp. (Int.) Combust. 27 (1998) 849–856.
[51] D. Bradley, P.H. Gaskell, X.J. Gu, A. Sedaghat, Combust. Flame 143 (3) (2005) 227–245.
[52] L. Vervisch, G. Lodato, P. Domingo, Reliability of large-eddy simulation of nonpremixed turbulent flames: scalar dissipation rate modeling and 3D-boundary conditions, in: Quality and Reliability of Large-Eddy Simulations, ISBN No.: 978-1-4020-8577-2, Springer, Netherlands, 2008, pp. 227–237.
[53] G.P. Smith, D.M. Golden, M. Frenklach, N.W. Moriarty, B. Eiteneer, M. Goldenberg, C.T. Bowman, R.K. Hanson, S. Song, W.C. Gardiner, V.V. Lissianski, Z. Qin, Technical Report, 1999. Available from: <http://www.me.berkeley.edu/gri-mech>.
[54] T. Poinsot, Using direct numerical simulations to understand premixed turbulent combustion, in: Proceedings of the 26th Symposium (International) on Combustion, The Combustion Institute, Pittsburgh, 1996, pp. 219–232.
[55] S.H. Chung, C.K. Law, Combust. Flame 72 (3) (1988) 325–336.
[56] P. Clavin, Annu. Rev. Fluid Mech. 26 (1994) 321–352.
[57] L.P.H. de Goey, J.H.M. ten Thije Boonkkamp, Combust. Flame 119 (1999) 253–271.
[58] L.P.H. de Goey, R.M.M. Mallens, J.H.M. ten Thije Boonkkamp, Combust. Flame 110 (1997) 54–66.
[59] J.A.M. de Swart, G.R.A. Groot, J.A. van Oijen, J.H.M. ten Thije Boonkkamp, L.P.H. de Goey, Combust. Flame 145 (2006) 245–258.
[60] T. Poinsot, D. Veynante, Theoretical and Numerical Combustion, R.T. Edwards, Inc., 2005.
[61] J.H. Chen, H.G. Im, Twenty-Seventh Symposium (International) on Combustion, The Combustion Institute, 1998. pp. 819–826.
[62] C.J. Mueller, J.F. Driscoll, D.L. Reuss, M.C. Drake, Twenty-Sixth Symposium (International) on Combustion, The Combustion Institute, 1996. pp. 347–355.
[63] I.F. Huang, S.S. Shy, C.C. Chang, S.C. Li, C.M. Huang, Proc. Combust. Inst. 32 (2009) 1755–1762.
[64] M.Z. Haq, C.G.W. Sheppard, R. Woolley, D.A. Greenhalgh, R.D. Lockett, Combust. Flame 131 (2002) 1–15.
[65] N. Peters, Turbulent Combustion, Cambridge University Press, 2000.
[66] H. Pitsch, Combust. Flame 143 (2005) 587–598.
[67] R.J.M. Bastiaans, J.A. van Oijen, L.P.H. de Goey, Phys. Fluids 21 (2009) 015105.
[68] C.K. Law, G. Jomaas, J.K. Bechtold, Proc. Combust. Inst. 30 (1) (2005) 159–167.
[69] M. Thiele, J. Warnatz, U. Maas, Combust. Theory Modell. 4 (2000) 413–434.
[70] M. Thiele, S. Selle, U. Riedel, J. Warnatz, U. Mass, Proc. Combust. Inst. 28 (2000) 1177–1185.
[71] S. Pascaud, M. Boileau, L. Martinez, B. Cuenot, T. Poinsot, First Workshop INCA, SNECMA, Villaroche, France, 2005, pp. 19–26.
[72] H. Hesse, N. Chakraborty, E. Mastorakos, Proc. Combust. Inst. 32 (2009) 1399–1407.
[73] C.F. Kaminski, J. Hult, M. Alden, S. Lindenmaier, A. Dreizler, U. Mass, M. Baum, Proc. Combust. Inst. 28 (2000) 399–405.
[74] R. Maly, M. Vogel, Seventeenth Symposium (International) on Combustion, The Combustion Institute, Pittsburgh, 1978.
[75] R. Owston, J. Abhraham, Int. J. Hydrogen Energy 34 (2009) 6532–6544.
[76] P. Sagaut, Large Eddy Simulation for Incompressible Flows – An Introduction, third ed., Springer, 2006.
[77] S.B. Pope, New J. Phys. 6 (2004).
[78] C. Jimenez, F. Ducros, B. Cuenot, B. Bedat, Phys. Fluids 13 (2001) 1748–1754.
[79] G. Boudier, L.Y.M. Gicquel, T.J. Poinsot, Combust. Flame 155 (1–2) (2008) 196–214.
[80] S.F. Ahmed, E. Mastorakos, Combust. Flame 146 (2006) 215–231.
[81] R.F. Alvani, M. Fairweather, Chem. Eng. Res. Des. 80 (2002) 917–923.
[82] D.A. Santavicca, Spark ignited turbulent flame kernel growth, Technical Report OSTI ID: 6605, Pennsylvania State University, University Park, PA, USA, 1995.
[83] S.K. Marley, S.J. Danby, W.L. Roberts, M.C. Drake, T.D. Fansler, Combust. Flame 154 (2008) 296–309.
[84] J. Xia, K.H. Luo, S. Kumar, Flow Turbulence Combust. 80 (1) (2008) 133–153.
[85] T. Marchione, S.F. Ahmed, E. Mastorakos, Combust. Flame 156 (2009) 166–180.

PAPER 2

Phuc-Danh Nguyen, Vervisch L., Subramanian V., Domingo P. Multidimensional flamelet-generated manifolds for partially premixed combustion, *Combustion and Flame*, **157(1)**: (2010) 43-61

Combustion and Flame 157 (2010) 43–61

Contents lists available at ScienceDirect

Combustion and Flame

journal homepage: www.elsevier.com/locate/combustflame

Multidimensional flamelet-generated manifolds for partially premixed combustion

Phuc-Danh Nguyen, Luc Vervisch, Vallinayagam Subramanian, Pascale Domingo *

CORIA – CNRS and INSA de Rouen, Technopole du Madrillet, BP 8, 76801 Saint-Etienne-du-Rouvray, France

ARTICLE INFO

Article history:
Received 17 March 2009
Received in revised form 15 May 2009
Accepted 10 July 2009
Available online 19 August 2009

Keywords:
Flamelet modeling
Turbulent combustion
Numerical simulation

ABSTRACT

Flamelet generated manifolds have been restricted so far to premixed or diffusion flame archetypes, even though the resulting tables have been applied to nonpremixed and partially premixed flame simulations. By using a projection of the full set of mass conservation species balance equations into a restricted subset of the composition space, unsteady multidimensional flamelet governing equations are derived from first principles, under given hypotheses. During the projection, as in usual one dimensional flamelets, the tangential strain rate of scalar isosurfaces is expressed in the form of the scalar dissipation rates of the control parameters of the multidimensional flamelet generated manifold (MFM), which is tested in its five dimensional form for partially premixed combustion, with two composition space directions and three scalar dissipation rates. It is shown that strain rate induced effects can hardly be fully neglected in chemistry tabulation of partially premixed combustion, because of fluxes across iso equivalence ratio and iso progress of reaction surfaces. This is illustrated by comparing the 5D flamelet generated manifold with one dimensional premixed flame and unsteady strained diffusion flame composition space trajectories. The formal links between the asymptotic behavior of MFM and stratified flame, weakly varying partially premixed front, triple flame, premixed and nonpremixed edge flames are also evidenced.

1. Introduction

Development of advanced combustion systems relies heavily on accurate turbulent combustion submodels and numerical tools [1], a very crucial point in improving existing burners or in dealing with fully new combustion chamber concepts. This is the case, for instance, in burners developed for low calorific residual gases, which can supplement the traditional fossil fuels in thermal units [2], and also in aeronautical engines, based on rich quench and lean premixed and prevaporized technologies [3], car engines using high levels of exhaust gas recirculation (EGR) [4], or, industrial burners operating on moderate or intense low oxygen dilution (MILD) [5] and again in flameless combustion [6]. In many of these combustion systems, hybrid combustion regimes are actually observed, ranging between fully premixed and fully nonpremixed reactants, with eventual dilution by recirculating burnt gases, to minimize pollutant emission and achieve accurate control of flame and global flow stability.

Among numerical combustion models proposed for such reacting flows, the flamelet concept has attracted great attention, for both premixed and nonpremixed turbulent combustion [7]. The local turbulent flame properties are obtained by averaging the behavior of prototypes laminar flames, usually assumed to be one dimensional, though laminar diffusion flamelet equations have been derived for two mixture fractions by use of a three scale asymptotic analysis [8]. Recently, this two mixture fractions diffusion flamelet model was extended to investigate multiple injections in direct injection Diesel engines using representative interactive flamelets (RIF) [9]. In a different context, a flamelet equation based on mixture fraction and a measure of the progress of reaction was derived to relate the contributions of self ignition and flame propagation in a vitiated air lifted flame [10]; a similar equation was also used to study the appearance of various combustion regimes [11]. Likewise, the premixed flamelet concept was also employed with success for reducing chemistry, to keep computational costs at a moderate level, as in the two equivalent approaches of flame prolongation of intrinsic low dimensional manifolds (FPI) [12] and flamelet generated manifolds (FGM) [13,14]. Both FPI and FGM consist of solving a set of one dimensional premixed laminar flames; reaction rates and species mass fractions are then tabulated as functions of defined coordinates (mixture fraction, progress of reaction, enthalpy, strain rates, etc.), a methodology that was in fact first introduced for Reynolds averaged Navier Stokes computations of premixed turbulent flames [15]. Alternative chemistry tabulation techniques exist, which are based on a systematic study of the dynamics of the chemical system, such as intrinsic low dimensional manifolds

* Corresponding author.
E-mail address: domingo@coria.fr (P. Domingo).

0010-2180/$ - see front matter © 2009 The Combustion Institute. Published by Elsevier Inc. All rights reserved.
doi:10.1016/j.combustflame.2009.07.008

(ILDM) [16] and the extension of this concept to reaction diffusion manifolds called REDIM [17] or in a different context to the compu tational singular perturbation (CSP) [18].

FPI and FGM have been successfully used in large eddy simu lation and Reynolds averaged Navier Stokes of turbulent flames, with premixed or nonpremixed (diffusion) generated manifolds [10,19,20], along with unsteady diffusion flamelets [21,22], for which an approximate version exists [23] that does not exactly conserve mass because fluxes in mixture fraction space are ap plied to the progress variable only. Obviously, diffusion flame generated manifolds are, *a priori*, not well suited to capture pre mixed or partially premixed flame propagation; on the other hand, premixed generated manifolds do lack some basic proper ties of flames evolving in a flow featuring a nonuniform equiva lence ratio, as fluxes through isomixture fraction surfaces, which cannot be fully neglected in a diffusion flame or in a curved partially premixed flame front. Because premixed flamelet tabulation cannot reproduce any of such diffusion controlled behavior in mixture fraction space, usually outside of the flamma bility domain, a simple extrapolation is assumed for all species and burning rates are abruptly set to zero. Additionally, impact on the flame chemical structure of strain induced by turbulent velocity fluctuations is not always included in premixed tabula tions applied to premixed or nonpremixed combustion. A system atic analysis of the applicability range of premixed flamelets to partially premixed and diffusion flames was previously reported [24]. The authors concluded that the premixed flamelet tabula tion, in general, fails when applied to rich partially premixed or diffusion flames. There exists an inner reaction zone, located in the vicinity of the stoichiometric region where premixed chemis try tabulation and diffusion combustion are almost similar, but outside of this inner reaction zone, chemistry becomes slower and competes with diffusive processes; hence, diffusive fluxes across isomixture fraction surfaces may dominate and drive the flame response [24].

To overcome such deficiencies, and in an attempt to address the three regimes, premixed, partially premixed, and diffusion flames, a multidimensional flamelet model is discussed in this pa per, in which interactions between reaction zones developing at various equivalence ratios are accounted for in a natural manner. These "multidimensional flamelet generated manifolds" (MFM) are then tested for detailed chemistry tabulation of premixed, nonpremixed, and partially premixed combustion. The multidi mensional flamelet governing equations are derived, under given hypotheses, by projection of the full set of unsteady mass conser vation species balance equations into a restricted subset of the composition space. Scalar dissipation rates appear in these equa tions, which are representative of the straining amplitude im posed on reaction zones. A usual subspace coordinates system based on mixture fraction, which describes fuel and oxidizer mix ing, and, on progress of reaction is defined in which three scalar dissipation rates are involved; the response of the corresponding MFM to its five control parameters is then studied. It is found that the thermochemical variables conveniently evolve in this five dimensional space, with flame propagation and reactants trans port in both mixture fraction and reaction progress directions included and coupled.

The derivation of MFM governing equations and the methodol ogy related to their numerical treatment are described in the next section. The conditions for MFM calculations and scalar dissipation rate expressions are also presented. To access the solving of prop agating flames in the proposed composition space, comparisons against physical space solutions are addressed in a subsequent sec tion, before unsteady diffusion flamelets are examined. Then the MFM response, in relation with triple or edge flame behavior, is discussed for chemistry tabulation, before concluding.

2. Multidimensional flamelet-generated manifolds (MFM)

2.1. MFM governing equations

Let us consider a set of N species mass fractions Y_i that verify the balance equation

$$\frac{\partial \rho Y_i}{\partial t} + \nabla \cdot (\rho \mathbf{u} Y_i) \quad \nabla \cdot (\rho D_i \nabla Y_i) + \dot{\omega}_i, \tag{1}$$

where ρ is the mass density, $\mathbf{u}$ the velocity vector, and D_i and $\dot{\omega}_i$ the diffusion coefficient and the burning rate of the ith species, respec tively. The temperature equation for constant pressure flames [25] is used without body force:

$$\frac{\partial \rho T}{\partial t} + \nabla \cdot (\rho \mathbf{u} T) \quad \frac{1}{C_p} \nabla \cdot (\lambda \nabla T) + \frac{1}{C_p} \sum_{i\ 1}^{N} \rho C_{P_i} D_i \nabla Y_i \cdot \nabla T \quad \frac{1}{C_p} \sum_{i\ 1}^{N} h_i \dot{\omega}_i. \tag{2}$$

The thermal conductivity is denoted as λ, $C_p \quad \sum_{i\ 1}^{N} C_{p_i} Y_i$ is the mixture averaged calorific capacity at constant pressure per unit of mass, and h_i is the enthalpy and C_{P_i} the calorific capacity of the ith species. This equation does not constitute an exact form of the energy budget, but is usually adopted in constant pressure and monodimensional laminar flame simulations [25].

To reduce the dimension of the problem, a subset of M variables ϕ_j is introduced ($M < N$). They are constructed from combinations of species mass fractions, so that

$$\phi_j \quad \sum_{k\ 1}^{N} \alpha_{jk} Y_k, \tag{3}$$

where α_{jk} are coefficients used to linearly combine the species. (A detailed discussion of the definitions of mixture fractions and pro gress variables may be found in [26].) The balance equation for ϕ_j reads

$$\frac{\partial \rho \phi_j}{\partial t} + \nabla \cdot (\rho \mathbf{u} \phi_j) \quad \nabla \cdot (\rho D_j^{\phi} \nabla \phi_j) + \dot{\omega}_j, \tag{4}$$

with

$$\dot{\omega}_j \quad \sum_{k\ 1}^{N} \alpha_{jk} \dot{\omega}_k, \tag{5}$$

where an effective diffusion coefficient D_j^{ϕ} has been introduced. This molecular diffusion coefficient must verify the relation

$$\sum_k \alpha_{jk} \nabla \cdot (\rho D_k \nabla Y_k) \quad \nabla \cdot \left(\rho D_j^{\phi} \nabla \left(\sum_k \alpha_{jk} Y_k \right) \right). \tag{6}$$

An estimate of D_j^{ϕ} would need to be introduced in the flow sol ver to evaluate the molecular diffusive fluxes of ϕ_j, the chemical ta ble control parameters. However, in practice, in building lookup tables, the molecular diffusion coefficients of the ϕ_j ($j \quad 1, M$) do not impact on the Y_i tabulated solutions, since they are obtained in the ϕ_j space for fixed ϕ_j values, as discussed below. A practical option for prescribing the molecular diffusion coefficients $\left(D_j^{\phi}\right)$ of flamelet tabulation control parameters in flow solvers was dis cussed in [19] for carefully reproducing methane air flame basic properties, such as flame speed and most species including minor ones. Some of the ϕ_j may also be passive scalars, such as the mix ture fraction in nonpremixed systems; then $\dot{\omega}_j \quad 0$.

Let us assume that there exists a set of ϕ_j and τ, so that they constitute a properly defined generalized (nonorthogonal) coordi nate system [27], in which the species vector $Y(x,t)$ can be decom posed to write $Y(\phi_1, \ldots, \phi_M, \tau)$. The exact definition of such a coordinate system may not be trivial; it can depend on the fuel and oxidizer considered and on the flame boundary conditions;

Obviously, a heavy hydrocarbon fuel that decomposes before heat is released (cool flame regime) may need more complex coordi nates than methane, for which a coordinate system is discussed be low in the case of combustion with vitiated air.

The following relations hold between derivatives expressed in the cartesian and the generalized systems,

$$\nabla Y_i \quad \sum_{j\ 1}^{M} \frac{\partial Y_i}{\partial \phi_j} \nabla \phi_j, \tag{7}$$

$$\nabla^2 Y_i \quad \sum_{j\ 1}^{M} \sum_{k\ 1}^{M} \frac{\partial^2 Y_i}{\partial \phi_j \partial \phi_k} \nabla \phi_j \cdot \nabla \phi_k + \sum_{j\ 1}^{M} \frac{\partial Y_i}{\partial \phi_j} \nabla^2 \phi_j, \tag{8}$$

$$\frac{\partial Y_i}{\partial t} \quad \frac{\partial Y_i}{\partial \tau} \frac{\partial \tau}{\partial t} + \sum_{j\ 1}^{M} \frac{\partial Y_i}{\partial \phi_j} \frac{\partial \phi_j}{\partial t}, \tag{9}$$

with τ verifying $\partial\tau/\partial t \quad 1$ (from $dt \quad (\partial t/\partial\tau)d\tau + \sum_{j\ 1}^{M}(\partial t/\partial\phi_j)d\phi_j$ and t that does not depend on ϕ_j). Introducing Eqs. (7) (9) in Eqs. (1) and (2), using Eq. (4) leads to

$$\rho \frac{\partial Y_i}{\partial \tau} + \sum_{j\ 1}^{M} \frac{\partial Y_i}{\partial \phi_j} (\dot{\omega}_j + \nabla \cdot (\rho D_i^* \nabla \phi_j)) \quad \sum_{j\ 1}^{M} \sum_{k\ 1}^{M} \frac{\rho \chi_{jk}}{\mathrm{Le}_i} \frac{\partial^2 Y_i}{\partial \phi_j \partial \phi_k} + \dot{\omega}_i, \tag{10}$$

$$\rho \frac{\partial T}{\partial \tau} + \sum_{j\ 1}^{M} \frac{\partial T}{\partial \phi_j} \times \left(\dot{\omega}_j + \nabla \left(\rho D_j^{\phi} \left(1 \quad \mathrm{Le}_j^{\phi} \right) \nabla \phi_j \right) \quad \sum_{k\ 1}^{M} \frac{\rho \chi_{jk}}{C_p} \left(\frac{\partial C_p}{\partial \phi_k} \right) + \sum_{i\ 1}^{N} \frac{C_{p_i}}{\mathrm{Le}_i} \frac{\partial Y_i}{\partial \phi_k} \right) \sum_{j\ 1}^{M} \sum_{k\ 1}^{M} \rho \chi_{jk} \frac{\partial^2 T}{\partial \phi_j \partial \phi_k} \quad \frac{1}{C_p} \sum_{i\ 1}^{N} h_i \dot{\omega}_i, \tag{11}$$

where χ_{jk} is a cross scalar dissipation rate

$$\chi_{jk} \quad (\lambda/\rho C_p) \nabla \phi_j \cdot \nabla \phi_k \tag{12}$$

and

$$D_i^* \quad D_i \left(\mathrm{Le}_i / \mathrm{Le}_j^{\phi} \quad 1 \right), \tag{13}$$

with $\mathrm{Le}_i \quad (\lambda/\rho C_p)/D_i$ and $\mathrm{Le}_j^{\phi} \quad (D_i/D_j^{\phi})\mathrm{Le}_i$.

With this formal transformation, the time and space evolution of the system is expressed in the ϕ_j composition space of dimen sion M and the scalar dissipation rates are the coefficients (the metric) of the coordinate transformation. The mass fraction and temperature Eqs. (10) and (11) are the exact multidimensional composition space governing equations derived from the projec tion of the mass species conservation and temperature balance Eqs. (1) and (2) into the composition (ϕ_j) space, assuming that this new coordinate system exists. These governing Eqs. (10) and (11) are referred hereafter to as multidimensional flamelet generated manifolds (MFM) equations. Notice that $N+1 \quad M$ MFM equations for Y_i and T (Eq. (10) for $N \quad M$ species and (11) for temperature) together with the M equations for ϕ_j (Eq. (4)) are equivalent to the full set of the original $N+1$ equations for Y_i and T (Eqs. (1) and (2)), if D_j^{ϕ} is properly expressed; bringing no reduction of the problem size at this point, but a simple reor ganization of the variables once the α_{jk} (Eq. (3)) are determined, though there is no proof of their existence at this stage. However, if the solution of Eqs. (10) and (11) is pretabulated for given con trol parameters (flame boundary conditions, scalar dissipation rates...), in the form

$$Y_i \quad Y_i^{\mathrm{MFM}}(\phi_1, \ldots, \phi_M, \tau; \underline{\chi}), \tag{14}$$

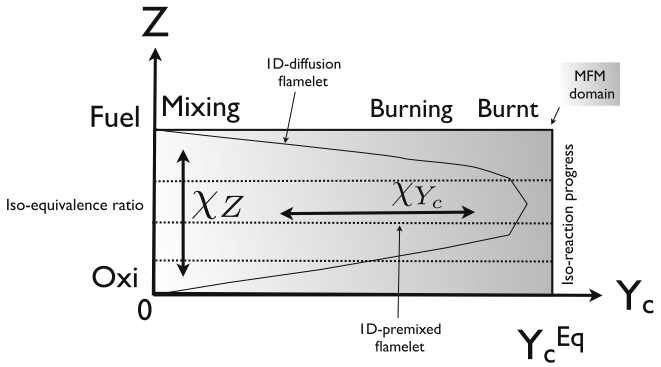

Fig. 1. Sketch of Z–Y_c flamelets composition space.

$$T \quad T^{\mathrm{MFM}}(\phi_1, \ldots, \phi_M, \tau; \underline{\chi}), \tag{15}$$

then the solution of the M balance equations for the ϕ_j provides an information to enter the Y_i^{MFM}, T^{MFM} table. Hence, as usual with any chemistry tabulation method, the solution of M ϕ_j equations would replace the $N+1$ primitive equations, to which the lookup table gi ven by Eqs. (14) and (15) is added, in this formal analysis it is as sumed that the ϕ_j are fully resolved for estimating all the χ_{jk} terms, denoted $\underline{\chi}$ in the relations (14) and (15). The unsteady term in Eqs. (10) and (11) plays a role similar to that of the usual one dimensional unsteady or Lagrangian flamelets [7,21]; the time history of the coupling between diffusion and reaction is then in cluded. This may be of importance in LES of turbulent flames, since it was previously discussed how unsteadiness can impact on flame response; for instance, diffusion flames submitted to scalar dissipa tion rate levels higher than the steady flame quenching value may not be quenched if the strain rate relaxes fast enough toward much smaller values, and using the steady state response would lead to erroneous solutions [28,29].

Eq. (10) contains a flux in composition space according to reac tion and diffusion; formally it may be seen as a convective compo sition space flux, whose velocity would read

$$V_{\phi_j} \quad \dot{\omega}_j + \nabla \cdot (\rho D_i^* \nabla \phi_j). \tag{16}$$

The diffusive part of this term, $\nabla \quad (\rho D_i^* \nabla \phi_j)$, which represents differential diffusion between species and the subspace coordi nates (Eq. (13)), may be partly written in composition space using Eq. (7),

$$\nabla \cdot (\rho D_i^* \nabla \phi_j) \quad \sum_{k\ 1}^{M} \frac{\partial \rho \chi_{jk}^*}{\partial \phi_k} \quad \rho D_i^* \nabla \phi_j \cdot \frac{\partial \nabla \phi_k}{\partial \phi_k}, \tag{17}$$

with $\chi_{jk}^* \quad D_i^* \nabla \phi_j \quad \nabla \phi_k$. A similar differential diffusion term was analyzed in [7,30] for diffusion flamelets, to conclude that it is important for soot predictions sensitive to reactive scalars with a very large diffusivity, such as hydrogen radicals, a phenomenon that is out of the scope of the present paper; the first objective being to start investigating chemical tables for partially premixed combustion regimes, this term is neglected in a first approach. In the temperature Eq. (11), W_{ϕ_j}, the composition space convective velocity is

Table 1
Z–Y_c flamelet boundary conditions, methane vitiated-air combustion [45].

	Z	$T(K)$	X_{O_2}	X_{N_2}	X_{H_2O}	X_{CH_4}
Fuel jet	Z 1	320	0.15	0.52	0.0029	0.33
Coflow	Z 0	1350	0.12	0.73	0.15	0.0003

Note. Z: Mixture fraction, T: temperature (in K), X_i: mole fraction.

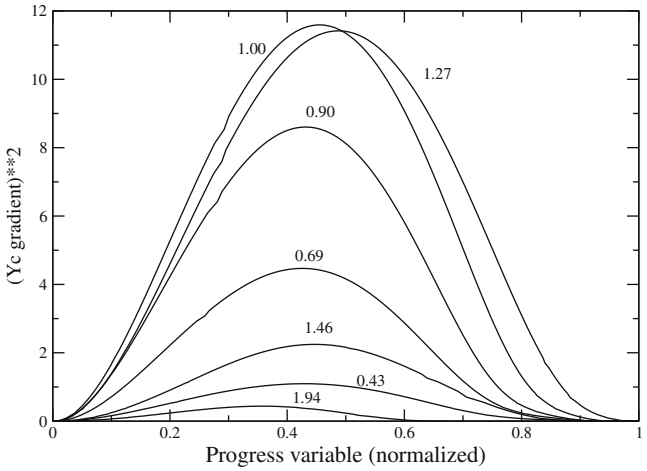

Fig. 2. $|\nabla Y_c|^2$ versus Y_c/Y_c^{Eq} (cgs units). Unstrained premixed flamelet; equivalence ratios given in graph.

$$W_{\phi_j} \quad \dot{\omega}_j + \nabla\cdot\left(\rho D_j^{\phi}\left(1 \quad \mathrm{Le}_j^{\phi}\right)\nabla\phi_j\right) \quad \sum_{k\ 1}^{M}\frac{\rho\chi_{jk}}{C_p}\left(\frac{\partial C_p}{\partial\phi_k}+\sum_{i\ 1}^{N}\frac{C_{P_i}}{\mathrm{Le}_i}\frac{\partial Y_i}{\partial\phi_k}\right). \tag{18}$$

For unity Lewis number of the ϕ_j, the second term vanishes; it is usual to adopt $\lambda/\rho C_P$ as a diffusion coefficient for passive scalars, and this hypothesis is also formulated for the ϕ_j in the following. The third term proportional to χ_{jk} represents the coupling between species and heat fluxes and it must be kept.

The MFM species equation reads

$$\rho\frac{\partial Y_i}{\partial\tau}+\sum_{j\ 1}^{M}\frac{\partial Y_i}{\partial\phi_j}\dot{\omega}_j \quad \sum_{j\ 1}^{M}\sum_{k\ 1}^{M}\frac{\rho\chi_{jk}}{\mathrm{Le}_i}\frac{\partial^2 Y_i}{\partial\phi_j\partial\phi_k}+\dot{\omega}_i \tag{19}$$

and the temperature one

$$\rho\frac{\partial T}{\partial\tau}+\sum_{j\ 1}^{M}\frac{\partial T}{\partial\phi_j}\left(\dot{\omega}_j \quad \sum_{k\ 1}^{M}\frac{\rho\chi_{jk}}{C_p}\left(\frac{\partial C_p}{\partial\phi_k}+\sum_{i\ 1}^{N}\frac{C_{P_i}}{\mathrm{Le}_i}\frac{\partial Y_i}{\partial\phi_k}\right)\right)$$
$$\sum_{j\ 1}^{M}\sum_{k\ 1}^{M}\rho\chi_{jk}\frac{\partial^2 T}{\partial\phi_j\partial\phi_k} \quad \frac{1}{C_p}\sum_{i\ 1}^{N}h_i\dot{\omega}_i. \tag{20}$$

These generic equations are for an arbitrary number M of ϕ_j, used to study subspace chemistry diffusion coupled trajectories, assuming that the ϕ_j coordinate system exists. In addition to the unsteady term, they contain on their left hand side a Lagrangian derivative with $\dot{\omega}_j$, the source of ϕ_j as convective velocity in ϕ_j space, to which an additional heat flux is added for temperature. On their right hand side, a composition space diffusive term pro portional to scalar dissipation rate, and the species $\dot{\omega}_i$ chemical source are found. These equations, including chemical and diffu sive terms, feature similarities with the model problems used in analyses of slow manifolds in reactive flows [17,31], where a re duced description of inhomogeneous mixtures is obtained from a set of PDEs including a diffusive term. The MFM equations were derived from the systematic projection of the thermochemical bal ance equations into a given subspace. The diffusion is also present along with the chemical source, and its amplitude is calibrated by both the curvature of the manifold in composition space and the scalar dissipation rates, which measure the mixing rate in each direction of the subspace. These mixing rates are proportional to the metric of the coordinate transformation between the physical space and the MFM sub space. This is better understood within the simplified case of one dimensional diffusion flamelets, obtained by reducing the subspace to the mixture fraction coordinate, which can be seen as a "flame fitted" coordinate. The mixture fraction scalar dissipation rate provides information on the topology of this coordinate in the original physical space. The proper subspace is not known a priori; however, it is shown there after how this can be easily overcome in the case of partially pre mixed methane air combustion. Also, in most cases and for all methods, in the end, the subspaces are usually constructed using major species mass fractions (CO, CO_2, H_2O), leading to quite obvi ous coordinates. The particular case of a two dimensional ϕ_j space, leading to a five dimensional flamelet generated manifold with three scalar dissipation rates, is now discussed.

2.2. Z Y_c flamelets

A two dimensional subspace obtained with ϕ_1 Z and ϕ_2 Y_c, is considered. Z is the mixture fraction, a passive scalar with Z 0 in the oxidizer stream and Z 1 at fuel injection. Y_c is a progress var iable, Y_c 0 in fresh gases and Y_c Y_c^{Eq} in equilibrium products; it is assumed that Z Y_c constitutes a well defined coordinate system in which the solution can be projected (Fig. 1). The exact definition of Y_c stays open at this stage, various progress of reaction defini tions exist in the literature to tabulate chemistry from flamelets or from other modeling approaches, all relying on given hypothe ses, more or less easy to fully evaluate. In the present paper, the Z, Y_c, τ coordinate system retained is validated from comparisons between composition space based solutions and physical space based ones, the Y_c definition being simply grounded on previous works devoted to FPI FGM modeling [12,13]. The underlying hypothesis is in fact similar to the one formulated when chemical responses are computed directly in species composition space, as done in phase space turbulent combustion modeling [32]. Never theless, as in FPI or FGM, the weak point lies in the need to deter mine the proper α_{jk} coefficients (Eq. (3)), so that Y_c is indeed properly defined. In the following, we rely on previous works to select a Y_c that constitutes the best compromise, for instance, so that there is a one to one correspondence between the MFM con trol parameters and flame solutions.

Eqs. (19) and (20) become

$$\rho\frac{\partial Y_i}{\partial\tau}+\frac{\partial Y_i}{\partial Y_c}\dot{\omega}_c \quad \frac{\rho\chi_{Y_c}}{\mathrm{Le}_i}\frac{\partial^2 Y_i}{\partial Y_c^2}+\frac{\rho\chi_Z}{\mathrm{Le}_i}\frac{\partial^2 Y_i}{\partial Z^2}+2\frac{\rho\chi_{Z,Y_c}}{\mathrm{Le}_i}\frac{\partial^2 Y_i}{\partial Z\partial Y_c}+\dot{\omega}_i, \tag{21}$$

$$\rho\frac{\partial T}{\partial\tau}+\frac{\partial T}{\partial Y_c}\dot{\omega}_c \quad \frac{1}{C_p}\left(\frac{\partial C_p}{\partial Y_c}+\sum_{i\ 1}^{N}\frac{C_{P_i}}{\mathrm{Le}_i}\frac{\partial Y_i}{\partial Y_c}\right)\left(\frac{\partial T}{\partial Y_c}\rho\chi_{Y_c}+\frac{\partial T}{\partial Z}\rho\chi_{Z,Y_c}\right)$$
$$\frac{1}{C_p}\left(\frac{\partial C_p}{\partial Z}+\sum_{i\ 1}^{N}\frac{C_{P_i}}{\mathrm{Le}_i}\frac{\partial Y_i}{\partial Z}\right)\left(\frac{\partial T}{\partial Z}\rho\chi_Z+\frac{\partial T}{\partial Y_c}\rho\chi_{Z,Y_c}\right)$$
$$\rho\chi_{Y_c}\frac{\partial^2 T}{\partial Y_c^2}+\rho\chi_Z\frac{\partial^2 T}{\partial Z^2}+2\rho\chi_{Z,Y_c}\frac{\partial^2 T}{\partial Z\partial Y_c} \quad \frac{1}{C_p}\sum_{i\ 1}^{N}h_i\dot{\omega}_i. \tag{22}$$

The solution of this system, and its related flame model problem expressed in physical space, are easily anticipated. Starting from fuel and oxidizer injection, Y_c 0 represents fuel and air mixing, up stream of reaction zones. Let us assume that a flame front is located at Z, $Y_c^*(Z)$, with $Y_c^*(Z)$ the location where the heat release source reaches its maximum. For $Y_c > Y_c^*$, burnt gases are found, up to Y_c^{Eq}, the chemical equilibrium condition. The scalar dissipation rates χ_Z and χ_{Y_c} may be related to characteristic diffusive layer thicknesses, via a global estimation of the local mixing layer thickness δ_Z $((\lambda/\rho C_p)/\chi_Z)^{1/2}$ and of the flame thickness δ_c $((\lambda/\rho C_p)/\chi_{Y_c})^{1/2}$. For χ_Z small compared to the maximum value of χ_{Y_c}, diffusive fluxes in mixture fraction space feature a moderate amplitude and δ_Z is

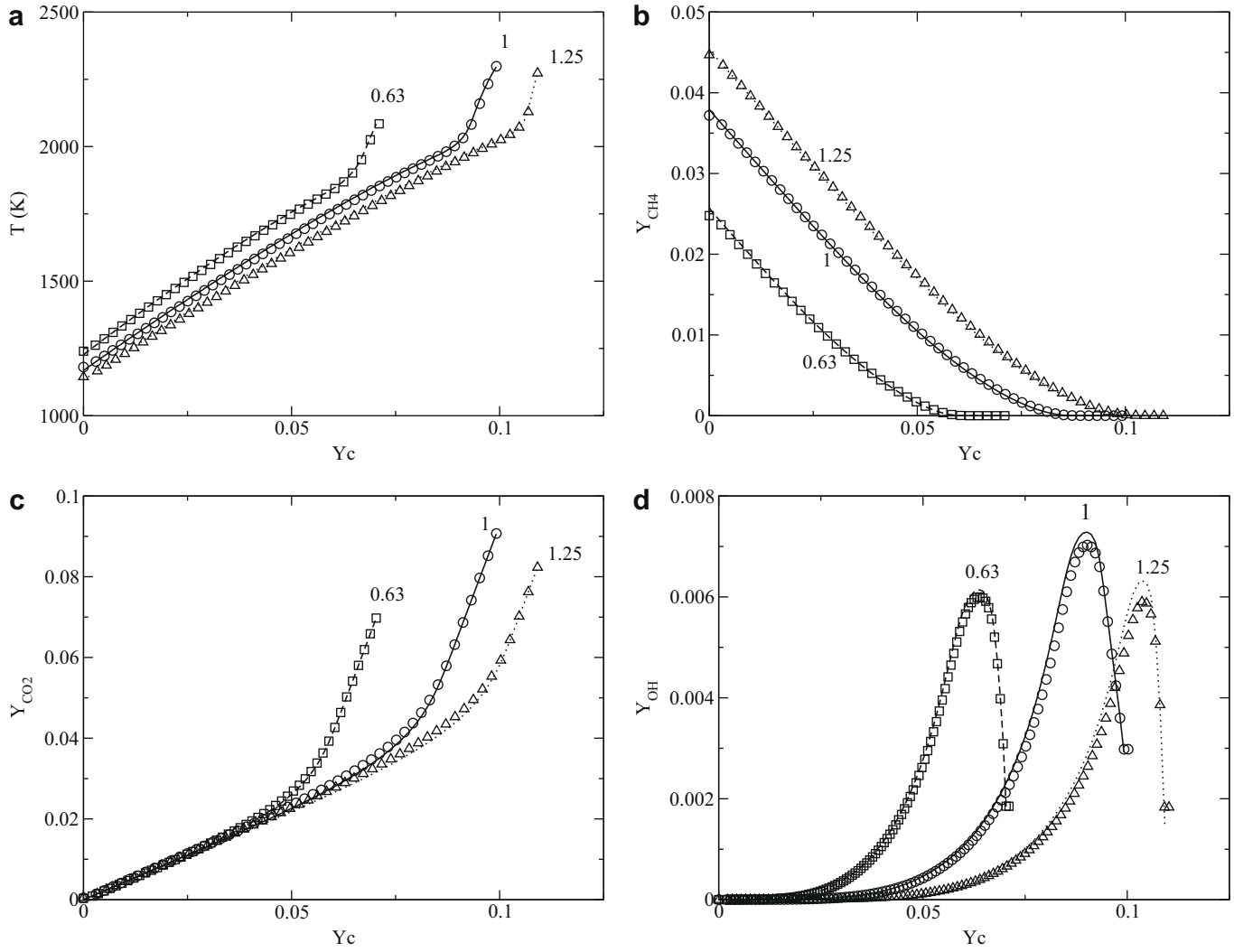

Fig. 3. Freely propagating premixed flame responses versus Y_c. Symbols: Composition space solution (Eqs. (27) and (28)). Lines: Physical space solution (Eqs. (1) and (2)). (a) Temperature; (b) mass fractions, CH_4; (c) CO_2; (d) OH. Equivalence ratios given in graphs.

much larger than δ_c; a flow condition pertaining to a thin flame front evolving into a nonuniform equivalence ratio mixture. Then fixing the position $Z \quad Z_o$ in the mixture fraction direction (i.e., fixing equivalence ratio, Fig. 1) and progressing along the Y_c direction from $Y_c \quad 0$ to Y_c^{Eq}, the system evolves in a premixed flame regime that is weakly influenced by its leaner ($Z < Z_o$) and richer ($Z > Z_o$) neigh boring reaction zones, as in a weakly varying partially premixed flame front or stratified flames [33]. Increasing χ_Z corresponds to a decrease of the local mixing layer thickness where the flame propa gates; the interactions between isoequivalence ratio (iso Z) surfaces play here a nonnegligible role and strongly interacting partially pre mixed flamelets are obtained, whose archetype would be a strained triple flame [34 36]. Further increasing χ_Z leads to diffusion edge flame behavior [37], since the partially premixed front is very local ized in both composition and physical space [38]. In physical space, the gradient of Y_c decreases in burnt gases; there χ_{Y_c} becomes neg ligible compared to eventual straining due to fuel air mixing, and, therefore, smaller than χ_Z. In this burnt gases zone, the flame is mainly influenced by transport in mixture fraction space, corre sponding to a trailing diffusion flame. Because the scalar dissipation rates are external and imposed parameters of the approximate for mulation given by Eqs. (21) and (22), nonpremixed diffusion con trolled combustion, as in diffusion flamelets, can also be observed for all values of Y_c from the above equations, by setting very small values of χ_{Y_c}. Accordingly, one dimensional strained premixed flames are found in Y_c space, if χ_Z vanishes and one makes use of these asymptotic behaviors in the following.

The governing equations of this two dimensional model prob lem were actually first derived in a simplified form in [10,39], where it was shown how they naturally degenerate into premixed flamelet equations, fixing the mixture fraction $\chi_Z \quad 0$, and into dif fusion flamelet equations, when the single coordinate Z is used. Also, for vanishing scalar dissipation rates, the look up table sim ply based on homogeneous reactors, which has been used in LES to tabulate autoignition, is retrieved [10,40]. This $Z \quad Y_c$ MFM is thus useful to discuss combustion regimes, as done in [36] from DNS and also in [11] from a careful flamelet based derivation. No tice also that, when Y_c is replaced by a second mixture fraction in Eqs. (21) and (22), the two mixture fractions flamelet equation de rived in [8] is recovered. The 'double conditioning of reactive scalar transport equation' (Eq. (6) in [41]) also leads to the same type of balance equations, along with advanced modeling of the scalar dis sipation rates [42] based on multiple mapping conditioning (MMC) for flames with partial premixing.

Eqs. (21) and (22) are integrated with a singly diagonal implicit Runge Kutta (SDIRK) scheme [43], after decomposition of the system following the splitting method discussed in [44]. During the solution time evolution, for a fixed Z value, fluxes in mixture

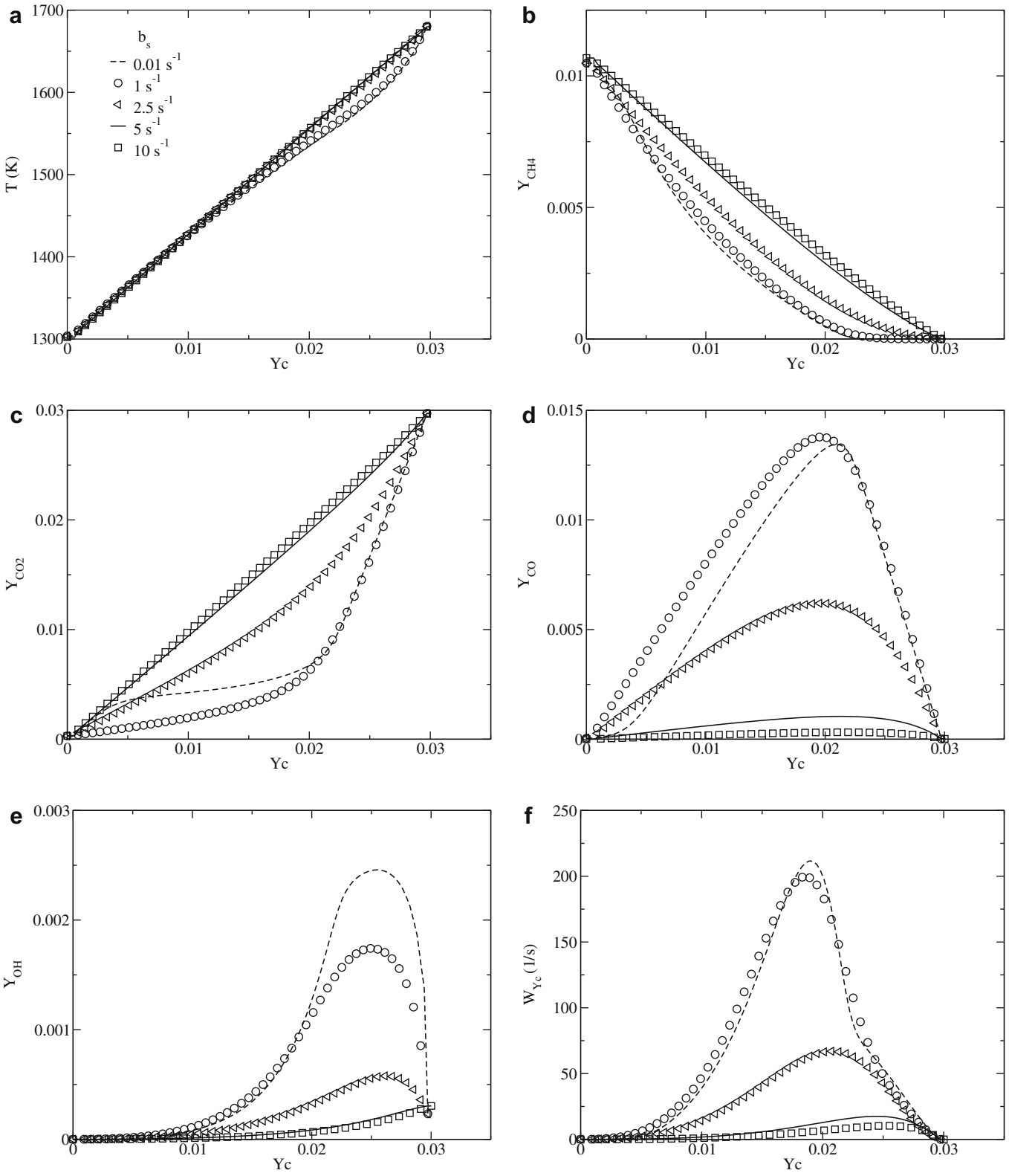

Fig. 4. Lean flame ϕ 0.25 (Z 0.05). (a) Temperature; (b) mass fractions, CH_4; (c) CO_2; (d) CO; (e) OH; (f) ω_{Y_c}. Dashed-line: (b_s, $b(Z$ 0.05)) [s ^{1}] (0.01, 0.0032); circle: (1,0.32); triangle-left: (2.5,0.8); line: (5,1.6); square: (10, 3.2).

fraction space impact on the solution up to the burnt gases; in con sequence, species mass fractions defining Y_c in Eq. (3) evolve also at the boundary and a moving Y_c mesh procedure is implemented to match the new species vector at each iteration, thus accounting for the moving burnt gases boundary. A 300 × 100 (Z Y_c) nonuni form grid is used, with refinement at the stoichiometric point. The Y_c direction is a zoom within the flame zone, and most of the 100 points are concerned with chemical reaction; while in the Z direc tion, outside of the flammability limits only diffusion is acting. Fixed values are imposed at Z 0, Z 1 and Y_c 0, and zero dif fusive fluxes in the Y_c direction at Y_c Y_c^{Eq}. For these given species concentration boundary conditions, at every instant in time τ the

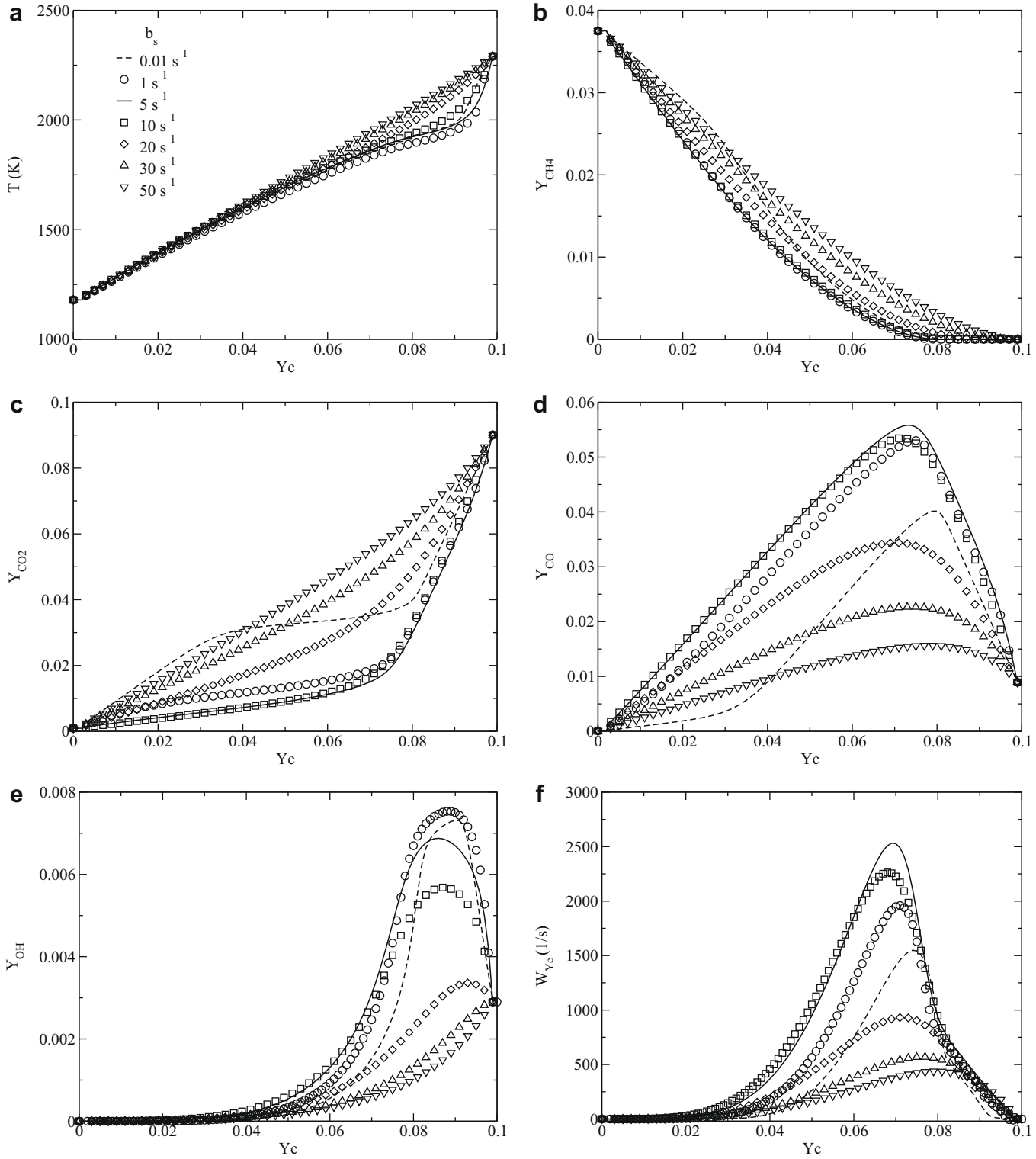

Fig. 5. Stoichiometric flame ϕ 1 (Z_s 0.1769). (a) Temperature; (b) mass fractions, CH_4; (c) CO_2; (d) CO; (e) OH; (f) ω_{Y_c}. Dashed-line: b_s [s ^{1}] 0.01 s ^{1}; circle: 1 s ^{1}; line: 5 s ^{1}; square: 10 s ^{1}; diamond: 20 s ^{1}; triangle-up: 30 s ^{1}; triangle-down: 50 s ^{1}.

species trajectories $Y_i(Z, Y_c, \tau; \chi_Z, \chi_{Y_c}, \chi_{Z,Y_c})$ are obtained, which de pend on five parameters.

2.3. Boundary conditions, chemistry, and scalar dissipation rate expressions

Partially premixed methane vitiated air combustion is consid ered. The conditions are those of the Cabra *et al.* burner [45] (see Fig. 1 of this reference for a burner view), a CH_4 air fuel mixture at equivalence ratio 4 and at room temperature is mixed with a H_2O air vitiated stream at 1350 K, composed of equilibrium burnt gases originated from hydrogen/air lean premixed combustion at equiva lence ratio 0.4. This laboratory flame provides interesting conditions for MFM, because various combustion modes may be found. The viti ated air brings the thermal energy that can promote self ignition of the mixture; in addition, the flow velocities are such that flame

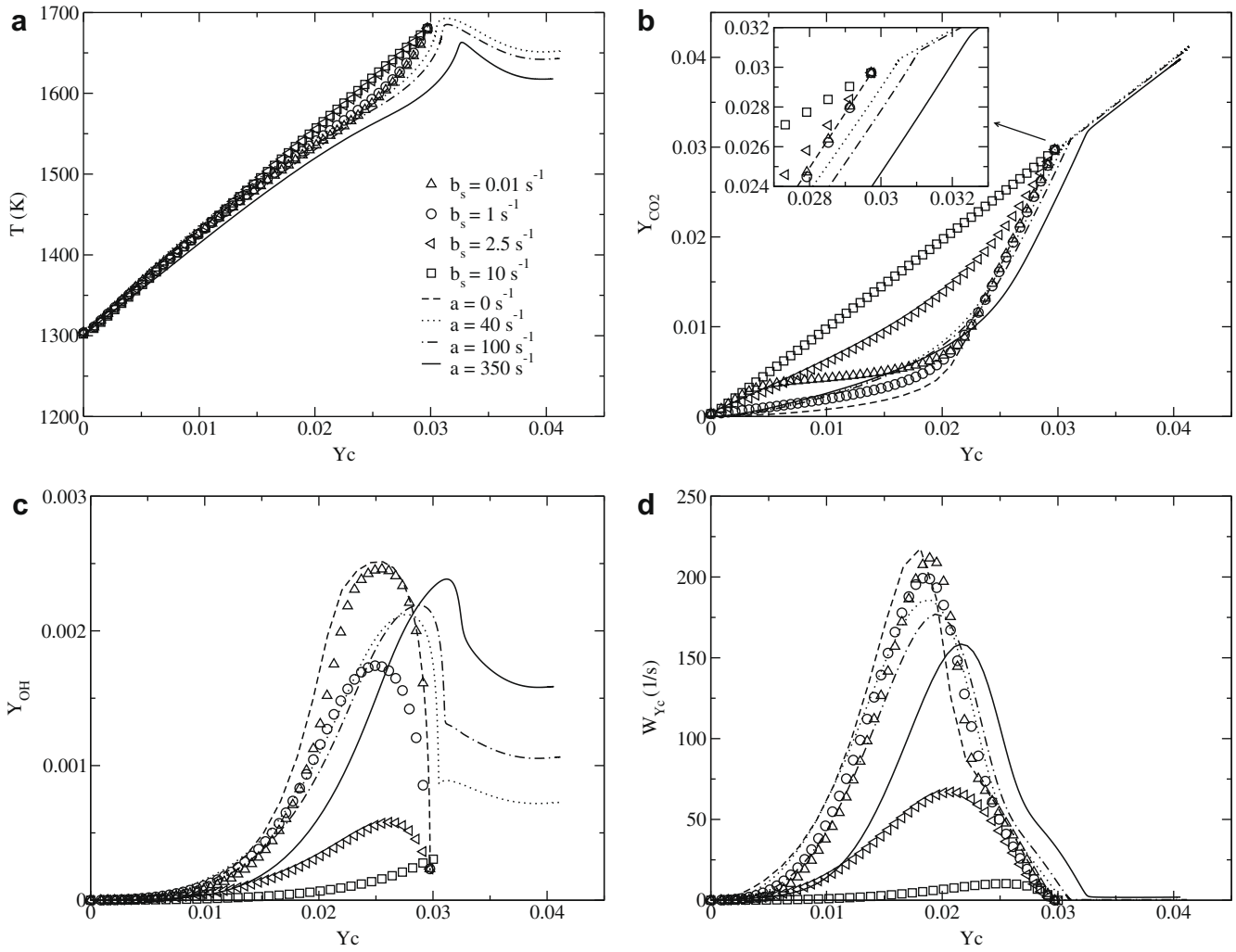

Fig. 6. Lean ϕ 0.25 (Z 0.05). (a) Temperature; (b) Mass fraction CO_2; (c) OH; (d) ω_{Y_c}. Symbols: premixed (Eqs. (27) and (28)) triangle-up: b_s 0.01 s ^{1}; circle: 1 s ^{1}; triangle-left: 2.5 s ^{1}; square: 10 s ^{1}. Lines: diffusion (Eqs. (29) and (30)) dashed: a 0 s ^{1}; dotted: 40 s ^{1}; dotted-dashed: 100 s ^{1}; solid: 350 s ^{1}.

propagation is also an option [10]. Finally, downstream of the par tially premixed turbulent flame base, diffusion flame elements may be expected, as discussed in DNS of lifted flames [36,46]. More discussion on combustion regimes of this flame may be found in [10,45].

Boundary conditions for species mass fractions are summarized in Table 1. Following premixed chemistry tabulation based large eddy simulations of this burner [10], the progress variable is defined as Y_c $Y_{CO} + Y_{CO_2}$, a choice that was motivated by the one to one correspondence between major species and this Y_c definition; in the MFM context, it is an arbitrary choice at this stage that is further addressed below from results. In the fuel jet (Z, Y_c) $(1,0)$ and in the vitiated air stream (Z, Y_c) $(0,0)$; from these inlets, Y_c is al lowed to evolve from 0 to $Y_c^{Max}(Z)$, its maximum level, which may differ from chemical equilibrium conditions because of fluxes in the direction of the mixture fraction coordinate, fluxes interacting with all other diffusive and reacting contributions.

A 15 step reduced chemical kinetic scheme available in the lit erature and developed from the GRI Mech 3.0 mechanism for methane combustion is used (ARM2 [47,48]), which was optimized to reproduce various flame properties, including ignition delay time for the lean mixture, a crucial phenomena in this burnt gases vitiated problem for which this kinetics has been previously vali dated [45]. Nineteen species, H_2, H, O_2, OH, H_2O, HO_2, H_2O_2, CH_3, CH_4, CO, CO_2, CH_2O, C_2H_2, C_2H_4, C_2H_6, NH_3, NO, HCN, and N_2, are in volved in the flame solution; their Lewis numbers are computed from a mixture averaged approximation [49].

Three scalar dissipation rates, χ_Z $(\lambda/\rho C_p)|\nabla Z|^2$ (scalar dissipa tion rate of mixture fraction), χ_{Y_c} $(\lambda/\rho C_p)|\nabla Y_c|^2$ (scalar dissipa tion rate of progress of reaction), and χ_{Z,Y_c} $(\lambda/\rho C_p)\nabla Z$ ∇Y_c (cross scalar dissipation rate defined between the mixture fraction and the progress of reaction), appear in Eqs. (21) and (22). They stand as quite critical parameters, since they must be representative of mixing time scales and related flame straining effects, as in usual one [50] or two dimensional flames [37] studied in composition space. In the coordinate transformation, they are also representative of the composition space shape in physical space. In a first step, both χ_Z and χ_{Y_c} are assumed time independent, which is of course a ma jor hypothesis in chemistry tabulation for turbulent flame simula tions, where local straining of flame surface is strongly unsteady, with even sometimes important statistical variability [28,29,51]. The mixture fraction dissipation rate is mainly influenced by flow mixing, its distribution is not expected to depend much on chemis try, except when heat release effects modify the flow field to impact on mixing, as triple flames do because of flow streamline deviations [52], an effect that is not included in the present study.

A generic functional dependence of χ_Z on mixture fraction for diffusive layers has been discussed previously [7],

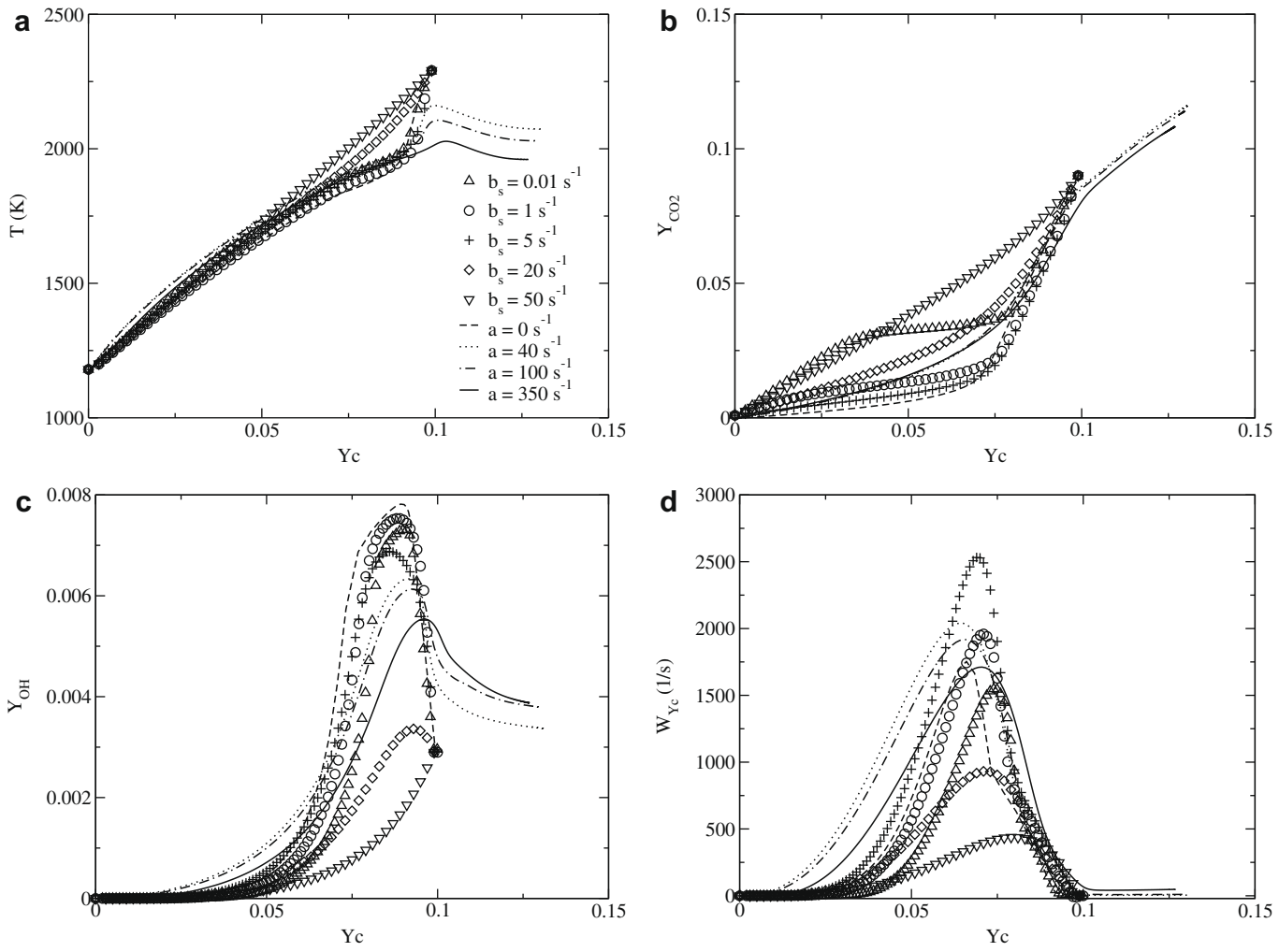

Fig. 7. Stoichiometric ϕ 1 (Z 0.1769). (a) Temperature; (b) mass fraction CO_2; (c) OH; (d) ω_{Y_c}. Symbols: premixed (Eqs. (27) and (28)) triangle-up: b_s 0.01 s ^{1}; circle: 1 s ^{1}; plus: 5 s ^{1}; diamond: 20 s ^{1}; triangle-down: 50 s ^{1}. Lines: diffusion (Eqs. (29) and (30)) dashed: a 0 s ^{1}; dotted: 40 s ^{1}; dotted-dashed: 100 s ^{1}; solid: 350 s ^{1}.

$$\chi_Z(Z) \quad \frac{a}{2\pi}\exp[\ 2(\mathrm{erfc}^{\ 1}(2Z))^2] \tag{23}$$

where a is the flow in plane strain rate. erfc ^{1} is the inverse of the complementary error function, Eq. (23) is adopted for all the study.

The progress of reaction gradient is influenced by both small scale mixing and chemistry; in the preheat zone of flames, where the local Damköhler number is small, χ_{Y_c} may be expected to be mostly mix ing driven, whereas in the thin reaction zone where the Damköhler number is large, the chemical source tends to enhance ∇Y_c, leading to greater χ_{Y_c}. It is thus quite difficult to anticipate a generic χ_{Y_c} dis tribution, which would be directly related to flame response to strain. To first presume the shape of $\chi_{Y_c}(Z, Y_c)$, which depends on both equivalence ratio and reaction progress, usual FPI freely prop agating premixed flamelet database is generated for the conditions under study [10], therefore, neglecting fluxes in mixture fraction space. The solving of one dimensional premixed flamelets in physi cal space [53] provides the ∇Y_c distribution, to compute χ_{Y_c} through the flame, a representative amplitude of χ_{Y_c} is then known in the Z Y_c space to start calibrating χ_{Y_c}. Fig. 2 displays $|\nabla Y_c|^2$ versus Y_c/Y_c^{Eq} for various equivalence ratios of freely propagating premixed flamelets. These curves could be approximated as $\chi_{Y_c}(Z, Y_c)$ $b(Z)\left(Y_c/Y_c^{Eq}\right)^{\alpha(Z)}\left(1 \quad \left(Y_c/Y_c^{Eq}\right)\right)^{\beta(Z)}$, where $b(Z)$ is the maximum va lue for a given Z, and $\alpha(Z)$ and $\beta(Z)$ are two functions to be deter mined, in order to have a χ_{Y_c} distribution representative of a ∇Y_c that is close to that of laminar flames, and, therefore, influenced by burning. This option is of interest to build chemical tables based on a so called strong flamelet hypothesis, where gradients through the flame are assumed, as in the laminar reference situation, or to validate composition space solutions against physical space ones, as done thereafter; but it cannot provide a generic χ_{Y_c} distribution in the case of multidimensional flamelets, since χ_{Y_c} would then need to be fitted, for instance, from two dimensional triple flame li braries simulated in physical space. Another option is to assume that straining is an external ingredient, mostly imposed by local velocity fluctuations, and that chemistry responds to this solicitation accord ing to MFM balance equations, for given composition space scalar dissipation rate distributions. In the latter case scalar dissipation rates are simply viewed as coefficients of Eqs. (21) and (22), used to parameterize MFM solutions. Both options are used in the follow ing, the first to compare composition and physical space solutions, the second to study multidimensional flamelet generated manifold response from MFM equations.

When it is not exactly taken from laminar flame solutions, the progress variable dissipation rate is cast in

$$\chi_{Y_c}(Z, Y_c) \quad b(Z)\exp\left[\ 2\left(\mathrm{erfc}^{\ 1}\left(2Y_c/Y_c^{Eq}(Z)\right)\right)^2\right], \tag{24}$$

where $b(Z)$ is the maximum value of χ_{Y_c} for mixture fraction varia tions. $Y_c^{Eq}(Z)$ is the chemical equilibrium value, or the final point in burnt gases in the case of partially premixed combustion. In Eq. (24), $\chi_{Y_c}(Z, Y_c)$ is determined once $b(Z)$ is known. To avoid prescrib

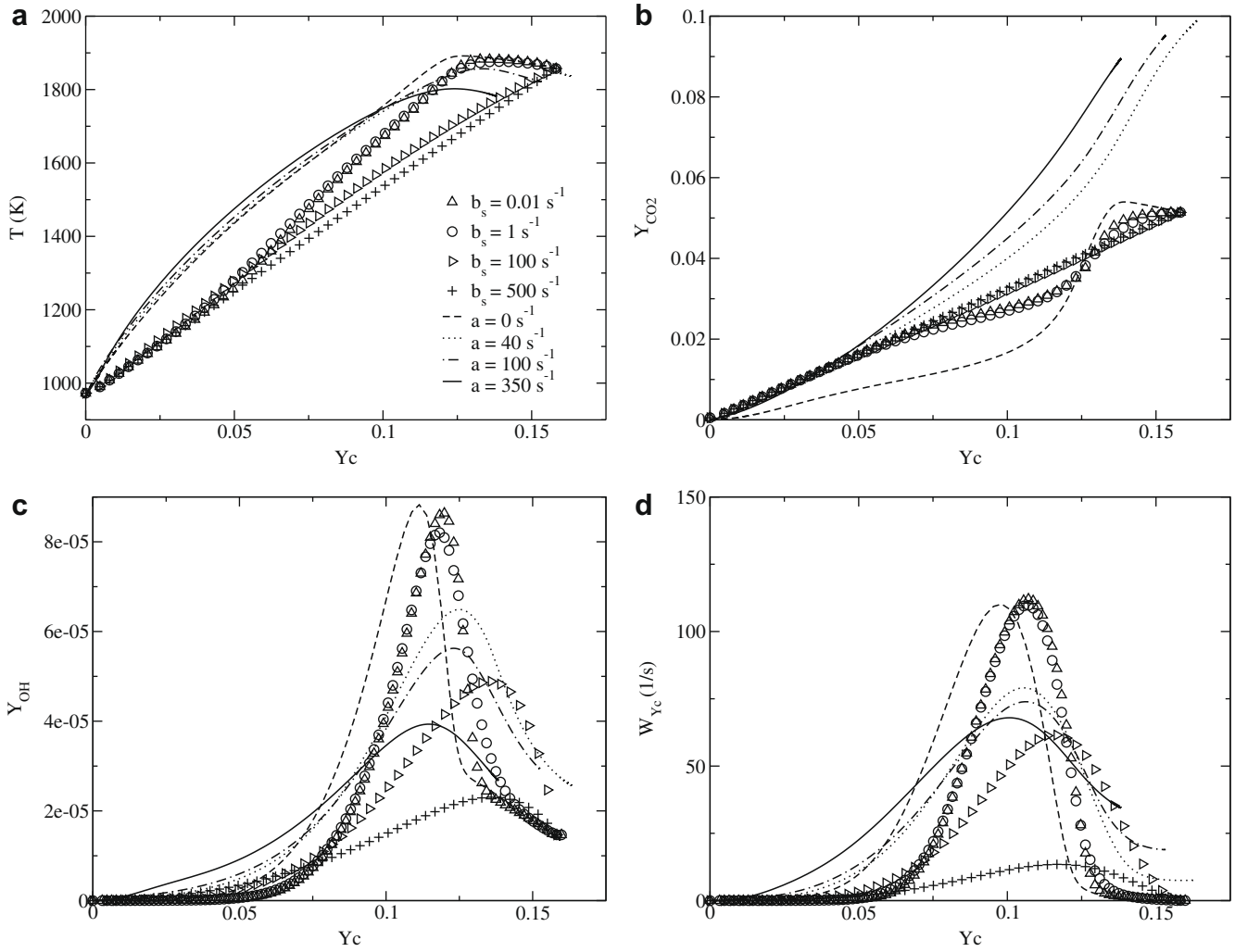

Fig. 8. Rich ϕ 2.8 (Z 0.375). (a) Temperature; (b) mass fraction CO_2; (c) OH; (d) ω_{Y_c}. Symbols: premixed (Eqs. (27) and (28)) triangle-up: b_s 0.01 s ^{1}; circle: 1 s ^{1}; triangle-right: 100 s ^{1}; plus: 500 s ^{1}; Lines: diffusion (Eqs. (29) and (30)) dashed: a 0 s ^{1}; dotted: 40 s ^{1}; dotted-dashed: 100 s ^{1}; solid: 350 s ^{1}.

ing unrealistic $b(Z)$ shapes, the premixed laminar flamelets are probed for this parameter, but only its normalized shape will be used, the level being imposed without considering laminar re sponses. The additional analysis of the premixed calculated flam elets set further reveals that, globally, the distribution of $b(Z)$ follows roughly the exponential of the inverse complementary error function of Z within the flammability domain, b reaching its peak value in the vicinity of the stoichiometric point,

$$b(Z) \quad b_s \exp[\ 2(\mathrm{erfc}^{\ 1}(Z/Z_s))^2], \tag{25}$$

where b_s is the maximum value of $b(Z)$ at the stoichiometric point (Z_s 0.1769 here). $b(Z)$ is assumed to vanish in fuel and oxidizer streams. b_s plays a role similar to the strain rate, a, in Eq. (23). The amplitude of the progress of reaction scalar dissipation rate is thus modulated with b_s to mimic the eventual external strain rate imposed to the flame, and assuming a single generic shape in com position space. In practice, it is found that varying the amplitude b_s has a much greater impact on the flame response that modifying the global χ_{Y_c} shape in Z Y_c space.

Cross scalar dissipation rates were previously discussed and modeled for turbulent flames [36,54,55]. To anticipate the behavior of χ_{Z,Y_c}, it is conveniently reorganized in

$$\chi_{Z,Y_c} \quad \frac{\lambda}{\rho C_p}\nabla Y_c \ \nabla Z \quad \frac{\lambda}{\rho C_p}|\nabla Z||\nabla Y_c|\mathbf{n}_Z \ \mathbf{n}_{Y_c} \quad \mathbf{n}_Z \ \mathbf{n}_{Y_c}(\chi_Z\chi_{Y_c})^{1/2} \tag{26}$$

with $\mathbf{n}_Z$ $\nabla Z/|\nabla Z|$ and $\mathbf{n}_{Y_c}$ $\nabla Y_c/|\nabla Y_c|$, the unit vectors nor mal to the iso Z and iso Y_c surfaces. The modeling of χ_Z and χ_{Y_c} has been discussed above; so once $\mathbf{n}_Z$ $\mathbf{n}_{Y_c}$ is known, the cross dis sipation rate can be approximated. In a moderately curved diffusion flame, Z and Y_c gradients are likely to be aligned; thus $\mathbf{n}_Z$ $\mathbf{n}_{Y_c}$ ± 1. In a weakly stratified and mostly premixed flame, or along the pre mixed branches of a triple flame [34] submitted to a low strain le vel, the flame front is perpendicular to isomixture fraction surfaces and $\mathbf{n}_Z$ $\mathbf{n}_{Y_c} \approx 0$. Intermediate partially premixed combustion re gimes would promote $-1 < \mathbf{n}_Z$ $\mathbf{n}_{Y_c} < +1$. In the following, both ex treme cases $\mathbf{n}_Z$ $\mathbf{n}_{Y_c}$ ± 1, leading to maximum magnitude of the cross scalar dissipation rate, are considered, to conclude that the introduction in Eqs. (21) and (22) of the cross terms does not pro foundly modify the tabulated chemical response, confirming previ ous DNS results, where contributions related, to this cross scalar dissipation rate were found negligible compared to others, see for instance Fig. 12 in [36].

3. Results

Four types of calculations have been performed. Freely propa gating premixed flames are first computed to validate the flame composition space numerical solver against solutions obtained in physical space. Steady strained premixed flames computed in Y_c space are then investigated and compared against unsteady

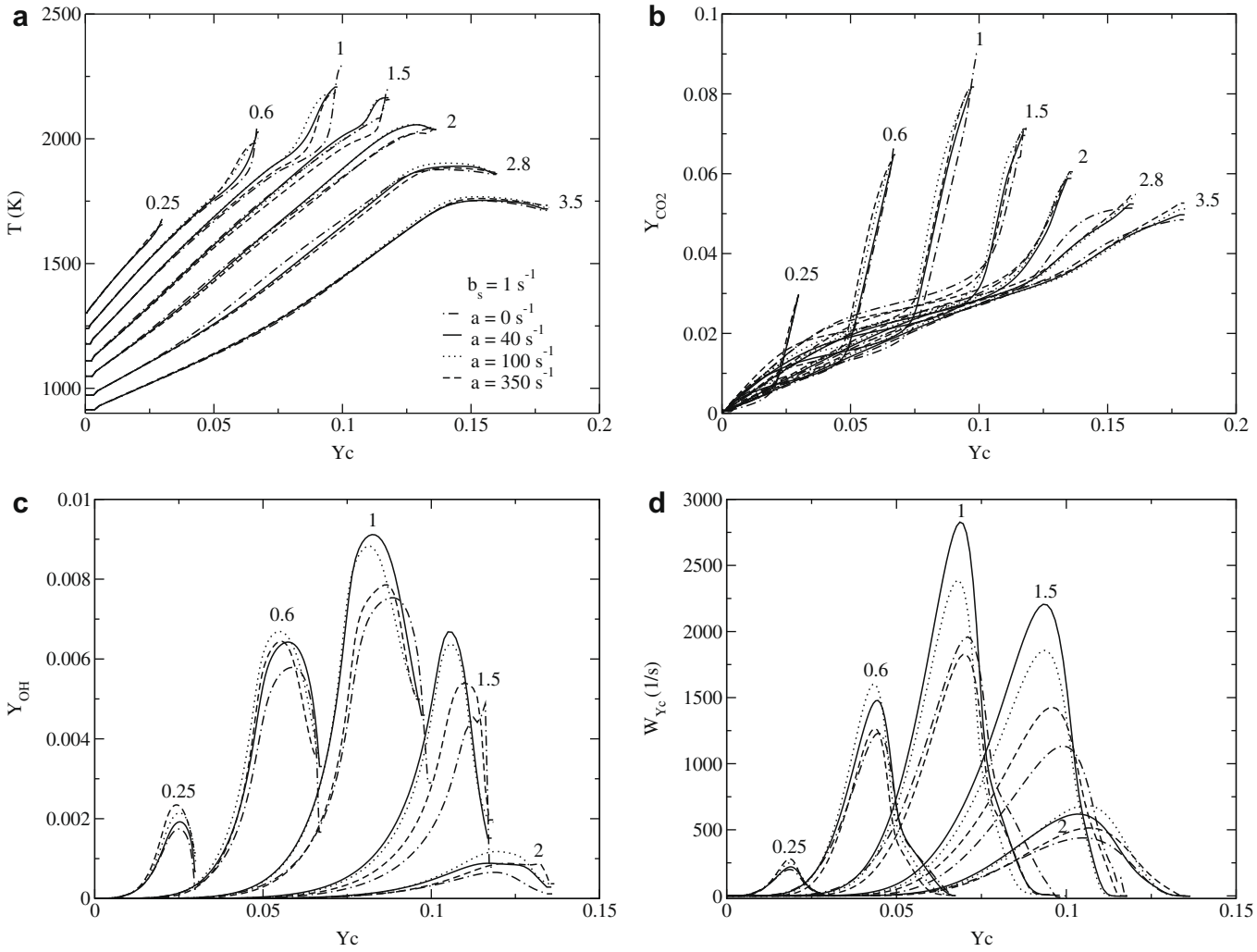

Fig. 9. Z–Y_c flame trajectories (Eqs. (21) and (22)) with χ_{Z,Y_c} 0. (a) Temperature; (b) mass fraction CO_2; (c) OH; (d) ω_{Y_c}. Equivalence ratios given in graphs. b_s 1 s ^{1} (Eq. (24)). Dashed-dotted: a 0 s ^{1}; line: 40 s ^{1}; dotted: 100 s ^{1}; dashed: 350 s ^{1}.

strained diffusion flame responses, projected in Y_c space but calcu lated by limiting the solver to Z space. The objective here is to compare major species trajectories that would be obtained from such tabulations. Finally, solutions of Eqs. (21) and (22) are studied with and without contribution of the cross scalar dissipation rate terms. Scalar dissipation rate values are considered over a large range in these tests, because in LES of turbulent flames, large var iation of scalar dissipation rates may be expected; from the burner exit up to well mixed products, the mixing rate can strongly vary.

3.1. Steady one dimensional premixed flamelets in Y_c space

The flame solution procedure in composition space is first eval uated by considering Eqs. (21) and (22), without fluxes in mixture fraction space,

$$\rho\frac{\partial Y_i}{\partial \tau}+\frac{\partial Y_i}{\partial Y_c}\dot{\omega}_c \quad \frac{\rho\chi_{Y_c}}{\mathrm{Le}_i}\frac{\partial^2 Y_i}{\partial Y_c^2}+\dot{\omega}_i, \tag{27}$$

$$\rho\frac{\partial T}{\partial \tau}+\frac{\partial T}{\partial Y_c}\dot{\omega}_c \quad \frac{1}{C_p}\left(\frac{\partial C_p}{\partial Y_c}+\sum_{i\ 1}^{N}\frac{C_{p_i}}{\mathrm{Le}_i}\frac{\partial Y_i}{\partial Y_c}\right)\frac{\partial T}{\partial Y_c}\rho\chi_{Y_c} + \rho\chi_{Y_c}\frac{\partial^2 T}{\partial Y_c^2} \quad \frac{1}{C_p}\sum_{i\ 1}^{N}h_i\dot{\omega}_i, \tag{28}$$

to compare the converged steady flame results against their coun terpart obtained from the PREMIX software [53] physical space solution. The Lewis numbers are set to unity in these preliminary calculations (Le_i 1), to focus on the validity of the composition space solution, aside from effects that could result from the ne glected differential diffusion terms, such as those of Eq. (17). In all premixed cases, the line from the fresh gases mixture (Y_c 0, $Y_{i,o}$) to equilibrium $\left(Y_c^{\mathrm{Eq}}, Y_{i,o}^{\mathrm{Eq}}\right)$ represents frozen flow mix ing between unburned and burned gases. As seen below, when the scalar dissipation rate increases from its freely propagating flame level, the premixed flame Damköhler number decreases, the burn ing rate diminishes strongly because of straining and the solution tends to recover this frozen flow mixing line. It is here intentionally assumed that there always exist burned gases interacting with fresh ones; as in already ignited, and operating away from full extinction, real combustion systems, where combustion occurs at different burning regimes depending on the local mixing rates, mimicked here by varying χ_{Y_c}. Hence, the full disappearance of burnt gases is not an option of the upper Y_c boundary condition in this part of the study and the frozen flow (fresh burned) mixing line is used as initial condition. Fig. 3 shows Y_c space evolutions of tempera ture, and CH_4, CO_2, and OH mass fractions for three different flames, lean at equivalence ratio ϕ 0.63 (Z 0.12), stoichiometric of ϕ 1 (Z 0.1769), and rich of ϕ 1.25 (Z 0.21). To perform

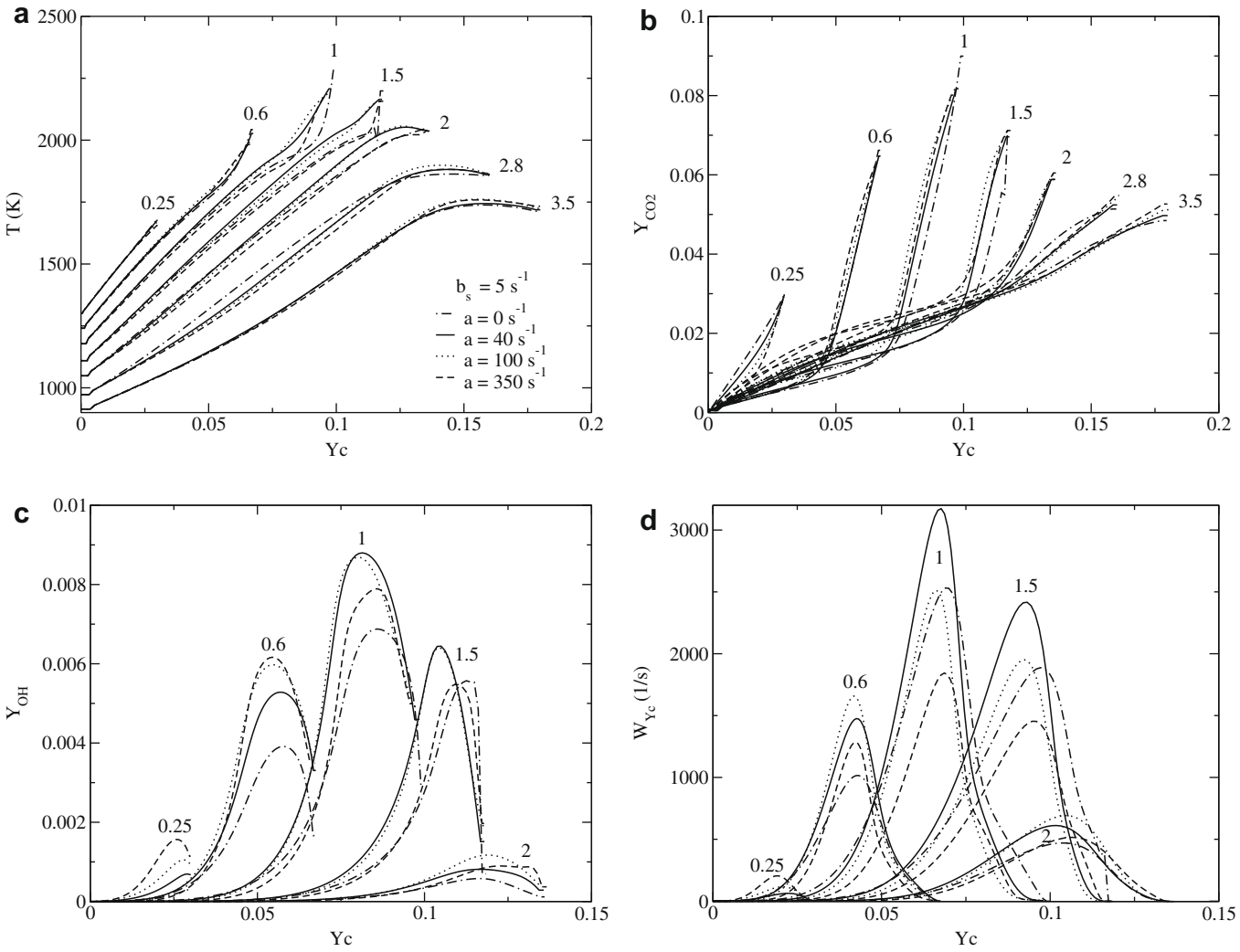

Fig. 10. Z–Y_c flame trajectories (Eqs. (21) and (22)) with χ_{Z,Y_c} 0. (a) Temperature; (b) mass fraction CO_2; (c) OH; (d) ω_{Y_c}. Equivalence ratios given in graphs. b_s 5 s ^{1} (Eq. (24)). Dashed-dotted: a 0 s ^{1}; line: 40 s ^{1}; dotted: 100 s ^{1}; dashed: 350 s ^{1}.

meaningful comparisons, the calculation is performed using the freely propagating value of the Y_c dissipation rate, as measured in the physical space solution. The composition space computed flame reproduces the PREMIX [53] physical space responses projected in Y_c space, with only a small deviation in minor species peak values (Fig. 3). This gives some confidence in the numerics of the MFM sol ver developed, and also suggests that the Y_c coordinate chosen allows for reproducing most of the flame properties from their Y_c space computations.

From now on, the unity Lewis number assumption is no longer retained ($Le_i \neq 1$); the amplitude of χ_{Y_c} is varied to examine the behavior of strained premixed flames computed in Y_c space. Strain rate effects in premixed flame were previously analyzed and re ported in the literature [56 60] and it is not intended here to re peat any of these investigations, but rather to restrict the study to the chemistry tabulation context. The progress variable scalar dissipation rate is varied by selecting various b_s values for three equivalence ratios: lean ϕ 0.25 (Z_L 0.05), stoichiometry ϕ 1 (Z_s 0.1769) and rich ϕ 2.8 (Z_R 0.38). Figs. 4 and 5 dis play distributions of temperature, CH_4, CO_2, CO, and OH mass frac tions, and $\dot{\omega}_{Y_c}$ for the lean and rich flamelets considered. For lean and rich flames, the couple $(b_s, b(Z^*))$ is given in figure legends, and Z^* Z_L or Z^* Z_R and $b(Z^*)$ is the maximum scalar dissipation rate actually seen by the flame, b_s giving the maximum level at stoichiometry in Eq. (25).

The lean flamelet ϕ 0.25 is only able to sustain small values of scalar dissipation rate (Fig. 4). At χ_{Y_c} 0.0032 s ^{1} (here χ_{Y_c} $b(Z^*)$; the maximum value of scalar dissipation rate through the flame is quoted for the discussion), the mixture nearly auto ignites without many molecular diffusion effects, because the fresh gases are ob tained from mixing with vitiated air at 1350 K, to burn strongly, as evidenced by a rapid consumption of CH_4 (Fig. 4b), a sharp in crease in production of OH radicals (Fig. 4e) and an important in crease of $\dot{\omega}_{Y_c}$, the source of reaction progress (Fig. 4f). Increasing the scalar dissipation rate is accompanied by a decrease of chemi cal reactions until very low burning, materialized by frozen flow mixing with burnt gases. At χ_{Y_c} 3.2s ^{1}, the chemical reactions have difficulty in surviving, as seen from the dramatic decrease of $\dot{\omega}_{Y_c}$ (Fig. 4f). Close to the frozen flow mixing limit, it is also ob served from Fig. 4 that the thermochemical response of the flame (temperature, species concentrations) is indeed almost linear between unburned and equilibrium burned states. Above χ_{Y_c} 3.2s ^{1}, the scalar dissipation rate is too high for this lean flame and almost no combustion remains.

Under stoichiometric conditions (Fig. 5), obviously the flame is able to sustain much higher levels of scalar dissipation rates, up to χ_{Y_c} 50 s ^{1}, with high burning rates. Around χ_{Y_c} 5 s ^{1} strong burning is observed, with a marked curvature of the CH_4 distribution and a peak of $\dot{\omega}_{Y_c} \approx 2500$ s ^{1}. The rich flame features values of $\dot{\omega}_{Y_c}$ an order of magnitude smaller than the stoichiometric ones (not

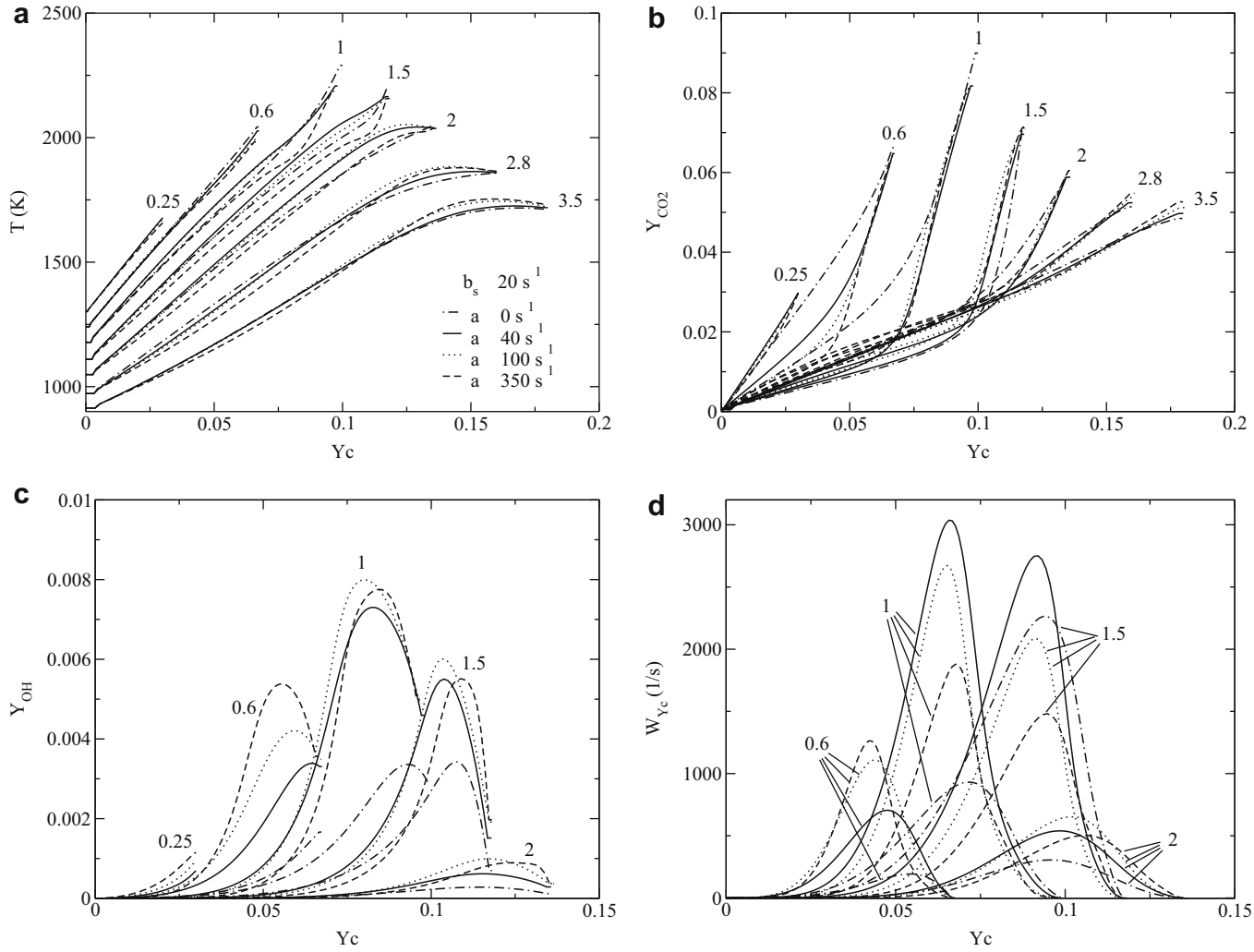

Fig. 11. Z–Y_c flame trajectories (Eqs. (21) and (22)) with χ_{Z,Y_c} 0. (a) Temperature; (b) mass fraction CO_2; (c) OH; (d) ω_{Y_c}. Equivalence ratios given in graphs. b_s 20 s ^{1} (Eq. (24)). Dashed-dotted: a 0 s ^{1}; line: 40 s ^{1}; dotted: 100 s ^{1}; dashed: 350 s ^{1}.

displayed for brevity). The global shape of trajectories is profoundly modified by both, equivalence ratio and scalar dissipation rate vari ations, for instance the temperature is below its mixing line for the lean and stoichiometric cases and above in the rich flame. The same is observed with intermediate species and CO_2, having fully different trajectories depending on the condition examined (equivalence ra tio and dissipation rate). Notice, however, that the usual shape of FPI lookup table for such flow condition is recovered (see Fig. 1 in [10]). Overall, and as expected, to vary χ_{Y_c} has a nonnegligible impact on one dimensional species and temperature trajectories in Y_c space. χ_{Y_c} varies and fluctuates in turbulent flames; therefore, it may be hazardous to tabulate chemistry with a single trajectory for a given equivalence ratio, as it is usually done, without allowing the possibility of varying the molecular diffusion amplitude, and thereby the flame Damköhler number.

3.2. Premixed versus unsteady diffusion flamelets

Despite their inherent limitations alluded in introduction, pre mixed flame databases have been used for chemistry tabulation of nonpremixed burners [10,20,61], mainly because they cover conveniently the full range of thermochemical variations, from fresh mixture up to chemical equilibrium. For sufficiently high lev els of temperature on the air side, unsteady diffusion flamelets un dergo spontaneous ignition and also evolve from a fresh mixture up to a burning steady state, therefore, covering the full range of mixture conditions, which are then easily tabulated. Thereby, be fore introducing the full coupling between fluxes in mixture frac tion and progress of reaction coordinates present in Eqs. (21) and (22), it is interesting to compare premixed and unsteady diffusion flame basic responses, to quantify, in a single framework, the im pact of interactions between iso equivalence ratio surfaces (diffu sive fluxes proportional to χ_Z), which are neglected in premixed flame databases; whereas, in counterpart, propagating effects are a priori not included in diffusion flame tabulation. In other words, the premixed flame response in Y_c space, therefore, without accounting for Z space fluxes, is compared with the unsteady diffu sion flame one, which accounts for fluxes in Z space. The unsteady diffusion flame solution $Y_i(Z,\tau;\chi_Z)$ is reorganized in $Y_i(Z,Y_c(\tau);\chi_Z)$ ($Y_c(\tau)$ evolving between fresh and burnt gases) to be examined side by side in Y_c space, and for a given Z (or equiv alence ratio value), with the steady premixed flame trajectory $Y_i(Z,Y_c;\chi_{Y_c})$.

Eqs. (27) and (28) are solved for the premixed flame; the un steady diffusion flame system reads

$$\rho\frac{\partial Y_i}{\partial\tau} \quad \frac{\rho\chi_Z}{\mathrm{Le}_i}\frac{\partial^2 Y_i}{\partial Z^2}+\dot{\omega}_i, \tag{29}$$

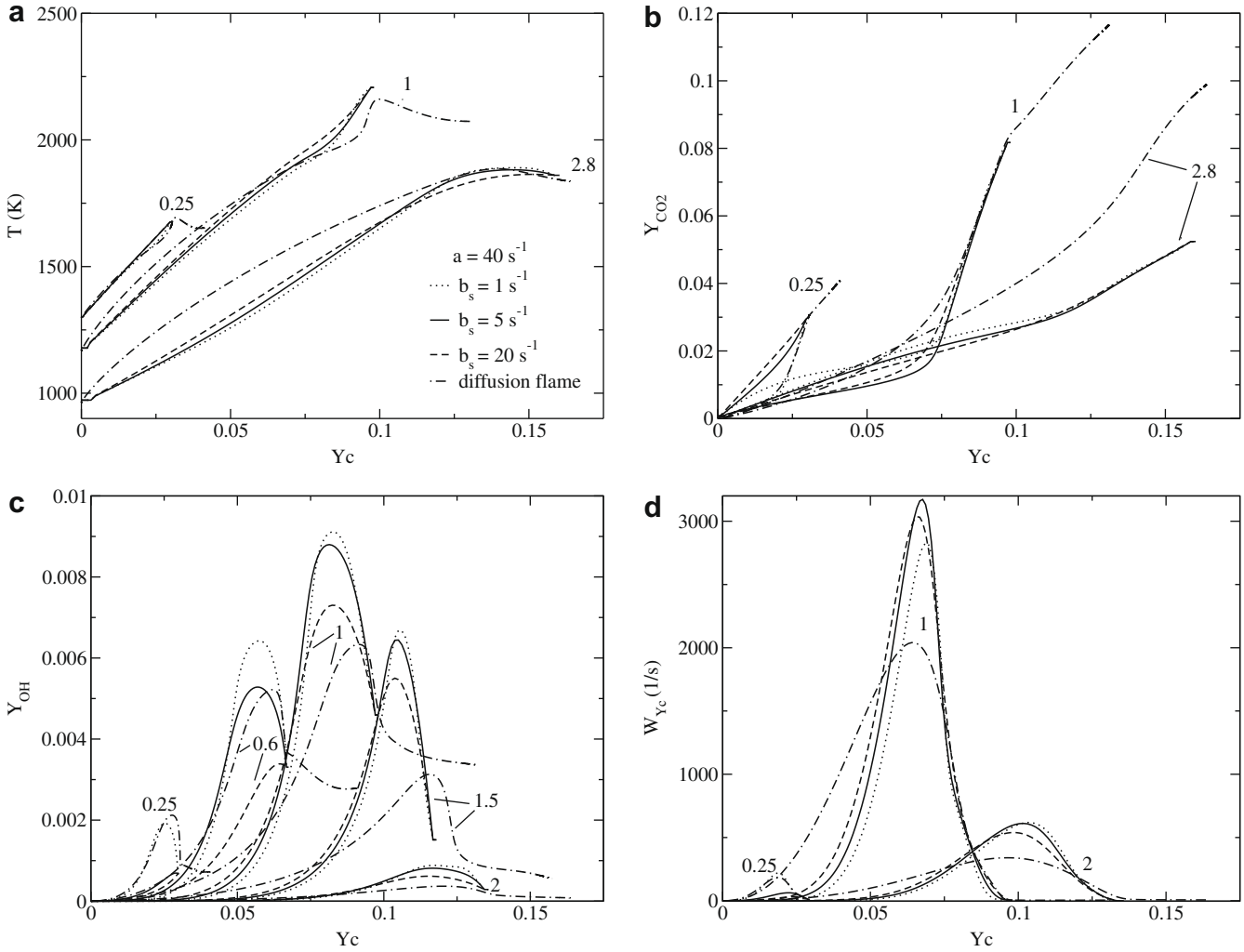

Fig. 12. Z–Y_c flame trajectories (Eqs. (21) and (22)) with χ_{Z,Y_c} 0. (a) Temperature; (b) mass fraction CO_2; (c) OH; (d) ω_{Y_c}. Equivalence ratios given in graphs. a 40 s ^{1} (Eq. (23)). Dotted b_s 1 s ^{1}; line: 5 s ^{1}; dashed: 20 s ^{1}. Dotted-dashed: diffusion flame (Eqs. (29) and (30)).

$$\rho\frac{\partial T}{\partial \tau} \quad \frac{1}{C_p}\left(\frac{\partial C_p}{\partial Z}+\sum_{i\ 1}^{N}\frac{C_{P_i}}{Le_i}\frac{\partial Y_i}{\partial Z}\right)\left(\frac{\partial T}{\partial Z}\rho\chi_Z\right) \quad \rho\chi_Z\frac{\partial^2 T}{\partial Z^2} \quad \frac{1}{C_p}\sum_{i\ 1}^{N}h_i\dot{\omega}_i. \tag{30}$$

The parameter a entering the mixture fraction scalar dissipation rate expression (Eq. (23)) has been varied from a 0 s ^{1}, up to a 350 s ^{1}, corresponding to $\chi_Z(Z_s)$ 23.5 s ^{1}. At t 0, the initial diffusion flamelet distribution is prescribed from the frozen flow mixing response in mixture fraction space. Because of the vitiated air (1350 K), the mixture self ignites and evolves till a steady state is reached; also, the premixed flame solution for vanishing values of χ_{Y_c} must provide results close to diffusion flame solutions for vanishing values of χ_Z, because Eqs. (27) and (28) and Eqs. (29) and (30) for χ_Z 0 and χ_{Y_c} 0 both lead to the simulation of self ignition without any diffusion effects (homogeneous system).

Fig. 6 presents trajectories collected in the unsteady diffusion flamelet under a lean (ϕ 0.25), Fig. 7 a stoichiometric (ϕ 1.0) and Fig. 8 a rich (ϕ 2.8) condition. In all cases, with a 0 (χ_Z 0) in Eqs. (29) and (30), the thermochemical trajectories are controlled by chemical sources only; autoignition at various equivalence ratios is thus calculated up to an equilibrium condition, which is also the premixed flame burned gases state. Aside from this equilibrium point, there is no premixed flame that exactly matches these χ_Z 0 trajectories (Figs. 6 8); the premixed flame with the smallest b_s (or χ_{Y_c}) nonetheless displays the closest response, as expected.

For nonzero scalar dissipation rates, one of the most striking features in the comparison between premixed and unsteady diffusion flame trajectories is the amplitude variation of the Y_c coordinate. Final (or equilibrium) points differ (see Figs. 6 8); a behavior that was reported in a different form in the literature, for instance comparing premixed and diffusion flamelet solutions in physical space [24]. Species diffusion in mixture fraction space interacts with the intermediate species dissociation balance to produce these nonnegligible variations of the burned gases compositions, also observed in experiments [62]. Therefore, part of the composition space covered by diffusion combustion is not accessible to premixed flamelets. The source $\dot{\omega}_{Y_c}$ is also nonzero in diffusion flame burnt gases, because it counterbalances mass diffusion according to the steady state form of Eq. (29). This is not the case in premixed flamelets, where it vanishes in burned gases. As expected from the diffusion flame solution [50], the amplitude of the Y_c space variation (compared to premixed flame) depends on χ_Z, as a result of scalar dissipation rate effects. In the Y_c extended part of lean or stoichiometric conditions, temperature and OH mass fraction decrease (Fig. 6a and c, Fig. 7a and c) and the CO_2 mass fraction increases almost linearly (Fig. 6b, Fig. 7b). In the rich location (Fig. 7), the length of the Y_c space is globally reduced, the Damköhler

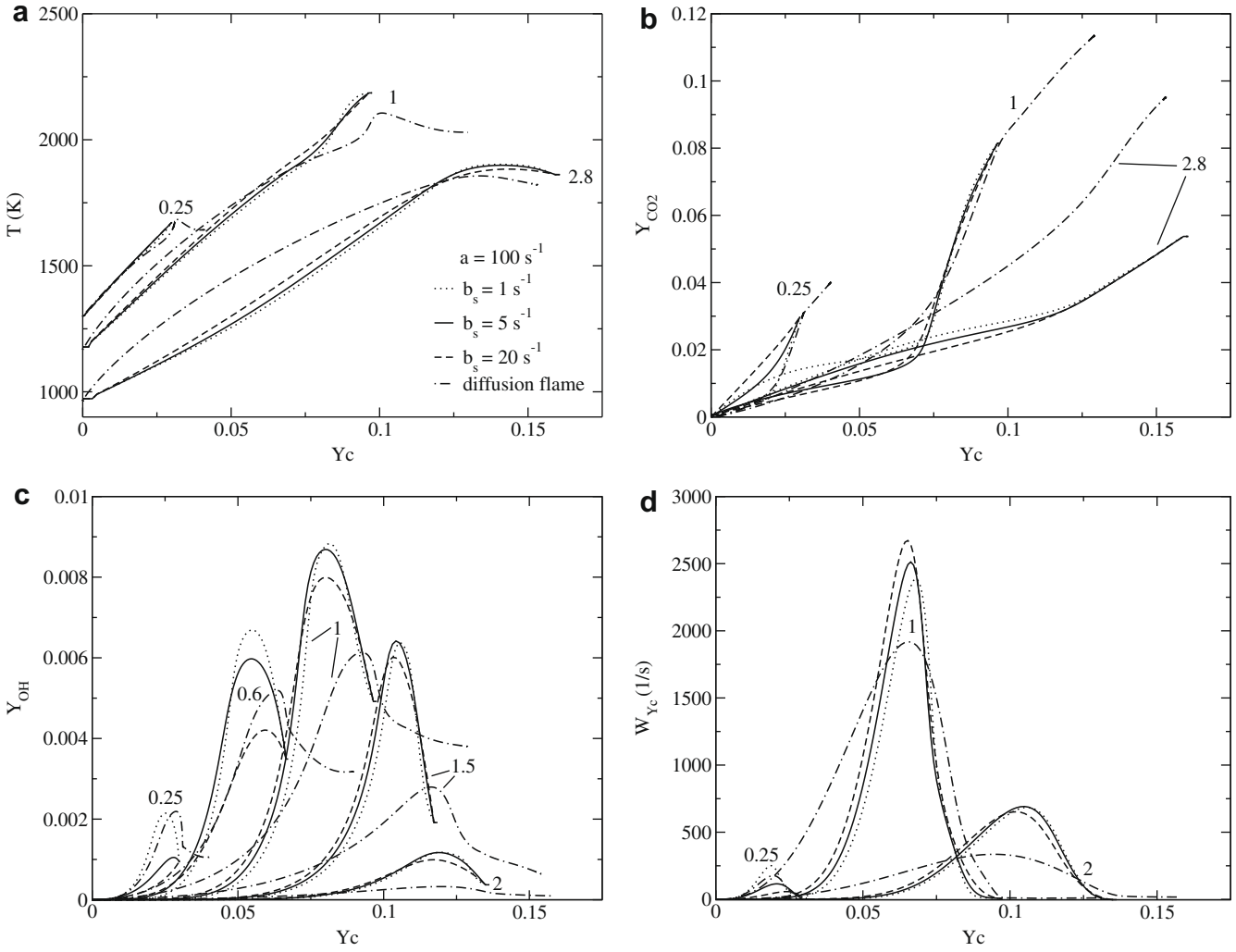

Fig. 13. Z–Y_c flame trajectories (Eqs. (21) and (22)) with χ_{Z,Y_c} 0. (a) Temperature; (b) mass fraction CO_2; (c) OH; (d) ω_{Y_c}. Equivalence ratios given in graphs. a 100 s $^{-1}$. Dotted b_s 1 s $^{-1}$; line: 5 s $^{-1}$; dashed: 20 s $^{-1}$. Dotted-dashed: diffusion flame (Eqs. (29) and (30)).

number is expected to be much less than in the burned gases viti ated air lean and stoichiometric zones, and the departure of spe cies trajectories from the premixed solution is, therefore, much more pronounced.

From these results, clear differences in tabulated trajectories based on either premixed or diffusion flamelets are observed; obvi ously they correspond to two quite different combustion arche types and the chemistry manifolds differ. The response of the hybrid model problem, which couples both combustion regimes in a natural manner, is now discussed for chemistry tabulation.

3.3. Z Y_c coupled flamelets

The objective of using Eqs. (21) and (22) is to account for diffu sive processes and scalar dissipation rate effects, or straining, act ing on both fuel air mixing and reaction progress simultaneously, to mimic mass fluxes that exist across iso mixture fraction sur faces and, from fresh to burnt gases, through partially premixed turbulent flames. Along these lines, the Z Y_c flame solution is examined now with and without the cross scalar dissipation rate term.

Eqs. (21) and (22) are solved with χ_{Z,Y_c} 0, and in a first set of figures, the progress of the reaction scalar dissipation rate b_s (Eq. (25)) is fixed (b_s 1 s $^{-1}$ in Fig. 9; b_s 5 s $^{-1}$ in Fig. 10; b_s 20 s $^{-1}$ in Fig. 11) to vary, in each figure, the mixture fraction scalar dissi pation rate (Eq. (23)) over a 0 s $^{-1}$ (unstrained), a 40 s $^{-1}$ (mod erate), a 100 s $^{-1}$ and a 350 s $^{-1}$. With a 0 s $^{-1}$, all fluxes in mixture fraction space vanish and the collection of independent premixed flame solutions is retrieved. For every b_s value, modify ing the mixture fraction dissipation rate has a strong impact on the species distribution and on the progress of reaction burning rate (Fig. 9 11). Looking at a given equivalence ratio, the trajecto ries peak values are modified, in terms of both amplitude and loca tion in progress of variable space, specifically on the lean and rich side (see for instance OH and $\dot{\omega}_{Y_c}$ at ϕ 1.5). The variation of b_s also has a nonnegligible effect on the flame response. For instance, in the lean zone ϕ 0.25, a close look into OH mass fraction and burning rate of reaction progress, for low and moderate values of progress variable scalar dissipation rate b_s 1 s $^{-1}$ and b_s 5 s $^{-1}$ (Figs. 9c d, and 10c d), illustrates how increasing scalar dissipa tion rate constantly enhances OH radicals production, followed by an increase of the progress of reaction burning rate, $\dot{\omega}_{Y_c}$. In the stoichiometric region (ϕ 1), OH mass fraction and source of progress variable $\dot{\omega}_{Y_c}$ attain their highest value with moderate sca lar dissipation rate a 40 s $^{-1}$, further increasing a leads to domi nation of fuel oxidizer mixing, and a significant decrease of $\dot{\omega}_{Y_c}$ can be observed in Fig. 10d, for a 350 s $^{-1}$, a quite high value that can be sustained because of the presence of burnt gases vitiated

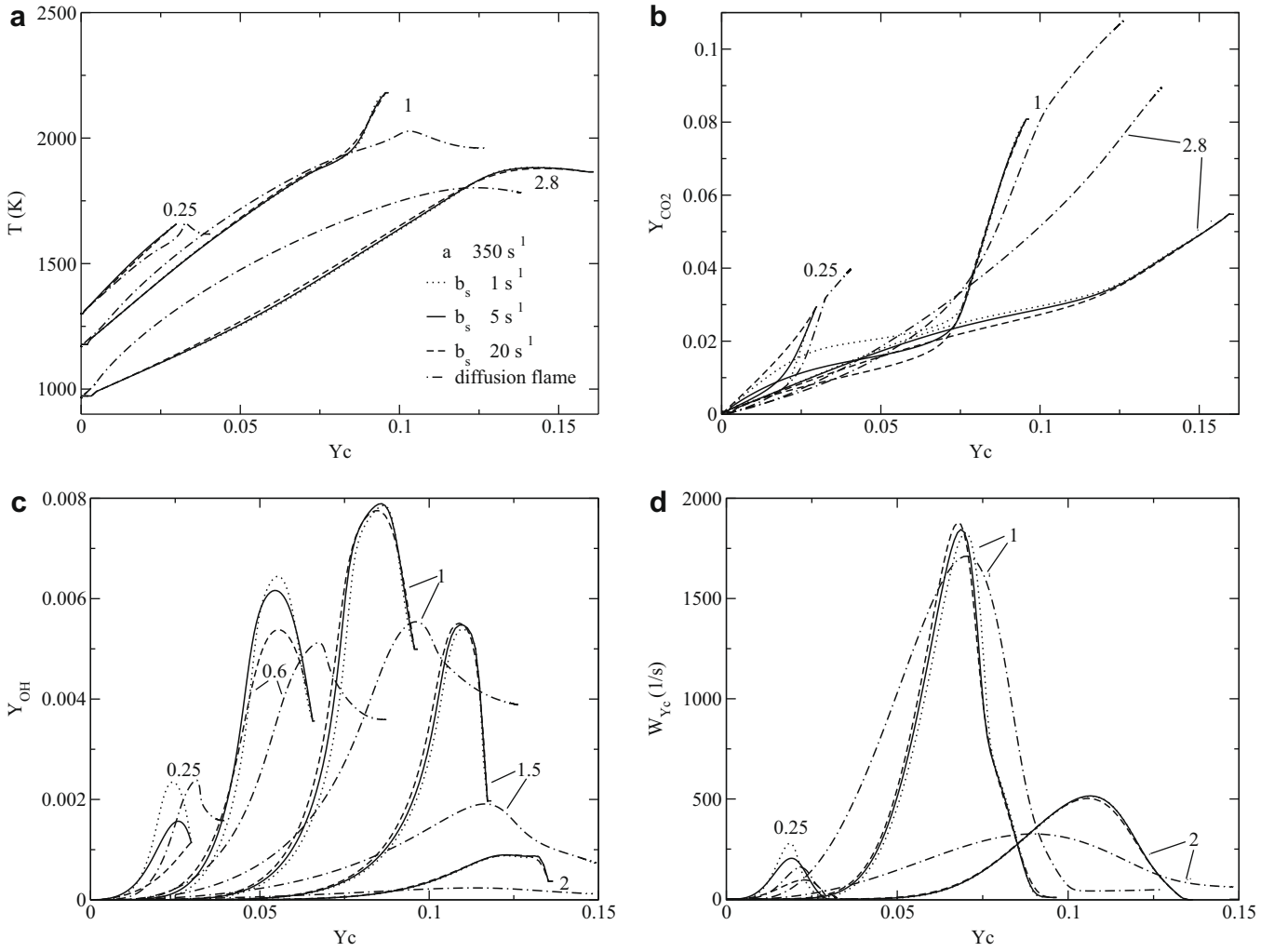

Fig. 14. Z–Y_c flame trajectories (Eqs. (21) and (22)) with χ_{Z,Y_c} 0. (a) Temperature; (b) mass fraction CO_2; (c) OH; (d) ω_{Y_c}. Equivalence ratios given in graphs. a 350 s ^{1}. Dotted b_s 1 s ^{1}; line: 5 s ^{1}; dashed: 20 s ^{1}. Dotted-dashed: diffusion flame (Eqs. (29) and (30)).

air. In the rich zone, the Z Y_c flame response is strongly modified when scalar dissipation rate effects are added. For b_s 20 s ^{1} (Fig. 11), a very low value of production rate of progress variable $\dot{\omega}_{Y_c}$ is observed for a 0 s ^{1} (Fig. 11d). Overall, for nonzero values of a, reaction zones at difference equivalence ratio become coupled and interacting diffusive fluxes help promoting chemical reaction, with a dramatic increase of OH radical level, as well as of the burning rate of reaction progress $\dot{\omega}_{Y_c}$ (Fig. 11c and d). Hence, a quite large departure between the premixed flamelets response (FPI) and the Z Y_c flamelet is observed, a departure that is quite sensitive to χ_Z and χ_{Y_c}.

In a second set of figures, the mixture fraction scalar dissipation rate a is fixed, (a 40 s ^{1} in Fig. 12; a 100 s ^{1} in Fig. 13; a 350 s ^{1} in Fig. 14) and b_s is varied from b_s 1 s ^{1} up to b_s 20 s ^{1}. For comparison, the unsteady diffusion flamelet calculations are also reported for the same a or χ_Z value. First, it is seen that significant differences between Z Y_c flame and unsteady diffusion flamelet responses are observed. The progress variable Y_c is more extended in unsteady diffusion flamelets (Figs. 12 14c and d), the Z Y_c flames Y_c envelope actually lies between premixed and diffusion flames. The rich branch of the Z Y_c flamelet is weakly affected by scalar dissipation rate variation before quenching. The influence, however, is amplified in the lean zone, which is visible, for instance, in OH mass fractions profiles for equivalence ratios of ϕ 0.25 and ϕ 0.6 (Figs. 12 14c).

Figs. 15 and 16 compare Z Y_c flame results obtained with and without the cross scalar dissipation rate term, when it is modeled as χ_{Z,Y_c} $\pm(\chi_Z\chi_{Y_c})^{1/2}$. Its impact is not fully negligible, as could be expected, with some differences observed in the temperature profiles in the rich zone (ϕ 2, ϕ 2.8, and ϕ 3.5, Fig. 15a and Fig. 16a). Aside from this observation, its influence on the burning rate is not that pronounced, and in a very first approach, it may be reasonably accurate to build a Z Y_c flamelet manifold for chemistry tabulation without this term.

Because they rely on the same basic control parameters, mixture fraction and a measure of the reaction progress, these Z Y_c flamelets can be filtered for LES or averaged in RANS with presumed pdfs, following existing procedures [10,20]. Similarly, previously developed modeling for scalar dissipation rates can also be adopted, though in a very first approach, the simple use of the Z Y_c flamelets response with fixed nonzero moderate values of χ_Z and χ_{Y_c}, would already improve both, the FPI premixed flamelet tabulation, by incorporating missing fluxes between flamelets in mixture fraction space, and the diffusion flamelet tabulation, by including the option of flame propagation in the Y_c direction.

Still, as with any pretabulated chemical behavior approach, there is room left for improvements; one point that would be missing in LES with this multidimensional flamelet manifold (or Z Y_c flamelets) is direct unsteady coupling with the velocity field. Indeed, properties of turbulent velocity fluctuations and of scalar

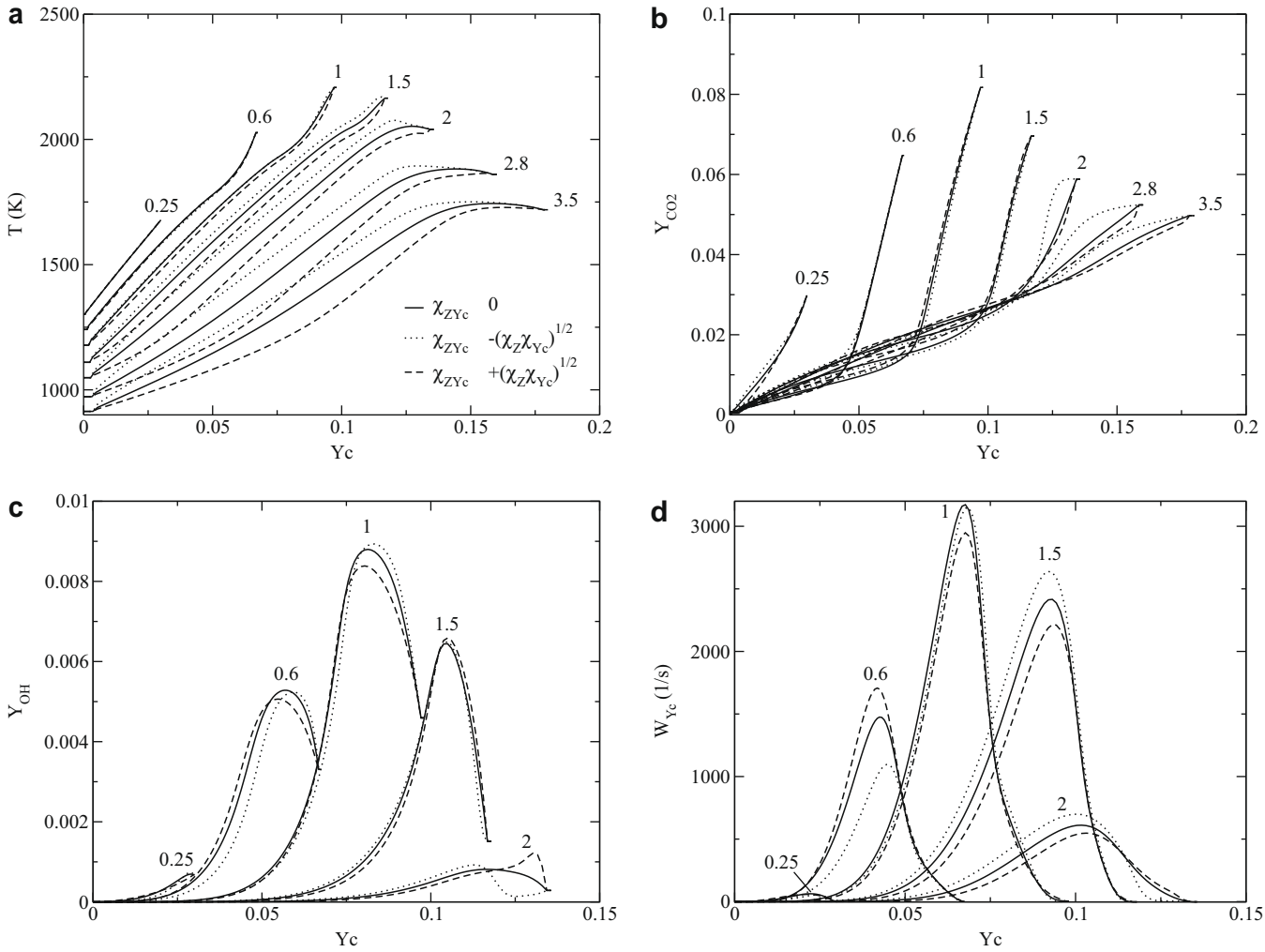

Fig. 15. Z–Y_c flame trajectories (Eqs. (21) and (22)). (a) Temperature; (b) mass fraction CO_2; (c) OH; (d) ω_{Y_c}. Equivalence ratios given in graphs. a 40 s ^{1}. Dotted b_s 5 s ^{1}. Line: χ_{Z,Y_c} 0; dotted: $-(\chi_Z\chi_{Y_c})^{1/2}$; dashed: $+(\chi_Z\chi_{Y_c})^{1/2}$.

dissipation control the scalar dissipation rates [63,64]; also, heat release modifies mass transport, which then feed back on the topology of the composition space coordinates and scalar dissipa tion rates, as for instance in partially premixed flame fronts [35,52,65,66]. Nevertheless, compared to the single dimensional approaches in use today, the multidimensional and coupled diffu sion/reaction information packed into MFM tabulation already constitutes a step forward. Moreover, in terms of unsteadiness, on flight calculations of MFM equations in their unsteady form can be envisioned for LES in massively parallel computers, where part of the processors would be devoted to MFM solving. The num ber of composition space directions used to build the MFM may then be increased to address combustion problem with multiple inlet (more than two) and/or burnt gases diluted flames with variable heat loss, still the exact determination of the proper com position space variables is open at this stage. The size of the lookup table can rapidly become a practical problem with MFM. One op tion would be to extend the method proposed in [67], which is based on self similar behavior of diffusive reactive flow problems filtered with probability density functions.

In LES of turbulent flames, the scalar dissipation rates are decomposed into resolved and sub grid scale (SGS) parts. The SGS mixture fraction dissipation rate could be modeled using a lin ear relaxation hypothesis (see Eq. (28) of [10]), the progress of reaction dissipation rate is sensitive to chemistry, and expressions exist combining a reactive part with a mixing part (Eq. (33) of [10]) and modeling for the cross scalar dissipation rate may be found in [36,54].

Notice that dealing with mixtures at room temperature that do not self ignite is straightforward with MFM; for high scalar dissi pation rate levels, a linear versus Y_c response is obtained by con sidering the two points composed of the fresh and burnt gases (computed at equilibrium), this linear distribution is used as an ini tial condition and then the solution is allowed to evolve according to the desired scalar dissipation rate values.

4. Summary

Combustion chemistry is highly sensitive to molecular diffusion and various attempts have been made in the literature to tabulate composition space species trajectories, in such a way that they are representative of the imbalance between chemical sources and species and heat diffusion. This is usually done with a one dimen sional archetype flame model problem, as premixed or diffusion flamelets, each of those being representative of a well defined combustion regime. In real nonpremixed systems, partial premix ing of reactants is quite often observed, and to deal with such re gimes, a multidimensional flamelet formalism may be derived from first principles equations and selected hypotheses. The

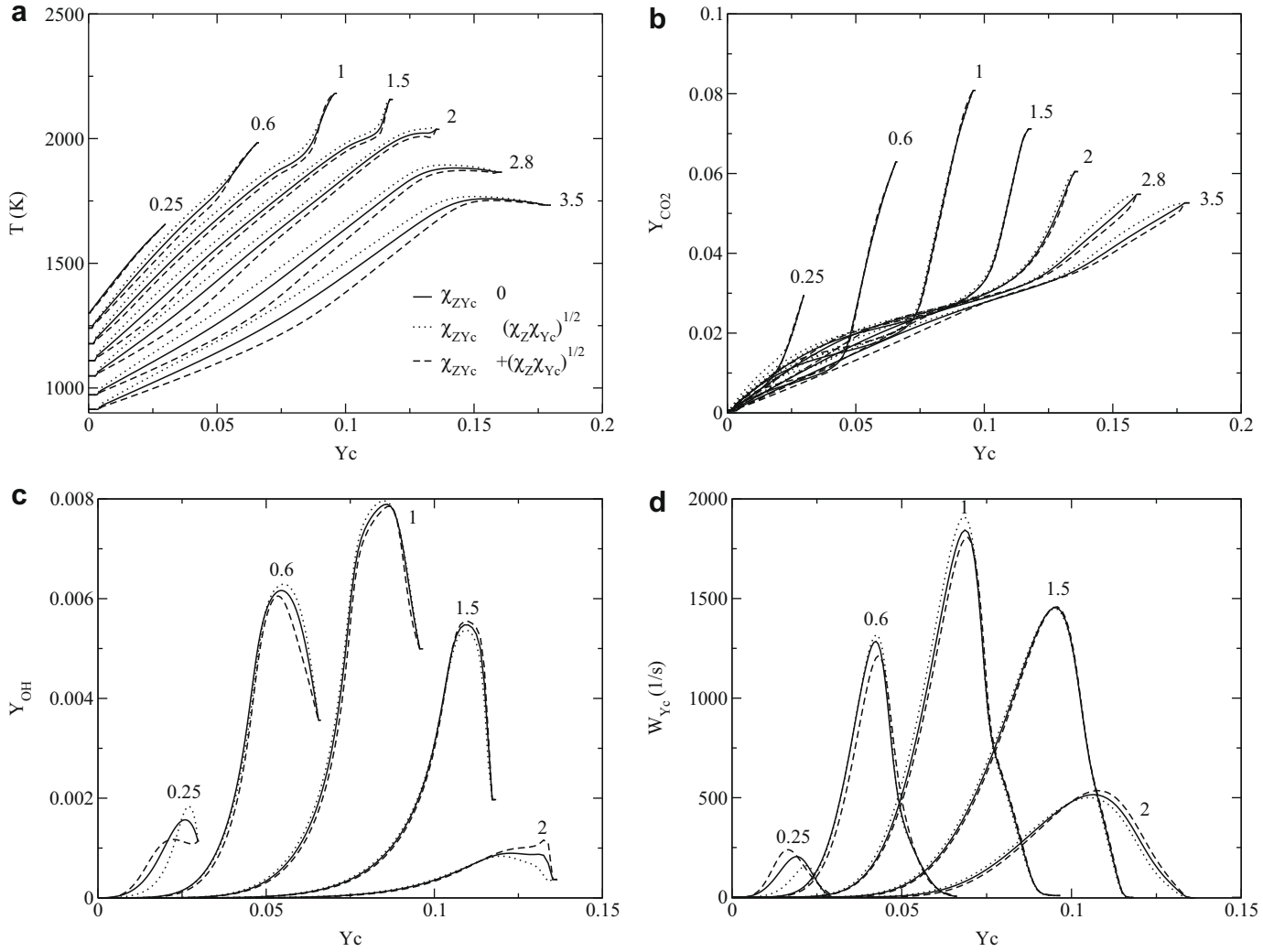

Fig. 16. $Z-Y_c$ flame trajectories (Eqs. (21) and (22)). (a) Temperature; (b) mass fraction CO_2; (c) OH; (d) ω_{Y_c}. Equivalence ratios given in graphs. a 350 s ^{1}. Dotted b_s 5 s ^{1}. Line: χ_{Z,Y_c} 0; dotted: $-(\chi_Z\chi_{Y_c})^{1/2}$; dashed: $(\chi_Z\chi_{Y_c})^{1/2}$.

corresponding flames would belong to stratified triple or edge flame types, including the fully premixed and diffusion flames as asymptotic conditions.

The response of coupled mixture fraction and progress of reac tion flamelets to scalar dissipation rate variations has been exam ined and compared in composition space with that of a strained one dimensional premixed flame and unsteady diffusion flame. The resulting multidimensional flamelet generated manifold, evolving in five dimensions (mixture fraction, progress of reaction, and three scalar dissipation rates), opens some perspectives for fu ture developments in partially premixed turbulent combustion modeling, for instance in the large eddy simulation context.

Acknowledgments

This work is supported by ADEME and AirLiquide through the SAFIR (Simulation Avancée de Foyers Industriels avec Recycle) pro jet. Computing resources were provided by IDRIS CNRS and CRIHAN.

References

[1] R.W. Bilger, S.B. Pope, K.N.C. Bray, J.F. Driscoll, Proc. Combust. Inst. 30 (2004).
[2] X. Paubel, A. Cessou, D. Honoré, L. Vervisch, R. Tsiava, Proc. Combust. Inst. 31 (2006).
[3] S.M. Correa, Proc. Combust. Inst. 27 (1998) 1793–1807.
[4] G. Subramanian, R. Bounaceur, A.P. Cruz, L. Vervisch, Combust. Sci. Technol. 179 (9) (2007) 1937–1962.
[5] A. Cavaliere, M. de Joannon, Prog. Energy Combust. Sci. 30 (4) (2004) 329–366.
[6] D. Tabacco, C. Innarella, C. Bruno, Combust. Sci. Technol. 174 (2002).
[7] N. Peters, Turbulent Combustion, Cambridge University Press, 2000.
[8] C. Hasse, N. Peters, Proc. Combust. Inst. 30 (2005) 2755–2762.
[9] C. Felsch, M. Gauding, C. Hasse, S. Vogel, N. Peters, Proc. Combust. Inst. 32 (2) (2009) 2775–2783.
[10] P. Domingo, L. Vervisch, D. Veynante, Combust. Flame 152 (3) (2008) 415–432.
[11] E. Knudsen, H. Pitsch, Combust. Flame 156 (3) (2009) 678–696.
[12] O. Gicquel, N. Darabiha, D. Thevenin, Proc. Combust. Inst. 28 (2000) 1901–1908.
[13] J.A. van Oijen, F.A. Lammers, L.P.H. de Goey, Combust. Flame 127 (3) (2001) 2124–2134.
[14] S. Delhaye, L.M.T. Somers, J.A. van Oijen, L.P.H. de Goey, Proc. Combust. Inst. 32 (1) (2009) 1051–1058.
[15] D. Bradley, L.K. Kwa, A.K.C. Lau, M. Missaghi, S.B. Chin, Combust. Flame 71 (2) (1988) 109–122.
[16] U. Maas, S. Pope, Combust. Flame 88 (1992) 239–264.
[17] V. Bykov, U. Maas, Combust. Theory Model. 11 (6) (2007) 839–862.
[18] S.H. Lam, D.A. Goussis, Int. J. Chem. Kinet. 26 (1994) 461–486.
[19] J. Galpin, A. Naudin, L. Vervisch, C. Angelberger, O. Colin, P. Domingo, Combust. Flame 155 (1/2) (2008) 247–266.
[20] A.W. Vreman, B.A. Albrecht, J.A. van Oijen, R.J.M. Bastiaans, Combust. Flame 153 (3) (2008) 394–416.
[21] H. Pitsch, H. Steiner, Phys. Fluids 12 (10) (2000) 2541–2554.
[22] H. Pitsch, Annu. Rev. Fluid Mech. 38 (2006) 453–482.
[23] J.-B. Michel, O. Colin, D. Veynante, Combust. Flame 152 (1–2) (2008) 80–99.

[24] B. Fiorina, O. Gicquel, L. Vervisch, N. Darabiha, S. Carpentier, Combust. Flame 140 (3) (2005) 147–160.
[25] T. Poinsot, D. Veynante, Theoretical and Numerical Combustion, R.T. Edwards, Inc., 2005.
[26] D.G. Talley, Combust. Flame 88 (1992) 83–101.
[27] J.H. ferziger, M. Perić, Computational Methods for Fluid Dynamics, Springer-Verlag, 1996.
[28] N. Darabiha, Combust. Sci. Technol. 86 (1992) 163–181.
[29] H.G. Im, J.H. Chen, J.-Y. Chen, Combust. Flame 118 (1/2) (1999) 204–212.
[30] H. Pitsch, E. Riesmeier, N. Peters, Combust. Sci. Technol. 158 (2000) 389–406.
[31] Z. Ren, S.B. Pope, Combust. Flame 147 (4) (2006) 243–261.
[32] R. Borghi, Prog. Energy Combust. Sci. 14 (1988) 245–292.
[33] P. Anselmo-Filho, S. Hochgreb, R.S. Barlow, R.S. Cant, Proc. Combust. Inst. 32 (2009) 1763–1770.
[34] J.W. Dold, Combust. Flame 76 (1989) 71–88.
[35] S. Ghosal, L.J. Vervisch, Fluid Mech. 415 (2000) 227–260.
[36] P. Domingo, L. Vervisch, J. Réveillon, Combust. Flame 140 (3) (2005) 172–195.
[37] J. Boulanger, L. Vervisch, Combust. Flame 130 (1) (2002) 1–14.
[38] V. Favier, L. Vervisch, Combust. Flame 125 (1/2) (2001) 788–803.
[39] K.N.C. Bray, P. Domingo, L. Vervisch, Combust. Flame 141 (2005) 431–437.
[40] J. Galpin, C. Angelberger, A. Naudin, L. Vervisch, J. Turbul. 9 (13) (2008).
[41] A. Kronenburg, Phys. Fluids 16 (7) (2004) 2640–2648.
[42] A. Kronenburg, M.J. Cleary, Combust. Flame 155 (1/2) (2008) 215–231.
[43] E. Hairer, G. Wanner, Solving ordinary differential equations II. Stiff and differential-algebraic problem, volume 14 of Springer series in computational mathematics, second ed., Springer-Verlag, Berlin, 1996.
[44] M.A. Singer, S.B. Pope, H.N. Najm, Combust. Theory Model. 10 (2) (2006) 199–217.
[45] R. Cabra, J.Y. Chen, R.W. Dibble, A.N. Karpetis, R.S. Barlow, Combust. Flame 143 (4) (2005) 491–506.
[46] Y. Mizobuchi, J. Shinjo, S. Ogawa, T. Takeno, Proc. Combust. Inst. 30 (2005) 611–619.
[47] <http://public.ca.sandia.gov/tnf/chemistry.html>.
[48] C.J. Sung, C.K. Law, J.-Y. Chen, Combust. Flame 125 (906–919) (2001).
[49] C.F. Curtiss, J.O. Hischfelder, J. Chem. Phys. 17 (1949) 550.
[50] A. Liñán, Acta Astronaut. (1) (1974) 1007–1039.
[51] D.C. Haworth, M.C. Drake, S.B. Pope, R.J. Blint, The importance of time-dependent flame structures in stretched laminar flamelet models for turbulent jet diffusion flames, in: Proceedings of the 22nd Symposium (Int.) on Combustion, The Combustion Institute, Pittsburgh, 1988, pp. 589–597.
[52] G.R. Ruetsch, L. Vervisch, A. Liñán, Phys. Fluids 6 (7) (1995) 1447–1454.
[53] R.J. Kee, J.F. Grcar, M.D. Smooke, J.A. Miller, A FORTRAN program for modeling steady laminar one-dimensional premixed flames, sand85-8240. Technical report, Sandia National Laboratories, 1985.
[54] P. Domingo, L. Vervisch, K.N.C. Bray, Combust. Theory Model. 6 (4) (2002) 529–551.
[55] C. Duwig, L. Fuchs, Study of a gas turbine combustion chamber: influence of the mixing on the flame dynamics, in: Proc. of ASME Turbo expo, GT2004-53276, Vienna, Austria, June 14–17, 2004.
[56] S.H. Chung, C.K. Law, Combust. Flame 72 (3) (1988) 325–336.
[57] P. Clavin, Annu. Rev. Fluid Mech. 26 (1994) 321–352.
[58] L.P.H. de Goey, J.H.M. Boonkkamp, Ten Thije. Combust. Flame 119 (1999) 253–271.
[59] L.P.H. de Goey, R.M.M. Malllens, J.H.M. Ten Thije Boonkkamp, Combust Flame 110 (1997) 54–66.
[60] J.A.M. de Swart, G.R.A. Groot, J.A. van Oijen, J.H.M. Ten Thije Boonkkamp, L.P.H. de Goey, Combust. Flame 145 (2006) 245–258.
[61] D. Bradley, P.H. Gaskell, X.J. Gu, The mathematical modeling of liftoff and blowoff of turbulent non-premixed methane jet flames at high strain rate, in: Twenty-Seventh Symposium (Int.) Symposium on Combustion, 1998, pp. 1199–1206.
[62] R.S. Barlow, J.H. Frank, A.N. Karpetis, J.-Y. Chen, Combust. Flame 143 (2005) 433–449.
[63] L. Wang, N.J. Peters, Fluid Mech. 554 (2006) 457–475.
[64] L. Wang, N. Peters, Phys. Scr. T132 (014006) (2008).
[65] H. Phillips, Flame in a buoyant methane layer, in: Proceedings of the 10th Symp. (Int.) on Combustion, 1965, pp. 1277–1283.
[66] P.N. Kioni, B. Rogg, K.N.C. Bray, A. Liñán, Combust. Flame 95 (1993) 276–290.
[67] D. Veynante, B. Fiorina, P. Domingo, L. Vervisch, Combust. Theory Model. 12 (6) (2008) 1055–1088.

Bibliography

[1] Abdel-Gayed, R. G. and Bradley, D. (1985). Criteria for turbulent propagation limits of premixed flames. *Combust. Flame*, **vol. 62**: pp. 61–68.

[2] Abdel-Gayed, R. G. and Bradley, D. (1989). Combustion regimes and straining of turbulent premixed flames. *Combust. Flame*, **vol. 76**: pp. 213–218.

[3] Ahmed, S. F. (2006). *Spark ignition of turbulent non-premixed flames.* Ph.D. thesis, University of Cambridge.

[4] Ahmed, S. F., Balachandran, R., Marchione, T. and Mastorakos, E. (2007). Spark ignition of turbulent nonpremixed bluff-body flames. *Combust. Flame*, **vol. 151**: pp. 366–385.

[5] Ahmed, S. F. and Mastorakos, E. (2006). Spark ignition of lifted turbulent jet flames. *Combust. Flame*, **vol. 146**: pp. 215–231.

[6] Akindele, O. O., Bradley, D., Mak, P. W. and McMahon, M. (1982). Spark ignition of turbulent gases. *Combust. Flame*, **vol. 47**: pp. 129–155.

[7] Al-Abdeli, Y. M. and Masri, A. R. (2003). Recirculation and flowfield regimes of unconfined non-reacting swirling flows. *Experimental thermal and fluid science*, **vol. 27**: pp. 655–665.

[8] Alvani, R. F. and Fairweather, M. (2002). Ignition characteristics of turbulent jet flows. *Chemical Engineering Research and Design*, **vol. 80**: pp. 917–923.

[9] Arcoumanis, C. and Kamimoto, T., *Flow and combustion in reciprocating engines* (Springer, 2009).

[10] Balachandran, R. (2005). *Experimental Investigation of the Response of Turbulent Premixed Flames to Acoustic Oscillations.* Ph.D. thesis, University of Cambridge.

[11] Barlow, R. S. and Frank, J. H., Effects of turbulence on species mass fractions in methane/air jet flames. In *Proceedings of the 27th Symp. (Int.) on Combustion*, (pp. 1087–1095) (1998).

[12] Bilger, R. W., *Turbulent reacting flows*, chap. Turbulent flows with nonpremixed reactants, (pp. 65–113). ISBN: 978-3-540-10192-5 (Springer Berlin / Heidelberg, 1980).

[13] Bilger, R. W. (1993). Conditional moment closure for turbulent reacting flow. *Phys. Fluids*, **vol. 5**: pp. 436–444.

[14] Bilger, R. W. (2000). Future progress in turbulent combustion research. *Progress in Energy and Combustion Science*, **vol. 26**: pp. 367–380.

[15] Bilger, R. W. and Klimenko, A. Y. (1999). Conditional moment closure for turbulent combustion. *Progress in Energy and Combustion Science*, **vol. 25**: pp. 595–687.

[16] Bilger, R. W., Starner, S. H. and Kee, R. J. (1990). On reduced mechanisms for methane-air combustion in nonpremixed flames. *Combust. Flame*, **vol. 80**: pp. 135–149.

[17] Birch, A. D., Brown, D. R. and Dodson, M. G., Ignition probabilities in turbulent mixing flows. In *Symposium (International) on Combustion*, vol. 18, (pp. 1175–1780) (1981).

[18] Boudier, G., Gicquel, L. Y. M. and Poinsot, T. J. (2008). Effects of mesh resolution on large eddy simulation of reacting flows in complex geometry combustors. *Combust. Flame*, **vol. 155(1-2)**: pp. 196–214.

[19] Bradley, D., Gaskell, P. H. and Gu, X. J. (1998). The modeling of aerodynamic strain rate and flame curvature effects in premixed turbulent combustion. *Twenty-Seventh Symp. (Int.) on Combustion*, **vol. 27**: pp. 849–856.

[20] Bradley, D., Gaskell, P. H., Gu, X. J. and Sedaghat, A. (2005). Premixed flamelet modeling: factors influencing the turbulent heat release rate source term and the turbulent burning velocity. *Combust Flame*, **vol. 143(3)**: pp. 227–245.

[21] Bradley, D., Kwa, L. K., Lau, A. K. C., Missaghi, M. and Chin, M. (1988). Laminar flamelet modelling of recirculating premixed methane and propane air combustion. *Combust. Flame*, **vol. 71**: pp. 109–122.

[22] Bradley, D., Lau, A. K. C. and Lawes, M. (1992). Flame stretch rate as a determinant of turbulent burning velocity. *Phil. Trans R Soc. Lond. A*, **vol. 338**: pp. 359–387.

[23] Bray, K. N. C. (1996). The challenge of turbulent combustion. *Proc. Combust. Inst.*, **vol. 26**: pp. 1–26.

[24] Candel, S. M. and Poinsot, T. (1990). Flame stretch and the balance equation for the flame surface area. *Combust. Sci. Tech.*, **vol. 70**: pp. 1–15.

[25] Chakraborty, N., Mastorakos, E. and Cant, R. S. (2007). Effects of turbulence on spark ignition in inhomogeneous mixtures: a direct numerical simulation (dns) study. *Combust. Sci. Tech.*, **vol. 179**: pp. 293–317.

[26] Chaparro, A. A. and Cetegen, B. M. (2006). Blowoff characteristics of bluff-body stabilized conical premixed flames under upstream velocity modulation. *Combust. Flame*, **vol. 144**: pp. 318–335.

[27] Chen, J. H. and Im, H. G. (1998). Correlation of flame speed with stretch in turbulent premixed methane/air flames. *Twenty-Seventh Symposium (International) on Combustion. The Combustion Institute*, (pp. 819–826).

[28] Cheng, R. K. (1984). Conditional sampling of turbulence intensities and Reynolds stress in premixed turbulent flames. *Combust. Sci. Tech.*, **vol. 41**: pp. 109–142.

[29] Cheng, R. K. and Shepherd, I. G. (1991). The influence of burner geometry on premixed turbulent flame propagation. *Combust. Flame*, **vol. 85**: pp. 7–26.

[30] Cheng, R. K., Shepherd, I. G. and Gokalp, I. (1989). A comparison of the velocity and scalar spectra in premixed flames. *Combust. Flame*, **vol. 78**: pp. 205–221.

[31] Chung, S. H. and Law, C. K. (1988). An integral analysis of the structure and propagation of stretched premixed flames. *Combust. Flame*, **vol. 72(3)**: pp. 325–336.

[32] Clavin, P. (1994). Premixed combustion and gasdynamics. *Annu. Rev. Fluid Mech.*, **vol. 26**: pp. 321–52.

[33] Clavin, P. and Williams, F. A. (1982). Effects of molecular diffusion and thermal expansion on the structure and dynamics of premixed flames in turbulent flows of large scale and low intensity. *J. Fluid Mech.*, **vol. 116**: p. 215.

[34] Colin, O., Ducros, F., Veynante, D. and Poinsot, T. (2000). A thickened flame model for large eddy simulations of turbulent premixed combustion. *Phys. Fluids*, **vol. 12**: pp. 1843–1863.

[35] Dally, B. B., Fletcher, D. F. and Masri, A. R. (1998). Flow and mixing fields of turbulent bluff-body jets and flames. *Combust. Theory Modeling*, **vol. 2(2)**: pp. 193–219.

[36] de Goey, L. P. H., Mallens, R. M. M. and ten Thije Boonkkamp, J. H. M. (1997). An evaluation of different contributions to flame stretch for stationary premixed flames. *Combust Flame*, **vol. 110**: pp. 54–66.

[37] de Goey, L. P. H. and ten Thije Boonkkamp, J. H. M. (1997). A mass-based definition of flame stretch for flames with finite thcikness. *Combust. Flame*, **vol. 122**: pp. 399–405.

[38] de Goey, L. P. H. and ten Thije Boonkkamp, J. H. M. (1999). A flamelet description of premixed laminar flames and the relation with flame stretch. *Combust. Flame*, **vol. 119**: pp. 253–271.

[39] de Swart, J. A. M., Groot, G. R. A., van Oijen, J. A., ten Thije Boonkkamp, J. H. M. and de Goey, L. P. H. (2006). Detailed analysis of the mass burning rate of stretch flames including preferential diffusion effects. *Combust. Flame*, **vol. 145**: pp. 245–258.

[40] Delaunay, D., Lakehal, D. and Pierrat, D. (1995). Numerical approach for wind loads prediction on buildings and structures. *Journal of Wind Engineering and Industrial Aerodynamics*, **vol. 57**: pp. 307–321.

[41] Domingo, P., Vervisch, L., Payet, S. and Hauguel, R. (2005). DNS of a premixed turbulent V flame and LES of a ducted flame using a FSD-PDF subgrid scale closure with FPI-tabulated chemistry. *Combust. Flame*, **vol. 143**: pp. 566–586.

[42] Domingo, P., Vervisch, L. and Veynante, D. (2008). Large-eddy simulation of a lifted methane jet flame in a vitiated coflow. *Combust. Flame*, **vol. 152**: pp. 415–432.

[43] Duclos, J. M. and Colin, O. (2001). Arc and kernel tracking ignition model for 3d si engines calculations. *Comodia, Nagoya, Japan*, (pp. 343–350).

[44] Ducros, F., Comte, P. and Lesieur, M. (1996). Large-eddy simulation of transition to turbulence in a boundary layer developing spatially over a flat plate. *J. Fluid Mech.*, **vol. 326**: pp. 1–36.

[45] Ducros, F., Laporte, F., Souleres, T., Guinot, V., Moinat, P. and Caruelle, B. (2000). High-order fluxes for conservative skew-symmetric-like schemes in structured meshes: application to compressible flows. *Journal of Computational Physics*, **vol. 161**: pp. 114–139.

[46] Duwig, C., Szasz, R. Z., Fuchs, L. and Troger, C. (2005). Large eddy simulation of a swirling flame response to swirl modulation with impact on combustion stability. *AIAA -2004-4941.*

[47] Eickhoff, H., Lenze, B. and Leuckel, W., Experimental investigation on the stabilization mechanism of jet diffusion flames. In *20th Symp. (Int.) on Combustion, Pittsburgh.*, (pp. 311–318) (1984).

[48] El-Asrag, H. and Menon, S. (2007). Large eddy simulation of bluff-body stabilized swirling non-premixed flames. *Proc. Combust. Inst.*, **vol. 31**: pp. 1747–1754.

[49] El-Mahallawy, F. and din Habik, S. E., *Fundamentals and technology of combustion* (Elsevier Science Ltd, 2005).

[50] Energy (2002). World energy outlook 2002. International Energy Agency, 533, Paris.

[51] Esquiva-Dano, I. and Escudie, D. (2005). A way of considering the influence of the bluff-body geometry on the nonpremixed flame stabilization process. *Combust. Flame*, **vol. 142**: pp. 299–302.

[52] Esquiva-Dano, I., Nguyen, H. T. and Escudie, D. (2001). Influence of a bluff-body's shape on the stabilization regime of non-premixed flames. *Combust. Flame*, **vol. 127**: pp. 2167–2180.

[53] Fabri, J., Siestrunck, R. and Foure, C. (1949). On the aerodynamics field of stabilized flames. *Recherche Aeronautique*, **vol. 25**: pp. 21–27.

[54] Fan, L., Li, G., Han, Z. and Reitz, R. D. (1999). Modeling fuel preparation and stratified combustion in a gasoline direct injection engine. *SAE paper 1999-01-0176.*

[55] Favier, V., Vervisch, L., Herrmann, M., Terhoeven, P., Binninger, B. and Peters, N. (1998). Numerical simulation of combustion in partial premixed turbulent flows. *Notes on Numerical Fluid Mechanics*, **vol. 66**: pp. 203–221.

[56] Favre, A. (1983). Turbulence: space-time statistical properties and behaviour in supersonic flows. *Phys. Fluids*, **vol. 10**: pp. 2851–2863.

[57] Ferreira, J. C. (1996). *Flamelet modelling of stablization in turbulent non-premixed combustion.* Ph.D. thesis, Swiss Federal Institute of Technology, Switzerland. Diss ETH No. 11984.

[58] Ferziger, J. and Perić, M., *Computational Methods for Fluid Dynamics* (Springer-Verlag Berlin Heidelberg, New York., 2002), 3rd edn.

[59] Filatyev, S. A., Driscoll, J. F., Carter, C. D. and Donbar, J. M. (2005). Measured properties of turbulent premixed flames for model assessment, including burning velocities, stretch rates, and surface densities. *Combust. Flame*, **vol. 141(1-2)**: pp. 1 – 21.

[60] Fiorina, B., Gicquel, O., Vervisch, L., Carpentier, S. and Darabiha, N. (2005). Approximating the chemical structure of partially premixed and diffusion counterflow flames using FPI flamelet tabulation. *Combust. Flame*, **vol. 140**: pp. 147–160.

[61] Fiorina, B., Gicquel, O., Vervisch, L., Carpentier, S. and Darabiha, N. (2005). Approximating the chemical structure of partially premixed and diffusion counterflow flames using FPI flamelet tabulation. *Combust. Flame*, **vol. 140(3)**: pp. 147–160.

[62] Fiorina, B., Gicquel, O., Vervisch, L., Carpentier, S. and Darabiha, N. (2005). Premixed turbulent combustion modeling using tabulated detailed chemistry and PDF. *Proc. Combust. Inst*, **vol. 30**: pp. 867–874.

[63] Flohr, P. and Pitsch, H., A turbulent flame speed closure model for LES of industrial burner flows. In *Proceedings of Summer Program 2000, CTR*, (pp. 169–179) (2000).

[64] Freitag, M., Klein, M., Gregor, M., Geyer, D., Schneider, C., Dreizler, A. and Janicka, J. (2006). Mixing analysis of a swirling recirculating flow using DNS and experimental data. *International Journal of Heat and Fluid Flow*, **vol. 27**: pp. 636–643.

[65] Fujimoto, Y., Inokuchi, Y. and Yamasaki, N. (2005). Large eddy simulation of swirling jet in a bluff body burner. *Journal of thermal science*, **vol. 14**: pp. 28–33.

[66] Fujimoto, Y. and Yamasaki, N. (2006). Large eddy simulation of swirling jet in a bluff body burner. *JSME International Journal*, **vol. 49**: pp. 1125–1132.

[67] Fureby, C., Grinstein, F. F., Li, G. and Gutmark, E. J. (2007). An experimental and computational study of a multi-swirl gas turbine combustor. *Proc. Combust. Inst.*, **vol. 31**: pp. 3107–3114.

[68] Galpin, J., Naudin, A., Vervisch, L., Angelberger, C., Colin, O. and Domingo, P. (2008). Large-eddy simulation of a fuel-lean premixed turbulent swirl-burner. *Combust. Flame*, **vol. 155**: pp. 247–266.

[69] Garcia-Villalba, M., Frohlich, J. and Rodi, W. (2005). Large eddy simulation of an annular swirling jet with pulsating inflow. *Proc. 4th Int. Symposium on Turbulence and Shear Flow Phenomena. Williamsburg. USA.*

[70] Ghedhaifi, W., Darabiha, N., Gicquel, O., Veynante, D. and Pierrot, L. (2005). A flame surface density model including tabulated chemistry and heat losses. *20th International Colloquium on the Dynamics of Explosions and Reactive systems, Montreal*, (pp. 445–469).

[71] Gicquel, O., Darabiha, N. and Thevenin, D. (2000). Laminar premixed hydrogen/air couterflow flame simulations using flame prolongation of ILDM with differential diffusion. *Proc. Combust. Inst.*, **vol. 28**: pp. 1901–1908.

[72] Glassman, I., *Combustion* (Academic press Inc, 1987), 2nd edn.

[73] Godel, G., Domingo, P. and Vervisch, L. (2009). Tabulation of nox chemistry for large-eddy simulation of non-premixed turbulent flames. *Proc. Combust. Inst.*, **vol. 32**: pp. 1555–1561.

[74] Haq, M. Z., Sheppard, C. G. W., Woolley, R., Greenhalgh, D. A. and Lockett, R. D. (2002). Wrinkling and curvature of laminar and turbulent premixed flames. *Combust. Flame*, **vol. 131**: pp. 1–15.

[75] Hassan, M. I., Aung, K. T. and Faeth, G. M. (1998). Measured and predicted properties of laminar premixed methane/air flames at various pressures. *Combust. Flame*, **vol. 115(4)**: pp. 539 – 550.

[76] Hawkes, E. R. and Cant, R. S. (2001). Implications of a flame surface density approach to large eddy simulation of premixed turbulent combustion. *Combustion and Flame*, **vol. 126(3)**: pp. 1617 – 1629. ISSN 0010-2180. doi:DOI: 10.1016/S0010-2180(01)00273-5.

[77] Hesse, H., Chakraborty, N. and Mastorakos, E. (2009). The effects of the Lewis number of the fuel on the displacement speed of edge flames in igniting turbulent mixing layers. *Proc. Combust. Inst.*, **vol. 32**: pp. 1399–1407.

[78] Jameson, A., Schmidt, W. and Turkel, E. (1981). Numerical solution of the Euler equations by finite volume methods Runge-Kutta time-stepping schemes. *AIAA Paper, Fluid and Plasma Dynamics Conference, 14th, Palo Alto, CA*, **vol. 1251**.

[79] Jenkins, K., Klein, M., Chakraborty, N. and Cant, R. (2006). Effects of strain rate and curvature on the propagation of a spherical flame kernel in the thin-reaction-zones regime. *Combustion and Flame*, **vol. 145(1-2)**: pp. 415 – 434.

[80] Jimenez, C., Ducros, F., Cuenot, B. and Bedat, B. (2001). Subgrid scale variance and dissipation of a scalar field in large eddy simulations. *Phys. Fluids*, **vol. 13**: pp. 1748–1754.

[81] Kaminski, C. F., Hult, J., Alden, M., Lindenmaier, S., Dreizler, A., Mass, U. and Baum, M. (2000). Spark ignition of turbulent methane/air mixtures revealed by time-resolved planar laser-induced fluorescence and direct numerical simulations. *Proc. Combust. Inst.*, **vol. 28**: pp. 399–405.

[82] Karlovitz, B., Denniston, D. W. J. and Wells, F. E. (1951). Investigation of turbulent flames. *Journal of Chemical Physics*, **vol. 19(5)**: pp. 541–547.

[83] Kee, R. J., Gracer, J. F., Smooke, M. D. and Miller, J. A. (1990). A Fortran program for modeling steady laminar one-dimensional premixed flames. *Tech. rep.*, Report no - Report No. SAND87-8248 UC-4, Sandia National Laboratories.

[84] Kempf, A., Lindstedt, R. P. and Janicka, J. (2006). Large-eddy simulation of a bluff-body stabilized nonpremixed flame. *Combust. Flame*, **vol. 144**: pp. 170–189.

[85] Kim, S. H. and Huh, K. Y. (2002). Use of the conditional moment closure model to predict NO formation in a turbulent CH_4/H_2 flame over a bluff-body. *Combust. Flame*, **vol. 130**: pp. 94–111.

[86] Klein, M., Sadiki, A. and Janika, J. (2003). A digital filter based generation of inflow data for spatially developing direct numerical or large eddy simulations. *Journal of Computational Physics*, **vol. 186**: pp. 652–665.

[87] Klimenko, A. Y. (1990). Multicomponent diffusion of various admixtures in turbulent flow. *Fluid Dymanics*, **vol. 25**: pp. 327–334.

[88] Klimenko, A. Y. (2001). On the relation between the conditional moment closure and unsteady flamelets. *Combust. Theory Modelling*, **vol. 5**: pp. 275–294.

[89] Krohenburg, A., Bilger, R. W. and Kent, J. H. (1998). Second order conditional moment closure for turbulent jet diffusion flames. *Proc. Combust. Inst.*, **vol. 29**: pp. 1097–1104.

[90] Lacaze, G., Richardson, E. and Poinsot, T. (2009). Large eddy simulations of spark ignition in a turbulent methane jet. *Combust. Flame*, **vol. 156(10)**: pp. 1993–2009.

[91] Law, C. K., *Combustion physics* (Cambridge University Press, 2006), 1st edn.

[92] Lee, J. G., Lee, T. W., Nye, D. A. and Santavicca, D. A. (1995). Lewis number effects on premixed flames interacting with turbulent Karman vortex streets,. *Combust. Flame*, **vol. 100(1-2)**: pp. 161 – 168.

[93] Liao, S. Y., Jiang, D. M. and Cheng, Q. (2004). Determination of laminar burning velocities for natural gas. *Fuel*, **vol. 83(9)**: pp. 1247 – 1250. ISSN 0016-2361. doi:DOI: 10.1016/j.fuel.2003.12.001.

[94] Linan, A. and Williams, F. A., *Fundamental aspects of combustion* (Oxford University press, 1993).

[95] Lodato, G., Domingo, P. and Vervisch, L. (2008). Three-dimensional boundary conditions for direct and large-eddy simulation of compressible viscous flows. *Journal of Computational Physics*, **vol. doi:10.1016/j.jcp.2008.01.038**.

[96] Lodato, G., Domingo, P. and Vervisch, L. (2009). A compressible wall-adapting similarity mixed model for large-eddy simulation of the impinging round jet. *Phys. Fluids*, **vol. DOI: 10.1063/1.3068761**.

[97] Lodato, G., Domingo, P., Vervisch, L. and Veynante, D., Scalar variances: LES against measurements and mesh optimization criterion. scalar gradient: a three-dimensional estimation from planar measurements using DNS. In *Proceedings of Summer Program 2008, CTR*, (pp. 387–398) (2008).

[98] Lund, T. S. (2003). The use of explicit filters in large eddy simulation. *Computers and Math. with Applications*, **vol. 46**: pp. 603–616.

[99] Magnussen, B. F. and Hjertager, B. H. (1976). On mathematical modelling of turbulent combustion with special emphasis on soot formation and combustion. *Proc. 16th Symp.(Inter.) on Combustion*, (pp. 719–729).

[100] Maly, R. (1981). Ignition model for spark discharges and the early phase of flame front growth. *Proc. 18th Symp.(Inter.) on Combustion*, (pp. 1747–1754).

[101] Maly, R. and Vogel, M. (1978). Initiation and propagation of flame fronts in lean CH_4-air mixtures by the three modes of the ignition spark. *Proc. 17th Symp.(Inter.) on Combustion, Pittsburgh*, (pp. 821–831).

[102] Marble, F. and Broadwell, J. (1977). The coherent flame model of non-premixed turbulent combustion. *Tech. rep.*

[103] Marchione, T., Ahmed, S. F. and Mastorakos, E. (2009). Ignition of turbulent swirling n-heptane spray flames using single and multiple sparks. *Combust. Flame*, **vol. 156**: pp. 166–180.

[104] Markstein, G. H., *Nonsteady flame propagation* (Pergamon press, Oxford, 1964).

[105] Marley, S. K., Danby, S. J., Roberts, W. L., Drake, M. C. and Fansler, T. D. (2008). Quantification of transient stretch effects on kernel–vortex interactions in premixed methane–air flames. *Combust. Flame*, **vol. 154**: pp. 296–309.

[106] Mass, U. and Pope, S. B. (1992). Implementation of simplified chemical kinetics based on intrinsic low-dimensional manifolds. *Proc. 24th Symp.(Inter.) on Combustion*, **vol. 24**: pp. 103–112.

[107] Matthews, R. (2003). Railplug ignition system for enhanced engine performance and reduced maintenance. *Tech. Rep. DE-FG26-01NT41334*, The University of Texas, Austin, TX 78712.

[108] Meneveau, C. and Poinsot, T. (1991). Stretching and quenching of flamelets in premixed turbulent combustion. *Combust. Flame*, **vol. 86**: pp. 311–332.

[109] Merci, B., Dick, E., Vierendeels, J., Roekaerts, D. and Peeters, T. W. J. (2001). Application of a new cubic turbulence model to piloted and bluff-body diffusion flames. *Combust. Flame*, (pp. 1533–1556).

[110] Métais, O. and Lesieur, M. (1992). Spectral large-eddy simulation of isotropic and stably stratified turbulence. *J. Fluid Mech.*, **vol. 239**: pp. 157–194.

[111] Moss, J. B. and Bray, K. N. C. (1977). A unified statistical model of the premixed turbulent flame. *Acta Astronaut*, **vol. 4**: pp. 291–319.

[112] Moureau, V., Fiorina, B. and Pitsch, H. (2009). A level set formulation for premixed combustion LES considering the turbulent flame structure. *Combust. Flame*, **vol. 156(4)**: pp. 801 – 812.

[113] Muradoglu, M., Liu, K. and Pope, S. B. (2003). PDF modeling of a bluff-body stabilized turbulent flame. *Combust. Flame*, **vol. 132**: pp. 115–137.

[114] Nguyen, P.-D., Vervisch, L., Subramanian, V. and Domingo, P. (2009). Multidimensional flamelet-generated manifolds for partially premixed combustion. *Combust. Flame*, **vol. 157**: pp. 43–61.

[115] Nicoud, F. and Ducros, F. (1999). Subgrid-scale stress modelling based on the square of the velocity gradient tensor. *Flow Turbulence and Combustion*, **vol. 62**: pp. 183–200.

[116] Pascaud, S., Boileau, M., Martinez, L., Cuenot, B. and Poinsot, T. (2005). LES of steady spray flame and ignition sequences in aeronautical combustors. *1st workshop INCA, SNECMA, Villaroche, France*, (pp. 19–26).

[117] Patte-Rouland, B., Lalizel, G., Moreau, J. and Rouland, E. (2001). Flow analysis of an annular jet by particle image velocimetry and proper orthogonal decomposition. *Measurement Science and Technology*, **vol. 12**: pp. 1404–1412.

[118] Peters, N. (1984). Laminar diffusion flamelet models in non-premixed turbulent combustion. *Prog. Energy Combust. Sci.*, **vol. 10**: pp. 319–339.

[119] Peters, N. (1999). The turbulent burning velocity for large scale and small scale turbulence. *J. Fluid Mech.*, **vol. 384**: pp. 107–132.

[120] Peters, N., *Turbulent Combustion* (Cambridge University Press, 2000).

[121] Peters, N. and Williams, F. A. (1983). Lift-off characteristics of turbulent jet diffusion flame. *AIAA Journal*, **vol. 21**: pp. 423–429.

[122] Peters, N. and Williams, F. A. (1987). Asymptotic structure of stoichiometric methane-air flames. *Combust. Flame*, **vol. 68**: pp. 185–207.

[123] Phillips, H. (1965). Flame in a bouyant methane layer. *Proc. 10th Symp.(Inter.) on Combustion*, (pp. 1277–1283).

[124] Poinsot, T., Using direct numerical simulations to understand premixed turbulent combustion. In *Proc. 26th Symp.(Inter.) on Combustion, Pittsburgh.*, (pp. 219–232) (1996).

[125] Poinsot, T. and Veynante, D., *Theoretical and Numerical Combustion* (R. T. Edwards, Inc., 2005).

[126] Poinsot, T. J. and Lele, S. K. (1992). Boundary conditions for direct simulations of compressible viscous flow. *Journal of Computational Physics*, **vol. 101**: pp. 104–129.

[127] Pope, S. B. (1985). PDF methods for turbulent reactive flows. *Progress in Energy and Combustion Science*, **vol. 11**: pp. 119–192.

[128] Pope, S. B. (1988). The evolution of surfaces in turbulence. *Int. J Engng. Sci.*, **vol. 26**: pp. 445–469.

[129] Pope, S. B. (2004). Ten questions concerning the large eddy simulation of turbulent flows. *New Journal of Physics*, **vol. 6**.

[130] Pope, S. B. and Anand, M. S. (1984). Flamelet and distributed combustion in premixed turbulent flames. *20th Symphosium (International) on Combustion*, (pp. 403–410).

[131] Raman, V. and Pitsch, H. (2005). Large-eddy simulation of a bluff-body-stabilized non-premixed flame using a recursive filter-refinement procedure. *Combust. Flame*, **vol. 142**: pp. 329–347.

[132] Ribert, G., Champion, M., Gicquel, O., Darabiha, N. and Veynante, D. (2005). Modeling nonadiabatic turbulent premixed reactive flows including tabulated chemistry. *Combust. Flame*, **vol. 141**: pp. 271–280.

[133] Richard, S., Colin, O., Vermorel, O., Benkenida, A., Angelberger, C. and Veynante, D. (2007). Towards large eddy simulation of combustion in spark ignition engines. *Proc. Combust. Inst.*, **vol. 31**: pp. 3059–3066.

[134] Richard, S., Colin, O., Vermorel, O., Benkenida, A., Angelberger, C. and Veynante, D. (2007). Towards large eddy simulation of combustion in spark ignition engines. *Proc. Combust. Inst.*, **vol. 31**: pp. 3059–3066.

[135] Richardson, E. S. and Mastorakos, E. (2007). Numerical investigation of forced ignition in laminar counterflow non-premixed methane-air flames. *Combust. Sci. Tech.*, **vol. 179**: pp. 21–37.

[136] Rodi, W. (1997). Comparison of LES and RANS calculation of the flow around bluff bodies. *Journal of Wind Engineering and Industrial Aerodynamics*, **vol. 69-71**: pp. 55–75.

[137] Rogg, B., Behrendt, F. and Warnatz, J. (1986). Turbulent non-premixed combustion in partially premixed diffusion flamelets with detailed chemistry. *Proc. 21st Symp.(Inter.) on Combustion*, (pp. 1533–1541).

[138] Rulland, M. (2004). *Modélisation de la combustion turbulente via une methode de tabulation de la cinétique chimique détailée couplée á des fonctions de densités de probabilité. Application aux foyers aéronautiques.* Ph.D. thesis, CORIA-CNRS lab.

[139] Sagaut, P., *Large Eddy Simulation for Incompressible Flows- An Introduction* (Springer, 2006), 3rd edn.

[140] Santavicca, D. A. (1995). Spark ignited turbulent flame kernel growth. *Tech. Rep. OSTI ID: 6605*, Pennsylvania State University, University Park, PA (US).

[141] Schlichting, H., *Boundary-Layer Theory* (Mc Graw Hill, New York, 1979), seventh edn.

[142] Scurlock, A. C. (1948). Flame stabilization and propagation in high velocity gas streams. *Tech. rep.*, MIT, Fuel Res. Lab.

[143] Sheen, H. J., Chen, W. J. and Wu, J. S. (1997). Flow patterns for an annular flow over an axisymmetric sudden expansion. *J. Fluid Mech.*, **vol. 350**: pp. 177–188.

[144] Singer, M. A. and Pope, S. B. (2004). Exploiting ISAT to solve the reaction-diffusion equation. *Combustion theory and modelling*, **vol. 8**: pp. 361–383.

[145] Sinibaldi, J. O., Mueller, C. H. and Driscoll, J. F. (19998). Local flame propagation speeds along wrinkled, unsteady stretched premixed flames. *Proc. 27th Symp.(Inter.) on Combustion*, (pp. 827–832).

[146] Smagorinsky, J. (1963). General circulation experiments with the primitives equations. *Mon. Weather Rev.*, **vol. 61**: pp. 99–164.

[147] Smith, G. P., Golden, D. M., Frenklach, M., Moriarty, N. W., Eiteneer, B., Goldenberg, M., Bowman, C. T., Hanson, R. K., Song, S., Gardiner, W. C., Lissianski, V. V. and Qin, Z. (1999). GRI-mech 3.0. *Tech. rep.*, University of California, Berkeley. Http://www.me.berkeley.edu/gri-mech/.

[148] Spadling, D. B., Mixing and chemical reactions in steady confined turbulent flames. In *Proc. 13th Symp.(Inter.) on Combustion, Pittsburgh.*, (pp. 649–657) (1971).

[149] Stone, C. and Menon, S. (2002). Parallel simulations of swirling turbulent flames. *Journal of Supercomputing*, **vol. 22**: pp. 7–28.

[150] Stone, C. and Menon, S. (2003). LES of partially-premixed unsteady combustion. *AIAA Journal 2003-310*, (pp. 1–11).

[151] Swaminathan, N. and Bilger, R. W. (1998). Assessment of combustion submodels for turbulent nonpremixed hydrocarbon flames. *Combust. Flame*, **vol. 116**: pp. 519–545.

[152] Swanson, R. and Turkel, E. (1992). On central-difference and upwind schemes. *Journal of Computational Physics*, **vol. 101(2)**: pp. 292–306.

[153] Taglia, C. D., Blum, L., Gass, J., Ventikos, Y. and Poulikakos, D. (2004). Numerical and experimental investigation of an annular jet flow with large blockage. *Journal of Fluid Engineering*, **vol. 126**: pp. 375–384.

[154] Taglia, C. D., Glass, J. and Dreher, H. (1984). Optimisation of a low-NOx combustion chamber using CFD simulations. *Progress in Computational Fluid Dynamics*, (pp. 117–130).

[155] Tan, Z. and Reitz, R. D. (2006). An ignition and combustion model based on the level-set method for spark ignition engine multidimensional modeling. *Combust. Flame*, **vol. 145**: pp. 1–15.

[156] Thiele, M., Selle, S., Riedel, U., Warnatz, J. and Mass, U. (2000). Numerical simulation of spark ignition including ionization. *Proc. Combus. Inst.*, **vol. 28**: pp. 1177–1185.

[157] Thiele, M., Warnatz, J. and Maas, U. (2000). Numerical study of spark ignition in two dimensions. *Combustion Theory and Modelling*, **vol. 4**: pp. 413–434.

[158] Triantafyllidis, A., Mastorakos, E. and Eggels, R. L. G. M. (2009). Large eddy simulations of forced ignition of a non-premixed bluff-body methane flame with conditional moment closure. *Combust. Flame*, **vol. 156**: pp. 2328–2345.

[159] Trouve, A. and Poinsot, T. (1994). The evolution equation for the flame surface density. *J. Fluid Mech.*, **vol. 278**: pp. 1–31.

[160] Turns, S. R., *An Introduction to Combustion* (Mc Graw Hill, 2000), 2nd edn.

[161] Valorani, M. and Goussis, D. A. (2001). Explicit time-scale splitting algorithm for stiff problems: auto-ignition of gaseous mixtures behind a steady shock. *Journal of Computational Physics*, **vol. 169**: pp. 44–79.

[162] van Oijen, J. A., Lammers, F. A. and de Goey, L. P. H. (2001). Modeling of complex premixed burner systems by using flamelet-generated manifolds. *Combust. Flame*, **vol. 127(3)**: pp. 2124–2134.

[163] Vervisch, L. (1992). Study and modeling of finite rate chemistry effects in turbulent non-premixed flames. *Annual Research Briefs. Center for Turbulence Research, Stanford Univ./NASA Ames*, **vol. 411**.

[164] Vervisch, L., Domingo, P., Rullaud, M. and Hauguel, R. (2004). Three facets of turbulent combustion modelling: DNS of premixed v-flame, LES of lifted nonpremixed flame and RANS of jet-flame. *Journal of turbulence*, **vol. 5**: pp. 1–36.

[165] Vervisch, L., Lodato, G. and Domingo, P., *Quality and Reliability of Large-Eddy Simulations*, chap. Reliability of Large-Eddy Simulation of Nonpremixed Turbulent Flames: Scalar Dissipation Rate Modeling and 3D-Boundary Conditions, (pp. 227–237). ISBN:978-1-4020-8577-2 (Springer Netherlands, 2008).

[166] Veynante, D., Lucas, F. and Candel, S. M. (1991). Numerical simulation of transient ignition regime of a turbulent diffusion flame. *AIAA Journal*, **vol. 29**: pp. 848–851.

[167] Veynante, D. and Vervisch, L. (2002). Turbulent combustion modeling. *Progress in Energy and Combustion Science*, **vol. 28**: pp. 193–266.

[168] Vreman, A. W., Albrecht, B. A., van Oijen, J. A. and Bastiaans, R. J. M. (2008). Premixed and nonpremixed generated manifolds in large-eddy simulation of Sandia flame D and F. *Combust. Flame*, **vol. 153(3)**: pp. 394–416.

[169] Warnatz, J., Maas, U. and Dibble, R., *Combustion* (Springer-Verlag, 2006), 4th edn.

[170] Williams, F. A. (1974). A review of some theoretical consideration of turbulent flame structure. *Agard conference proceedings*, (p. No. 164).

[171] Williams, F. A. (1985). The mathematics of combustion. *SIAM, Philadelphia*, (pp. 97–131).

[172] Williams, G. C., Hottel, H. C. and Scurlock, A. C. (1949). Flame stabilization and propagation in high velocity gas streams. *Proc. 3rd Symp.(Inter.) on Combustion*, (pp. 21–40).

[173] Wray, A. A. (1986). Minimal storage time-advancement schemes for spectral methods. Computational fluid dynamics branch, NASA Ames research centre, Moffett Field, CA 94035.

[174] Xia, J., Luo, K. H. and Kumar, S. (2008). Large-eddy simulation of interactions between a reacting jet and evaporating droplets. *Flow Turbulence Combust.*, **vol. 80(1)**: pp. 133–153.

[175] Xu, J. and Ma, H. (2009). Applications of URANS on predicting unsteady turbulent separated flows. *Acta Mechanica Sinica*, **vol. 25**: pp. 319–324.

[176] Zhu, M., Han, X., Ge, H. and Chen, Y. (2007). Simulation of bluff body stabilized flows with hybrid RANS and PDF method. *Acta Mechanica Sinica*, **vol. 23**: pp. 263–273.

[177] Ziegler, G. F. W., Wagner, E. P. and Maly, R. (1984). Ignition of lean methane-air mixtures by pressure glow and arc discharges. *Proc. 20th Symp.(Inter.) on Combustion*, (pp. 1817–1824).